NEXT-GENERATION SURFACE-ENHANCED RAMAN SCATTERING (SERS) NANOPARTICLES FOR BIODIAGNOSTICS AND INTRAOPERATIVE IMAGING

BY

RUIYANG XUE

DISSERTATION

Submitted in partial fulfillment of the requirements
for the degree of Doctor of Philosophy in Materials Science and Engineering
in the Graduate College of the
University of Illinois Urbana-Champaign, 2022

Urbana, Illinois

Doctoral Committee:

Professor Shuming Nie, Chair and Director of Research
Professor Paul Braun
Associate Professor Cecilia Das Neves Barbosa Leal Lauten
Assistant Professor Hua Wang

ABSTRACT

My Ph.D. research focuses on the design of novel SERS nanotags with superior brightness, signal stability and mono-dispersibility for biomedical applications. Chapter 1 starts with a systematic introduction of SERS nanotags, including fundamental theories of SERS (Chapter 1.1), labeled and label-free SERS detection (Chapter 1.2), the design principles of SERS nanotags (Chapter 1.3), and their applications in bio-diagnostics, bioimaging and spectroscopy-guided surgery (Chapter 1.4).

Chapter 2 to Chapter 6 discuss five of my research projects. In Chapter 2, aiming at improving signal robustness of dye-encoded SERS nanoparticles (NPs) in biological fluids, I introduced a hydrophobic inner layer on gold nanoparticle surface using an amphiphilic PEG. The hydrophobic domain brought a 5-10 times SERS intensity improvement compared with its PEG counterpart. The main mechanism behind was hypothesized to be a dielectric medium change at the plasmonic surface leading to electromagnetic enhancement. The rigid hydrophobic shell also provided better resistance to electric field coupling between nanoparticles in high-ionic-strength biological buffers, and prevented severe protein corona formation on SERS NPs, which consequently stabilized SERS signal in serum.

In Chapter 3, to realize non-invasive metastatic sentinel lymph node detection by SERS, the hydrophobic locked Au nanostars (AuNS) were applied as the detection agents using a dual-tracer strategy to minimize the influence of non-specific binding. Good signal linearity and signal independency were achieved. The paired SERS agents show similar surface properties, hydrodynamic size and in-vivo lymph node binding kinetics. A whole spectrum identification algorithm was applied to identify the SERS signal of the paired SERS NPs respectively from the detected mixed signal. The presence of tumor cells at breast cancer metastatic sentinel lymph node was detected based on statistically significant different ratio of the target and non-target SERS NPs in health and tumor mice model.

In Chapter 4, natural derived membranes from red blood cells (RBC) were employed as a novel type of biocompatible layer for SERS NPs. RBC membrane (RBCM) coating offered enhanced SERS intensity with the dyes embedded in the hydrophobic environment of the lipid bilayer. Good cryo-protection ability of the RBCM was observed against harsh storage conditions

such as lyophilization and freezing of the colloids. With lipid-insertion strategy, RBCM coated SERS NPs can be further functionalized with target ligands, and an increased cellular uptake was demonstrated compared with the non-target controls.

In Chapter 5, RBCM coated AuNSs are being used as a dual-modality imaging agent for both preoperative photoacoustic (PA) imaging and intraoperative SERS detection for tumor resection. Star-shaped AuNPs were chosen as the core of the imaging agents due to its superior SERS enhancement as well as energy conversion efficiency for PA compared with spherical nanostructures. A bovine tissue phantom experiment have proved excellent PA and SERS performance demonstrated by these NPs. Natural red-blood-cell membrane was shown to provide better biocompatibility by reducing macrophage uptake, and to realize target ligand conjugation by lipid-insertion strategy. An ex-vivo tissue tumor detection phantom study was then conducted to show the potential of RBCM-coated AuNSs as imaging agents for SERS-PA dual-modality.

In Chapter 6, a quantitative evaluation of near-infrared (NIR) tissue penetration *ex vivo* with the use of SERS was first presented. A preliminary experiment to compare the spectral and tissue scattering properties of SERS in the first and second NIR windows was first performed. Tissue penetration depths were evaluated to be much improved in NIR-II window compared to that at of the first near-infrared (NIR-I) window, as well as a dramatically lower auto-fluorescence background. Aiming at developing SERS NPs excited at the second near-infrared (NIR-II) region for ‘bio-transparent’ in-vivo imaging, I successfully synthesized SERS nanostars with strong resonance in NIR-II range as well as small size around 60 nm for in-vivo purpose. The synthesized NIR-II AuNS with long and sharp tips exhibited strong SERS intensity with NIR-II resonant dye attached, and the high NIR-II absorbance was well preserved after 14 days with the inner hydrophobic layer. The NIR-II SERS AuNSs show great potential for a variety of biomedical applications such as intraoperative imaging, wearable spectroscopic devices development, etc.

ACKNOWLEDGMENTS

Words cannot express my gratitude to my research advisor and chair of my committee, Dr. Shuming Nie, for his invaluable guidance and feedback. I also could not have undertaken this journey without my defense committee members, Dr. Paul Braun, Dr. Cecilia Leal and Dr. Hua Wang, who generously provided knowledge and expertise.

I am also grateful to my postdoc mentor, Dr. Li Lin, for her kind guidance to me at my early stage of the PhD life. I'd also like to thank all my colleagues and my collaborators for their contributions and support. Thanks should also go to the research assistants and staff members from the university shared facilities for giving advices and guidance to me.

Lastly, I would be remiss in not mentioning my family and friends, especially my parents and my partner. Their belief in me has kept my spirits and motivation high during this process. I would also like to thank my cat, Penelope, for her emotional support.

TABLE OF CONTENTS

CHAPTER 1: INTRODUCTION

Surface-enhanced Raman scattering (SERS) effect was first discovered from pyridine molecules absorbed on electrochemically roughened silver surface over 40 years ago [1]. Since then, as a landmark of spectroscopic and analytic techniques, SERS had gained significant attention in the research community. Specifically in biomedical area, SERS is a technique of great potential for sensing or detection because of its excellent selectivity, sensitivity and capability to be performed in aqueous biological systems. With increasing demands of healthcare industry, biomedical applications of SERS are being developed in lots of areas, including quantitative and ultra-sensitive sensing of biomolecules [2, 3], pathogens identification and classification [4, 5], cells labelling and profiling [6], drug metabolites monitoring [7], cellular processes imaging [8], cancer diagnosis and staging [9, 10], and spectroscopy guided surgery [11, 12].

In this chapter, fundamental theories of SERS is first introduced, followed by the introduction of SERS nanotags, a type of detection/imaging agents based on SERS. Then, various biomedical applications of SERS nanotags including biomedical diagnostics, bio-imaging and spectroscopy-guided surgery are briefly summarized.

1.1 Fundamental Theory of Surface-enhanced Raman Scattering (SERS)

Raman scattering is a rare event that happens when photons colloid inelastically with molecules (with a possibility of only one of 10 million collision), during which the scattered photon gain or lose energy. As shown in Figure 1A, if the photon in-elastically interacts with the molecule in the ground state, it loses energy to the molecule, which is the so-called stokes

scattering; otherwise, it is the so-called anti-stokes scattering. In both circumstances, the energy change corresponds to the characteristic vibration energy of the molecules.

Surface-enhancement Raman scattering (SERS) refers to the phenomenon that Raman scattering can be strongly amplified when it takes place at plasmonic surface, in most of the cases, metal surfaces. To describe the Raman enhancement ability of the SERS-active substrates or nanostructures in a universal manner, enhancement factor (EF) is defined, which can be directly calculated by the ratio of the Raman signal intensities of a certain amount of molecules at the present and without the SERS substrate [13], as described in Equation 1.1:

$$\mathrm{EF} = \frac{I_{SERS}/N_{surface}}{I_{RFM}/N_{bulk}} \qquad \text{(Equation 1.1)}$$

Here, I_{SERS} and I_{RFM} are the intensities of the Raman spectra obtained from the SERS and free molecules; and $N_{surface}$ and N_{bulk} are the number of the molecules that are within the excitation volume in the metal surface and in the bulk, respectively.

Since SERS was observed, two main mechanisms had been raised and discussed through the years to explain the enhancement: the electromagnetic enhancement (EM) [14] and the chemical enhancement (CE) [15]. These two mechanisms co-exist in SERS process but contribute in different ways. Electromagnetic field enhancement theory is based on the surface plasmon resonance (SPR) effect. Surface plasmons are delocalized electrons oscillations at the interface that can be induced by incident optical fields [16] . Specifically, localized surface plasmon resonance (LSPR) effect is generated by metal nanoparticles of size comparable to or smaller than the wavelength of excitation light (Figure 1B) rather than traditional SPR generated by continuous metallic films. When electromagnetic waves interact with metal nanoparticles, localized surface plasmons are excited on the surface, generating a field that is tightly confined to the nanoparticle, which results in a redistribution of the EM field intensity in the vicinity of the particle surface. Due

to the resonance effect, the metal nanoparticle function as an amplifier to enhance the Raman scattering of the molecules absorbed at the plasmonic surface (Figure 1C). With the enhancement of incident light field and the Raman scattering field each results in a Raman signal enhancement of the second power of the field amplification enhancement, the overall SERS EF is roughly the fourth power of the electromagnetic field amplification enhancement [14]:

$$G_{SERS} \approx \left|\frac{E_{loc}}{E_0}\right|^4 = \left|\frac{\varepsilon_m - \varepsilon_s}{\varepsilon_m + 2\varepsilon_s}\right|^4 \left(\frac{R}{R+d}\right)^{12} \quad \text{(Equation 1.2)}$$

Chemical enhancement is associated with charge transfer between metal and molecules. It is a much shorter-range effect and usually requires that the molecules attach to the metal surface via direct contact or chemical bonds [15]. CE is weaker than the EM mechanism, typically with an EF of 10-10^3 compared with that of EM mechanism up to 10^9. In fact, chemical enhancement is more of an inclusive name for several different processes rather than a specific one, such as polarizability change of the molecule-metal complex [17] or charge-transfer state in resonance with the incident frequency [18]. Chemical enhancement is thus hard to estimate by experiment, therefore computational approaches are usually utilized to single out and quantify different origins of CE. Since CE does not rely on SPR and electromagnetic field redistribution, the SERS materials can be non-plasmonic substrates such as semiconductors [19, 20].

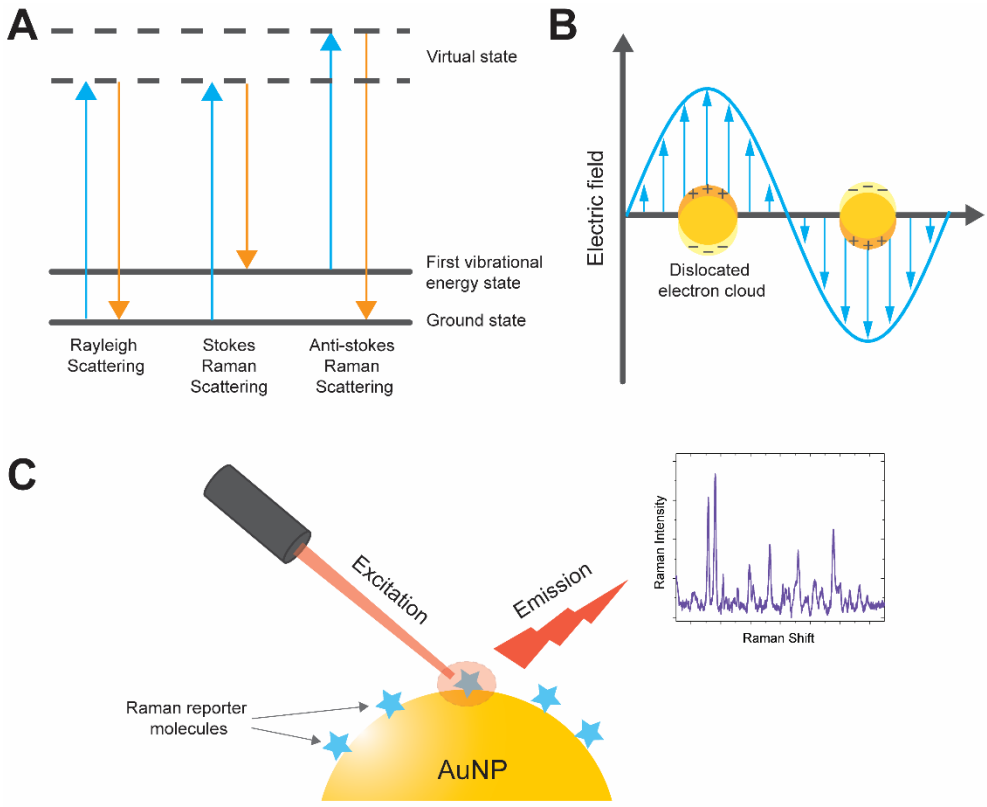

Figure 1.1 SERS fundamentals. **A)** Different light scattering: Rayleigh scattering, stokes Raman scattering and anti-stokes Raman scattering; **B)** Illustration of the oscillating electron cloud, which moves in opposite direction of the electric field vector, for a nanoparticle smaller than the wavelength of light; **C)** Electromagnetic enhancement mechanism of SERS.

1.2 Label-free and Labeled SERS

Based on the origin of the Raman signal, biological applications by SERS can be classified into two types: direct (or label-free) detection [21, 22], where SERS-active substrate directly capture the analytes so the collected Raman spectra comes from the intrinsic ‘footprints’ of the biomolecules of interest; and indirect (or labeled) detection [23], where a Raman reporter molecule is used as the extrinsic signal source to monitor the detection (Figure 2A). Different SERS-active substrates platforms are developed for various biomedical applications, such as nanostructured surfaces, aggregated colloidal nanoparticles and single nanoparticle tags. Surface substrates or aggregated colloids are mostly designed for direct detection of bio-analytes, where generation of hotspots is often involved to improve the detection limit. For direct detection, spectral interference from the other components in the system and precise structure control of hotspots for quantitative sensing are main issues. On the other hand, SERS nanotags are functioned with internal reporter molecules with strong and distinct Raman signals, and are usually further linked to targeting ligands for detection [24, 25]. Within 10-100 nanometer range, these nanoparticles are protected by biocompatible coatings and are versatile for a variety of biochemical sensing and imaging functions.

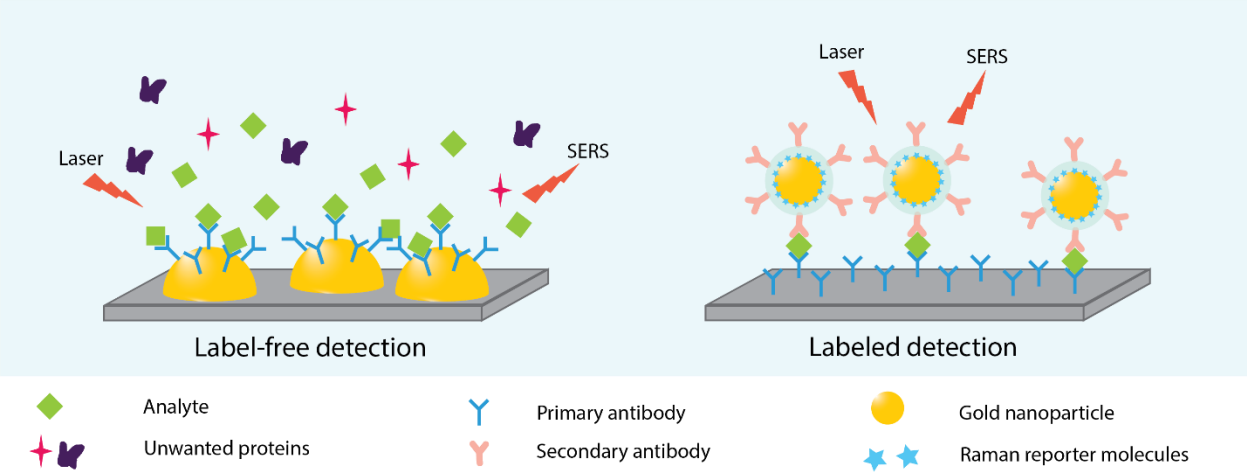

Figure 1.2 Illustration of SERS-based label-free detection (left) and labeled detection (right).

1.3 Design Principles of SERS Nanotags

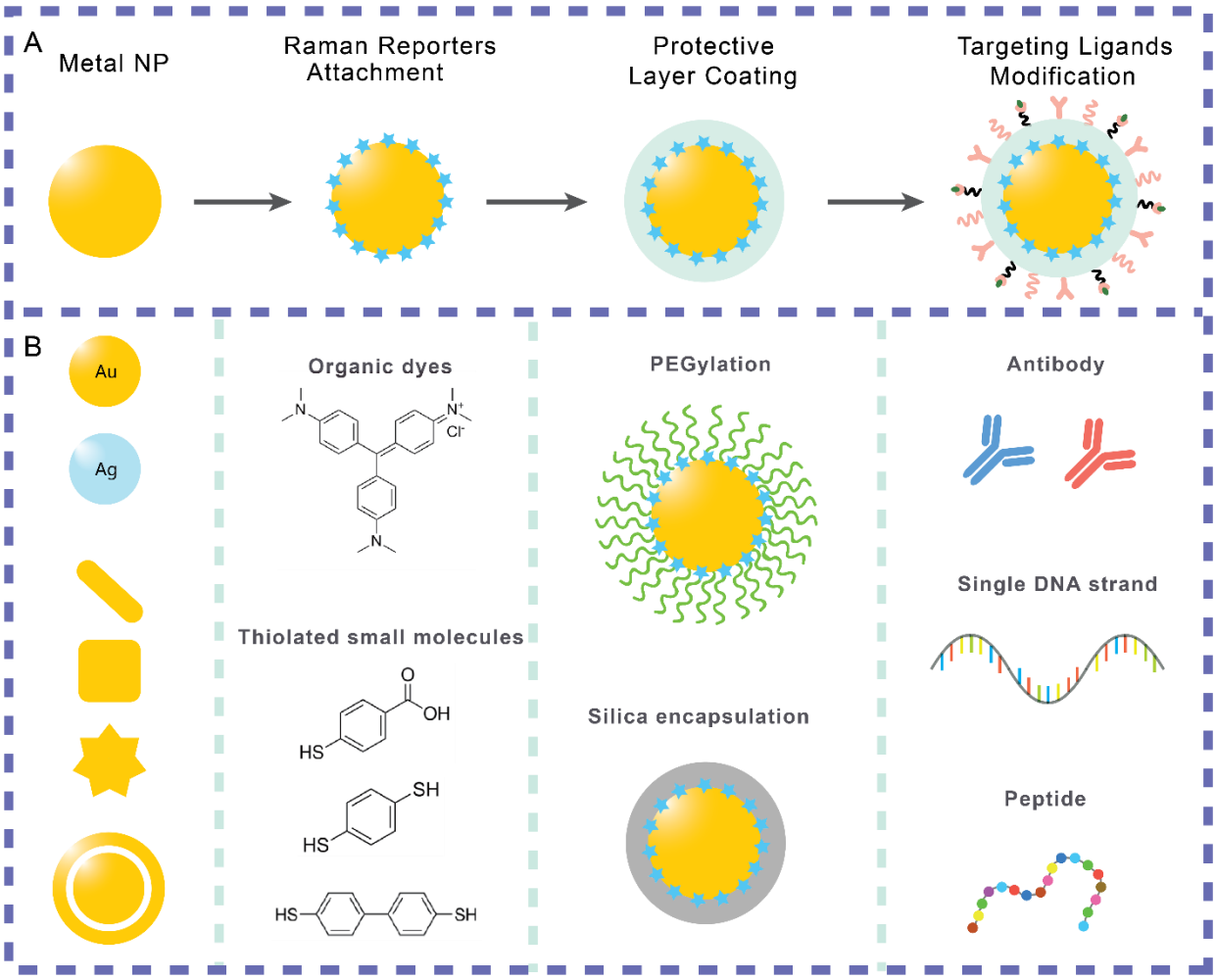

Figure 1.3 Scheme of SERS nanotag synthesis and library of SERS nanoparticle components: metal core, Raman reporter molecules, protective coatings and targeting ligands.

1.3.1 Metal core

Figure 2B illustrates the typical synthesis process of a SERS nanoparticle (NP). Silver or gold is usually used as the metal core since the LSPR frequencies of noble metals fall within the visible and near-infrared (NIR) range. In the same condition, silver NPs show better plasmonic activity than gold and usually lead to stronger SERS enhancement [26]; however, silver is reported to be toxic to mammalian cells, and its surface gets oxidized easily in biological environment [27]. Gold is more chemically inert and has been demonstrated to show little toxicity in human clinical trials, therefore are more frequently employed for in-vivo studies [28]. Optical properties of the metal NPs depend on their size and geometry. Larger size red-shifts the LSPR frequency of the NP. Anisotropic shapes, such as rods, triangles or stars, create multipole modes with more than one resonance peak and enable their optical properties tunable to the NIR region, which is known as the biologically 'transparent' region and is thus ideal for ultra-sensitive and high-resolution detection and imaging [12, 29].

Another aspect of designing metal core of SERS NPs is the creation of SERS 'hotspots' [30]. A broad definition of 'hotspots' could be any highly localized region of intense local field enhancement. Hotspots are commonly created by the following two approaches: 1) generation of sharp tips where high radius of curvature renders high electric field favorable for strong SERS due to the 'nanoantenna' effect, such as gold prisms or nanostars [31, 32]; 2) creation of junctions or gaps of two or more plasmonic surfaces where at least one of the objects has a curvature in nanometer scale, such as the so-called 'nanomatryoshka' core-shell structures with an internal gap for improved SERS properties [33, 34].

1.3.2 Raman reporter molecule

Raman reporter molecule is the source of Raman signal that represents the nanoparticle. Theoretically, any Raman-active molecules could be used as reporter molecule, but their Raman cross section differ. Most of the commonly used reporter molecules are chromophores with aromatic rings, for example, malachite green, crystal violet and rhodamines. Choosing a dye molecule with absorption spectrum that overlaps with the excitation laser can further enhance the overall SERS intensity for an additional 2 orders of magnitude by surface-enhanced resonance Raman scattering (SERRS), which is one of the chemical enhancements due to electrons transition between highest occupied molecular orbital (HOMO) and lowest unoccupied molecular orbital (LUMO) in resonance with the optical field [18, 35].

It is important that the reporter molecules are closely attached to the metal since electric field intensity decays tremendously with distance away from the plasmonic surface. Therefore, small molecules with anchoring groups such as thiol (-SH) or isothiocyanate (-NCS) that can form chemical bond with gold atoms is a class of popular reporter molecules, for example, 1,4-benzenedithiol (BDT) and 4-mercaptobenzoic acid (MBA) [36, 37]. These small thiolated aromatic molecules are advantageous in multiplex labeling because there are only a few distinct peaks in each of their Raman spectra so it is hard to overlap with each other [38]. Most of the fluorophores lack anchoring groups and thus can only attach to the gold nanoparticle via electrostatic interaction [39]. Beyond commercially available molecules, rational design of reporter molecules remains a hot topic with the purpose of creating molecules with desired resonance frequency, large Raman cross section and strong anchoring group to enable intense and stable SERS signals [40]. Also, since biological tissues barely show Raman peaks in 1800-2800 cm^{-1} (also called bio-silent region), the bio-orthogonal Raman reporters with characteristic peaks

in this region, such as Prussian blue, have been studied to reduce the interference from the bio-environment [41-43].

1.3.3 Biocompatible coating

As-synthesized gold nanoparticles are stabilized with charged ligands such as citrate, CTAB or CTAC to ensure good dispersion in aqueous solutions. However, electrostatic force alone cannot stabilize nanoparticles in high ionic-strength buffers due to surface charge screening effect [44]. Moreover, bare gold nanoparticles are easily to be contaminated by proteins in biological fluids, leading to reporter molecules damage, unexpected NP aggregation and severe immune response [45, 46]. It is thus necessary to function SERS nanotags with a 'stealth' coating to resume normal SERS performance. The most popular biocompatible coating for SERS NPs is polyethylene glycol (PEG), which was reported to enable prolonged blood-circulation lifetime of NPs because the ultra-hydrophilic ethylene glycol (EG) chains prevent biofouling due to unfavorable interaction with proteins [25]. Another advantage of PEG is its facile chemistry to enable well-defined end groups, making it convenient for further targeting moiety conjugation. However, though PEG can reduce protein adsorption, it is unable to completely suppress it. Recently, zwitterionic polymer was proposed as an alternative hydrophilic coating instead of PEG [47]. In a zwitterionic ligand, a positively charged moiety and a negatively charged moiety are linked by a small carbon chain to result in an overall neutral charge. Similar to PEG, the strong affinity with water of zwitterions has been postulated as the reason for the great antifouling properties of this type of ligands. The drawback of zwitterionic polymers, however, is that their pH-dependence makes their performance unstable in complex biological environment.

Silica encapsulation is a widely used inorganic coating for SERS NPs. Typically, the silica coating of encoded metal NPs follows the classic Stöber method involving tetraethyl orthosilicate

(TEOS) to deposit a mesoporous silica layer with controllable thickness [48]. The silica coating provides robust mechanical protection of the NPs, but also limits the selection of reporter molecules because only molecules with strong anchoring groups can stay during the coating process [49]. Another drawback of silica layer is that the charged surface is prone to have non-specific binding with biological materials, making it not favorable for in-vivo applications. As an improved method, silane-PEG which adds an additional layer of PEG coating outside of silica are employed to improve the water-solubility and biocompatibility [50].

High-molecular-weight proteins such as bovine serum albumin (BSA) have also been reported as biocompatible layer by forming an effective protection corona around encoded SERS NPs [51]. It is believed that the disulfide residues of the BSA interact with remaining gold sites on NP surface and form strong Au-S bond. The BSA corona provides protection of reporter molecules and steric repulsion to avoid NP aggregation. It also reduces cytotoxicity of the nanotags since BSA is a common serum protein.

1.3.4 Targeting ligand conjugation

The last step of SERS nanotag synthesis is targeting ligand conjugation [52]. In most of the cases, targeting ligands such as antibodies, peptides or DNA single strands are connected to the SERS tags via the functional groups at the surface of the protective coating. For example, typical terminal functional groups for antibody conjugation are amine or carboxyl groups, which can easily form amide bond with amine or carboxyl groups of the ligand via carbodiimide activation (EDC/NHS reaction) in aqueous environment. For PEG coating, end group can be introduced using bifunctional PEG with one end of thiol group to link with gold NPs, and the other end of active functional group for bioconjugation [25]. For silica shell, silane with amino or thiol groups can be

employed after the silica layer deposit to enable outward functional groups [50]. The choice of ligand depends on the tissue or biomolecule of interest and will not be elaborated here.

1.4 Biomedical Applications of SERS Nanotags

SERS nanoparticles gain special attention because of its unique advantages over other bio-sensing nano-agents. First, SERS is a rather sensitive and selective technique that is able to realize molecular-level detection of biological analytes in complex systems. Typical detection limit of SERS NPs is around pico- to femto-molar range, giving it great potential for trace analysis such as circulating tumor cell detection [53, 54], biomarker quantification [55] and point-of-care (POC) metabolic sensing [56, 57]. Second, in contrast to other optical agents such as fluorescence, SERS NPs are extremely photostable over a long period, enabling sufficient operation window for repeated or long-term measurement [24]. Third, SERS NPs are ideal for multiplexing spectroscopy such as parallel detection or multiple biomarker quantification owing to the narrow full-width at half maximum (FWHM) of Raman signal peaks, which is typically 1-2 nm (10-30 cm^{-1}) compared with 50-100 nm of fluorescence emission band [11, 41, 58]. Last, the use of SERS NPs with resonance at NIR region elegantly suppress unwanted biological auto-fluorescence and is thus ideal for in-vivo studies that require NIR excitation [12, 59]. Specific examples will be given in the following sections focusing on functions, applications and corresponding outstanding features of the SERS nanotags.

1.4.1 SERS nanotags for biodiagnostics

Robust biodiagnostic platforms based on SERS NPs have been widely explored. the high-sensitivity, multiplexing and quantitative SERS biodetection techniques offer abundant choices to analyte disease-specific biomarkers, particularly in body fluids such as blood or urine. One

example is the detection of nucleic acids, including virus DNA, circulating DNA and microRNA, which are important biomarkers of diseases or virus-positive disease. The nucleic acid SERS detection can be achieved via the regular sandwich assay using SERS NPs. Kim et al. have reported the Au core-Ag shell SERS NPs with an enhancement factor of up to 10^9 [60]. Combined with the DNA-modified magnetic beads, these NPs were used to detect target hepatitis A virus (HAV) DNA strands with an impressive LOD of 10-100 aM. Another example is SERS based lateral flow assay (LFIA), a new and promising technique in point-of care treatment (POCT) diagnostics for quantitative, sensitive and rapid detection of biomarkers. SERS NPs as LFIA labels can highly improve the detection limit and quantification capability [55]. The pioneering work of Choo group in detecting HIV DNA and staphylococcal enterotoxin B has demonstrated an LOD with 3 orders of magnitude lower than the colorimetric LFIAs [61, 62]. The fingerprint spectrum further renders SERS nanotag excellent multiplexing capability. This can be achieved by making multiple TLs to capture different SERS NP labels [63]; or, by using a single TL to capture multiple SERS labels that exhibit different Raman signal, and then separating each signal from the mixed spectrum collected at TL. This is of significance for the rapid detection of multiplexing markers in the same sample without additional reagents or multiple-stage pretreatments.

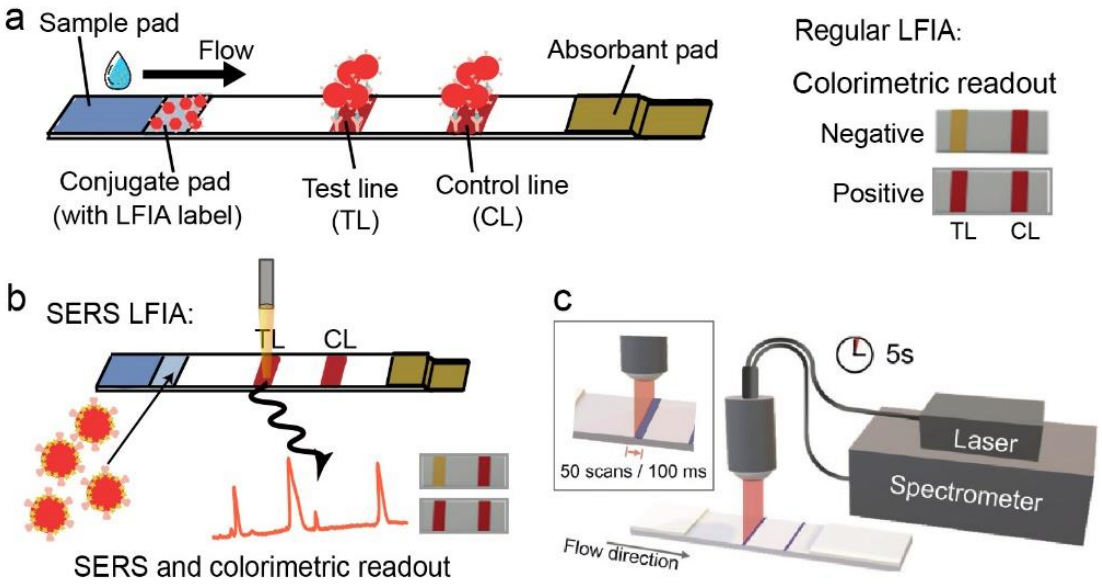

Figure 1.4 (A) The regular LFIA test procedure with the colorimetric readout. (B) SERS LFIA for both SERS and colorimetric analysis. (C) A portable Raman reader with a line laser that can shorten the acquisition time to 5s. Reproduced from Ref. [57]

1.4.2 SERS nanotags for bioimaging

Among various biomedical areas that SERS has been employed, the most exciting of all is its imaging performance. Compared to conventional optical or non-optical imaging techniques, SERS demonstrates superiority in many aspects. The most well-known strength is its high sensitivity together with great photo-stability, which are proven advantageous with respect to fluorescence imaging. High brightness of SERS tags allows detection limit down to atto-molar level unmatched by any other imaging methods such as MRI, X-ray CT or PET [64, 65]. Furthermore, SERS also shows superior resolution of micro-meter range and high-speed real-time imaging, making it competent as an intraoperative imaging technique.

Live cell imaging that studies dynamic activities both in space and time in single cells is thus one of the most important areas in biomedical research. A pioneering work by Kang et al. reported a high speed and high resolution multiplexed live cell Raman imaging using small spherical gold NPs with highly narrow intra-nanogap structures (Au-NNP) [66]. Because of the great brightness of Au-NNPs, the photothermal damage to the cells were negligible with the use of low laser power (200 μW) and fast scanning speed (30 s for 50 × 50 pixel) with an integration time of 10 ms per pixel). These features make it possible to monitor the rapidly changing cell morphologies during cell death by the high-speed Raman live cell imaging technique. The type and expression of biomarkers on cell surfaces and related cell phenotype classification is important to various disease diagnosis, especially in the case of cancer [9, 10]. One example for SERS imaging of cell-surface species is immuno-SERS (iSERS) [67]. The advantage of SERS in biomarker and cell phenotype identification is its tremendous multiplexing capability that can realize parallel detection of several proteins. For example, Lee et. al reported an iSERS-based cellular imaging technique to quantify multiple breast cancer phenotype biomarkers on cell

membranes [68]. The multiplexing SERS mapping demonstrated successful identification of expressed biomarkers and tumor cell phenotypes faster and more accurate than traditional western blot results (Figure 6D).

In addition to cells, SERS nanotags are also applied to image tumors, especially to elucidate tumor margins, and to detect tumor metastasis in organs. Before discussing various SERS tissue imaging applications, we briefly introduce two types of NPs targeting strategies in vivo: passive targeting and active targeting. In passive targeting, SERS nanotags are injected into the animal and passively accumulate in organs, among which tumor becomes a preferable accumulating place due the enhanced permeability and retention (EPR) effect [69]. Active targeting enables NPs to actively target specific tumor cells via the conjugated receptors. It was illustrated by several studies that active targeting showing advantages over passive targeting in aspects of elongated NPs retention time in tumor tissues and increased receptor-mediated internalization of NPs [46]. However, there are still debates about the relative contributions of the active and passive targeting mechanisms. For example, Chan et al. reported recently that EPR effect is more related to an 'active' trans-endothelial pathway rather than a 'passive' process through inter-endothelial gaps [70].

An example of SERS nanotags used for tissue imaging is metastatic lymph node (LN) mapping. In a pioneering work, Ye group presented progresses regarding SERS-based precise sentinel lymph node (SLN) detection both ex-vivo and in-vivo. [71, 72] Due to specific uptake of GERTs by the SLN and the high specificity of Raman spectrum of GERTs, high-contrast images were obtained both in situ and ex vivo showing clear boundary of the SLN to distinguish it with the adjacent fat (Figure 6G) [71].

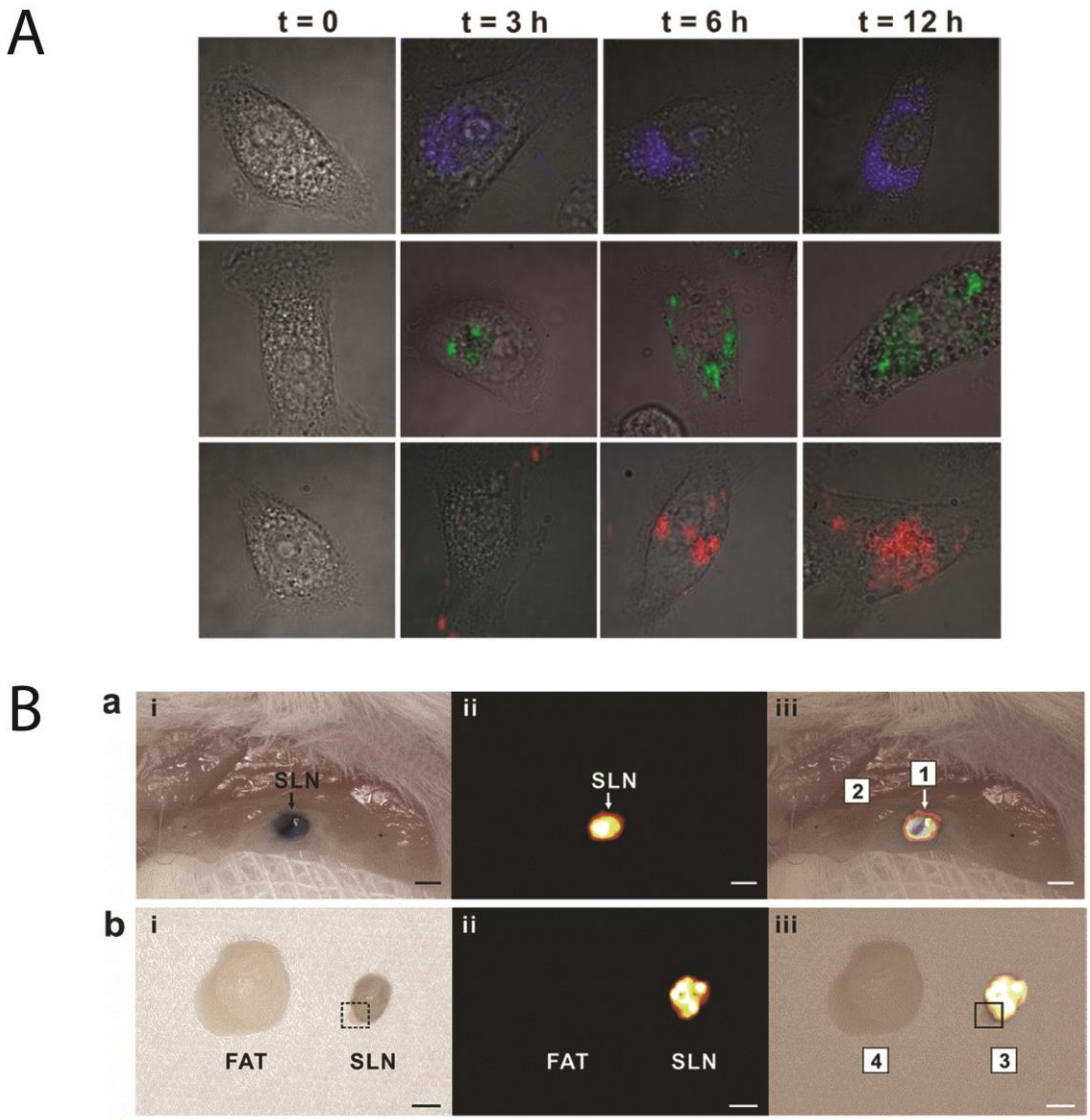

Figure 1.5 SERS nanotags used for live cell imaging and tumor tissue imaging. A) Time-dependent live cell Raman images after incubating with three types of subcellular targeting NPs. [73] B) High-contrast intraoperative Raman imaging of SLNs. [71]

1.4.3 SERS nanotags for spectroscopy-guided surgery

Surgery remains the main options for most solid tumor treatments. SERS NPs are highly promising intraoperative contrast agents for the identification of lesion margins, including primary tumors, draining lymph nodes, and metastatic sites, with their excellent sensitivity, specificity, targeting capability and biocompatibility. The hand-held Raman probes revealed their potential in open surgery, particularly the brain tumor resection. Kircher group evaluated the performance of a hand-held Raman scanner in identifying the microscopic glioblastoma tumor in mice [74]. The portable hand-held scanner provided variable angles, showing prognostic benefit for the search on residual tumors that were invisible by a static Raman microscope. In another example, A miniature Raman endoscope enabling rotational scanning and axial pull-back was employed to image the SERS NPs bound on the esophagus lumen [75]. These point-detection endoscope devices were combined with SERS NPs to screen cancers of the esophagus, colon, cervix where small areas of tissue is under examination.

The invention of multimodality and multifunctional SERS NPs revealed “all-in-one” strategy for precision cancer theranostics. [76] These approaches allow preoperative staging and location (MRI, CT, PEI), intraprocedural guidance (Raman, fluorescence and photoacoustics) and post-surgery examination (Raman), facilitating the precision tumor diagnostics. The multi-modality SERS NPs not only enables the incorporation of Raman technique into current paradigms to facilitate its clinical translation, but offer additinoal advantages for SERS imaging. For instance, PA, CT and MRI exhibit higher penetration depth in human body than optical imaging. Their integration with SERS NPs assisted the localization of tumors in deep layer. For example, Kircher et al. reported a triple-modality SERS NPs combined with PA and MRI imaging to successfully to monitor tumor localization and margins during the resection of malignant brain tumors [77]. It is

also expected to load the radiotracers to the silica coating of SERS NPs to realize the PET/SERS dual-modality [78].

CHAPTER 2: BRIGHT AND STABLE SERS NANOTAGS WITH HYDROPHOBIC INNER DOMAIN

2.1 Motivation – To Improve Signal Robustness of Dye-encoded SERS NPs in Biological Fluids

In solutions, nanoparticles frequently collide with each other due to Brownian motion. Strong electrostatic or steric repulsion are employed between NPs to avoid irreversible aggregation during collision. However, in biological media with high ionic strength, nanoparticles are more prone to aggregate due to the charge screening effect, which in return compromises the stability of SERS signal. For SERS nanotags with intrinsic Raman reporters as the inner standard, integrity of the reporter and their close attachment on the NP surface are essential to a stable and uniform SERS intensity in biological fluids, especially for quantitative sensing. Chromophores own large cross-section and generally stronger SERS intensity, but their drawback is that they typically adsorb on plasmonic surface only by electrostatic force instead of covalent bond [39], and as a result they are easily to dissociate from NPs surface to the solution and result in SERS signal loss with time.

Abundant proteins and cells in physiological environments such as blood interact with SERS nanoparticles once they enter the circulation system, changing the so-called "synthetic identity" of the NPs – such as surface chemistry, size and shape of the NPs as-synthesized – into their "biological identity" by forming protein corona [79]. Protein corona are known to cause nonspecific binding of the NPs by hindering the targeting ability of the conjugated ligands; it also accelerates the uptake of NPs by mononuclear phagocyte system [45, 46]. For SERS NPs encoded

with weakly attached chromophore, adsorbed proteins easily replace or deform the reporters, leading to reduced signals and unreal Raman peaks with high auto-fluorescence background.

Commonly used protective layers that stable SERS signal in biological include thiolated poly(ethylene) glycol (SH-PEG) and silica shell. The mushroom-like configuration of PEG chains, though have some resistance to unfavorable protein attachment, still allows serum proteins permeation and reporter molecules diffusion, and its ability to avoid NP aggregation depends a lot on the molecular weight and packing density of the polymer [44, 80, 81]. Silica encapsulation enable SERS NPs with better mechanical properties against NP coupling, but the deposition of silica shell competes with physically adsorbed chromophores [49]. Some novel classes of biocompatible coatings for SERS NPs emerge recent years such as amphiphilic block-copolymers [82], zwitterionic polymers [47] or layer-by-layer deposition of polymer electrolytes [83], but almost all of them requires complicated chemical synthesis and multiple coating steps. It is thus important to find a simple, universal and versatile protective coating for biological applications of SERS NPs.

2.2 Experimental Section

Chemicals and materials. Deionized water (DI water) was used throughout the work. The following chemicals were used as purchased without any further purification: citrate stabilized gold nanospheres (60-nm) at a concentration of 2.6×10^{10} /ml (4.32×10^{-2} nM) from Ted Pella Inc., 11-mercaptoundecanoic acid (MUA, 95%), diethyl ether (≥ 99.7%), Dimethylformamide (DMF), sodium citrate, 5k poly(ethylene glycol) methyl ether (mPEG, Mn 5000 Da), 2k poly(ethylene glycol) methyl ether (mPEG, Mn 2000 Da), 2k poly(ethylene glycol) methyl ether thiol (mPEG thiol, Mn 2000 Da), 2-[2-[2-Chloro-3-[(1,3-dihydro-3,3-dimethyl-1-propyl-2H-

indol-2-ylidene)ethylidene]-1-cyclohexen-1-yl]ethenyl]-3,3-dimethyl-1-propylindolium iodide (IR-780, dye content ≥ 95%), malachite green (MG), crystal violet (CV, ≥ 90%), 4-[2-[2-Chloro-3-[(2,6-diphenyl-4H-thiopyran-4-ylidene)ethylidene]-1-cyclohexen-1-yl]ethenyl]-2,6-diphenylthiopyrylium tetrafluoroborate (IR-1061, dye content 80%), gold(III) chloride trihydrate ($HAuCl_4 \cdot 3H_2O$), L-ascorbic acid, silver nitrate ($AgNO_3$), poly(sodium 4-styrenesulfonate) (Na-PSS) solution (average Mw ~70,000, 30 wt. %), hexadecyltrimethylammonium bromide (CTAB), bovine serum albumin (BSA) and fetal bovine serum (FBS) from Sigma Aldrich; 3,3'-Diethylthiatricarbocyanine iodide (DTTC, ≥ 96%) was purchased from Alfa Aesar; 4-nitrobenzene-1-thiol (4-NBT) from TCI; ethylenediaminetetraacetic acid dihydrate ($EDTA \cdot 2H_20$) and 5,5-dithio-bis-(2-nitrobenzoic acid) (DTNB) from Thermo Scientific; poly(ethylene glycol) methyl ether thiol (mPEG thiol, Mn 5000 Da) from Laysan Bio Inc..

Hydrophobic domain PEG ligand synthesis. Synthesis of MUA-PEG ligand follows the method outlined in Schultz et al [84]. In brief, 11-mercaptoundecanoic acid (MUA) and mPEG (5k Da or 2k Da) was mixed in 3:1 molar ratio in a round-bottom flask and kept under vacuum at 110 ℃ for 1 hour. Then the temperature was ramped up to 160 ℃ under N_2 atmosphere with a reflux condenser and kept for 72 hours. The unreacted MUA was removed by multiple washings of cold diethyl ether.

Synthesis of shape varied AuNPs. Glassware and stir bars for gold nanoparticle synthesis were washed by aqua regia before use. Gold nanorods were synthesized by a seed-mediated growth method [85]. A seed solution was first synthesized by quickly adding 600 μL of ice-cold 10 mM $NaBH_4$ solution to a mixed solution of CTAB (5 mL, 0.2 M) and $HAuCl_4$ (5 mL, 0.5 mM) under vigorous stirring. The seed solution was continued stirring for 2 min and then kept at room temperature for over 1 h before the next step. For the growth of nanorods, a CTAB solution (20

mL, 0.2 M) was first mixed with a $HAuCl_4$ solution (20 mL, 1 mM) and a $AgNO_3$ solution (1.2 mL, 4 mM) at a 30 ℃ water bath. To the above solution, 380 μL of 0.0788 M ascorbic acid solution was added, followed by gentle shaking. The growth solution was observed to change from yellow to colorless. After that, 48 μL seed solution from the first step was added followed by gentle shaking, and the growth solution was kept at 30 ℃ unstirred. After 1 h, the growth was stopped by centrifuging the resulted Au nanorods solution at 4000 g. The washed nanorods solution was re-dispersed to 2 mM CTAB solution. The as-synthesized Au nanorods were then treated with a surfactant exchange process to enable Raman reporter molecules attachment [86]. Typically, 10 mL of nanorods dispersed in 2 mM CTAB solution was first centrifuged at 4000 g. 9.5 mL of the supernatant were removed, and pellet were re-dispersed to 10 mL by DI water. The resulted nanorods solution (current CTAB concentration 0.1 mM) was then added to 100 mL of Na-PSS solution (0.15 wt.%) and kept at room temperature for over 1 h. After the incubation, the nanorods solution was centrifuged at 4000 g and re-dispersed to 0.15 wt.% Na-PSS solution for two cycles, and then centrifuged again at 4000 g and re-dispersed to 5 mM sodium citrate solution. The Au nanorods were incubated in sodium citrate solution overnight. Finally, the Au nanorods were washed again at 4000 g by 5 mM sodium citrate. The concentrations of the citrate-stabilized Au nanorods were determined by ICP-MS. The Au nanorods solution were finally diluted to 32 mg/L in 5 mM sodium citrate for long-term storage. Gold nanostars were synthesized using a seed-mediated method [87]. First, 15-nm small AuNPs were synthesized as the seed. A water solution of 2.2 mM sodium citrate (60 mL) was heated to boiling under vigorous stirring. Once boiling had commenced, 400 μL of $HAuCl_4$ solution (25 mM) was quickly injected. The reaction completed within 10 min where the solution turned from yellow to purple grey and then to burgundy. The resulted solution was centrifuged 3 times and stored as Au seed for the next step. For Au nanostars

synthesis, to 4 mL $HAuCl_4$ solution (0.25 mM), 4 μL of 1N HCl and 280 μL of 15-nm citrate gold seeds were added followed by simultaneous addition of 40 μL $AgNO_3$ solution (3 mM) and 40 μL of ascorbic acid solution (100 mM) under stirring. The reaction was performed at room temperature, and the process was completed in less than 2 min.

Raman reporter (RR) molecules attachment on AuNPs. Raman reporter molecules DTTC, IR-780, MG, CV and IR-1061 stock solutions were prepared by dissolving 1 mg of the dye molecules into 1 mL of DMF. The stock solutions were diluted by DI water to form a dye concentration of 2.62 μM for fresh use. Typically, 10 μL above dye molecule solution was dropwise added to 600 μL AuNPs (4.32×10^{-2} nM) under moderate stir to form a dye molecule concentration of 1000 dye per nanoparticle. Raman reporter molecule 4-NBT stock solution was prepared by dissolving 1.62 mg 4-NBT into 1 mL ethanol. The stock solution was then diluted by DI water to form a molecule concentration of 26.2 μM for fresh use. Typically, 30 μL above NBT solution was dropwise added to the prepared Au nanostar solution under moderate stir to form a dye molecule concentration of approximately 4000 dye per nanoparticle.

PEGylation of reporter molecules attached AuNPs. After 30 min incubation with RR molecules, the AuNP@RR solution was mixed with PEG solutions (51.8 μM) at certain molar ratio for 1 hour to achieve various PEG coating densities. The SERS nanoparticles were then washed twice by centrifugation at 1100 g to 3000 g to remove excess PEG and RR molecules.

Quantitative PEG ligands adsorption measurement. PEG ligand packing density was determined by quantitatively measuring free thiol group concentration in centrifugation supernatant using Ellman's reagent. Briefly, the reaction buffer solution was prepared by dissolving 18.6 mg $EDTA{\cdot}2H_2O$ in 50 mL 10× PBS (1 mM, pH=7.4). A 10 mM Ellman's reagent solution was prepared by adding 4 mg DTNB into 1 mL above reaction buffer solution. Then, the Ellman's

reagent solution was mixed with reaction buffer solution by a volume ratio of 1:50 to obtain a test solution with a DTNB concentration of 0.2 mM. After PEGylation, the supernatants of the centrifuged samples were collected, and test solution was added to each sample at a volume ratio of 1:8. The reaction was allowed for 15 min under room temperature, and the absorbance of the mixture was read on plate reader (BioTek, Winooski, VT). Free thiol group concentration was calculated based on the standard absorbance-concentration curve of PEG or MUA-PEG solutions. The footprints of self-assembled PEG on AuNPs was previously reported to be 0.35 nm^2, based on which the maximum PEG ligand packing densities are estimated to be 32,297/NP [88].

AuNP surface protein quantification by Bradford assay. Quantification of protein on each AuNP was conducted using a Pierce™ Coomassie Plus (Bradford) assay kit. Briefly, the SERS nanotags dispersed in 5% FBS for 24 hours were centrifuged and re-dispersed to 1× PBS for 4 times to wash out unbonded proteins. 1 mL of the washed SERS nanotags (AuNP concentration: 4.32 x 10^{-2} nM) were then concentrated to 150 μL by centrifugation, to which 150 μL of the Coomassie Plus reagent was added. The solution was mixed with plate shaker for 30 seconds, then incubated without shaking at room temperature for 10 min. Absorbance of each sample was measured at 595 nm on a BioTek Synergy 2 plate reader (BioTek, Winooski, VT). Considering AuNPs have intrinsic absorbance near 595 nm, SERS nanotags of the same concentration but was not incubated in serum solution were used as blank replicates to subtract the influence of Au absorbance. Protein concentration of each sample was then determined based on the standard BSA curve.

SERS nanotags characterization. Absorbance spectra of AuNP solutions were obtained from a GENESYS™ 10S UV-Vis Spectrophotometer. Dynamic light scattering (DLS) was fulfilled on a Malvern Nano ZS90 Zetasizer. Weight concentrations of AuNPs in solutions were measured by

inductively coupled plasma-mass spectrometry (ICP-MS, NexION 350D, PerkinElmer). Transmission electron microscope (TEM) pictures were taken by a JEOL 2100 Cryo TEM.

Raman spectrum measurement. Raman spectra at 785 nm and 1064 nm were obtained using an Agility transportable 785/1064 nm dual-band benchtop Raman spectrometer (East JHX, Inc.). 200 mW of laser power was used for both 785 nm and 1064 nm as the excitation source. The band intensities were calibrated by standard sample (benzonitrile) spectrum. Raman spectra at 532 nm were obtained using a Nanophoton Raman 11 confocal microscope at a laser power of 50 mW. All the Raman spectra were baseline corrected to remove fluorescence background.

2.3 Results

Hydrophobic domain locked SERS nanotags were prepared by introducing an amphiphilic polymer ligand coating on AuNPs via Au-S binding. The amphiphilic polymer, which we refer to as MUA-PEG, was synthesized by an esterification reaction of 11-mercaptoundecanoic acid (MUA) and poly (ethylene glycol) methyl ether (mPEG). Once conjugated to AuNPs via Au-S bonds, the aliphatic parts of the polymer ligands form an inner hydrophobic shell wrapping the AuNP, while the hydrophilic PEG serves as the biocompatible coating towards the outside (Scheme 2.1). The successful introduction of the inner hydrophobic layer on gold surface was demonstrated by the hydrodynamic size change of the AuNP after ligand exchange, where the hydrodynamic diameter of MUA-PEG coated NPs was measured to be 76-77 nm compared with that of 74-75 nm for PEG coated NPs (Figure 2.1B). The total 2-3 nm size increase is in accordance with the fact that the molecular length of single MUA is around 1.5 nm (Figure S2.1A) [89]. Also, the absorbance peaks of MUA-PEG samples showed a slightly red-shift from 536.3 nm to 537.3 nm compared with PEG samples (Figure 2.1A), giving the evidence that the AuNP surface was

replaced by an aliphatic layer, a medium of higher RI compared with water-enriched PEG surroundings [90].

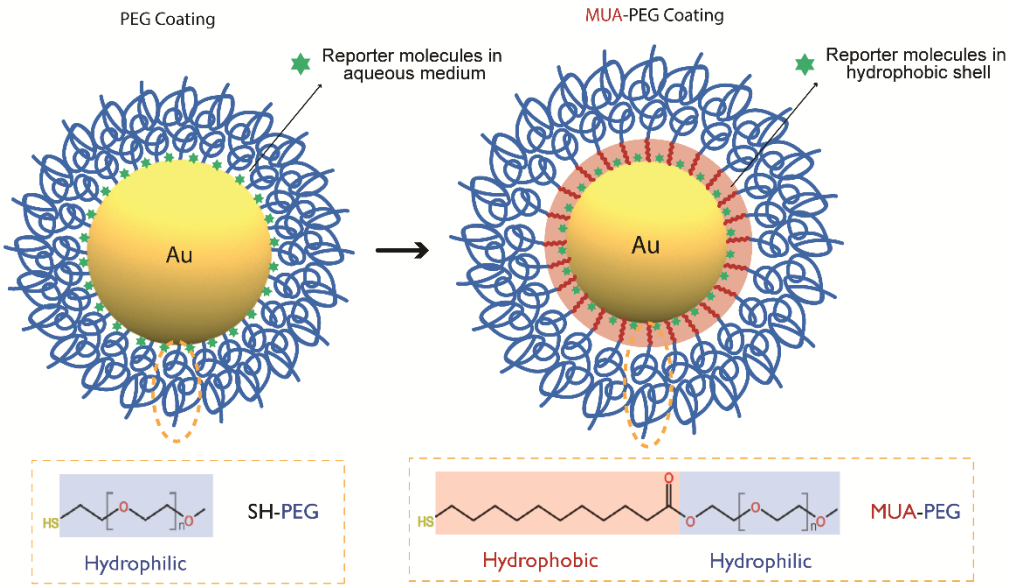

Scheme 2.1 Illustration of the hydrophobic locking AuNPs (AuNP@MUA-EPG) and traditional PEG locking AuNPs (AuNP@PEG). The red layer represents the introduced aliphatic shell between hydrophilic PEG chains and AuNPs. Chemical structures of thiolated PEG and MUA-PEG are shown at the bottom.

A

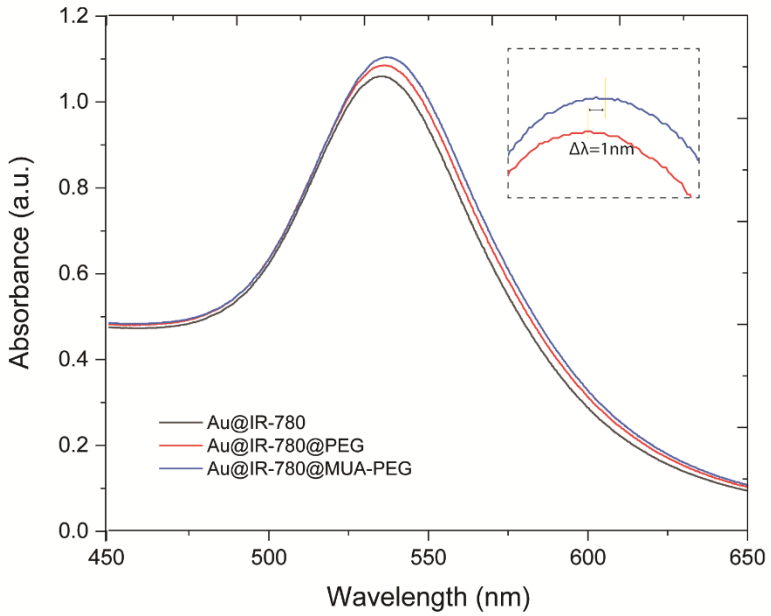

B

	AuNP	AuNP@IR-780	AuNP@IR-780@PEG	AuNP@IR-780@MUA-PEG
Hydrodynamic size (d.nm)	*56.90 ± 0.23*	*58.04 ± 0.50*	*74.76 ± 0.28*	*76.99 ± 0.37*

Figure 2.1 A) UV-Vis spectra of dye-attached AuNPs and dye-attached AuNPs with PEG and MUA-PEG coatings, respectively. Inserted: LSPR peak shift of PEG and MUA-PEG coatings. B) Hydrodynamic sizes of AuNPs, dye-attached AuNPs and dye-attached AuNPs with PEG and MUA-PEG coatings, respectively.

The binding kinetics of MUA-PEG ligand was first studied to quantify PEG ligand packing densities on AuNPs. Ellman's reagent was used to quantify the conjugated PEG ligand amount by measuring the leftover free thiol group concentrations in the supernatant of the centrifuged AuNPs after ligand exchange. Both ligands (PEG and MUA-PEG) were mixed with 50-nm Au nanospheres at room temperature for 1 hour to achieve ligand exchange balance. Based on the ligand quantification, 15,000:1 and 10,000:1 ratio of ligand to AuNP were used for PEG and MUA-PEG coatings respectively to occupy a low percentage of AuNP surface area (~30%), while to achieve a high surface ratio (~70%), 50,000:1 (PEG) and 30,000:1 (MUA-PEG) ratio was applied (Figure S2.2). It is noticed that to achieve the same surface ratio, a lower MUA-PEG ligand concentration was needed than traditional PEG due to the denser and more organized conformation of the inner aliphatic chains that allows more favorable self-assembly on AuNPs [81]. To ensure fair comparison between MUA-PEG and PEG coated SERS nanotags, only NPs with the same ligand surface ratio were compared in the following discussion to make sure the property improvements are independent of PEG ligand packing density. The packing density estimation can also be applied to AuNPs with different sizes and shapes by converting the surface area to that of the 60-nm Au nanospheres.

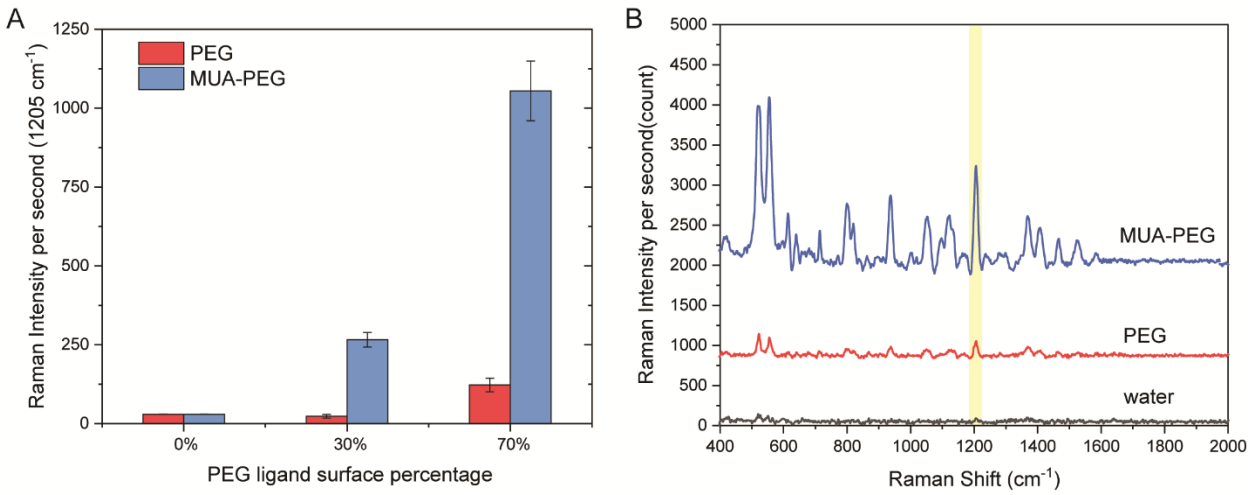

Figure 2.2 A) Hydrophobic PEG Raman signal enhancement effect of the samples with different PEG and MUA-PEG surface ratios. Selected Raman peak: 1205 cm^{-1}. B**)** Raman spectra of samples with different PEG coatings at 70% surface ratio for PEG and MUA-PEG. Laser: 785 nm, 200 mW.

A SERS intensity enhancement effect brought by the MUA-PEG coating was first observed, which is particularly obvious at high PEG surface ratio (70%) where the aliphatic domain forms a hydrophobic layer. As shown in Figure 2.2, MUA-PEG shows its advantage over traditional PEG for up to 10 times SERS signal improvement. The possibility of hot-spot boosted SERS intensity caused by NP aggregation was first eliminated based on the good mono-dispersibility of the NPs indicated by the absorption spectra and DLS sizes (Figure S2.3 and Table S2.1). A series of experiments aiming at exploring the SERS enhancement mechanism by the hydrophobic domain were then conducted. First, the SERS enhancement effect was observed using PEG ligands with different molecular weights, where the length of the hydrophobic block was kept the same while the PEG block changes from 5k Da to 2k Da (Figure S2.5). It was also noticed that 2k Da MUA-PEG coating showed slightly higher SERS signal than 5k Da MUA-PEG coating, probably due to the fact that shorter PEG ligands tend to pack closer to each other and thus create a denser hydrophobic shell. Second, MUA-PEG were applied on different shapes of AuNPs (nanorods and nanostars). Unlike a strong enhancement on Au nanospheres, the hydrophobic enhancement on Au nanorods was only 2-3 folds, and the enhancement effect becomes even less obvious on star-shaped AuNPs (Figure S2.5). These two findings imply that the hydrophobic environment change at the plasmonic surface and its interaction with reporter molecules is critical for the SERS enhancement.

We also investigated the hydrophobic SERS enhancement effect with different Raman reporter molecules. For both chromophores IR-780 and DTTC that resonant at the laser line, 785 nm, MUA-PEG coating showed improved SERS intensity than hydrophilic PEG coating (Figure 2.2 and Figure S2.6B). Next, we chose two off-resonance dye molecules at 785 nm, malachite green (MG) and 4-nitrobenzenethiol (4-NBT) as the reporter. No obvious enhancement of MUA-

PEG coating was observed compared with PEG coating (Figure S2.6C&D). Finally, we measured Raman spectra of AuNPs excited at both the resonant and off-resonant laser line of the reporter dye respectively, where crystal violet (CV, resonant at 532 nm) and IR-1061 (resonant at 1064 nm) were employed as the reporters. The results showed that CV-encoded AuNPs exhibit hydrophobic SERS enhancement at 532 nm, but no significant enhancement at 785 nm (Figure S2.6E&F). Similarly, IR-1061 encoded AuNPs show SERS improvement by MUA-PEG at 1064 nm, but no enhancement at 785 nm (Figure S2.6G&H).

The competition for free surface space between reporter molecules and PEG ligands, especially MUA-PEG ligands, occurs along with the hydrophobic enhancement effect. The competitive adsorption becomes obvious when MUA-PEG ligands are added excessively. As is illustrated in Figure S2.7, when MUA-PEG ligands were mixed with AuNP at a ratio of 100,000:1 (excess), the enhancement effect drops considerably. The reason for the competition is probably that reporter molecules are edged out when MUA-PEGs self-assemble into a densely organized structure due to hydrophobic interaction. Though some of the dye molecules are replaced by MUA-PEG ligands as hypothesized, MUA-PEG coating still exhibits better SERS enhancement than conventional hydrophilic PEG coating at up to 70% surface ratio, indicating broad prospects to develop near-surface dielectric medium modification for SERS enhancement. It is believed that the novel strategy for SERS enhancement, if combined properly with other reported enhancement methods, would turn out to have a considerable overall signal amplification. For future SERS intensity improvement based on this idea, a tradeoff should be considered. The key issue that needs attention is to ensure the compatibility of the near-surface dielectric medium with reporter molecules so that the signal enhancement is the most effective with concentration and functionality of the reporters being significantly maintained.

For practical biomedical applications, SERS nanotags should also maintain strong intensity in a long time period to allow sufficient operation time window without imaging signal drift. The hydrophobic inner domain was observed to show better Raman signal protection ability than conventional PEG coating. SERS intensity of the MUA-PEG coated SERS nanotags remained ~65% of the initial intensity after 24 hours, while the signal of PEG coated samples drops to ~50% (Figure S2.8A). The structure of inner hydrophobic domain is believed to be responsible for the better signal time stability. SERS signal time-drift arises mostly because the Raman reporters detach from the surface and diffuse away from the confined EM field. Here, though organic dye reporter molecules lack anchoring groups on AuNPs, they experience strong hydrophobic attraction with the inner alkane chains and thus are not preferable to leak from the AuNP surface. It is notable that a repeated experiment using 4-NBT as reporter molecule shows similar results (Figure S8B), indicating that the hydrophobic inner domain functions well on preventing both organic dye reporter molecules and small aromatic reporter molecules from detaching.

In additional to SERS enhancement, the introduced inner hydrophobic domain also significantly improved the resistance to NP aggregation in high-ionic-strength saline buffers. Figure 2.3B shows the SERS signal changes of the two samples with different PEG coatings that were dispersed in 10× PBS for 24 hours. In saline buffer solutions, the conventional PEG coated nanotags showed increased SERS intensity, indicating generation of hotspots and partial aggregation of NPs, while the MUA-PEG coated samples remained consistent SERS intensity. The absorbance spectra (Figure 2.3C) further proved the EM field coupling of PEG coated samples by showing a broader peak extending to longer wavelength region due to the low-frequency plasmon modes resulted from the coupling between two dipole modes of each particle [91], while absorbance spectra of MUA-PEG coated NPs didn’t show such trend. Resistance to AuNP clusters

formation by the hydrophobic inner domain was also proved by the hydrodynamic size change of the SERS nanotags within 10× PBS for 24 hours, as shown in Figure 2.3D. The reason for stability against electrolyte-induced aggregation of MUA-PEG is similar with what was reported in previous literature [84], where the inner alkane chains form a 'rigid' shell around AuNPs and physically prevents the nanospheres from getting too close to generate hotspots and unwanted SERS signal change (Figure 2.3A). The introduction of the inner hydrophobic domain separates two nanoparticles by a distance of at least 3 nm from plasmonic surface to surface according to the thickness of the hydrophobic layer, which decreases the SERS enhancement factor by at least 10^3 folds compared with a gap size of 1 nm [92]. Therefore, with the introduced hydrophobic layer, MUA-PEG coated SERS nanotags were proved to be more stable and well-dispersed in saline buffers for quantitative detection or complicated procedures.

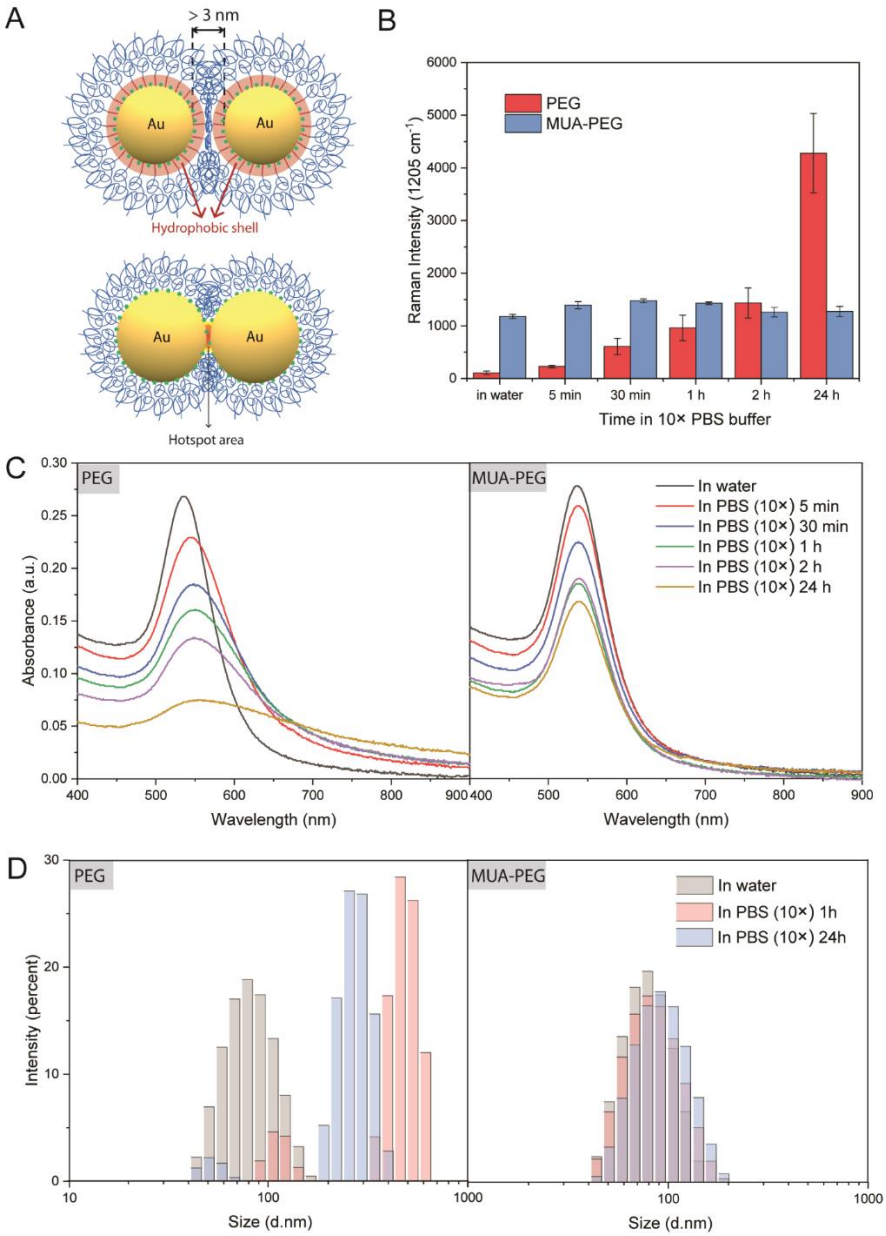

Figure 2.3 SERS signal stability of PEG and MUA-PEG coated nanotags dispersed in 10× PBS buffer solutions. A) Schematic illustration of EM field hotspots prevention by the inner hydrophobic domain. B) SERS signal change of PEG and MUA-PEG coated nanotags before and after dispersed in 10× PBS buffers for up to 24 hours. C) Absorbance spectra change of the above nanotags before and after dispersed in 10 × PBS buffer solutions for up to 24 hours. D) Hydrodynamic size distribution evolution of PEG and MUA-PEG coated nanotags before and after dispersed in PBS buffer solutions for 1 and 24 hours. PEG coatings are at 70% surface ratio for both PEG and MUA-PEG.

Protein corona is known to hinder in-vivo functions of NPs by changing their physical and chemical properties. Here, to mimic the in-vivo environment, we dispersed both PEG and MUA-PEG coated AuNPs to 5% fetal bovine serum (FBS) at 37 ℃. Both samples were blocked by bovine serum albumin (BSA) as a standard surface treatment before adding to FBS [93]. The signal of PEG coated AuNPs drop to only ~10% after dispersed in FBS for 8 hours, indicating rapid reporter contamination by adsorbed serum proteins. On the other hand, SERS signal of MUA-PEG coated NPs changed slowly with time, and over half of the signal was well-preserved after 8 hours (Figure 2.4A). Raman spectra of the nanotags also showed that though with increased background noise (which was resulted from abundant proteins), distinct Raman peak of MUA-PEG coated nanotags was well preserved 8 hours after dispersed in 5% FBS, while for PEG coated nanotags the Raman peak was immersed in increased noisy background (Figure 2.4C&D). A quantitative measurement of protein on each AuNP was conducted next using a Coomassie protein assay. To eliminate the influence of blocking BSA, AuNPs that was not blocked by BSA were applied, and both samples were washed four times after being kept in 5% FBS at 37 ℃ for 24 hours. As shown in Figure 2.4B, the proteins absorbed on AuNP@MUA-PEG were only 10% of that on AuNP@PEG. It was reported that the self-assembled alkyl chains on AuNP helped prevent protein adsorption due to unfavorable interaction between charged protein molecules and the dense hydrophobic shell [94]. Here, our work further shows that the hydrophobic domain can maintain real SERS signal in complex biological systems by reducing unfavorable protein adsorption, making these SERS NPs promising for quantitative in-vivo detection. We believe that the novel hydrophobic domain modified MUA-PEG exhibited good protection of SERS nanotags in biological buffers by preventing hotspots generation and protein corona formation, bringing possibility to achieve quantitative SERS sensing through biological processes or in-vivo activities.

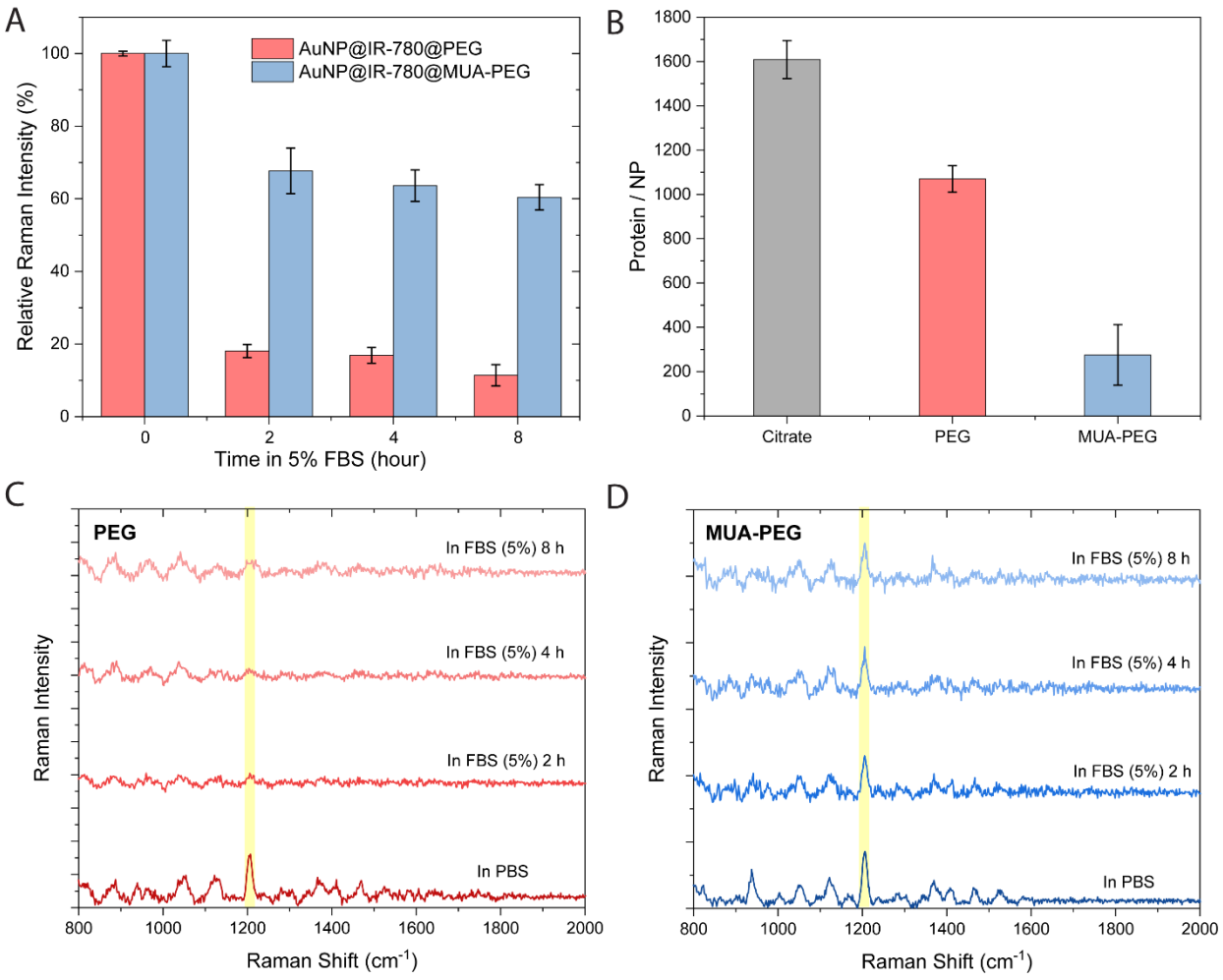

Figure 2.4. Hydrophobic domain provides better resistance to protein corona formation. A) SERS signal change of PEG and MUA-PEG coated AuNPs after dispersed in 5% FBS solution at 37 ℃. Both samples were blocked by BSA before adding to FBS. B) Quantitative protein amount per AuNP measured by Coomassie protein assay 24 hours after dispersed in 5% FBS at 37 ℃. C, D) Raman spectra evolution of AuNP@IR780@PEG (C) and AuNP@IR780@MUA-PEG (D) dispersed in 5% FBS solution at 37 ℃ for up to 8 hours.

2.4 Discussion – Hydrophobic Domain Geometry and SERS Enhancement Mechanism

The formation of the hydrophobic domain by the alkay-modified PEG on AuNP surface was first studied. In fact, the preparation and characterization of well-organized self-assembled monolayer (SAM) of long-chain alkanethiolates ($HS(CH_2)_n$ R) on bulk gold (111) surface have been extensively studied since the last century [95-97]. Typically, long chain alkanethiolates chemisorb as ordered densely packed arrays on Au with an average tilt angle of ~30º from the surface normal, forming a semi-crystalline domain that allows totally surface properties of bulk Au such as wettability, electron transfer and adhesive strength [97]. It was reported that sulfur atoms of unfunctionalized long-chain alkanethiolates form a commensurate hexagonal ($\sqrt{3} \times \sqrt{3}$)R30º overlayer with an S-S spacing of 4.97 Å and an idealized packing density of 21.4 $Å^2$/thiolate (Scheme 2.2) [96]. The SAM of alkanethiolates was further developed with oligo (ethylene glycol) (OEG) or poly (ethylene glycol) (PEG) as the end group to provide protein resistance ability of the film on Au surfaces [94, 98]. Though PEG in its helical form has a larger molecular cross section, but can be accommodated on top of the crystalline alkanethiol layer with an in-plane packing density of 21.4 $Å^2$/thiolate.

However, if the SAM of MUA-PEG happens on the surface of nanoscale Au particles instead of planar Au surface, the packing density of 5k MUA-PEG is thus reported to decrease from 21.4 $Å^2$/thiolate to 30-35 $Å^2$/thiolate on 100-nm Au nanorods [99] and 50-58 $Å^2$/thiolate on 15-nm Au nanospheres [100] due to higher curvature of smaller nanostructures [101]. In this study, we observed a number of ~14,000 MUA-PEG (5k) ligand being adsorbed on each 50-nm Au nanospheres measured by Ellman's reagents of free –SH group, which corresponds to a density of 1.78 PEG/nm^2, or 56 $Å^2$/thiolate, or a grafting density of ~7.5 Å (D, average distance between neighboring PEG chains). It is known that when D is smaller than the Flory radius ($R_F \sim aN^{3/5}$,

where N is the degree of polymerization, and a is the effective monomer length = 0.35 nm for PEG), the PEG stretch away from the NP surface and forms a "brush" layer instead of a "mushroom" formation ($D > R_F$) [102]. At very high coverage with $R_F/D \geqslant 2.8$, the PEG-coating enters the "dense-brush" regime. With a grafting density D of ~7.5 Å and R_F of 5.9 nm for 5k MUA-PEG, R_F/D is calculated to equal to 7.8 in this study, indicating that the packing density of MUA-PEG is high enough to form a dense inner hydrophobic layer and a completed different surface environment on AuNPs.

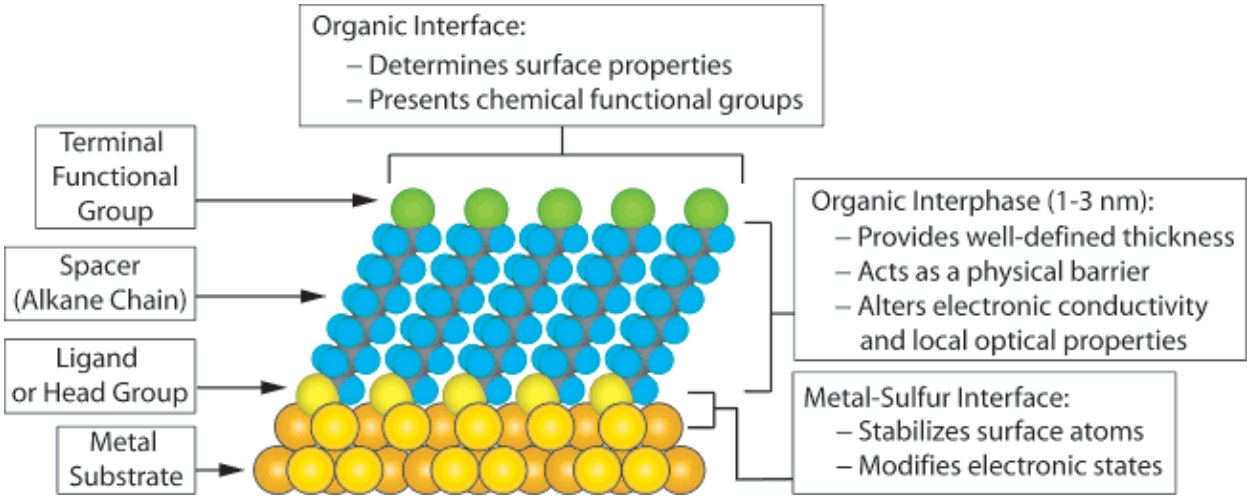

Scheme 2.2 Schematic diagram of an ideal, single-crystalline SAM of alkanethiolates supported on a gold surface with a (111) texture. Scheme reproduced from Ref. 97. [97]

The mechanism study of the observed SERS enhancement effect was followed. The electromagnetic enhancement mechanism was hypothesized to be the primary reason of the enhancement, where the dielectric medium around plasmonic NPs changing from polar aqueous medium to non-polar alkane layer leads to an amplified local EM field. According to the EM enhancement mechanism of SERS, the overall SERS enhancement factor is roughly the fourth power of the EM field amplification enhancement, as shown in Equation 1 [24]:

$$G \approx \left|\frac{E_{loc}}{E_0}\right|^4 = \left|\frac{\varepsilon_m - \varepsilon_s}{\varepsilon_m + 2\varepsilon_s}\right|^4 \left(\frac{R}{R+d}\right)^{12} \qquad \text{(Equation 2.1)}$$

Here, G is the SERS enhancement factor. E_{loc} and E_0 are the EM field amplitude of the local field near NP surface and that of the incident field, respectively. ε_m and ε_s are dielectric constants of the metal core and the surrounding medium. R and d are the radius of the NP and the distance between the molecule and the plasmonic surface. The dielectric constant of gold (ε_m) is determined based on the excitation wavelength [103]. The dielectric constant of the nanoscale alkanethiolate layer was reported by several groups to be in a range of 2.0 to 2.7 measured via different methods [104-106], which was also shown to slightly vary on alkane chain length and the monolayer thickness [89]. It was shown that for a MUA film with a thickness of ~1.55 nm, the dielectric constant was determined to be 2.1 using surface plasmon resonance spectroscopy (SPR) [89]. Considering a Raman reporter molecule attached on a AuNP with fixed radius and distance to the plasmonic surface, when dielectric constant (ε_s) of the surrounding medium changes from 80.4 (ε_{water}) to 2.1 (ε_{alkane}), the enhancement factor change ($G_{hydrophobic}/G_{water}$) for 785 nm laser excitation (ε_m = *-22.9+1.4i*) is calculated as Equation 2, which is qualitatively within the range of enhancement that we observed experimentally:

$$\frac{G_{hydrophobic}}{G_{water}} = \left|\frac{\varepsilon_m - \varepsilon_{alkane}}{\varepsilon_m + 2\varepsilon_{alkane}}\right|^4 \left|\frac{\varepsilon_m + 2\varepsilon_{water}}{\varepsilon_m - \varepsilon_{water}}\right|^4 \approx 17 \qquad \text{(Equation 2.2)}$$

On the other hand, the competition of MUA-PEG with reporter dyes molecules on the AuNP surface could be a counter-effect that result in weak or no SERS enhancement on anisotropic Au structures such as rods and stars. It is known that the strong SERS enhancement of Au nanorods and nanostars come from the reporter molecules sitting in the high SERS-active "hotspot" areas on high-curvature structures due to the "lightning rod" effect [32]. It is thus possible that the densely packed MUA layer shows a fiercer competition with reporter molecules compared with flexible PEG regime, causing some signal loss due to "hotspot" area being occupied by the hydrophobic layer. The combination of the two effects explains the strong SERS enhancement by the hydrophobic layer in spherical AuNPs (where the electromagnetic environment change is the dominant effect), but weak or no SERS enhancement in rod- and star-shaped AuNPs (where the competition with reporter molecules at "hotspots" becomes the dominant effect).

In addition to electromagnetic enhancement mechanism, the SERS enhancement brought by the hydrophobic domain was observed to differ with various Raman reporter molecules, so it was hypothesized that there co-exists a resonance enhancement effect, where the electronic resonance of the chromophore reporter was sharpened by the hydrophobic-hydrophobic interaction between the molecules and the non-polar aliphatic layer, thus only Raman scattering of resonant reporter dyes that go through electronic transition under the laser excitation were greatly enhanced. The exact mechanism of the hydrophobic enhancement, though is still not fully understood, is believed to be a combination of the electromagnetic surface enhancement and the chemical resonant enhancement, both resulted from the surface dielectric medium change from water to the hydrophobic layer.

2.5 Conclusion

To summarize, in this work I modified the traditional PEG coating of SERS nanotags with an inner hydrophobic domain. The introduced hydrophobic layer brings three effects. First, it provides a new strategy of SERS enhancement by changing the near-surface dielectric medium of the nanotags. The introduced hydrophobic inner domain creates an aliphatic shell around AuNPs with reporter molecules embedded, offering different optical properties at the surface compared with that of aqueous environment, bringing in an additional 5-10 times higher SERS enhancement than traditional PEG coating. This SERS enhancement was observed in nanotags with different AuNP shapes and different PEG ligand molecular weights, but varies with different Raman reporter molecules, thus the enhancement mechanism is hypothesized to be a combination of both an EM surface enhancement and a chemical enhancement. Additional advantage of hydrophobic domain PEG coating is found about its better protection of Raman reporters from leaking out via hydrophobic interaction with the reporters, enabling SERS nanotags better time stability. Second, the rigid inner hydrophobic layer improves the ability of PEG ligands to prevent NPs coupling in high-ionic-strength biological fluids, which avoids unwanted SERS intensity change caused by the formation of hotspots. Last, unfavorable interaction between the hydrophobic inner domain and charged biomolecules such as proteins reduces protein adsorption on AuNPs, leading to not only stable SERS signal but also distinct and real Raman peaks after dispersed in serum solutions. Such imaging probes with improved brightness and signal stability in biological fluids is believed to be ideal candidates for biological applications with enhance detection efficiency and imaging sensitivity.

2.6 Supplementary Figures and Table

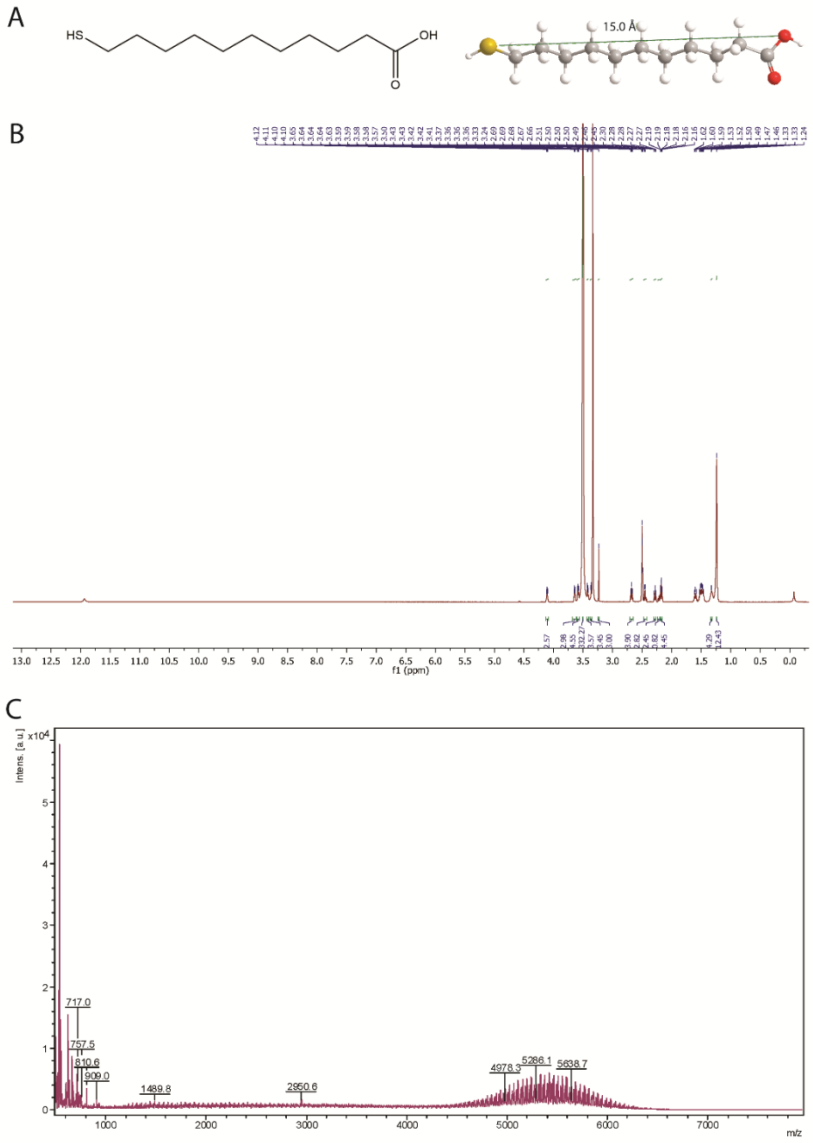

Supplementary Figure 2.1 MUA molecule characterization. **A)** Chemical structure of MUA molecule. White: H atom; Grey: C atom; Red: O atom; Yellow: S atom. The length of the molecule is estimated to be 1.5 nm. **B)** H^1 nuclear magnetic resonance (NMR) of the synthesized MUA-PEG (5k Da). **C)** Mass spectrum of the synthesized MUA-PEG (5k Da).

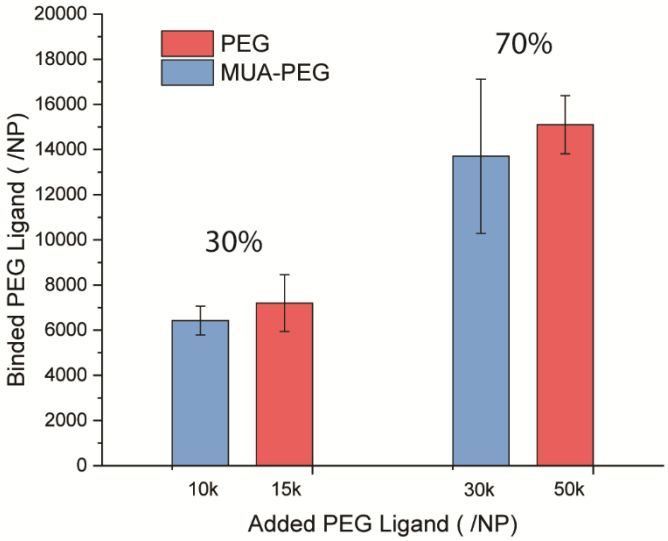

Supplementary Figure 2.2 Quantification of conjugated PEG ligands when listed PEG ligands amount were mixed with AuNPs. Addition of 10k/NP and 15k/NP of PEG and MUA-PEG, respectively, occupies 30% of AuNP surface area, and 30k/NP and 50k/NP occupiess 70% of AuNP surface area.

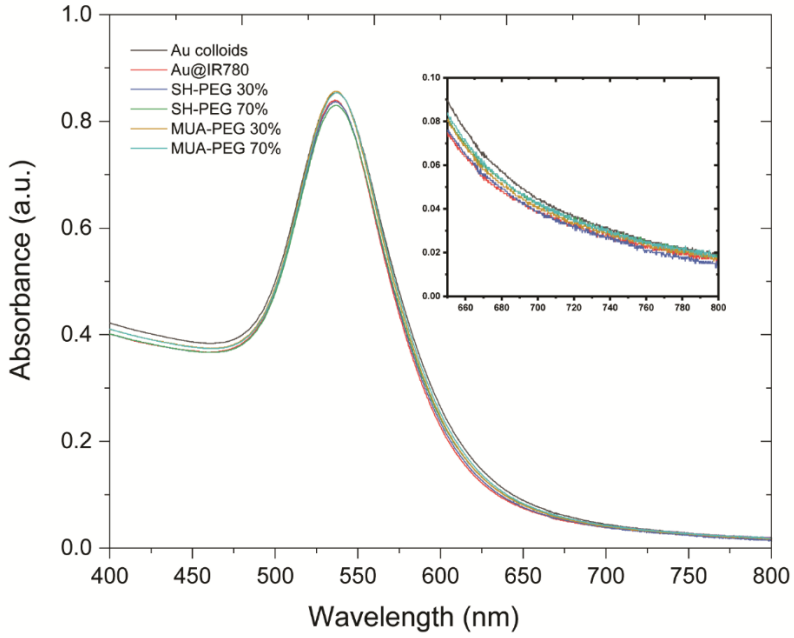

Supplementary Figure 2.3 Absorbance spectra of AuNPs, IR-780 attached AuNPs and IR-780 attached AuNPs with different PEG coatings. Inserted: zoom-in spectra from 650 nm to 800 nm showing no NP aggregation.

Supplementary Table 2.1 Hydrodynamic size and polydispersity index (PdI) of SERS nanoparticles.

	PEG surface ratio	**SH-PEG**		**MUA-PEG**	
		Size ave (d. nm)	PdI	Size ave (d. nm)	PdI
AuNP@IR-780	0%	*58.04 ± 0.50*	*0.207*	*58.04 ± 0.50*	*0.207*
	30%	*74.39 ± 0.29*	*0.170*	*76.84 ± 0.61*	*0.169*
	70%	*74.76 ± 0.28*	*0.150*	*76.99 ± 0.37*	*0.159*

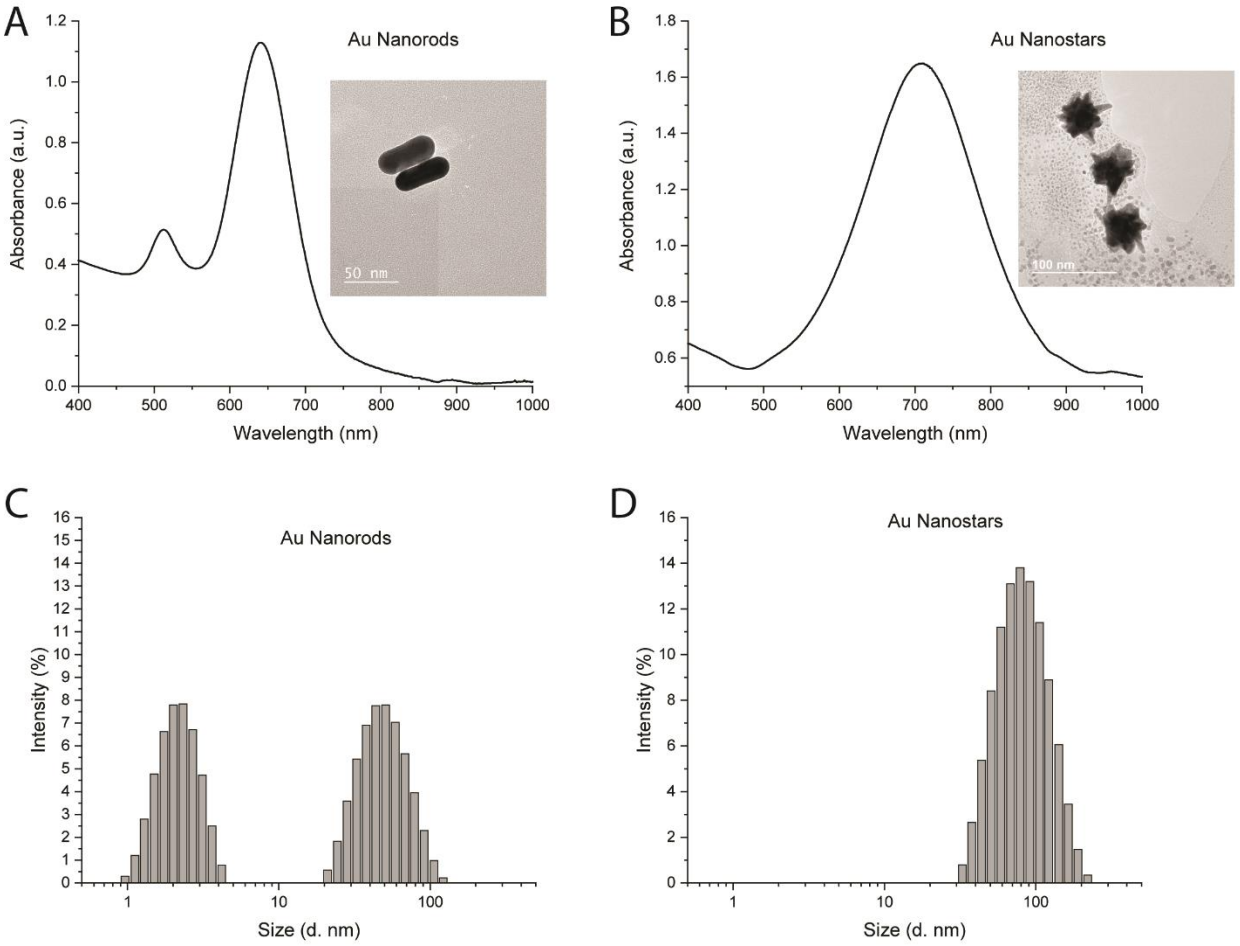

Supplementary Figure 2.4 A) UV/Vis spectrum of 20-nm × 50-nm Au nanorods. Inserted: TEM picture of 50-nm Au nanorods. B) UV/Vis spectrum of Au nanostars. Inserted: TEM picture of Au nanostars. C) Hydrodynamic size distribution of Au nanorods. D) Hydrodynamic size distribution of Au nanostars.

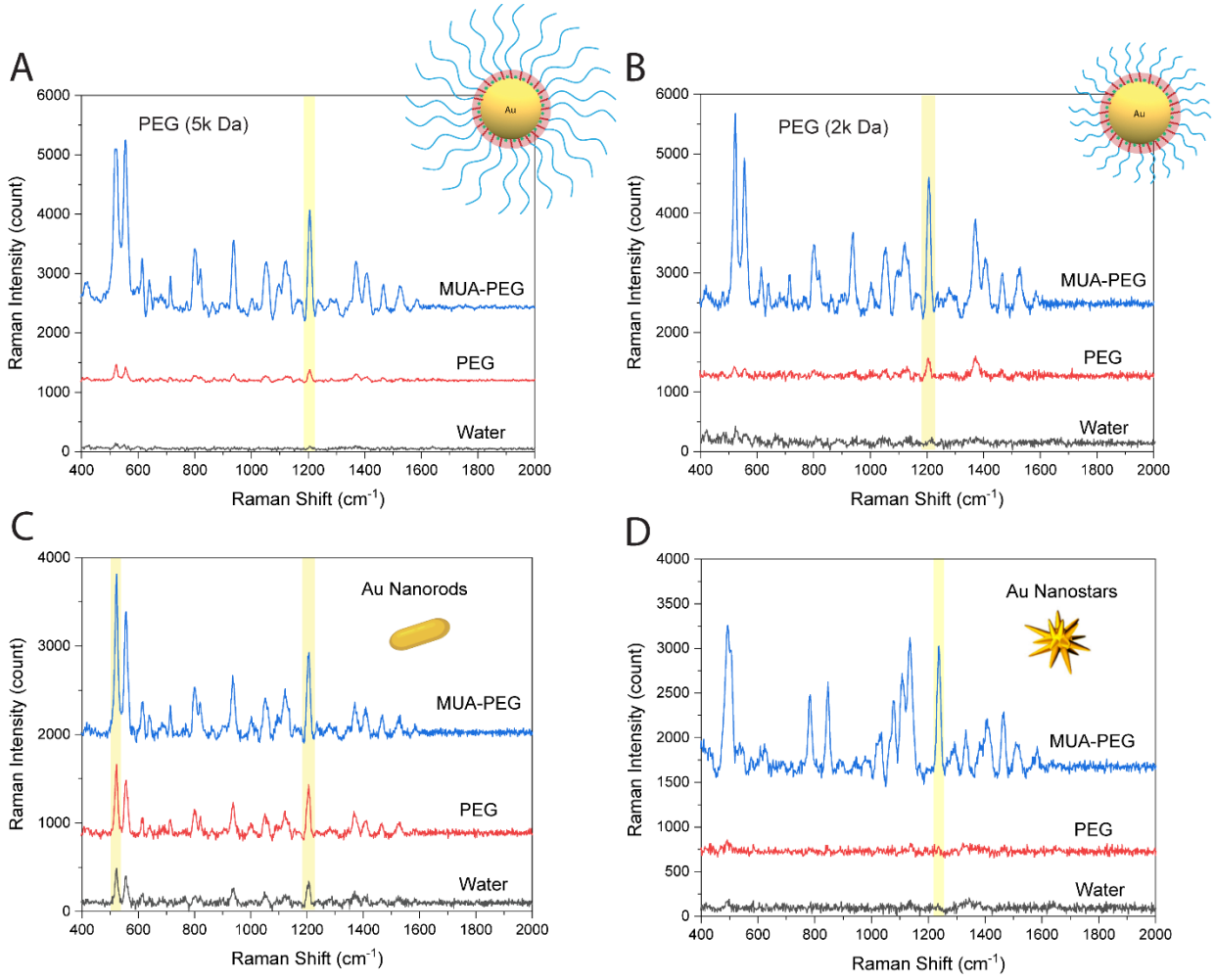

Supplementary Figure 2.5 Raman spectra of dye attached AuNPs with different PEG ligand molecular weight: A) 5k Da PEG and MUA-EPG, B) 2k Da PEG and MUA-EPG, and with different AuNPs nanostructures: C) Au nanorods and D) Au nanostars. All spectra measured at 785 nm, 200 mW. PEG ligands surface ratio was 70% for both PEG and MUA-PEG coatings.

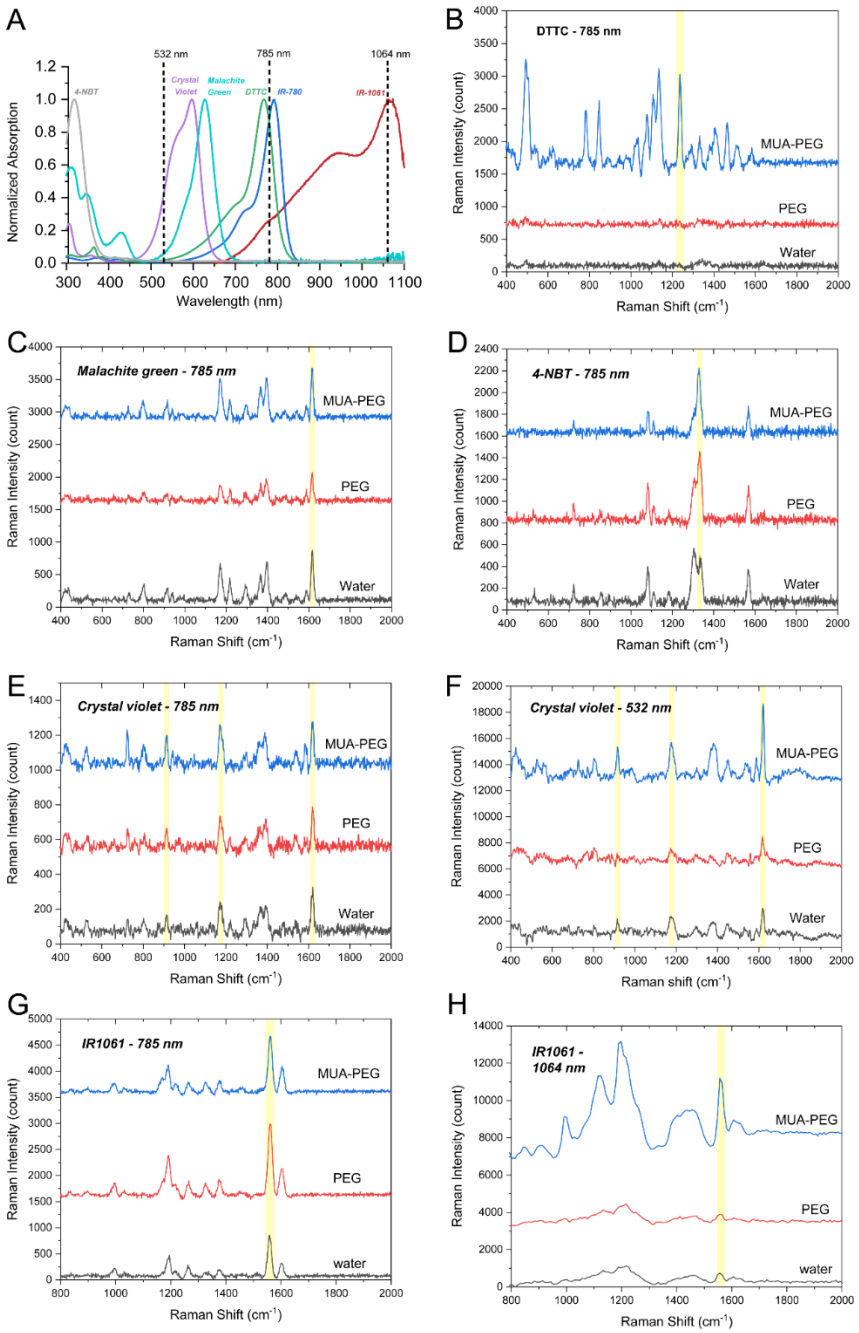

Supplementary Figure 2.6 A) Normalized absorption spectra of IR-780, DTTC, malachite green (MG), 4-NBT, crystal violet (CV) and IR-1061 plotted together with 532-nm, 785-nm and 1064-nm laser lines. All dye molecules were measured in DMF solution. B-H) Raman spectra of AuNPs attached with Raman reporter B) DTTC measured at 785 nm, C) MG measured at 785 nm, D) 4-NBT measured at 785 nm, E) CV measured at 785 nm, F) CV measured at 532 nm, G) IR-1061 measured at 785 nm and H) IR-1061 measured at 1064 nm, with different PEG coatings. PEG ligands surface ratio was 70% for both PEG and MUA-PEG coatings.

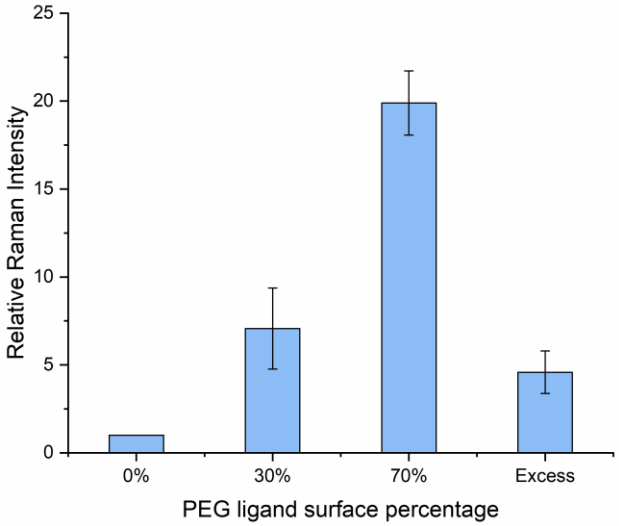

Supplementary Figure 2.7 Competitive adsorption between MUA-PEG ligands and reporter molecule IR-780 on AuNP surface. Relative Raman intensities (normalized by non-coating samples) of SERS NPs with different MUA-PEG surface ratios are shown.

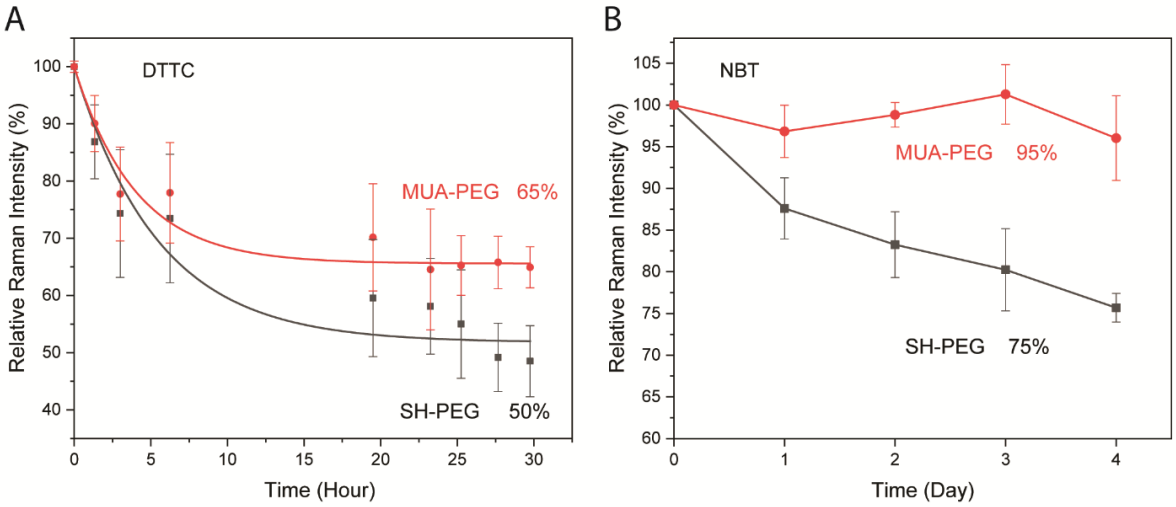

Supplementary Figure 2.8 Long-term SERS signal stability of MUA-PEG coated and PEG coated nanotags, respectively. A) DTTC-attached SERS nanotags and B) 4-NBT attached SERS nanotags are shown here. PEG ligands surface ratio was 70% for both PEG and MUA-PEG coatings.

CHAPTER 3: DUAL-TRACER NON-INVASIVE METASTATIC SENTINEL LYMPH NODE DETECTION

3.1 Motivation – To Improve Tumor-Targeting Specificity in Metastatic Lymph Node Detection

Identifying the presence or absence of cancer in tumor-draining lymph node (sentinel) is the key for cancer staging and diagnostics [71, 107]. While the clinical protocol of sentinel lymph node location and biopsy being time-consuming and causing pain to patients, optical techniques such as fluorescence and SERS have emerged as an alternative for non-invasive and real-time lymph node metastasis detection [108]. Tafreshi et al. has shown non-invasive detection of breast cancer lymph node metastases with high sensitivity in a mouse model using mAbs specific for binding carbonic anhydrase isozymes conjugated to a near-infrared (NIR) fluorescent dye [109]. After peritumoral injection, these agents were shown to transit through the mammary fat pad and to be specifically retained in target-expressing breast cancer metastases of the axillary lymph node (ALN), and cleared from non-cancerous nodes.

Imaging agents bind to tumor cells through specific interaction between the conjugated ligands and the corresponding cell receptors. However, in real-life practice, non-specific binding of NPs to normal lymph node tissue often causes false negative results that reduces detection sensitivity and specificity. To eliminate the false-positive signal stemming from non-specific binding, a paired-agent strategy (also called ratiometric approach) was presented in many studies where a control (non-targeted) imaging agent and a targeted imaging agent were co-administrated. [107, 110, 111] The second “un-targeted” tracer can be used to account for binding-independent characteristics of the target tracer’s uptake (Scheme 3.1).

Recent work by the Pogue group has advanced the dual-tracer strategies to quantify cell-surface cancer receptor concentrations in primary tumor using fluorescence tomography [110]. In a mouse model of breast cancer metastasis, they injected equal amount of the targeted agent, EGFR-specific antibody labeled with an NIR dye, and the untargeted tracer, isotype control antibody labeled with a different NIR dye, simultaneously intradermally into each front footpad [110]. It was observed that though average targeted tracer uptake was not significantly different from the average untargeted tracer uptake, targeted tracer retention was significantly higher than untargeted tracer retention in tumor-bearing lymph nodes, and a statistically significant correlation between the EGFR concentration measured and the number of cells detected in lymph nodes were observed with a slope of 0.4 pM $cell^{-1}$ cm^{-2}. Based on the same principle, Oseledchyk and co-workers reported a robust ratiometric imaging approach using anti-folate recepter (FR)-SERRS-NPs (αFR-NPs) and non-targeted SERRS-NPs (nt-NPs) multiplexing for microscopic tumor lesions detection in a murine model of human ovarian adenocarcinoma [50]. The unique SERRS-NP spectrum of each Raman probe allows for very sensitive imaging by ratiometric signal analysis. Precise delineation of tumor metastases was demonstrated regardless of their localization and can sense tumors as small as 370 μm as verified by bioluminescence imaging and histological correlation. The great contrast between lesion and the surrounding brought by ratiometric imaging approach makes it promising for cancer detection at molecular level.

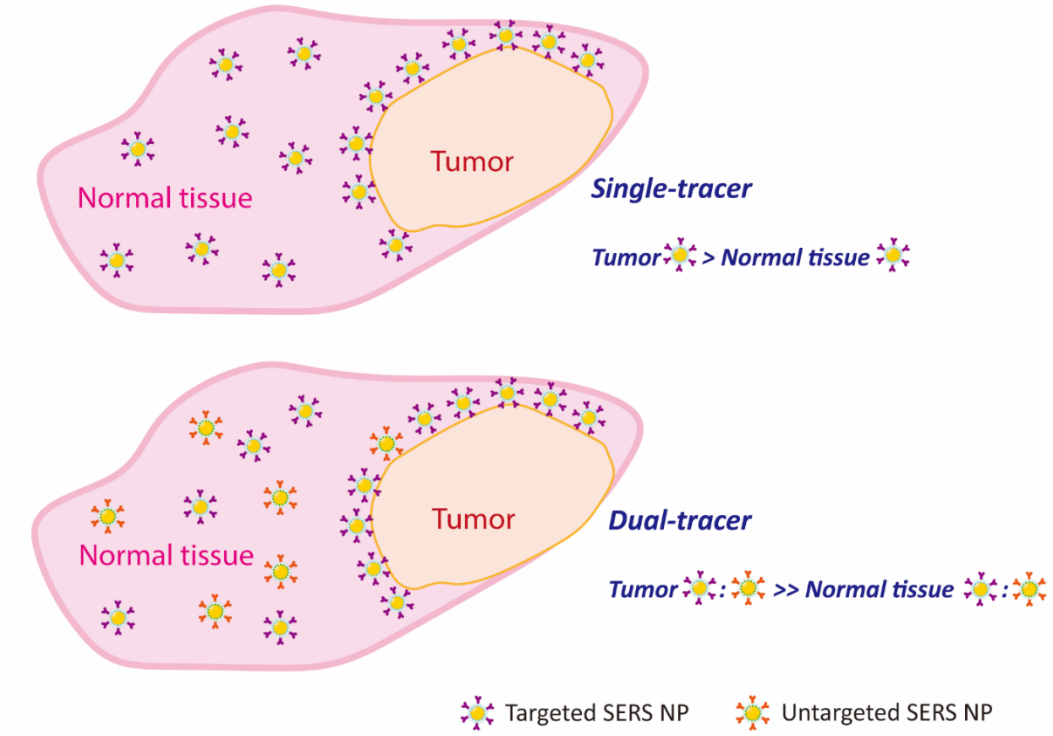

Scheme 3.1. Illustration of dual-tracer SERS strategy. In the single-tracer scenario, the targeted SERS NPs bind to both normal tissue and cancer tissue. Poor contrast between tumor and the surroundings is obtained. In the dual-tracer scenario, when both targeting agents and control agents are used, the ratio of targeting to control agents will be larger in tumor tissue than that in normal tissue, resulting in good contrast.

Motivated by the novel dual-tracer tumor detection strategy, in this chapter I employed a paired SERS NPs agents for sentinel lymph node detection, where both a targeting SERS NP and non-targeting (control) SERS NP are injected to create contrast between tumor cells and normal lymph node tissue to improve detection sensitivity. Compared to fluorescence imaging, SERS agents offers favorable properties including ultrahigh sensitivity, enormous multiplexing capability with narrow spectral bandwidth, and particularly high specificity with the 'fingerprint' spectrum of Raman molecules that can be well distinguished from the background signal of the living organisms, and thus are expected to show improvement of limit of detection in non-invasive metastatic sentinel lymph node detection.

3.2 Theory – Dual-Tracer Compartmental Modeling

The lymph node molecular concentration imaging (LN-MCI) approach is based on a dual-tracer compartmental modeling that describes targeted and untargeted tracer uptake [112]. The whole system was modeled to be driven by the concentration of tracer in the upstream lymphatic vessels, C_l, which enters the lymph node at flow rate, F_l. The targeted tracer was modeled to only be able to exit the lymph node into the downstream lymphatics at the same flow rate, F_l, assuming flow equilibrium conditions. By assuming that the unbound (freely associated) concentration of tracer in the lymph node is always homogeneously distributed and that the concentration of targeted tracer in the lymph node is negligible compared to the concentration of targeted receptor, a system of first-order differential equations can be developed to govern the rate of change of tracer concentration in each compartment. For the targeted SERS NPs:

$$\frac{dC_f(t)}{dt} = F_l C_l(t) - F_l C_f(t) - k_3 C_f(t) + k_4 C_b(t)$$

$$\frac{dC_b(t)}{dt} = k_3 C_f(t) - k_4 C_b(t)$$

$$SERS_T(t) = \alpha_T\left[C_f(t) + C_b(t)\right] \qquad \text{(Eauqation 3.1)}$$

Within the lymph node, the targeted tracer was modeled to be freely associated (C_f) or bound (C_b) to targeted tumor cell receptors, and rate-constants k_3 and k_4 were used to describe the rate of tracer-receptor association and dissociation, respectively. $SERS_T(t)$ represents the measured SERS signal from the uptake of the targeted SERS NPs in the lymph node as a function of time, t. The parameter α_T represents the detection efficiency of the Raman system for the targeted SERS NPs. For the untargeted SERS NPs:

$$\frac{dC_U(t)}{dt} = F_l C_l(t) - F_l C_U(t)$$

$$SERS_U(t) = \alpha_U C_U(t) \qquad \text{(Equation 3.2)}$$

, where $C_U(t)$ is the concentration of untargeted SERS NPs in the lymph nodes. $SERS_U(t)$ represents the measured SERS signal from the uptake of the untargeted SERS NPs in the lymph node as a function of time, and the parameter α_U represents the detection efficiency of the Raman system for the untargeted SERS NPs. If we further assume that the free concentrations of the targeted and untargeted SERS tracers share roughly the same time course (i.e., $C_f(t) = C_U(t)$), and that the binding is an adiabatic process (i.e., that $C_b(t)/C_f(t)$ remains a constant), then the following equation will be derived:

$$\frac{\frac{\alpha_U}{\alpha_T} SERS_T(t) - SERS_U(t)}{SERS_U(t)} = \frac{C_b(t)}{C_f(t)} = \frac{k_3}{k_4} \equiv Binding\ Potential\ (BP) \qquad \text{(Equation 3.3)}$$

This equation, which amounts to normalizing a targeted SERS NP uptake signal, subtracting from it an untargeted SERS NP uptake signal, and dividing that difference by the untargeted SERS NP uptake signal, can be shown to be proportional to the receptor concentration in the lymph node.

The defined binding potential, *BP*, which equals to $\frac{k_3}{k_4}$, is the main parameter of interest in this model, because it is directly related to the tracer-receptor affinity. Equation 3.3 was used to estimate receptor concentration in the following animal experiments in this study. The ratio of detection efficiencies, $\frac{\alpha_U}{\alpha_T}$, was estimated to roughly equal to 1, because the optical properties of the tissues are not significantly different for targeted and untargeted SERS NP signal measurement, considering only a single laser wavelength 785 nm was used.

3.3 Experimental Section

Chemicals and materials. Deionized water (DI water) was used throughout the work. The following chemicals were used as purchased without any further purification: 11-mercaptoundecanoic acid (MUA, 95%), diethyl ether (≥ 99.7%), Dimethylformamide (DMF), sodium citrate, 5k poly(ethylene glycol) methyl ether (mPEG, Mn 5000 Da), 2-[2-[2-Chloro-3-[(1,3-dihydro-3,3-dimethyl-1-propyl-2H-indol-2-ylidene)ethylidene]-1-cyclohexen-1-yl]ethenyl]-3,3-dimethyl-1-propylindolium iodide (IR-780, dye content ≥ 95%), 2-[2-[2-Chloro-3-[2-(1,3-dihydro-1,3,3-trimethyl-2H-indol-2-ylidene)-ethylidene]-1-cyclohexen-1-yl]-ethenyl]-1,3,3-trimethyl-3H-indolium chloride (IR-775, dye content ~ 90%), gold(III) chloride trihydrate ($HAuCl_4 \cdot 3H_2O$), L-ascorbic acid, silver nitrate ($AgNO_3$), Pluronic® F-127, bovine serum albumin (BSA) and fetal bovine serum (FBS) from Sigma Aldrich; poly(ethylene glycol) methyl ether thiol (mPEG thiol, Mn 5000 Da) from Laysan Bio Inc.; thiol PEG succinimidyl glutaramide (SH-PEG-NHS) from JenKem Technology USA; Rat IgG from Equitech- Bio, Inc.; Cetuximab was given as a gift from our collaborator from Illinois Institute of Technology.

Hydrophobic domain PEG ligand synthesis. Synthesis of MUA-PEG ligand follows the method outlined in Schultz et al [84]. In brief, 11-mercaptoundecanoic acid (MUA) and mPEG (5k Da)

was mixed in 3:1 molar ratio in a round-bottom flask and kept under vacuum at 110 ℃ for 1 hour. Then the temperature was ramped up to 160 ℃ under N_2 atmosphere with a reflux condenser and kept for 72 hours. The unreacted MUA was removed by multiple washings of cold diethyl ether.

Synthesis of paired SERS NPs. Glassware and stir bars for gold nanoparticle synthesis were washed by aqua regia before use. Gold nanostars (AuNS) were synthesized using a seed-mediated method [87]. First, 15-nm small AuNPs were synthesized as the seed. A water solution of 2.2 mM sodium citrate (60 mL) was heated to boiling under vigorous stirring. Once boiling had commenced, 400 μL of $HAuCl_4$ solution (25 mM) was quickly injected. The reaction completed within 10 min where the solution turned from yellow to purple grey and then to burgundy. The resulted solution was centrifuged 3 times and stored as Au seed for the next step. For Au nanostars synthesis, to 4 mL $HAuCl_4$ solution (0.25 mM), 4 μL of 1N HCl and 280 μL of 15-nm citrate gold seeds were added followed by simultaneous addition of 40 μL $AgNO_3$ solution (3 mM) and 40 μL of ascorbic acid solution (100 mM) under stirring. The reaction was performed at room temperature, and the process was completed in less than 2 min. Raman reporter molecules IR-780, and IR-775 stock solutions were prepared by dissolving 1 mg of the dye molecules into 1 mL of DMF. The stock solutions were diluted by DI water to form a dye concentration of 2.62 μM for fresh use. Before adding dye to the as-synthesized AuNS, a 1% Pluronic® F-127 solution was first added to the system to a final concentration of 0.1% to avoid aggregation during dye addition. Typically, 400 μL above dye molecule solution was dropwise added to AuNS under moderate stir. After 10 min incubation with reporter molecules, 60 μL SH-PEG-NHS solution (51.8 μM) was dropwise added to the AuNS@dye solution, followed by the addition of 640 μL MUA-PEG solution (51.8 μM) 2 minutes later. The solution was then incubated at room temperature for 1 hour, then the SERS nanoparticles were washed twice by centrifugation at 1100g to remove excess PEG and dye

molecules. The PEGylated SERS NPs were finally dispersed in 2 mL of PBS 1x, followed by addition of 150 μL antibody solution (2 mg/ml in PBS 1x). The antibody conjugation was allowed to react at 4 ℃ overnight. On the next day, a 1% BSA solution was first added to the SERS NP system with the final concentration of 0.1% BSA, and the solution was allowed to incubate for 30 min at 4 ℃. Then the SERS NPs were washed twice by centrifugation at 1000g to remove excess antibodies. The paired SERS NPs were finally re-dispersed in PBS 1x with 0.05% BSA (final NP concentration of 600 pM) and stored at 4℃.

SERS nanotags characterization. Absorbance spectra of AuNP solutions were obtained from a GENESYS™ 10S UV-Vis Spectrophotometer. Dynamic light scattering (DLS) was fulfilled on a Malvern Nano ZS90 Zetasizer. Weight concentrations of AuNPs in solutions were measured by inductively coupled plasma-mass spectrometry (ICP-MS, NexION 350D, PerkinElmer). Transmission electron microscope (TEM) pictures were taken by a JEOL 2100 Cryo TEM.

Whole Raman spectrum identification. All Raman spectra collected were first extracted tissue background Raman signal. Pure NP-A or NP-B solution in glass vial were measured as the reference spectra, respectively. The whole spectrum identification algorithm was developed using Minimum Mean Square Error (MMSE) fitting, by making the error between the simulated spectrum and the background subtracted spectrum to be the smallest, following the equation:

$$xA_{ref} + yB_{ref} + error + BGD = Spectra$$

$$\frac{concentration\ of\ B_{ref}}{concentration\ of\ A_{ref}} = m$$

$$Contribution\ of\ A = \frac{x}{x+my} \qquad \text{(Equation 3.4)}$$

IRDye800 NHS Ester – Cetuximab Conjugation. Cetuximab solutions (2 mg/mL in PBS) were graciously donated by the laboratory of Dr. Brian Pogue. Cetuximab solution was conjugated to

IRDye800-NHS ester as a fluorescent label. Dissolve 1:2 molar ratio of cetuximab and IRDye800 NHS ester in deionized water at pH 9.0. Allow to stir at room temperature in the dark for 2 hours. For purification, the conjugated antibody solution was passed through a Zeba desalting spin column with a 7 kDa molecular weight cutoff (Thermo Fisher, Walthan MA).

IRDye800-Cetuximab Fluorescent Binding Assay. To assess binding affinity, three cell lines with known EGFR expression were cultured and incubated with the conjugated cetuximab-IRDye800 solution made prior for 1 hour in the dark.

Cell lines. All cell lines were donated by the laboratory of Dr. Kimberly Samkoe. Cell lines were: FaDu (low EGFR expression, cultured in RPMI 1640 medium w/ 10% FBS) MDA-MB-231 (mid-EGFR expression, cultured in DMEM w/ High Glucose (4500 g/L) and 10% FBS), and U251 (high EGFR expression, cultured in DMEM w/ High Glucose (4500 g/L) and 10% FBS).

Cells were cultured in T25 flasks until confluence was reached and were then trypsinized and counted. Cells were seeded into a 96 well plate, with 5×10^4 cells seeded in each well. The seeded plates were allowed to sit in the incubator for 24 hours to allow cells to properly adhere, and were then treated with 0.5 mg cetuximab-IRDye800 per well for 1 hour in the dark at 37 degrees C. After 1 hour, each well was rinsed with 1 mL sterile PBS 3x, and the plate was then imaged on the PEARL near-infrared imager at 800 nm. ROIs were then drawn in the subsequent images and the mean pixel value and variance for each well was calculated.

Animals. Nude, athymic mice were purchased from The Jackson Laboratory (Bar Harbor, ME) and housed in the vivarium maintained by the Illinois Institute of Technology. Of the nine mice used, three were eight months old, and the remaining six mice were six months old. All mice were fed a standard rodent diet in pellet form, supplied from Envigo Teklad Diets (Indanapolis, IN), and water bottles were filled with filtered water.

In-vitro cell culture & tumor implantation. MDA-MB-231 cells were cultured in a T175 flask in DMEM (high glucose, 4500 g/L) supplemented with 10% FBS. Upon confluence, cells were then trypsinized and counted. Each animal received 2×10^6 cells with the cells suspended in a 1:1 volume of DMEM:Matrigel. Each injection was 25 μL total volume. Per mouse, 2×10^6 cells were suspended in 12.5 μL chilled medium and 12.5 μL chilled Matrigel solution and loaded into a 300 μL chilled insulin syringe. All materials, including the cell-filled syringe(s), were placed on ice until immediately before injection into the right foot pad of the mouse. Animals were then monitored bi-weekly post-injection for signs of injection and/or decline.

Anesthesia of Animals. Animals were placed in small induction chamber, measuring approximately 5 cm × 15 cm. Tubing is attached at the inlet of the chamber and connected to an anesthesia apparatus, and mice were first brought under with 0.8 L/min O_2 with 2.5% isoflurane gas. Once the mouse appeared properly anesthetized, a toe pinch was preformed to assess the animal's reflexes and plane of anesthesia. When proper sedation is reached, isoflurane/O_2 is redirected to the nose cone, and the animal was quickly weighed and transferred to the surgical table and its head delicately mounted into an anesthesia nose cone. The animal was allowed to acclimate to anesthesia through the nose cone, and after 2-5 minutes the reflexes are checked again via a toe pinch. Following proper sedation, the mouse was placed in the supine position for imaging. To remove any small hair at the location of the lymph node, a generic hair removing cream was applied and wiped away with water after 1 minute. Generous amounts of tape were then used to secure the animals limbs in place as well as reduce the possibility of movement artifacts during later imaging.

SERS NP administration. To facilitate rapid identification of the lymph node under the skin, 10 μL of 1 mg/mL methylene blue solution was injected into the foot pad. After a short period of time

(30-60 seconds), a light is placed under the mouse and the shadow of the popliteal lymph node can be clearly seen. The Raman spectrometer probe is then positioned above the lymph node. Upon localization of the lymph node, 25 μL of SERS nanoparticle solution was injected into the animal's footpad, and imaging via Raman spectroscopy was done for 3 hours.

Sacrifice of animal and lymph node resection. Upon completion of the imaging session (3 hr), the mouse is sacrificed and both the tumor-bearing and non-tumor bearing lymph nodes, as well as the tumor-bearing foot pad. These samples are promptly stored on liquid nitrogen for later RNA extraction and qPCR analysis (yet to be completed) to quantify the extent of human cancer metastasis to the popliteal lymph node, relative to the amount of primary tumor in the foot pad. To sacrifice, the mouse is first given an overdose of isoflurane (5%), followed by an intracardiac injection of 5 mL of 1 M KCl aqueous solution. Shortly after (~30 s - 1 min) a successful KCl injection the heart and respiration stopped, after which the tissues of interest were harvested and stored.

In-vivo Raman spectroscopy. Raman spectra at 785 nm were obtained using an Agility transportable 785/1064 nm dual-band benchtop Raman spectrometer (East JHX, Inc.). 200 mW of laser power was used as the excitation source. The band intensities were calibrated by standard sample (benzonitrile) spectrum. All the Raman spectra were baseline corrected to remove fluorescence background. During spectra acquisition, breathing motion effects were minimized by lightly applying tape to the extended leg that was imaged.

3.4 Results and Discussion

SERS NPs for non-invasive in-vivo imaging must be bright enough to be detected after most of the signals have been absorbed and scattered by the covered tissues. Here, Au nanostars

(AuNS), a group of nanostructures that enlarge the electric field at its intrinsic sharp tips were employed to amplify SERS intensity of the NPs (Figure 3.1A). Compared with Au nanospheres of the same size, Au nanostars showed 1-2 orders of magnitude of enhancement of same amount of reporter molecules due to the "lighting rod" effect (Figure 3.1B). For the paired-agent method, one important consideration is that the pair SERS agents share same nanostructures (same metallic cores and biocompatible coatings) but are functioned with different reporter molecules and antibodies (one targeted, another non-targeted) to show similar delivery and retention kinetics but different targeting specificity to tumors. Here we prepare two types of AuNSs that have similar shape, size and surface chemistry to ensure similar physiologic kinetics (Figure 3.1C), without which the quantitative comparison of targeting and control signals in the lymph node becomes unreliable. The surface coating of the AuNSs consists ~80% of MUA-PEG, and ~20% of traditional thiolated PEG with NHS group at the outside for antibody conjugation. The antibody conjugated to the targeted SERS NP was Cetuximab, known as its brand name Erbitux, working by inhibiting the growth and survival of epidermal growth factor receptor (EGFR)-expressing tumor cells with high specificity and a 2-log higher affinity than epidermal growth factor (EGF) and transforming growth factor-alpha (TGF-α). The reactivity of Cetuximab was first validated by an in-vitro cell assay, where 3 different cell lines with low, medium/high and high expression of EGFR were incubated with Cetuximab conjugated IR dyes. After 2-h incubation, excess IR-dye Cetuximab conjugates were washed out, and the cells were transferred to well plate for a field fluorescence imaging. It was shown that the fluorescence signal increases with higher expression of the cell line, indicating the reactivity of the Cetuximab and its high binding affinity with EGFR on the cells (Figure S3.1). The paired SERS NPs exhibited similar SERS brightness, hydrodynamic

size and zeta potential (Figure 3.1D&E), laying the foundation for the next-step binding kinetics study and in-vivo quantitative detection.

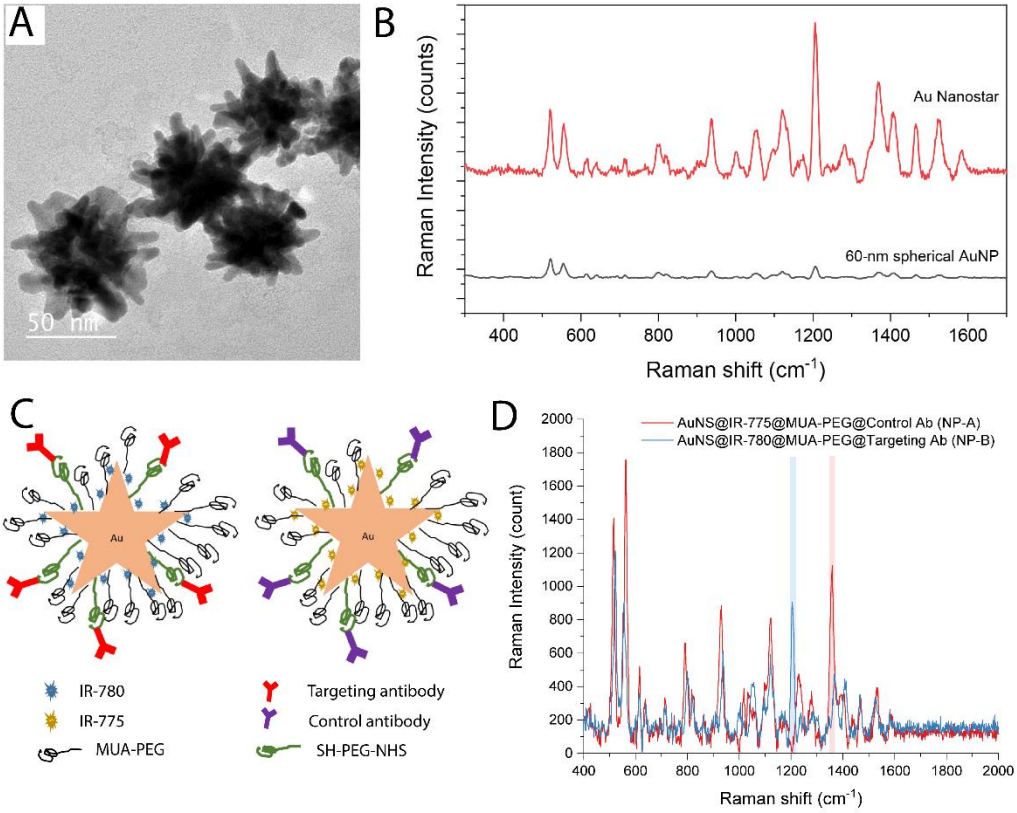

E

Sample	*Hydrodynamic size (d. nm)*	*Zeta potential (mV)*
AuNS@IR-775@MUA-PEG	95.44 ± 0.7	-16.1 ± 0.4
AuNS@IR-780@MUA-PEG	94.4 ± 0.8	-15.5 ± 1.3
AuNS@IR-775@MUA-PEG@Control Ab	118.6 ± 1.4	-3.8 ± 0.3
AuNS@IR-780@MUA-PEG@Targeting Ab	112.0 ± 1.2	-1.7 ± 0.5

Figure 3.1 A) Cryo-TEM image of as-synthesized SERS agents for in-vivo lymph node detection. B) SERS enhancement comparison of AuNSs and Au nanospheres of the same size. C) Schematic illustration of the paired AuNSs SERS agents with the same gold core and surface coating but different reporter molecules and conjugated antibodies. D) SERS spectra of the as-synthesized paired SERS agents, with red and blue highlighted peaks from NP-A (IR-775 encoded) and NP-B (IR-780) encoded, respectively. E) Table of hydrodynamic sizes and zeta potential values of the as-synthesized paired SERS NPs.

Good linearity between NP concentration and Raman signal is essential for quantitative detection. We thus tested the SERS intensity change of the paired agents with NP concentration in aqueous solution, and calculated the limit of detection (LOD) of each NP as the lowest NP concentration where the SERS signal-to-noise ratio (SNR) is larger than 3. As shown in Figure S3.2, both NP-A and NP-B exhibits a broad SERS signal linear range from femto- to pico-molar level. The LODs of NP-A and NP-B were calculated to be 20 fM and 4 fM, respectively (Figure S3.3). At the other end of the range when NP concentration exceeds ~4 pM, SERS signal drops instead of increasing due to the interplay between NP extinction and SERS enhancement (Figure S3.4) [113-115]. The real-life local NP concentration in the tissues, however, is typically below this threshold and thus the SERS signal can be considered as linear.

On the other hand, as paired agents, the SERS signal from each of the NPs must be independent and does not affect each other when mixed together. Since both of the SERS NPs are attached with 785 nm resonant chromophores, IR-775 and IR-780, a spectrum of the mixed NPs can be obtained with single-laser excitation. We separated the spectra of mixed solution by an identification algorithm that restored the ratio of the mixed NP-A and NP-B, and compared the calculated ratio with the real one to confirm the signal independency. The identification algorithm separated the mixed spectra by minimum mean square error fitting. After background subtraction, the algorithm calculated the percentage of NP-A and NP-B (x and y) respectively to make the difference between the spectra and x part of NP-A plus y part of NP-B (the error) minimal. As shown in Figure 3.2B, the algorithm was able to distinguish signal from NP-A and NP-B from the mixed spectra even when the working concentration of the mixed NPs were as low as 20 fM.

The SERS signal of the synthesized paired SERS agents were found to be very stable if stored at 4 ℃. As shown in the Figure S3.5, the SERS signal of both SERS NPs remains ~90%

after 2-week storage. The SERS signal drift of the paired NPs in biological environment were also investigated by incubating the paired SERS NPs in 5% cell culture media. Both targeted and untargeted NPs show similar SERS signal drift in cell media, resulting in a 1:1 SERS signal ratio if incubated with NP mixture (Figure S3.6). These preliminary results showed the potential of the paired SERS NPs for sensitive in-vivo tumor cell quantification.

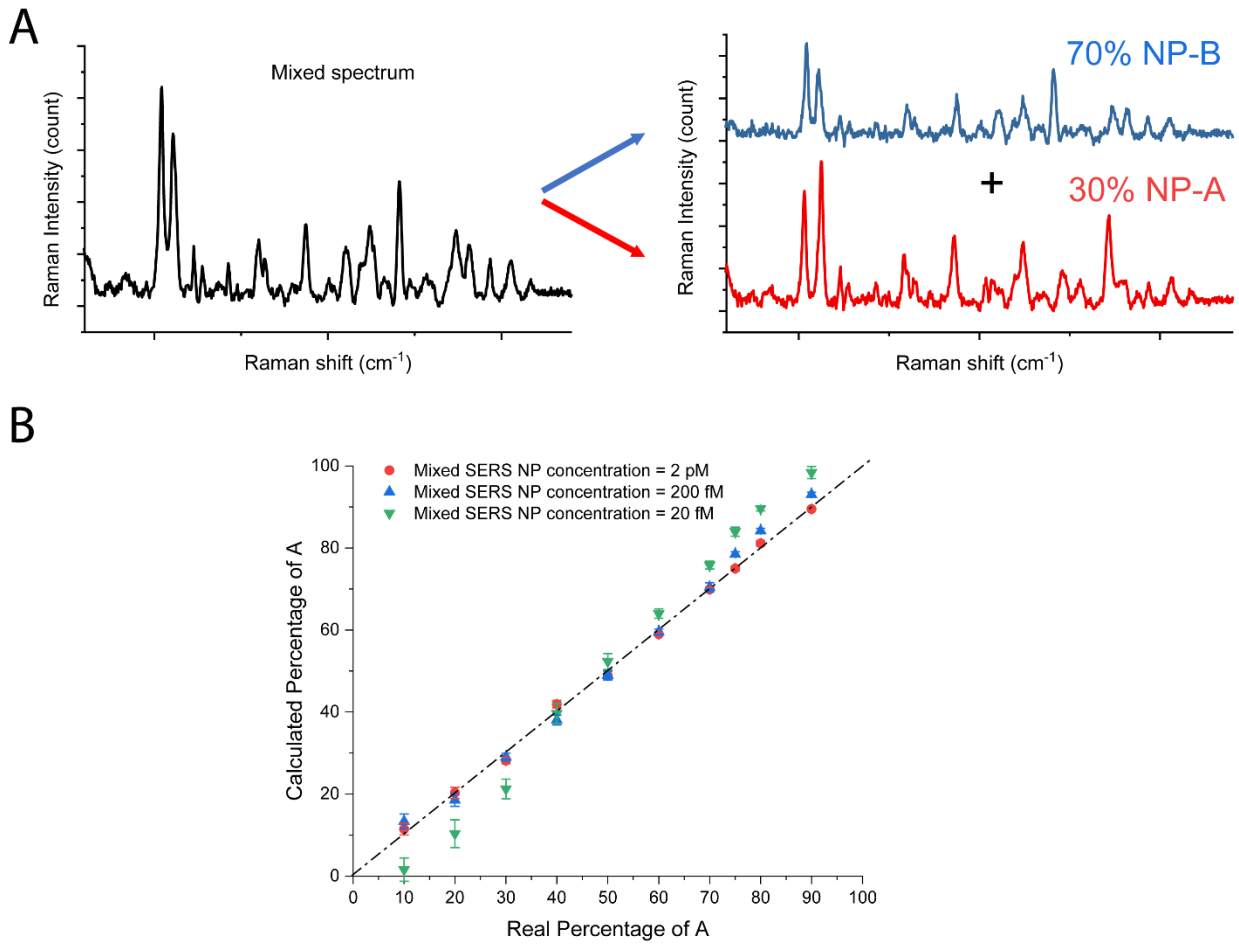

Figure 3.2 A) Scheme showing the whole-spectrum separation algorithm for mixed spectra identification. B) Calculated percentage of NP-A by the identification algorithm compared with real percentage of NP-A.

As the first step of in-vivo study, we injected two SERS NPs separately to the mice through subcutaneous administration at the footpads, and monitored their draining and retention kinetics to the popliteal lymph node independently. Before administration of SERS NPs, 10 μL of 1% methylene blue solution was first injected to locate the popliteal lymph node. Then, 25 μL of the SERS NPs solution (OD = 6) was injected via footpad, and the SERS signal was detected at the marked lymph node site non-invasively. As shown in Figure 3.3A, both the laser probe and the animal were fixed throughout the detection to minimize deviations arising from under focus. Figure 3.3B demonstrates that both NP-A and NP-B showed similar kinetic curve within two-hour range after injection, which is essential for them functioning as paired agent for tumor detection.

The mixture of NP-A and NP-B was then administrated to both control mice model and tumor metastatic mice model (3 week after tumor cell implantation), and the SERS spectra from the uptake of both the NPs at the popliteal lymph nodes were recorded 3 hours post-injection. The collected Raman spectra were then analyzed by the identification algorithm to identify the ratio of NP-A and NP-B in the lymph node. It was shown that the ratio of SERS signal from targeted NPs versus untargeted NPs keeps 1:1 in the control lymph node model, while in metastatic lymph node the ratio keeps increasing (Figure 3.4). The collected Raman spectra at the sentinel lymph node 3 h post-injection was selected to demonstrate the spectra identification by the whole spectrum identification algorithm, as shown in Figure 3.5A&B. The calculated ratio of targeted SERS NP versus untargeted SERS NP was shown in Figure 3.5C, where significant difference was found between metastatic LN and control LN.

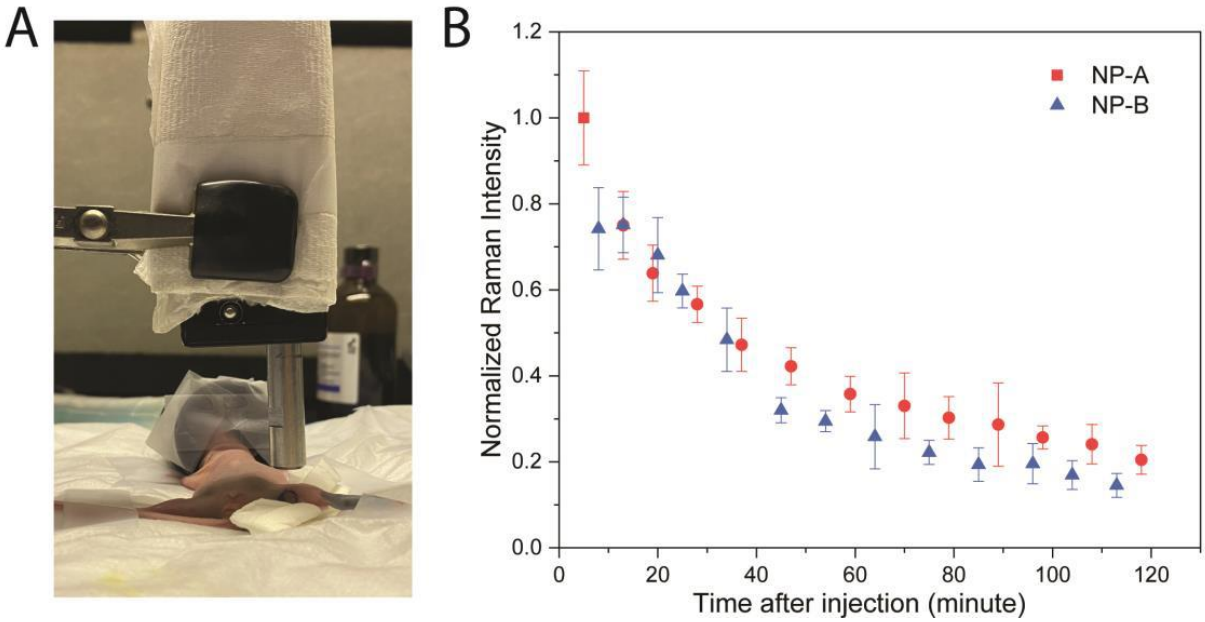

Figure 3.3 A) Experiment setup for non-invasive lymph node SERS detection on mice model. B) Normalized SERS intensity measured at popliteal lymph nodes of mice of NP-A and NP-B, respectively. Laser: 785 nm, 100 mW, 10-second integration time.

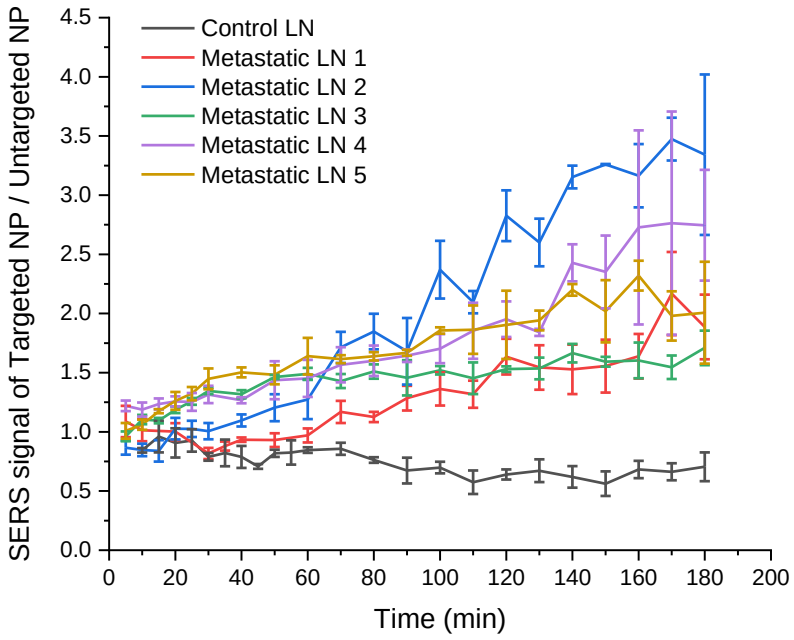

Figure 3.4 Calculated SERS signal ratio of targeted NPs / untargeted NPs 3-hour post-injection.

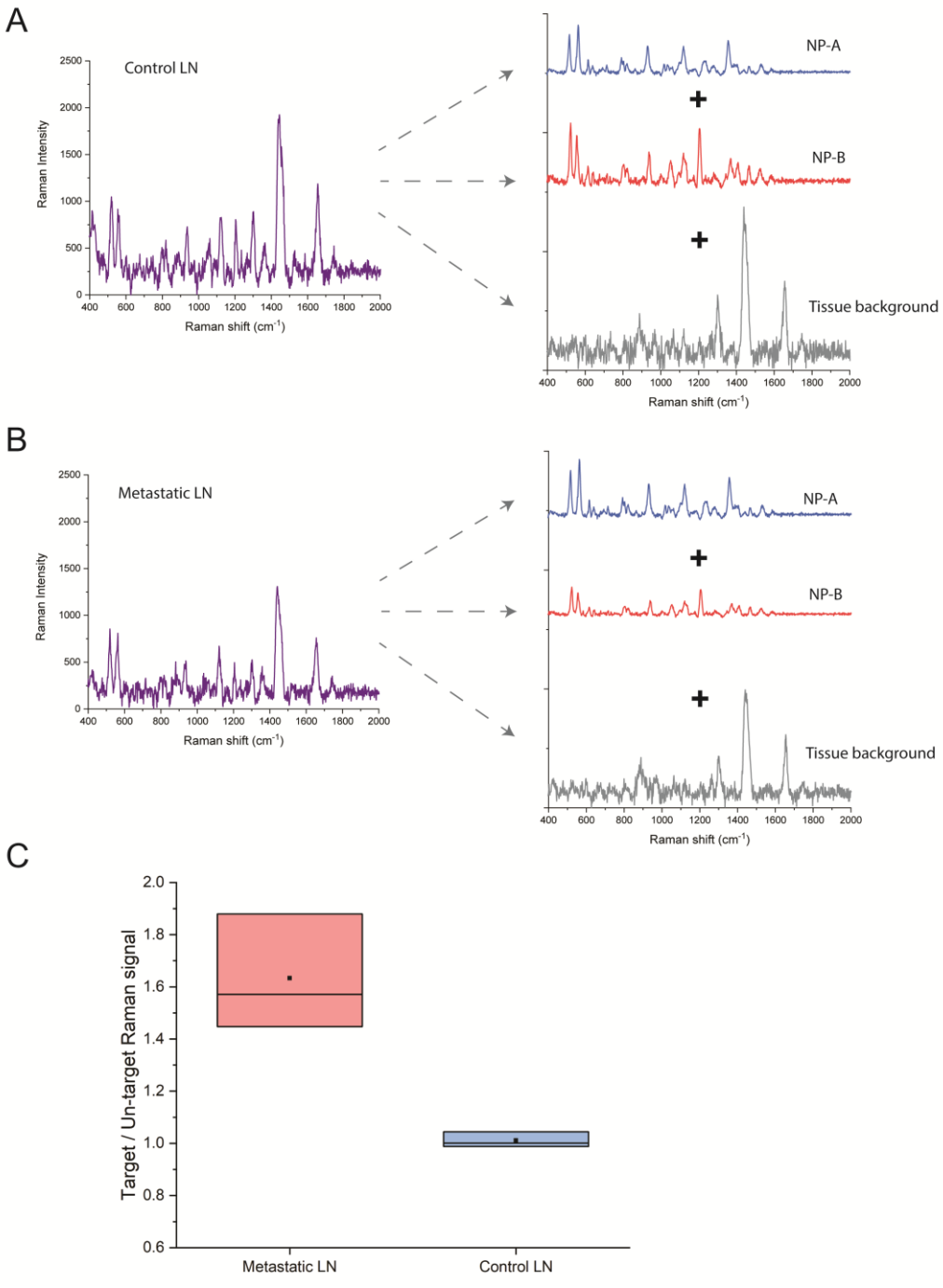

Figure 3.5 Whole spectrum identification of A) Raman spectrum collected at control SLN 1h post-injection; and B) Raman spectrum collected at metastatic SLN 3h post-injection. C) Calculated SERS signal ratio of NP-A (targeted) versus NP-B (untargeted) in metastatic SLN and control SLN, respectively.

3.5 Conclusion

In this chapter, a paired SERS nanotags were applied to realize non-invasive in-vivo metastatic lymph node detection. The paired SERS nanotags were designed to have similar surface properties and size distribution, but were encoded with different Raman reporter molecules, and were conjugated with different antibodies to eliminate the false positive signal caused by non-specific binding. A star-shaped gold nanostructure was employed to enable 1-2 orders of magnitude brighter SERS nanotags. The hydrophobic locked PEG ligands, MUA-PEG, were coated on 80% the AuNS surface, resulting in stable Raman signal over long-term storage and in biological buffer solutions. 20% of the AuNS were coated with SH-PEG-NHS, with which antibodies were conjugated through the reaction with the amine groups. The tumor specific antibody used here is Cetuximab, which has a strong affinity to bind with EGFR on breast cancer cells. A whole spectrum identification algorithm was developed to identify the ratio of targeted versus untargeted SERS NPs from the spectra of the mixture, and it shows great sensitivity even when the NP concentration is at femto-molar level. The binding kinetics of the paired SERS NPs were investigated in-vivo by injecting targeted and untargeted NPs separately, and they show similar draining kinetics in the sentinel lymph node. The paired SERS agents were then co-administrated to both control and metastatic mice model, and statistically significant difference was found between the ratio of NP-A and NP-B in metastatic and control sentinel lymph nodes. These results demonstrated that dual-tracer SERS detection can realize tumor cell detection in metastatic sentinel lymph node only 3-week post tumor cells implantation. Further study on more quantitative tumor cell detection in metastatic lymph node by paired SERS agents is ongoing.

3.6 Supplementary Figures and Table

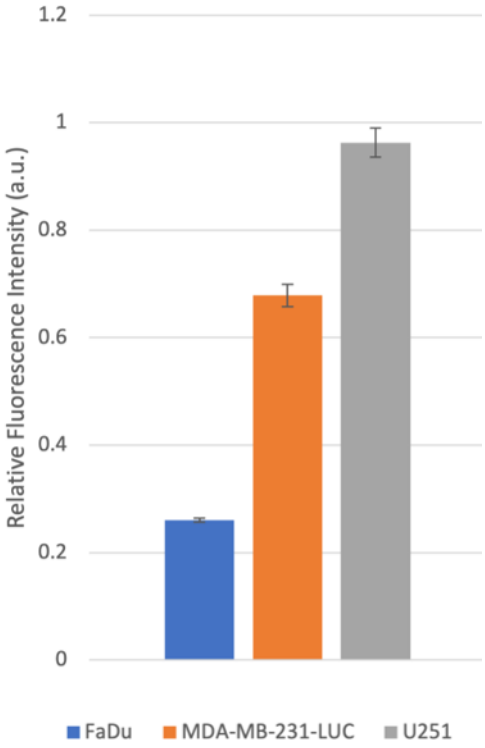

Supplementary Figure 3.1 Cetuximab reactivity cell assay. 3 cell lines with different EGFR expression were cultured: FaDu (low EGFR expression), MDA-MB-231-LUC (medium/high EGFR expression), U251 (high EGFR expression).

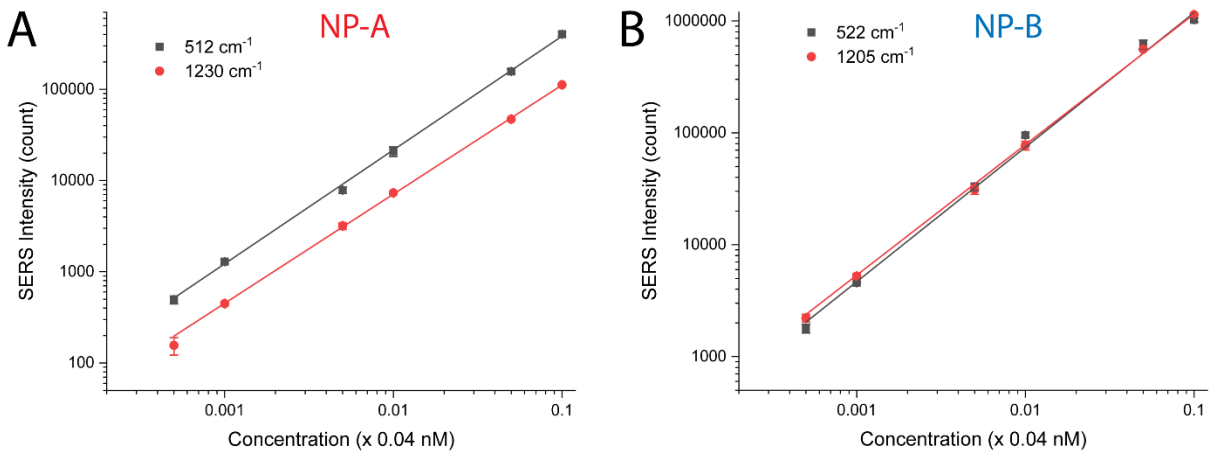

Supplementary Figure 3.2 SERS intensity linearity of A) NP-A and B) NP-B.

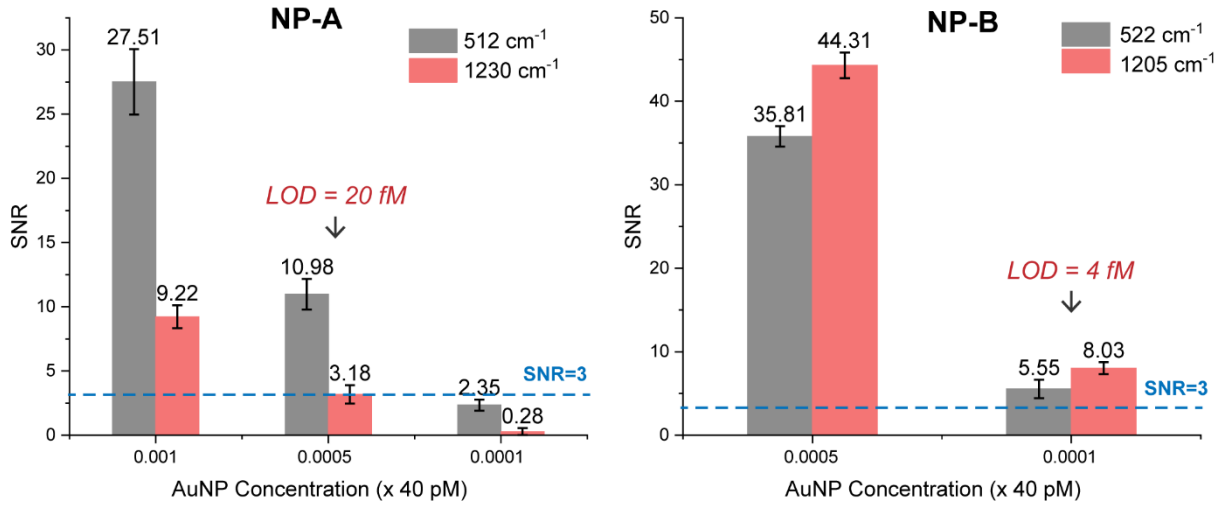

Supplementary Figure 3.3 Limit of detection (LOD) of NP-A (left) and NP-B (right) calculated by signal-to-noise ratio (SNR) of the Raman spectra. LOD is defined at the lowest detected concentration where SNR $\geqslant$ 3.

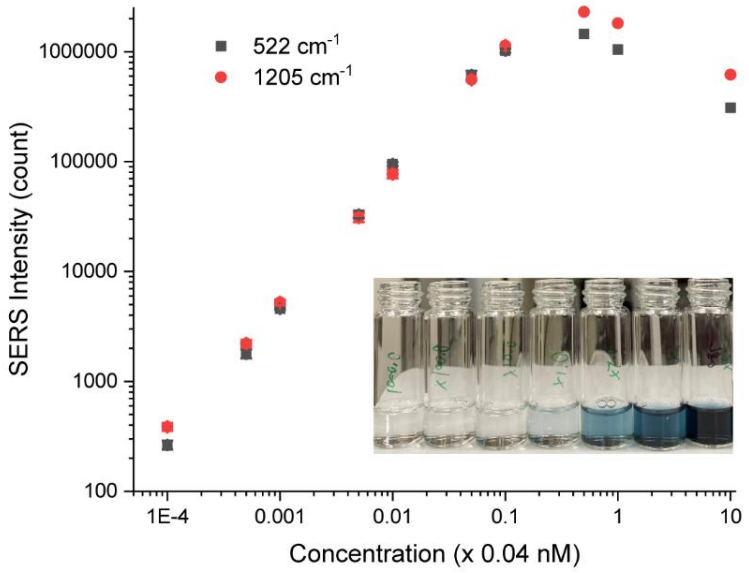

Supplementary Figure 3.4 SERS Intensity of IR-780 coded AuNS drops when NP concentration exceeds 4 pM due to strong NP extinction. AuNS sample concentration in the inserted photo from left to right: 4 fM, 40 fM, 400 fM, 4 pM, 20 pM, 40 pM, 400 pM.

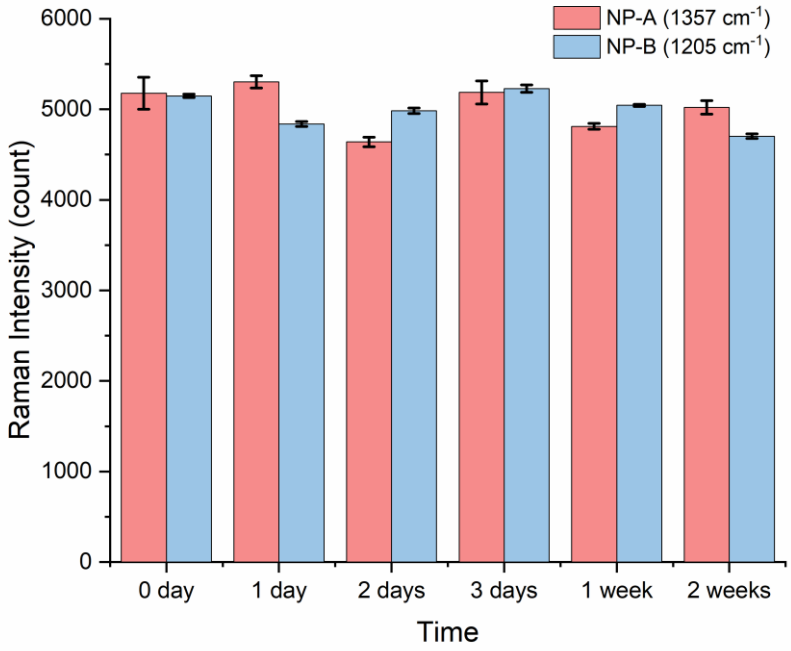

Supplementary Figure 3.5 SERS signal change of the paired SERS agents stored at 4 °C.

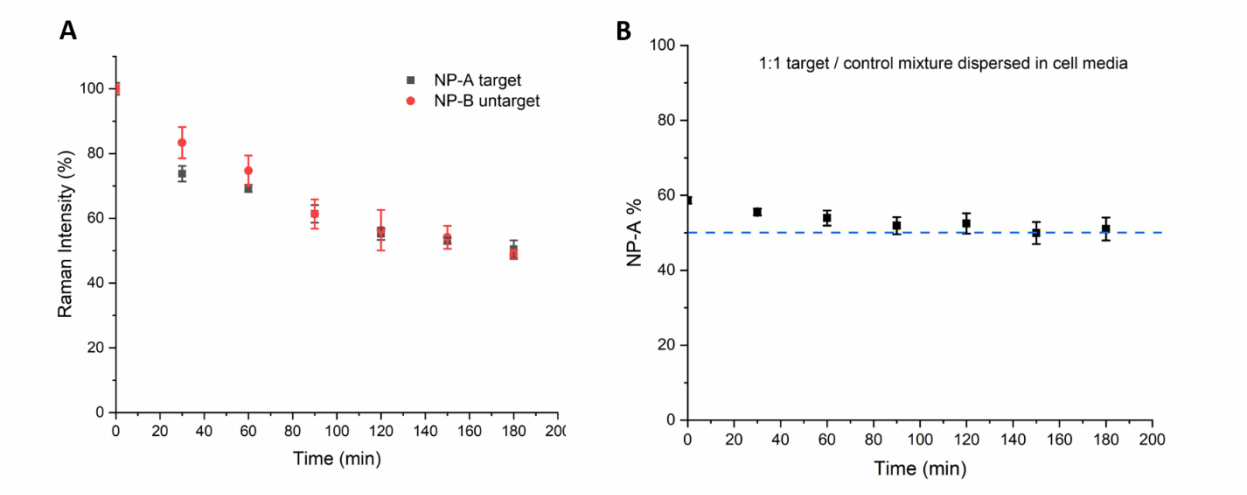

Supplementary Figure 3.6 A) SERS signal drift in cell culture media. B) Calculated ratio of NP-A and NP-B of the mixture incubated in cell culture media.

Supplementary Table 3.1 Weight log for the animals.

		Weight (g)							
Age (Mo.)	Mouse ID	6/4/22	6/10/22	6/17/22	6/18/22	6/24/22	6/27/22	7/1/22	7/5/22
6	LW-1	26.5	26.1	26.4	28.0	n/a	n/a	n/a	n/a
6	LW-5	29.1	29.2	28.8	29.8	n/a	n/a	n/a	n/a
6	LW-6	29.2	29.0	29.2	30.3	n/a	n/a	n/a	n/a
8	LK-1	25.7	25.2	25.5	26.1	25.3	26.3	n/a	n/a
8	LK-2	25.6	25.6	25.2	24.5	25.1	23.7	n/a	n/a
8	LK-3	24.1	24.9	24.5	23.2	24.2	25.6	n/a	n/a
6	LW-8	25.5	25.8	26.3	26.1	26.5	27.2	26.5	26.9
6	LW-9	28.5	28.3	28.0	27.8	27.9	28.8	28.5	25.1
6	LW-10	29.8	29.6	28.8	28.6	29.1	30.2	28.9	27.6

CHAPTER 4: BIOMIMETIC SERS NANOTAGS COATED WITH RED-BLOOD-CELL MEMBRANES (RBCM)

4.1 Introduction – Natural Cell Membrane as a Novel Biomimetic Coating for SERS NPs

Gold nanoparticles (AuNPs) functionalized with Raman-active dye molecules have been extensively used as SERS nanotags owing to their intriguing attributes of size and shape tunability, high photostability, low cytotoxicity, high biocompatibility, and narrow spectral bandwidth [64]. Recent advances have developed SERS nanoparticles or nanotags for a multitude of biomedical applications including in-vivo imaging [116], in-vitro diagnostics [117], and image-guided cancer surgery [118]. A major component in these SERS nanotags is an external coating layer that serves several important purposes. First, this coating layer prevents loss or leaching of the Raman reporter molecules into the surrounding media, hence avoiding toxicity issues and cross-contamination with vibrational signatures of other nanotags. Second, this layer minimizes the influence of other molecules present in the medium and prevents undesired intensity variations. Third, it also minimizes plasmonic coupling interactions between nanoparticles which could lead to the uncontrolled generation of plasmonic hot spots. Fourth, this coating increases the colloidal stability of nanoparticles and provides an outer layer for further chemical modification.

The external coatings are often comprised of silica [119-123], polymers [124-128] or liposomes [129-131]. A silica coating has the advantage of biodegradability but for long-term studies, it has been known to cause degradation and agglomeration problems. Polymers such as polyethylene glycol (PEG) have been extensively used for coating, but the ability of PEG coatings to prevent aggregation is limited in high ionic strength buffer solutions. Amphiphilic polymers

have been recently utilized as a coating material for SERS nanotags based on hydrophobic interactions between the polymer and Raman reporter dye [63, 132], but these constructs have limited dispersion stability (irreversible aggregation upon freeze-drying) limiting their clinical translatability [133-138]. Recently, liposome composed of zwitterionic phosphatidyl-choline lipid-coated SERS nanotags have been developed by several research groups [129, 139]. These lipids mimic the natural cell membranes and possess advantageous functions of improved dispersibility, biocompatibility, and the potential of tumor cell targeting via antibody conjugation or lipid-functionalized antibody fragments. However, such artificial membranes are unable to recapitulate the structure or protein composition of natural cell membranes including their intrinsic properties of homologous tumor targeting, enhanced blood circulation, etc. [132, 140]. Hence, coating NPs with naturally derived cell membranes is an interesting biomimetic engineering top-down approach [141, 142] imparting NPs with properties of specific cell types. This approach overcomes the limitations of biomaterials designed specifically to mimic cell membranes via the bottom-up strategies. Biomimetic cell membrane-coated nanomaterials have been developed for drug delivery to treat cancer, microbial infections, etc. [63, 143-145] However, to the best of our knowledge, biomimetic membranes have not been used to coat SERS nanotags and it is not known how such cell membrane coatings might influence the SERS signal brightness, dispersion stability properties, and how they could be modified to impart tumor targeting functions.

In this chapter we demonstrate that biomimetic red-blood-cell membranes can provide enhanced dispersion stability to AuNPs with varied shapes (sphere, rod and cube). Specifically, we show that the RBCM coating strategy imparts AuNPs stability against lyophilization, freezing, heating, and under different physiological conditions. In addition, a noncovalent lipid-insertion strategy [146] could be adopted to functionalize these AuNP-RBCM with tumor targeting ligands.

AuNP-RBCM do not lose their activity or stability upon further freeze-thaw cycles, establishing functionalization on RBCM with other proteins or molecules of interest. As such, the RBCM coating strategy on AuNPs imparts these constructs with enhanced dispersion stability with fast and efficient functionalization, enabling their long-term storage for biomedical and clinical applications which cannot be achieved by the current unstable surfactant stabilized or PEGylated AuNPs. In addition, the SERS signal intensities of RBCM-coated particles are considerably higher (by about 5) in comparison with that PEGylated AuNPs. This additional enhancement is most likely to arise from a hydrophobic environment effect (RBCM consists of a large number of lipid hydrocarbon chains) which reduces electronic dampening and boosts electromagnetic field enhancement. The improved SERS signals are well-protected by RBCM during freeze-thaw cycles and on long-term storage for 2 weeks. In a proof-of-concept study, we utilized a lipid-insertion strategy to conjugate tumor-targeting cyclic cRGD peptides onto these biomimetic SERS nanoparticles so that they exhibited improved intracellular uptake in αvβ3 integrin receptors expressing cells (MDA-MB231) with minimal cytotoxicity. These RBCM encapsulated SERS tags could be used for future in-vitro and in-vivo SERS detections with better sensitivity, signal stability, and long-term storage.

4.2 Experimental Section

Materials. Deionized water (DI water) was used throughout the work. The following chemicals were used as purchased without any further purification: IR-780 iodide (dye content ≥95%), N,N-dimethylformamide (DMF), sodium citrate tribasic dihydrate, gold(III) chloride trihydrate ($HAuCl_4$), sodium borohydride ($NaBH_4$), poly(sodium 4-styrenesulfonate) (Na-PSS) solution (average Mw ~70,000, 30 wt. %), silver nitrate ($AgNO_3$), L-ascorbic acid, sodium bromide (NaBr),

hexadecyltrimethylammonium bromide (CTAB) and poly(ethylene glycol) methyl ether thiol (mPEG-thiol, Mn 2000 Da) from Sigma Aldrich, hexadecyltrimethylammonium chloride (CTAC) from Tokyo Chemical Industry Co., LTD., poly(ethylene glycol) methyl ether thiol (mPEG-thiol, Mn 5000 Da) from Laysan Bio Inc.

Synthesis of citrated-stabilized size and shape varied AuNPs. Glassware and stir bars for gold nanoparticle synthesis were washed by aqua regia before use. Gold nanospheres were synthesized via a kinetically controlled seeded growth method [147]. First, a water solution of 2.2 mM sodium citrate (60 mL) was heated to boiling under vigorous stirring. Once boiling had commenced, 400 μL of $HAuCl_4$ solution (25 mM) was quickly injected. The reaction completed within 10 min where the solution turned from yellow to purple grey and then to burgundy. 30 mL of the resulted gold particle solution was stocked as 15-nm Au nanospheres (AuNP15), and the other 30 mL of the particle solution was used as the Au seeds for the next step. Immediately after the Au seeds synthesis, in the same reaction vessel, the solution was cooled to 90 ℃, then 200 μL of $HAuCl_4$ solution (25 mM) was injected. After 30 min, the reaction was finished. This process was repeated once. After that, the particle solution was diluted two times by 2.2 mM sodium citrate solution. 30 mL of the diluted particle solution was then used as the seed solution, and the process was repeated until Au nanospheres with a hydrodynamic size of 50 ± 5, 80 ± 5 nm in diameter were obtained sequentially, and the corresponding Au nanospheres solutions were stocked as AuNP45 and AuNP80, respectively. A condenser was utilized throughout the synthesis process to keep consistent volume of the solution. The weight concentration of the obtained citrate stabilized Au nanospheres were determined by inductively coupled plasma mass spectrometry (ICP-MS). The size varied Au nanospheres solutions was finally diluted to 32 mg/L in 5 mM sodium citrate for long-term storage.

Gold nanorods (AuNP2) and gold nanocubes (AuNP3) were synthesized by seed-mediated growth methods [85, 148]. A seed solution was first synthesized by quickly adding 600 μL of ice-cold 10 mM $NaBH_4$ solution to a mixed solution of CTAB (5 mL, 0.2 M) and $HAuCl_4$ (5 mL, 0.5 mM) under vigorous stirring. The seed solution was continued stirring for 2 min and then kept at room temperature for over 1 h before the next step. For the growth of nanorods, a CTAB solution (20 mL, 0.2 M) was first mixed with a $HAuCl_4$ solution (20 mL, 1 mM) and an $AgNO_3$ solution (1.2 mL, 4 mM) at a 30 ℃ water bath. To the above solution, 380 μL of 0.0788 M ascorbic acid solution was added, followed by gentle shaking. The growth solution was observed to change from yellow to colorless. After that, 48 μL seed solution from the first step was added followed by gentle shaking, and the growth solution was kept at 30 ℃ unstirred. After 1 h, the growth was stopped by centrifuging the resulted AuNP2 solution at 4000 g. The washed AuNP2 solution was re-dispersed to 2 mM CTAB solution.

For the synthesis of AuNP3, 10-nm gold nanospheres were first synthesized with the previously prepared CTAB-capped Au seeds. 2 mL of 0.2 M CTAC solution, 1.5 mL of 0.1 M ascorbic acid solution, and 50 μL of the Au seeds solution were mixed in a 10-ml vial. Under stirring of constant speed, 2 mL of 0.5 mM $HAuCl_4$ solution was injected. The solution was incubated at room temperature for 15 min under stirring at 300 rpm. The resulted 10-nm Au nanosphere solution was then washed twice at 20,000 g and re-dispersed to 1 mL in 20 mM CTAC solution for further use. For the growth of AuNP3, 72 mL of 0.1 M CTAC, 360 μL of 20 mM NaBr and 84 μL of previously prepared 10-nm Au nanospheres were mixed, then 4.68 mL of a 10 mM ascorbic acid solution was added and mixed thoroughly. Finally, 72 mL of 0.5 mM $HAuCl_4$ solution was quickly injected into the solution under stirring at 500 rpm. The solution was

incubated at room temperature for 30 min. The resulted AuNP3 solution was washed by centrifugation at 4000 g and re-dispersed to 2 mM CTAC solution.

The surfactant exchange process of AuNP2 and AuNP3 follows a literature protocol [86]. Typically, 10 mL of AuNP2 or AuNP3 dispersed in 2 mM CTAB or CTAC solution was first centrifuged at 4000 g. 9.5 mL of the supernatant were removed, and the AuNP2 or AuNP3 were re-dispersed to 10 mL by DI water. The resulted AuNP2 or AuNP3 solution (current CTAB or CTAC concentration is 0.1 mM) was then added to 100 mL of Na-PSS solution (0.15 wt%) and kept at room temperature for over 1 h. After the incubation, the NP solution was centrifuged at 4000 g and re-dispersed to 0.15 wt. % Na-PSS solution for two cycles, and then centrifuged again at 4000 g and re-dispersed to 5 mM sodium citrate solution. The AuNPs were incubated in sodium citrate solution overnight. Finally, the AuNP2 or AuNP3 were washed again at 4000 g by 5 mM sodium citrate. The concentrations of the citrate-stabilized AuNP2 and AuNP3 were determined by ICP-MS. The AuNP2 and AuNP3 solution were finally diluted to 32 mg/L in 5 mM sodium citrate for long-term storage.

Synthesis of shape varied AuNP-PEGs. Typically, 3 mL of AuNPs solution (32 mg/L) was mixed with 500 μL of mPEG-thiol solution (51.8 μM) for 1 h at room temperature. The AuNPs were then washed by DI water twice via centrifugation at 4000 g to remove excess PEG ligands and re-dispersed to 3 mL of DI water.

RBCM collection and coating on AuNPs. RBCs derived from BALB/C mouse blood were purchased directly from BioIVT. Subsequently, it was subjected to hemolysis where the RBCs was suspended in lysis buffer, i.e., 0.25X PBS at 4ºC for 1h. The resulting solution was centrifuged 4 times at 20000g to eliminate hemoglobin until a pink pellet (RBCM concentrate) was obtained, and the supernatant solutions was colorless. The pink pellet was resuspended in distilled water

(~50mL) and vigorously mixed and sonicated for 10 minutes in ice-water mixture. The RBCM solution was eventually added to AuNP solution with the RBCM vesicle/AuNP volume ratio of 3/9 and bath sonicated for 10 minutes to form AuNP-RBCMs. The resulting solution was centrifuged at 700g for 15 minutes to eliminate residual RBCM vesicles.

Characterization of RBCM-coated nanoparticles. Dynamic light scattering (DLS) measurements were conducted to measure the hydrodynamic size distribution (intensity average) of the nanoparticles on Malvern Zetasizer ZS90 instrument (Malvern Instruments Ltd, United Kingdom) at a fixed angle of 90°. Zeta potential (ζ) values were determined using a Malvern Zetasizer (Malvern Instruments Ltd, United Kingdom) of Nano series. Ultraviolet-visible (UV-Vis) absorbance of was recorded on GENESYSTM 10S UV-Vis Spectrophotometer (Thermo Scientific, MA, USA). Absorbance spectra were collected at an interval of 1 nm scanning from 300nm-1000 nm. To evaluate the presence of CD47 on the surface of the particle, allophycocyanin-labeled anti-mouse CD47 antibody was used (BioLegend, San Diego, CA) according to a previously established protocol [149].

Transmission Electron Microscopy (TEM) Imaging. A drop of RBC-coated or bare (non-RBC-coated) nanoparticle solution was deposited onto a glow-discharged, carbon-coated TEM grid and incubated for 5 minutes. Excess liquid was removed, and samples dried overnight in a desiccation chamber. For negative staining, samples were stained with 1% uranyl acetate for 30 seconds immediately before imaging. All samples were imaged using a JEOL JEM-2100 transmission electron microscope at 200kV.

Dispersion stability against freeze-thaw cycle. AuNPs having different shapes and sizes with citrates only, RBCM coating, and PEG coating, respectively were taken in glass vials (2 mL, 0.032mg/mL). The resulting solutions were frozen at -80°C for 30 minutes and then thawed at

room temperature for 10 minutes. The thawed solutions were briefly sonicated and analyzed using UV-Vis spectrophotometry, and DLS.

Dispersion stability against lyophilization. AuNPs having different shapes and sizes with citrates only, RBCM coating, and PEG coating, respectively were taken in glass vials (2 mL, 0.032 mg/mL). The resulting solutions were frozen by placing them in liquid nitrogen for a few minutes and then connected immediately to a freeze-drier (-47°C) with an applied vacuum (53×10^{-4} mbar) for ~24h. The freeze-dried products were reconstituted with deionized water (1 mL).

Stability of AuNPs in human serum. AuNPs were added to undiluted human serum in a ratio of 1:1 (final solution containing 50% serum). The samples were incubated for 24 hours at 37°C. Samples were then centrifuged at 10,000 rpm and the dispersion solution was removed. The AuNPs were resuspended in distilled water and centrifuged down at 10,000 rpm, this process was repeated twice. Finally, DLS profiles of AuNPs in water were recorded using a Malvern Zetasizer Nano ZS.

AuNP-Dye physisorption for SERS studies. Raman reporter dyes were physically attached to AuNPs before the PEG or RBCM coating process. Raman reporter molecules IR-780 stock solution was prepared by dissolving 1 mg of IR-780 into 1 mL of DMF. The stock solutions were diluted by DI water to form a dye concentration of 2.62 μM for further use. Typically, 10 μL above IR-780 solution was dropwise added to 1 mL of gold AuNP1 (32 mg/L) under vigorous stirring. The resulted dye concentration for 45-nm gold AuNP1 were calculated to be 450 dye molecules per AuNP.

SERS data collection and processing. Raman spectra were obtained using a BaySpec Agility transportable 785/1064 nm dual-band benchtop Raman spectrometer (East JHX, Inc.). 785 nm laser (200 mW) was used as the excitation source. Each Raman measurement includes 3 scans, and the averaged Raman spectrum was plotted. Averaged Raman intensity of 1205 cm^{-1} peak from

the 3 scans was chosen to show Raman signal change for the SERS AuNPs, and the error bars represent the standard deviations of the scans performed for 3 separate experiments. All the Raman spectra were baseline corrected to remove fluorescence background, and the band intensities were calibrated by standard sample (benzonitrile) spectrum.

Lipid-insertion of tumor-targeting peptides. Stock solutions of DSPE-PEG-Cy5 with concentrations (1000 μg/mL, 500 μg/mL, 200 μg/mL, 100 μg/mL, 50 μg/mL, 10 μg/mL, and 1 μg/mL) were made in DI water. RBCM prepared earlier were thawed, bath-sonicated in ice water. Subsequently, 1mL of RBCM was added to 1 mL of each DSPE-PEG-Cy5 of different concentrations and vortexed vigorously for 1 min. The solutions were incubated for 30 minutes in the refrigerator followed by centrifugation at 600g for 15 minutes at 4℃. The supernatant was removed, and 2 mL of DI water was added to each tube. The UV-Vis absorption was collected in addition to acquiring their fluorescence excitation and emission spectra at 633 nm and 650-700 nm, respectively.

MTT Assay of different AuNPs. The cytotoxic effects of various AuNPs in two different endothelial cell lines (MDA-MB231, PANC-1) was investigated using MTT assay established previously.

In vitro SERS study. To verify the effective binding of AuNP-RBCM@cRGD to endothelial cells, a comparative targeting study was performed in vitro with MDA-MB231 and PANC-1 cells. Both cell lines were grown in Eagle's Minimum Essential Medium (MEM), supplemented with 1.5 g/L sodium bicarbonate, non-essential amino acids, L-glutamine and sodium pyruvate and cultured until they reached ~80-90% confluency. Subsequently, they were plated in a 6-well plate and allowed to grow for 24h at 37°C at the cell density of 10^6 cells/well. Dye-tagged AuNPs (AuNP-PEG, AuNP-RBCM, and AuNP-RBCM@cRGD) were added to the media and allowed to incubate overnight. Following this, AuNP-containing media was removed by aspiration, and cells were

rinsed two times with PBS. Subsequently, the same cell samples were fixed with Karnovsky's fixative (paraformaldehyde-glutaraldehyde solution) and imaged using darkfield microscopy to visualize the AuNPs associated with the cells. Darkfield microscopy was performed using a Zeiss Axiovert inverted microscope. All images were acquired using a 50×objective lens.

4.3 Results

4.3.1 Functionalization of AuNPs with Biomimetic RBCM

In this work, an interesting biomimetic top-down method was employed to coat SERS NPs with natural derived red blood cell membranes (RBCM). As illustrated in Figure 4.1A, the process of functionalizing AuNPs with mouse-derived RBC membranes was conducted by generating membrane vesicles from RBCs and subsequently fusing the RBC membranes onto the surface of AuNPs *via* bath sonication. First, RBC ghosts were derived from mouse RBCs via hypotonic treatment followed by centrifugation steps. Uniform RBC membrane vesicles (hydrodynamic size ~190 nm, Figure S4.1) formed after bath sonication and probe sonication. The obtained RBCM were then mixed with Raman reporter dye encoded AuNPs under bath sonication to function the AuNPs with RBCM layer. Under negative-staining TEM, the RBCM layer was clearly seen around the AuNPs compared with bare NPs (Figure 4.1B). AuNP-RBCM also showed a red-shifted LSPR in the UV-vis spectrum, and a characteristic peak of RBCM around 420 nm (Figure 4.1D). Besides, the hydrodynamic size of the NP increased from ~ 44 nm to 64 nm after RBCM coating, and zeta potential dropped from -37 to -28 mV (Figure 4.1C). These changes correspond well with the thickness of the lipid bilayer and the intrinsic surface charge of the RBCM vesicles (Figure S4.1). In addition to Au sphere, we also observed successful coating of RBCM on AuNPs with various shapes: Au nanorods (AuNP2) and Au nanocubes (AuNP3), as shown in Figure S4.2.

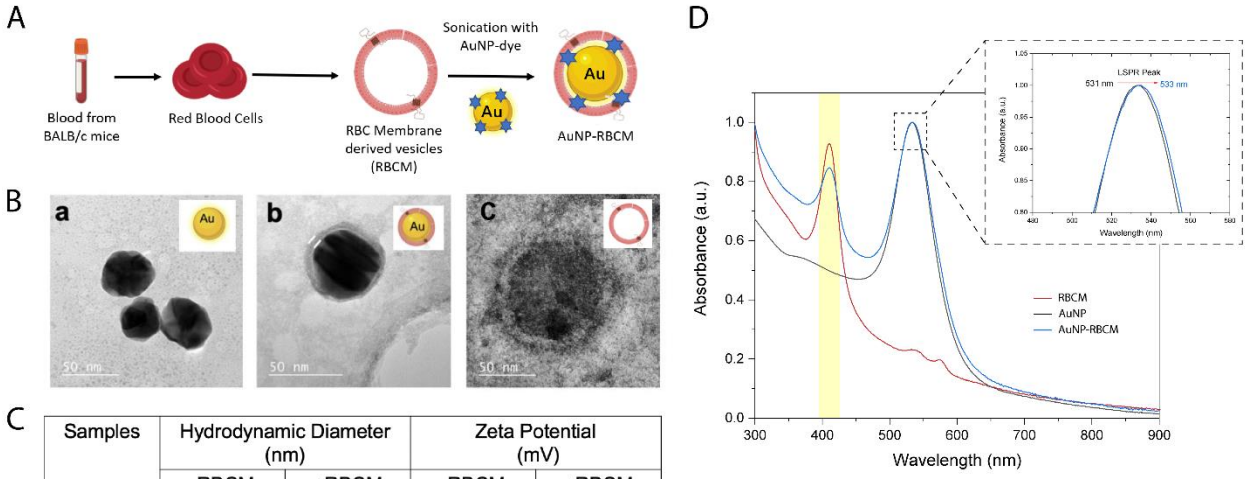

C

Samples	Hydrodynamic Diameter (nm)		Zeta Potential (mV)	
	-RBCM	+RBCM	-RBCM	+RBCM
AuNP	44 ± 5	64 ± 4	-37 ± 6	-28 ± 3

Figure 4.1 A) Schematic diagram showing preparation of RBC membrane (RBCM) vesicles and successful coating on AuNPs, leading to RBCM-coated AuNPs. B) Negative-stained transmission electron micrographs (TEM) of (a) AuNP-Cit, (b) AuNP-RBCM, (c) RBCM vesicles. (C) Hydrodynamic diameter and zeta potential measurements for AuNPs before and after RBCM coating. (D) UV-vis absorbance spectra of AuNP's, AuNP-RBCM's and RBCM's, with the inset boxes zoomed. The inset shows the intrinsic plasmonic absorbance peak shift for AuNPs upon RBCM coating.

To understand if the RBCM coating on AuNPs still remains its full functionality as natural RBC, we further performed an indirect study to confirm the presence of CD47 proteins on the surface of the particles. CD47 protein is a “marker of self” receptor on the surface of RBCs which bind to the signal regulatory protein alpha receptors on macrophages and inhibit phagocytosis of RBCs. Consequently, the presence of CD47 on RBCM coated AuNPs would indicate successful functionalization without the loss in activity of the RBCMs [149]. Here, different samples including RBCM, AuNPs, and AuNP-RBCMs were mixed with fluorescent antibody for CD47, and we observed the highest fluorescent signal intensity for RBCM, followed by AuNP-RBCMs. The AuNPs had barely any signal intensity due to the lack of CD47 receptors on their surface (Figure S4.2). Together, these results indicate that both size- and shape-tuned AuNPs were successfully coated with RBC-derived membranes with the right-side out.

4.3.2 Biomimetic AuNP-RBCM SERS Nanoparticles with Signal Enhancement

The biomimetic RBCM was coated on a dye attached AuNPs to function as the protective coating of SERS NPs. The resulted SERS NPs were referred to as AuNP-dye-RBCM. Dye attached AuNPs without coating (AuNP-dye) and dye-attached AuNPs coated with 5k Da SH-PEG (AuNP-dye-PEG) was employed as controls. Raman spectra of different AuNPs were measured in aqueous NP solutions with the same particle concentration and laser parameter (integration time and laser power). It was first observed that, after RBCM coating, SERS intensity increases to 5 times the original intensity of AuNP-dye (Figure 4.2). Hotspot-induced SERS intensity change was excluded by good mono-dispersity of AuNP-dye-RBCM that is indicated in the absorbance spectrum and hydrodynamic size distribution (Figure 4.1). The compact wrapping of RBCM around AuNPs was proved to be important for the SERS enhancement by three supplementary trials (Fig. S4.4). In the first trial, the AuNP-dye solution was simply mixed with RBCM fragments

without bath sonication treatment. Only a ~3 times enhancement was observed after the mixing, which is probably due to membrane fragments attaching to AuNPs and forming an incomplete RBCM shell. The mixture was then treated with a 10-min bath sonication, and the SERS signal increases to 5 times the original intensity as a result of a complete and compact membrane packing (Fig. S4.4A). In the second trial, the RBCM was coated on the surface of AuNP-dye-PEG (Fig. S4.4B), and in the third trial, AuNPs were mixed with dye solution after RBCM coating (Fig. S4.4C). None of these experiments resulted in a SERS intensity enhancement as high as directly attaching RBCM on dye absorbed AuNPs, indicating that a tight and direct encapsulation of RBCM on AuNPs is essential for the observed SERS enhancement. The enhancement effect is then believed to be related to the electromagnetic enhancement mechanism, where the dielectric medium around plasmonic NPs changing from polar water (dielectric constant of 80.4) to the non-polar lipid bilayer (averaged dielectric constant of 2 to 3) leads to an amplified reduction of electron dampening and boosts the electromagnetic field enhancement. Based on electromagnetic enhancement mechanism of SERS, the overall SERS enhancement factor is roughly the fourth power of the EM field amplification enhancement as shown in the following equation [64]:

$$G \approx \left|\frac{E_{loc}}{E_0}\right|^4 = \left|\frac{\varepsilon_m - \varepsilon_s}{\varepsilon_m + 2\varepsilon_s}\right|^4 \left(\frac{R}{R+d}\right)^{12} \quad \text{(Equation 4.1)}$$

Here, G is the SERS enhancement factor. E_{loc} and E_0 are the EM field amplitude of the local field near NP surface and that of the incident field, respectively. ε_m and ε_s are dielectric constants of the metal core and the surrounding medium. R and d are the radius of the nanoparticle and the distance between the molecule and the plasmonic surface. The dielectric constant of gold (ε_m) is determined based on the excitation wavelength of 785 nm: [103]

$$\varepsilon_m = -22.9 + 1.4\mathrm{i} \quad \text{(Equation 4.2)}$$

Considering a Raman reporter molecule attached on a gold NP with fixed radius and distance to the plasmonic surface, when dielectric constant (ε_s) of the surrounding medium changes from 80.4 (water) to 3.0 (lipid), the enhancement factor change ($\mathrm{G}_{lipid}/\mathrm{G}_{water}$) is calculated as the following equation:

$$\frac{\mathrm{G}_{lipid}}{\mathrm{G}_{water}} = \left|\frac{\varepsilon_m - \varepsilon_{lipid}}{\varepsilon_m + 2\varepsilon_{lipid}}\right|^4 \left|\frac{\varepsilon_m + 2\varepsilon_{water}}{\varepsilon_m - \varepsilon_{water}}\right|^4 = 17.5 \qquad \text{(Equation 4.3)}$$

, which matches well with the enhancement we observe from the RBCM coating.

Besides, the enhanced SERS signal was observed to be quite stable over time, as the intensity of AuNP-dye-RBCM stays ~90% after up to 2-month storage at 4 ℃. Unfortunately, AuNP-dye-Cit irreversible aggregated over this period. AuNP-Cit are generally stable for long-term storage due to their negative surface charge. However, after the attachment of the positively charged dye, the net surface charge of AuNP-Cit drops below -20mV (Fig. S4.4) and hence they are eventually aggregate during long-term storage. We further demonstrated that the SERS signal for AuNP-dye-RBCM remains stable (Fig. S4.5) in presence of serum proteins (50%) for 24 hours, highlighting the importance of using these biomimetic SERS tags for different *in vivo* biosensing and biomedical applications.

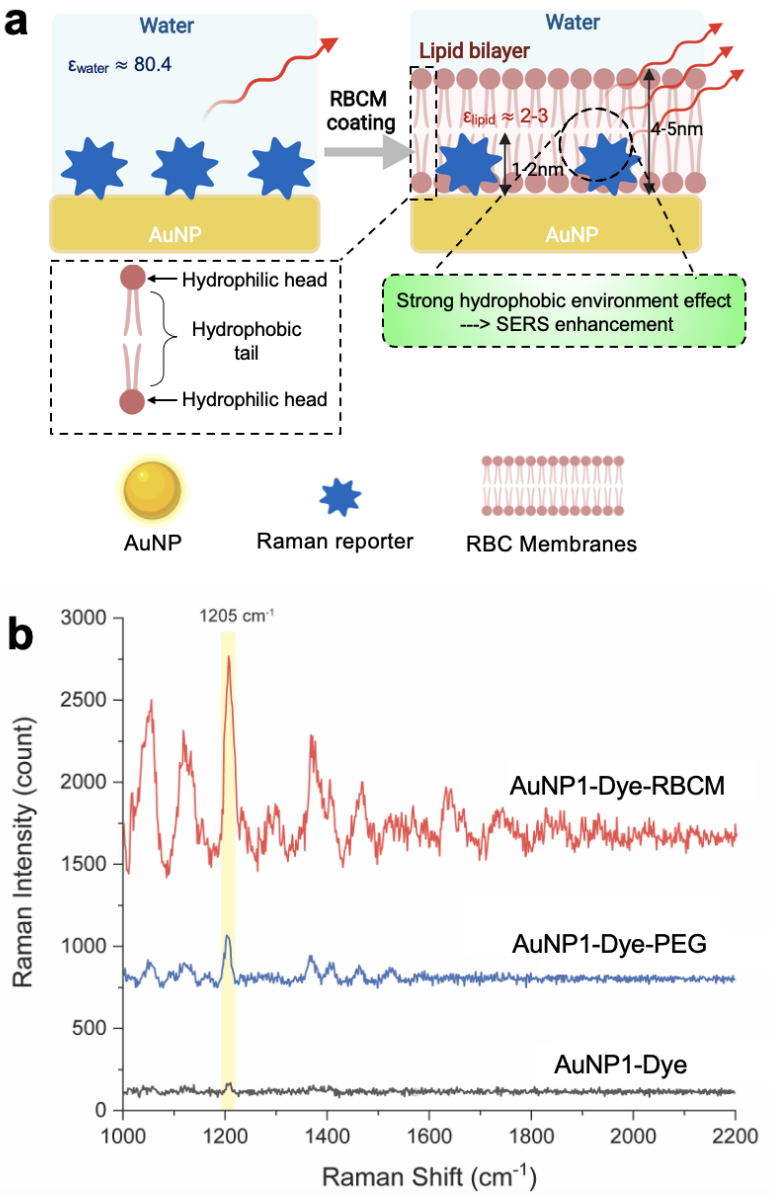

Figure 4.2 A). Schematics depicting the hydrophobic structure of RBCM and surface Raman enhancement. The dielectric constant of the surrounding medium changes from 80.4 (water) to 2-3 (lipid bilayer), which leads to an amplified local electromagnetic field. (B). Raman spectra of AuNP-dye, AuNP-dye-PEG and AuNP-dye-RBCM, respectively, showing enhanced SERS intensity after RBCM coating. Spectra were acquired at laser power of 200 mW, integration time of 500 ms.

4.3.3 Dispersion Stability of AuNP-RBCM against Freezing and Lyophilization

We proceeded to investigate the enhanced dispersion stability aspects imparted by the biomimetic AuNP-RBCM and compared it with linear PEG functionalized AuNPs (AuNP-PEG), which is used for biological applications [80, 136, 150-152]. We first investigated the freeze-thaw behavior of AuNP-RBCM by freezing them at -80 C for 30 minutes, followed by thawing them at room temperature, repeating these freeze-thaw cycles 4 times (Figure 4.3). RBCM exhibited excellent protection of SERS NPs against freezing, demonstrating not only well-preserved NPs dispersity, but also stable and intact SERS signal (Figure 4.3). As the control, AuNP-PEG though did not aggregate, but showed continuous SERS intensity decrease with ongoing freeze-thaw cycles (Figure 4.3B).

Based on these results, we next attempted to evaluate the effects of lyophilization. Here, the samples were frozen in liquid nitrogen followed by sublimation of the solvent under reduced pressure. After lyophilization, AuNP-RBCM dispersed well in water, while AuNP-PEG aggregated after re-dispersion (Figure 4.4A). As a result of NP coupling, SERS signal of AuNP-PEG dramatically increases (Figure 4.4B). SERS intensity of AuNP-RBCM drops to ~60% of the original signal, but the characteristic Raman peak stays distinct (Figure 4.4C). The cryo-protection of dye reporter molecules and SERS brightness from RBCM is hypothesized to be related with the strong hydrophobic-hydrophobic interaction between aromatic dye molecules and the alkyl tails of the lipids. However, the exact mechanism remains unclear and requests further investigations. These experiments indicate that the RBCM coating on AuNPs endows them with superior dispersion stability against lyophilization and freezing, which is an essential step for the clinical translation and commercialization of Au colloids-based SERS sensors.

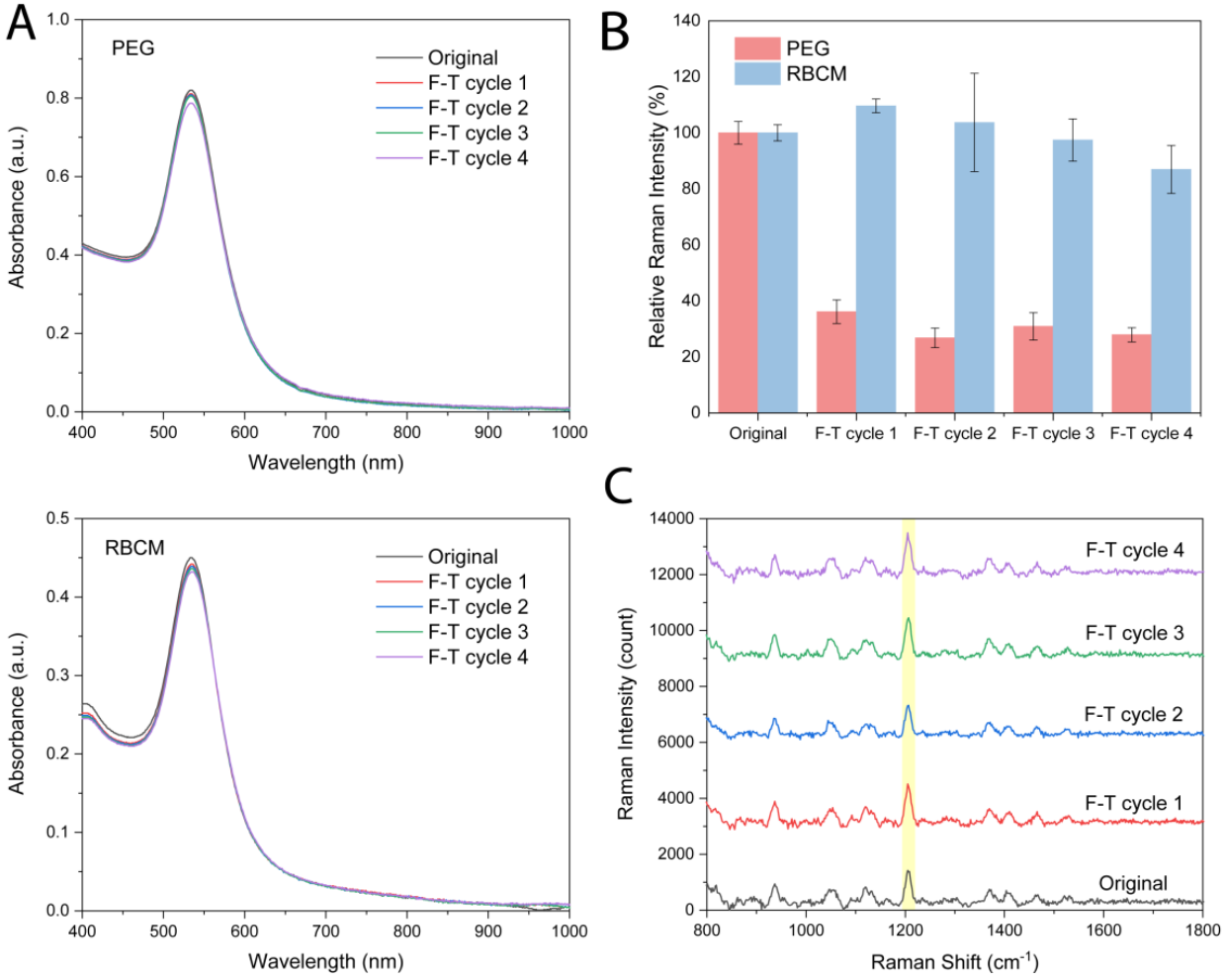

Figure 4.3 A) UV-vis spectra of AuNP-PEG (up) and AuNP-RBCM (down) during 4 cycles of freeze-thaw. B) Relative Raman intensity change of AuNP-PEG and AuNP-RBCM during freeze-thaw cycles. C) Raman spectra evolve of AuNP-RBCM during freeze-thaw cycles.

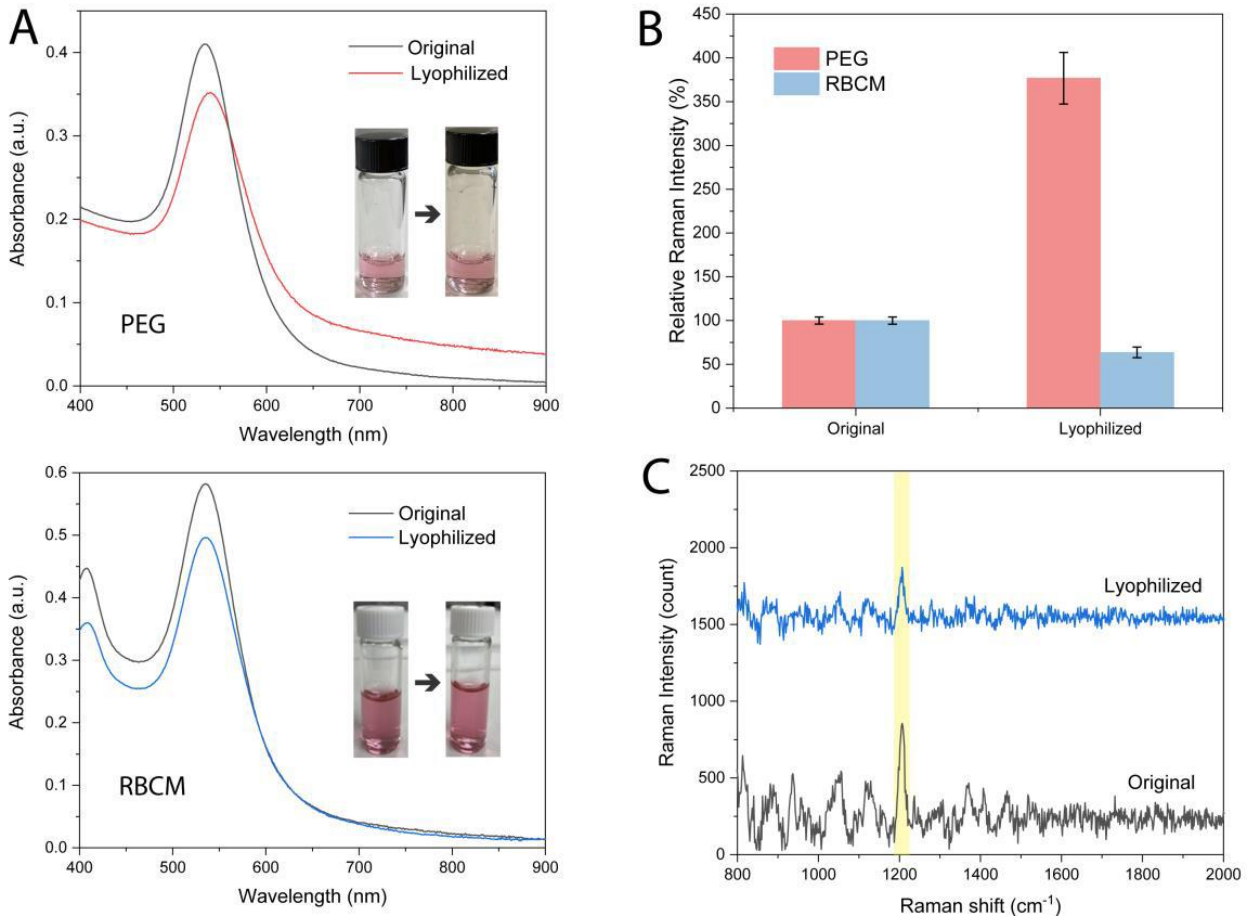

Figure 4.4 A) UV-vis spectra of AuNP-PEG (up) and AuNP-RBCM (down) before and after lyophilization. Inserted: photos of the samples before and after lyophilization. B) Relative Raman intensity change of AuNP-PEG and AuNP-RBCM after lyophilization. C) Raman spectra change of AuNP-RBCM after lyophilization.

4.3.4 Spectroscopic Detection of Cancer Cells Using Ligand-Inserted, Biomimetic SERS Nanoparticles.

We next attempted to impart these biomimetic nanoparticles with the cancer-targeting ability so that they could be used for *in vitro* SERS detection. A lipid-insertion strategy was adopted to functionalize RBCM with tumor-targeting peptides and subsequently coated them onto AuNPs. Towards this direction, we first attempted to optimize the lipid-insertion strategy in RBCM by using a lipid-tethered fluorescent probe (DSPE-PEG-Cy5, excitation/emission = 633 nm/660 nm). Fluorescent intensities were measured for DSPE-PEG-Cy5 at increasing concentrations (1 μg/mL to 1000 μg/mL) to generate a calibration curve that would help us characterize the lipid-insertion efficiency and saturation level (Fig. S4.6). Subsequently, DSPE-PEG-Cy5 at different concentrations were incubated with RBCM for 30 minutes at 4°C followed by centrifugation, washing, referred to as RBCM-Cy5 1, 10, or 100 (depending on DSPE-PEG-Cy5 concentrations) and examined via fluorescence intensity measurements. Fig. S4.7 demonstrates the ligand density on the RBCM by controlling the amount of lipid-tethered ligand added. We further demonstrated by flow cytometry that compared to unmodified RBCM, modified RBCM-Cy5 100 had a significantly higher signal under the Cy5 channel (Fig. S4.8).

Once we had validated the successful incorporation of lipid-tethered fluorescent dyes, we utilized a lipid-tethered tumor-targeting ligand (DSPE-PEG-cRGD) to functionalize AuNP-RBCM. Cancer targeting using nanoparticles has been achieved in the last two decades by exploiting specific proteins that are upregulated in cancer cells. For example, integrins receptors are highly upregulated on tumor-associated endothelial cells during angiogenesis and metastasis of a wide range of rapidly growing tumors. Several integrins, including the αv integrins, have been shown to recognize the Arg-Gly-Asp (RGD) sequence as a critical determinant in their ligands.

These RGD-functionalized nanocarriers have been extensively developed and utilized for tumor imaging and delivering cargoes (chemotherapeutics drugs). In this work, we attempted to selectively target αvβ3 integrin-expressing cancer cells and their spectroscopic detection using lipid-inserted biomimetic SERS nanoparticles (AuNP-RBCM). For cancer cell detection, cRGD-functionalized AuNP-RBCM were prepared using RBCM inserted with cRGD-PEG-lipid, followed by sonicating with AuNPs (Figure 4.5). Hydrodynamic diameter and zeta potential values did not change appreciably before- and after- the lipid-insertion strategy (Figure S4.9). UV-Vis absorption spectroscopy was also conducted to show successful conjugation of cRGD peptides onto AuNP-RBCM. As the targeting ability of cRGD-functionalized nanoparticles has been established in literature, we picked two model cancer cells lines, a high αvβ3 integrin expressing cell line, MDA-MB231 and another with low αvβ3 integrin expressing cell line, PANC-1 to confirm successful functionalization. Prior to conducting *in vitro* SERS spectroscopy studies, the cellular viability of AuNP and AuNP-RBCM@cRGD were evaluated in MDA-MB231 and PANC-1 cell lines using MTT assay and exhibited minimal cytotoxicity (Fig. S4.10). After overnight incubation of the cells with different dye-tagged AuNPs (AuNP-PEG, AuNP-RBCM, and AuNP-RBCM@cRGD), cellular binding was evaluated using SERS spectroscopy and darkfield microscopy. The MDA-MB231 cells were αvβ3 integrins positive and were detected with strong SERS signals (Figure 4.5C). In contrast, the PANC-1 cells did not express αvβ3 integrins, showing little or minimal SERS signals (Fig. S4.11). In addition, we further validated the *in vitro* targeting efficacy of AuNP-RBCM@cRGD in the endothelial cells using darkfield microscopy (Figure 4.5D). Darkfield imaging allows the generation of images from light scattering of the samples. AuNPs are detected for their increased scattering properties compared to the surrounding signals. For MDA-MB231 cells, AuNP-RBCM@cRGD appeared to bind with the

cells at a high degree, unlike AuNP-RBCM which had minimal or low binding. Contrastingly, for PANC-1 cells, there was no enhanced binding amongst any of the investigated samples. Our results from SERS spectroscopy agrees well with the expression levels of αvβ3 integrins evaluated with the flow cytometry for these cells lines using FITC-conjugated mouse antibody, which show high expression for MDA-MB231 cell line and low expression for PANC-1 cell line [153, 154].

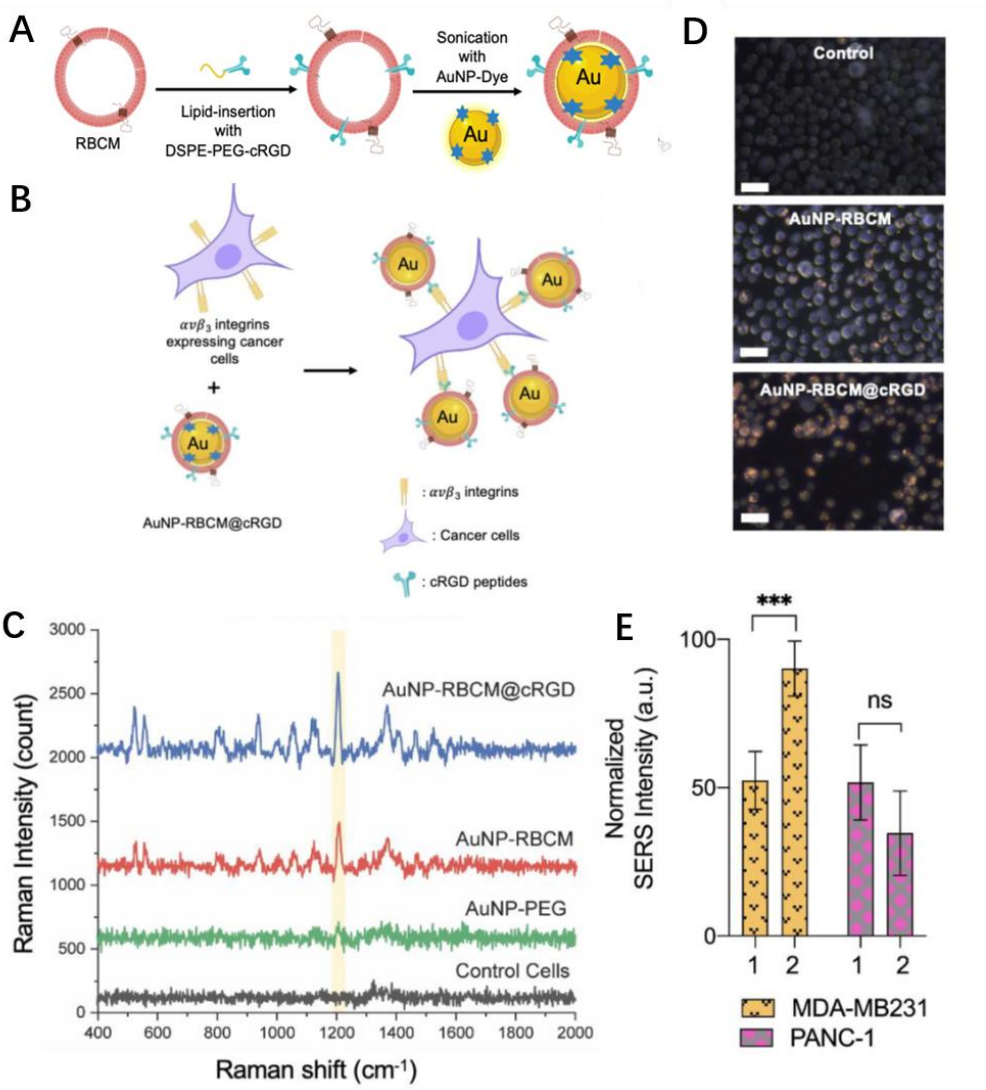

Figure 4.5 A) Schematic showing the preparation of AuNP-dye-RBCMs with tumor targeting ability by lipid insertion. B) Schematic depicting the targeting and spectroscopic detection of αvβ3 expressing cancer cells using biomimetic and tumor targeted AuNP-RBCM@cRGD. C) Raman spectra of control cells, AuNP-PEG, AuNP-RBCM and AuNP-RBCM@cRGD treated MDA-MB231 cells after 24h incubation. Each sample contains nanoparticle-cells suspensions dispersed in PBS. Spectra were acquired at laser power of 200 mW, the integration time of 2 seconds. D) Dark-field microscopy images of MDA-MB231 cells incubated with PBS1x, AuNP-RBCM, and AuNP-RBCM@cRGD, respectively. E) Normalized Raman intensity of 1: AuNP-RBCM, 2: AuNP-RBCM@cRGD treated cells at 1205 cm^{-1} Raman peak. MDA-MB231 and PANC-1 were selected as representative cell lines with and without cRGD targeted receptors, respectively.

4.4 Discussion – Red-Blood Cell Membrane Coating Driving Force and Functionality

Though lots of work have reported using cell membrane as a coating technique for nanoparticles in a wide range of biomedical applications, the interaction between natural membrane and the synthetic nanoparticles still demands in-depth molecular analysis [141, 142, 155]. Here, I briefly discuss the interaction between nature RBC membranes and citrate-stabilized AuNPs.

Already in the early 1970's it was known that the human erythrocyte membrane displays leaflet asymmetry in the phospholipid composition. [156] As is shown in Scheme 4.1, most phosphatidylcholine (PC) and sphingomyelin (SM) present in the outer leaflet, whereas phosphatidylserine (PS) and phosphatidylethanolamine (PE) are in the inner leaflet. [157] Due to the net negative charges borne by PS at physiological pH, the phospholipids show respectively neutral and negative charges between the outer and the inner lipid leaflets. The negative charge displayed on the RBC surface, however, is contributed from the ionization of sialic acid on copious surface glycans, which are highly hydrophilic and give the RBC steric stabilization. [157] On the other hand, the surface chemistry of synthetic AuNPs is more straightforward: the hydrophobic AuNPs are dispersed in aqueous solutions by various stabilizers: charged small molecules such as citrate (negatively charged), CTAB or CTAC (positively charged), or hydrophilic polymers that can provide steric repulsion such as PVP, etc.

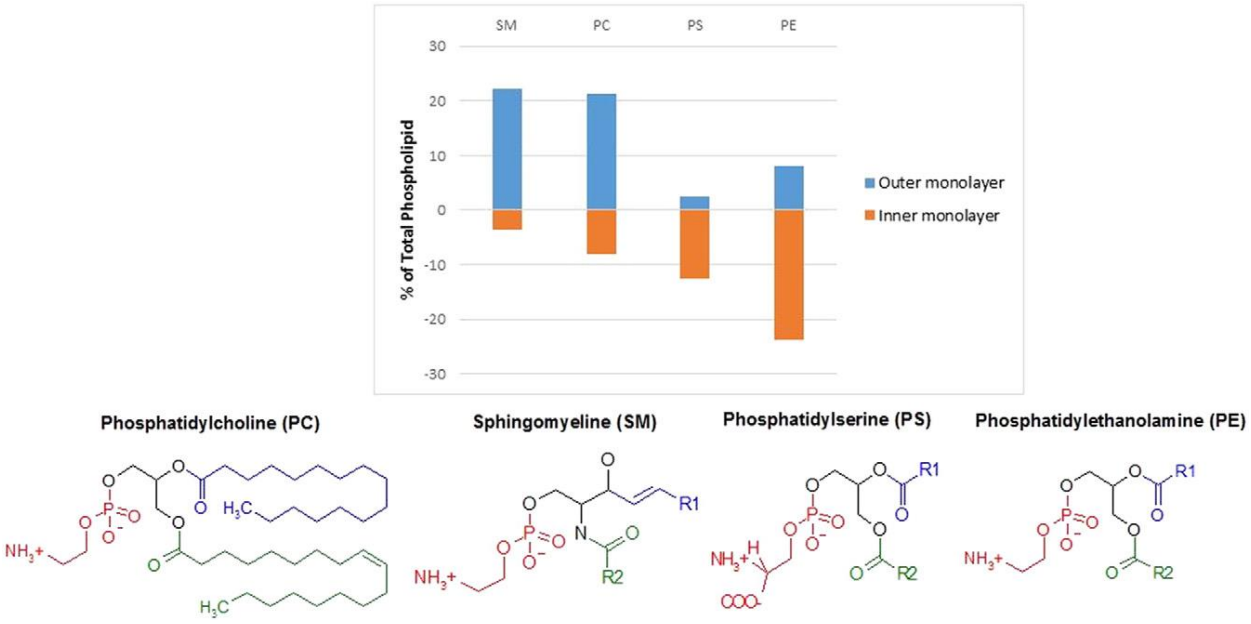

Scheme 4.1 Asymmetrical distribution of lipid in erythrocyte membrane. Reproduced from Ref. 157.

Some interesting facts were discovered regarding the surface properties of RBCM and the NPs in the process of membrane coating. First, the surface charge of nanoparticle dramatically affects RBCM coating, according to one of the pioneering work by the Zhang group [158]. It showed that while the positively charged polymeric cores formed observable aggregates upon mixture with the RBCM vesicles, the negatively charged cores formed consist spherical particles with a core-shell structure observed by Cryo-TEM. It was suggested that a more subtle membrane-particle interaction that is less disruptive to the membrane structure and fluidity could be achieved using negatively charged NPs, while the strong affinity of the negatively charged sialyl residues to positively charged NPs could collapse the fluidic lipid bilayer and impede the local arrangement necessary for lipid coverage [158]. Second, the negative charge of NPs was likely to repulse the more negatively charged extracellular membrane surface, resulting in a right-side-out membrane coating. Lastly, the phospholipid bilayer alone is not sufficient to stabilize the particles, and the steric stabilization was enabled by the poly-saccharides on RBCM [158]. As synthetic polysaccharides have been commonly reported for NP stabilization [159, 160], it is believed that the stabilizing capability of hydrophilic glycans comes from the sialic acid groups on the surface. As the glycans were cleaved by trypsinization, a significant aggregation of RBCM-NP was observed. [158]

Our work matches very well with these findings. First, while coating RBCM on AuNPs, both a negative stabilized AuNP (citrate) and a positive stabilized AuNP (CTAB) were applied for sonication with RBCM vesicles, only citrated stabilized AuNPs could be successfully coated with RBCM. Second, we examined the presence and orientation of CD47 on the RBCM coating, and the fluorescence assay proved that the CD47 protein remained its functionality (Figure S4.2k), indicating that the RBCM is coated with a right-side out. Moreover, we observed very stable

RBCM coating of these SERS AuNPs for up to 2 month under a 4 ℃ storage condition, which was indicated by that the SERS signal of these AuNPs remain ~80-90% of the original SERS intensity after 2 months. The long-term storage ability was likely attributed to the stabilization brought by surface glycan. Additionally, the cryo-protection capability of these RBCM-coated AuNPs showed in our results was hypothesized to be attributed to the polysaccharides on RBCM, which has been known as a natural cryo-protection agent for frozen food preservation [161].

Based on previous literature and our findings, the mechanism of forming stable RBCM coating on SERS AuNPs could be explained in this manner. First, sonication is used to cause damages to large cell membranes vesicles by forming air bubbles in a liquid to implode in a process called cavitation. Then, the membrane debris were mixed with citrate-stabilized hydrophilic AuNPs under sonication to facilitate entrapment of AuNPs. This process is similar to passive loading of hydrophilic drugs during forming of liposome vesicles [162, 163], but the difference is that the glycan-stabilized RBCM could bring a lower surface-energy and higher colloidal stability of weak citrate-stabilized AuNPs and thus the process is energy favorable. The completeness of RBCM coverage was reported to depend on the membrane-to-nanoparticle ratio [158]. It was also observed that not only spherical nanoparticles can be coated with membrane, but also some anisotropic nanoparticles despite their increased curvature [149]. Once the membrane coating is formed, the AuNP-RBCM structure could be quite stable for up to months attributed to the glycan-driven colloidal stability by both electrostatic repulsion and steric repulsion.

Translocating natural RBC membranes onto the nanoparticles is expected to bring their biological functionality to the resulting RBCM-NPs. A wide range of experiments were conducted with this goal and are briefly summarized here. First, the CD47 protein markers was shown to retain and function well on the RBCM coating surface by both Zhang's and our work, and their anti-phagocytosis capability against macrophage uptake due to the contribution of CD47 was also proved [164]. Second, the composition of membrane proteins is mostly retained throughout the RBCM-NPs synthesis determined by polyacrylamide gel electrophoresis (PAGE), except a loss of peripheral membrane proteins which was observed as a missing band near 51kDa if mechanical extrusion process was employed to facilitate membrane coating [165]. Finally, RBCM functionalized NPs showed elongated in-vivo blood circulation time, with 29% and 16% overall blood retention compared with 11% and 2% exhibited by the PEG-coated NPs after 24h and 48h, respectively. [165] This finding further confirms that the NPs were modified with the functional components on the RBCM membranes, which contain immunosuppressive proteins that inhibit macrophages uptake. However, it still requires further studies on whether these RBCM coated NPs could retain other physiological functions of RBC while interacting with different cell types, and whether the surface biomarkers that is responsible for blood type classification could be retained on extracted and re-assembled RBCM vesicles to match to patient's blood type when human erythrocytes are used for NPs modification. To sum up, the proposed technique of erythrocyte membrane-camouflaged nanoparticles is believed to remain an interesting research direction due to not only their attractive biomimetic properties for nanoparticle delivery, but also the unsolved mysteries on their physiological functions.

4.5 Conclusions

In summary, we have shown that when the RBCM coating was applied to AuNPs functionalized with Raman-active dye molecules, it resulted in a further improvement in the particle brightness with excellent reproducibility, long-term retention of the signal intensity, and improved dispersion stability, allowing AuNPs to be frozen, lyophilized with superior performances than previous PEGylated SERS nanotags. These biomimetic SERS AuNPs were further modified with tumor-targeting peptides (cyclic-RGD) using a lipid-insertion strategy to target the αvβ3 integrin receptors expressed on cancer cells and consequently used for *in vitro* SERS detection. Our data indicate that a biomimetic RBCM coating could be used as an alternative to PEGylated coating imparting AuNPs with improved dispersibility, enhanced SERS signal brightness, and tumor targeting functions. We anticipate that biomimetic membranes of different origins (cancer cells, immune cells, bacteria, etc.) could be employed to impart plasmonic nanoparticles with features of increased dispersion stability, improved SERS signal intensity, biocompatibility, and biofunctionalization capabilities for biomedical applications facilitating their introduction at a clinical level.

4.6 Supplementary Figures

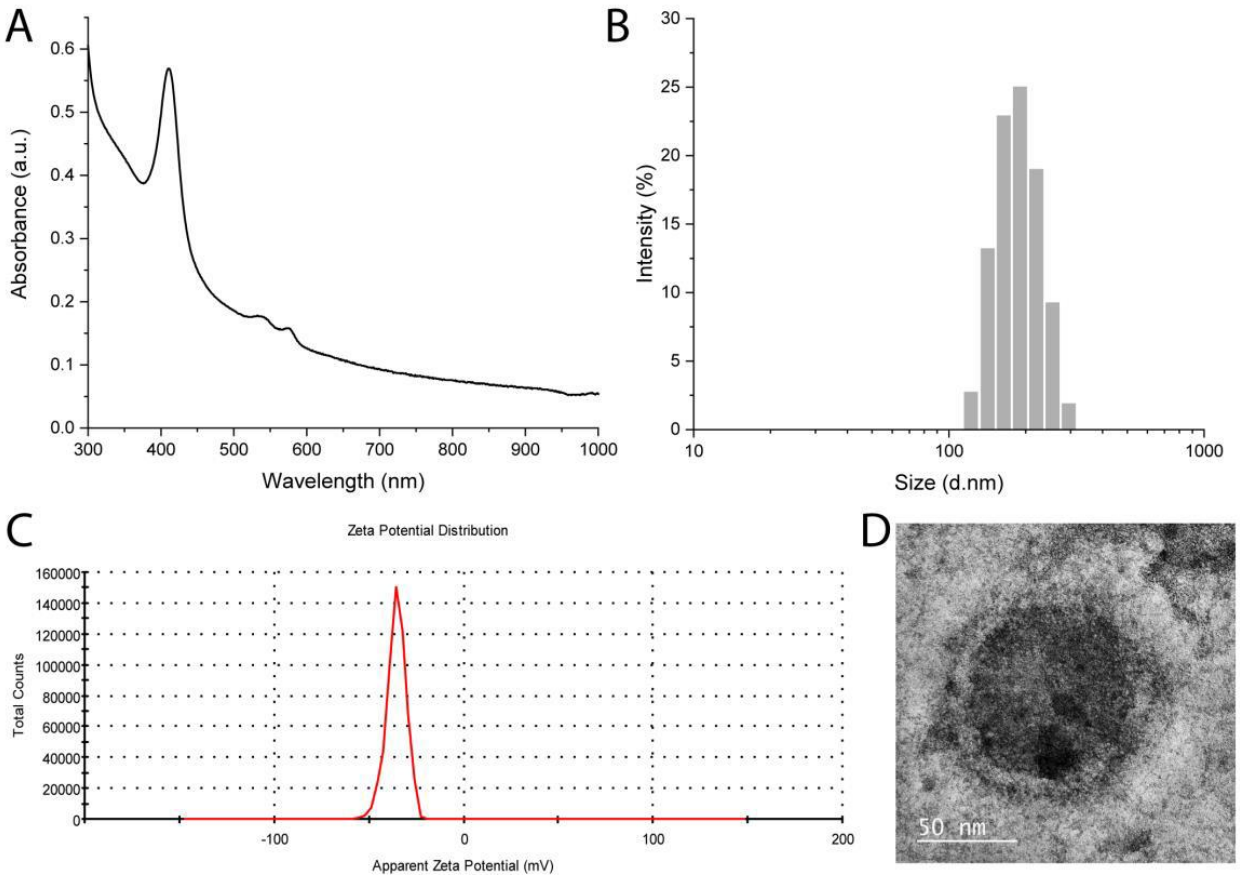

Supplementary Figure 4.1 Characterization of RBCM vesicles. A) UV-vis spectrum of pure RBCM vesicles. B) Hydrodynamic size distribution of RBCM vesicles. C) Zeta potential distribution of RBCM vesicles. D) Negative staining TEM image of RBCM vesicles.

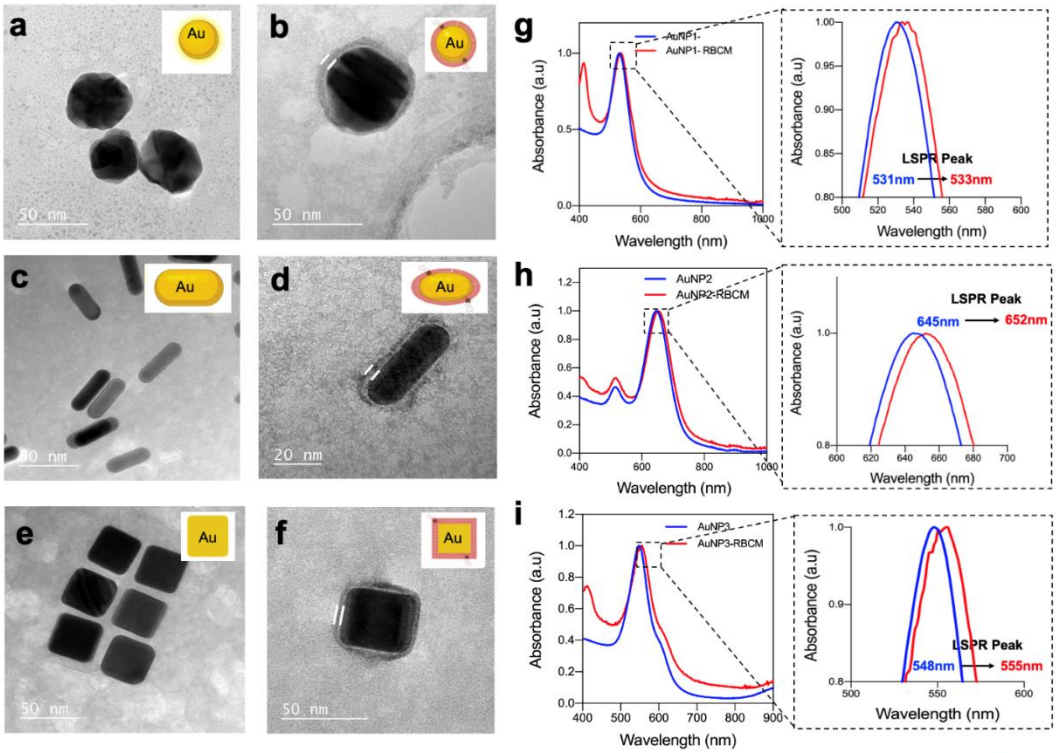

j

Samples	Hydrodynamic Diameter (nm)		Zeta Potential (mV)	
	-RBCM	+RBCM	-RBCM	+RBCM
AuNP1	44 ± 5	64 ± 4	-37 ± 6	-28 ± 3
AuNP2	54 ± 4	66 ± 4	-38 ± 6	-27 ± 4
AuNP3	53 ± 5	68 ± 4	-40 ± 6	-30± 2

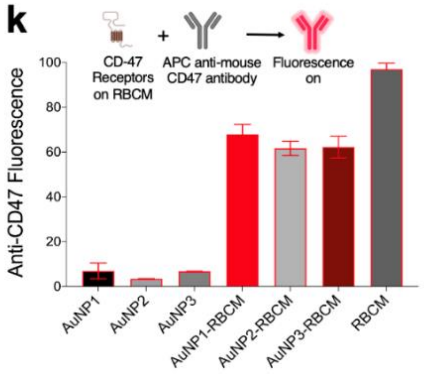

Supplementary Figure 4.2 Physicochemical characterization of anisotropic RBCM-coated AuNPs. Negative-stained transmission electron micrographs of (a) AuNP-Cit, (b) AuNP-RBCM, (c) AuNP2-Cit, (d) AuNP2-RBCM, (e) AuNP3-Cit, and (f) AuNP3-RBCM, with the membrane coating in (b), (d), and (f) highlighted with white lines. (g-i) UV-Vis absorbance spectra of AuNP's and AuNP-RBCM's, with the inset boxes zoomed. The inset shows the intrinsic plasmonic absorbance peak shift for different anisotropic AuNPs upon RBCM coating. (j) Hydrodynamic diameter and zeta potential measurements for AuNPs before and after RBCM coating. (k) Anisotropic AuNPs uncoated and coated with RBCM were stained with a fluorescent anti-CD47 antibody. Data shown as mean ± standard deviation, n = 3.

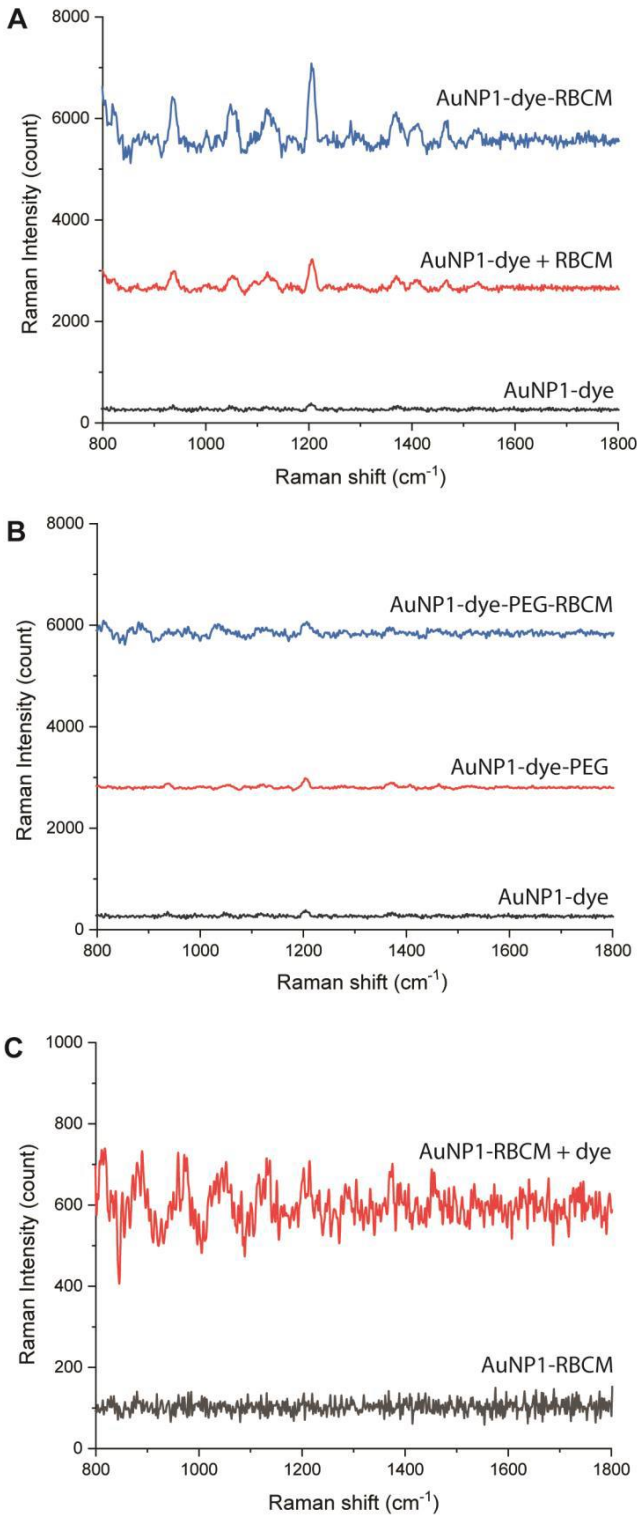

Supplementary Figure 4.3 A) AuNP-dye first mixed with RBCM solution, then the mixture was bath sonicated for 10 min. B) AuNP-dye first coated with 2k Da PEG, then coated with RBCM. C) AuNP first coated with RBCM, then mixed with dye solution. All spectra taken at 200 ms, 200 mW.

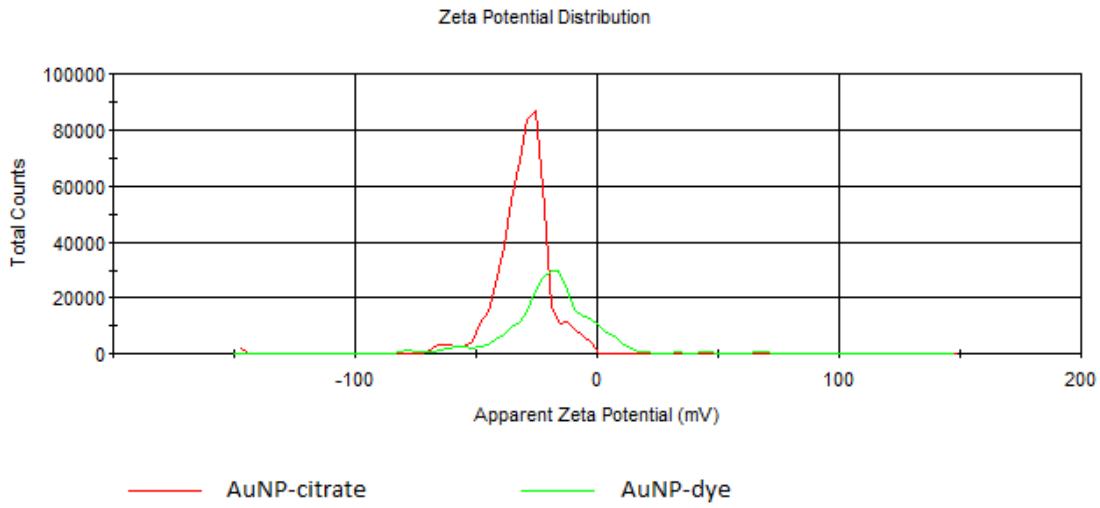

Supplementary Figure 4.4 Zeta potential profile of AuNP-citrate before and after reporter dye attachment

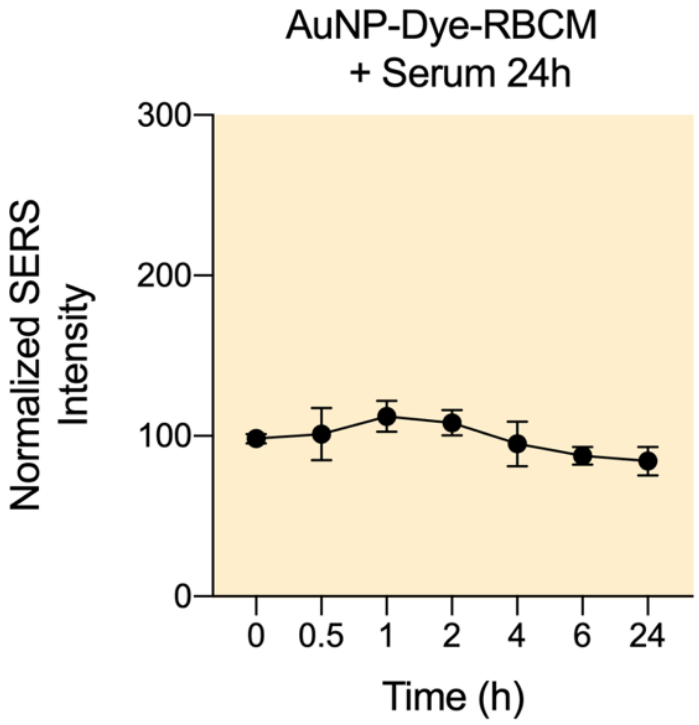

Supplementary Figure 4.5 SERS signal stability of AuNP-Dye-RBCM was evaluated in serum proteins (50%) by collecting their Raman intensity values at 1205 cm-1 for different time points.

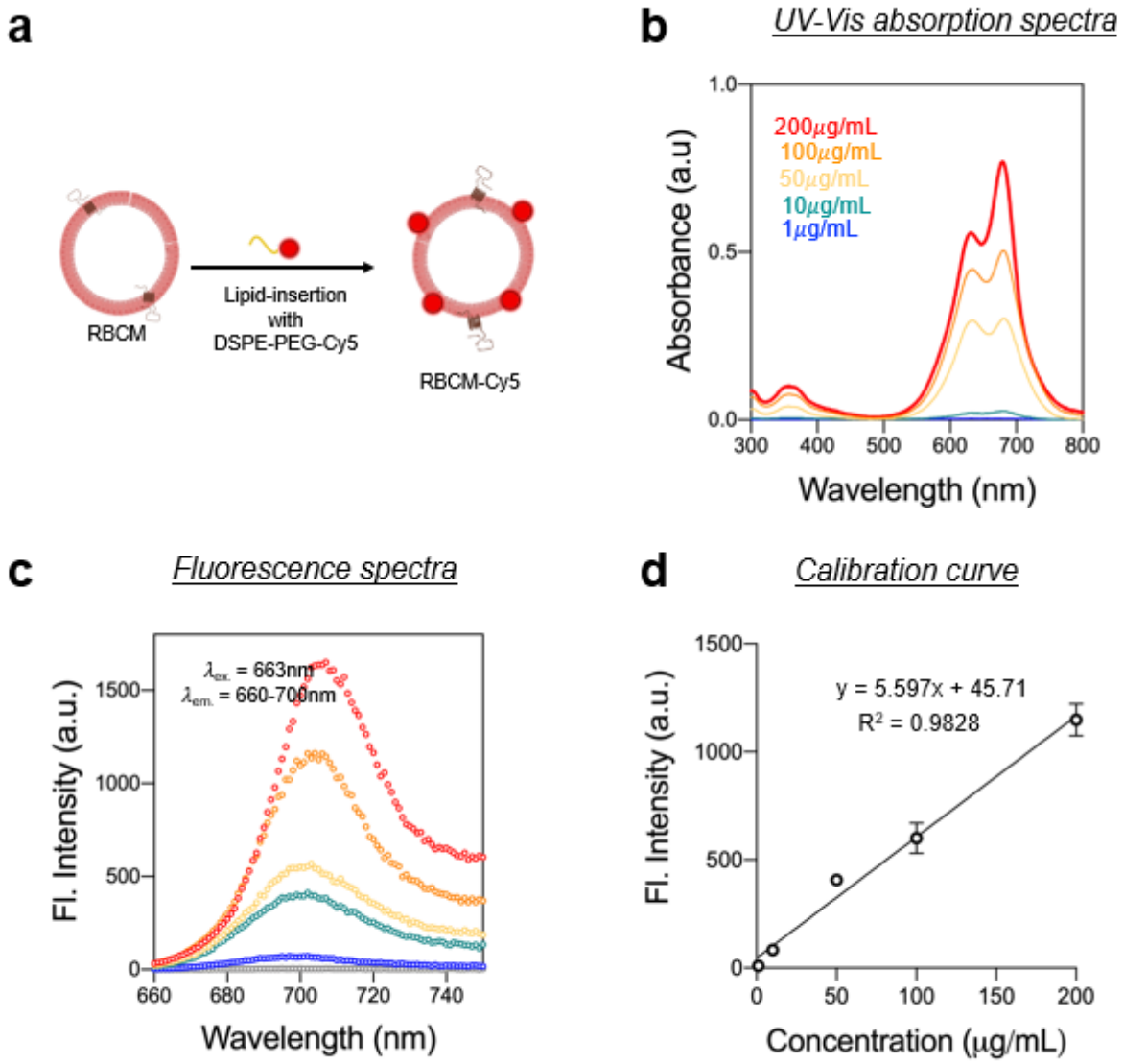

Supplementary Figure 4.6 (A) Schematic illustration of lipid-insertion modification of RBCM with DSPE-PEG-Cy5. DSPE-PEG-Cy5 was incubated with RBCM and subsequently (B) UV-Vis absorption spectra and (C) Fluorescence spectra were evaluated for increasing concentration ranging from 1μg/mL to 200μg/mL. (D) Calibration curve obtained by plotting the fluorescence intensity with respect to concentration of DSPE-PEG-Cy5 lipid-inserted onto RBCM.

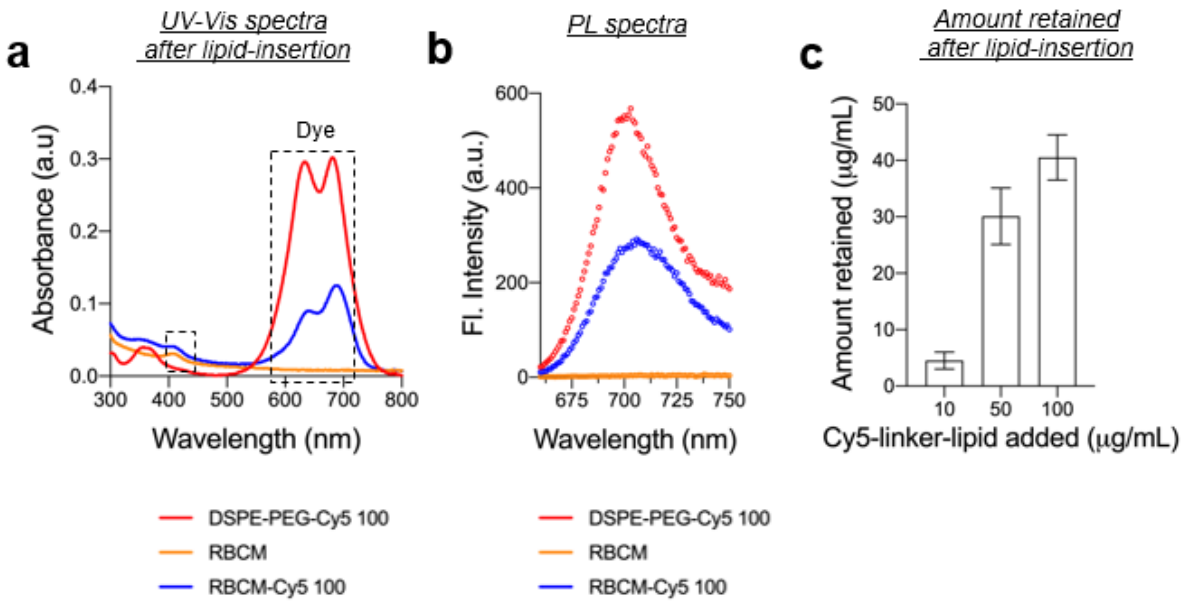

Supplementary Figure 4.7 (A) UV-Vis absorption spectra and (B) Fluorescence spectra were collected for RBCM, DSPE-PEG-Cy5 100 μg/mL (referred as DSPE-PEG-Cy5 100), and RBCM lipid-inserted with 100 μg/mL of DSPE-PEG-Cy5 (referred as RBCM-Cy5 100). (C) Subsequently, the amount of DSPE-PEG-Cy5 incorporated onto the RBCM was then quantified after 30 min of incubation and plotted against the initial amount added. This was further extended to DSPE-PEG-Cy5 having concentrations of 50 μg/mL and 10 μg/mL, respectively.

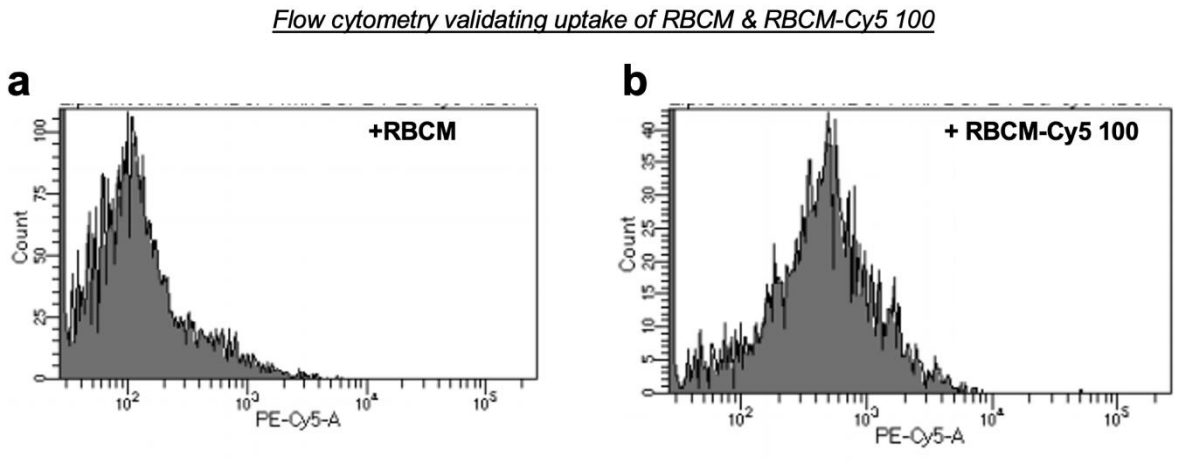

Supplementary Figure 4.8 Flow cytometry histograms of (A) RBCM, and (B) RBCM incorporated with DSPE-PEG-Cy5.

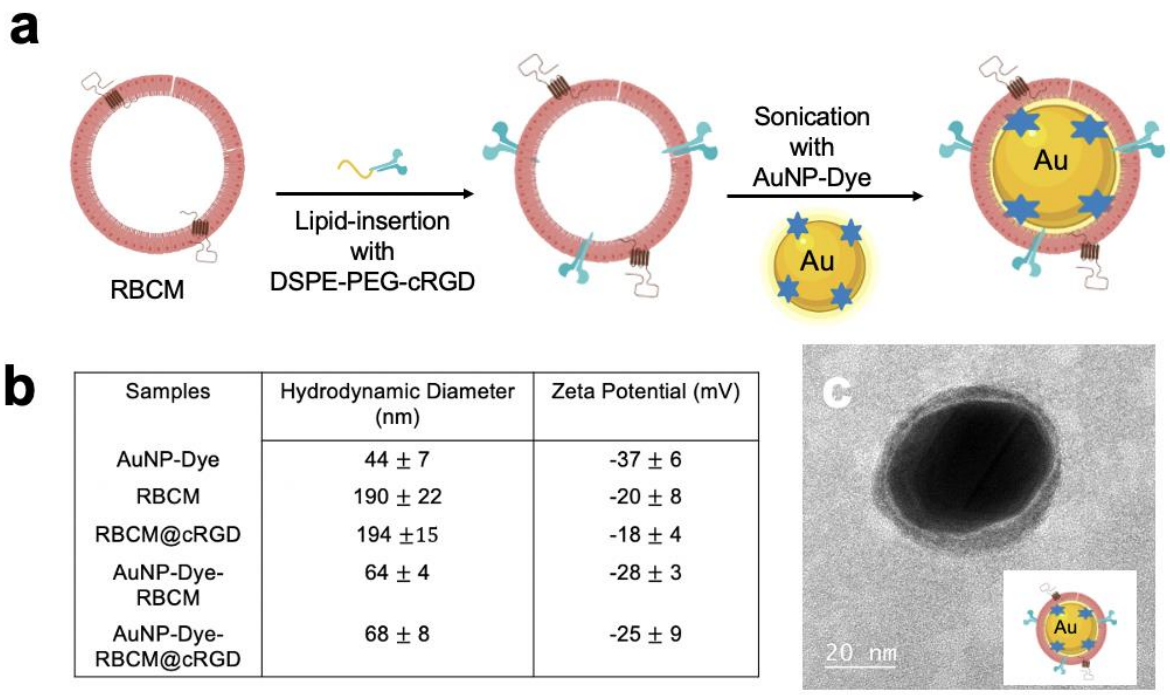

Samples	Hydrodynamic Diameter (nm)	Zeta Potential (mV)
AuNP-Dye	44 ± 7	-37 ± 6
RBCM	190 ± 22	-20 ± 8
RBCM@cRGD	194 ±15	-18 ± 4
AuNP-Dye-RBCM	64 ± 4	-28 ± 3
AuNP-Dye-RBCM@cRGD	68 ± 8	-25 ± 9

Supplementary Figure 4.9 (A) Schematic showing the preparation of AuNP-dye-RBCMs with tumor targeting ability by lipid insertion. (B) Hydrodynamic diameter and zeta-potential measurements of different samples. (C) Negative-stained transmission electron microscopy of AuNP1-dye-RBCM@cRGD.

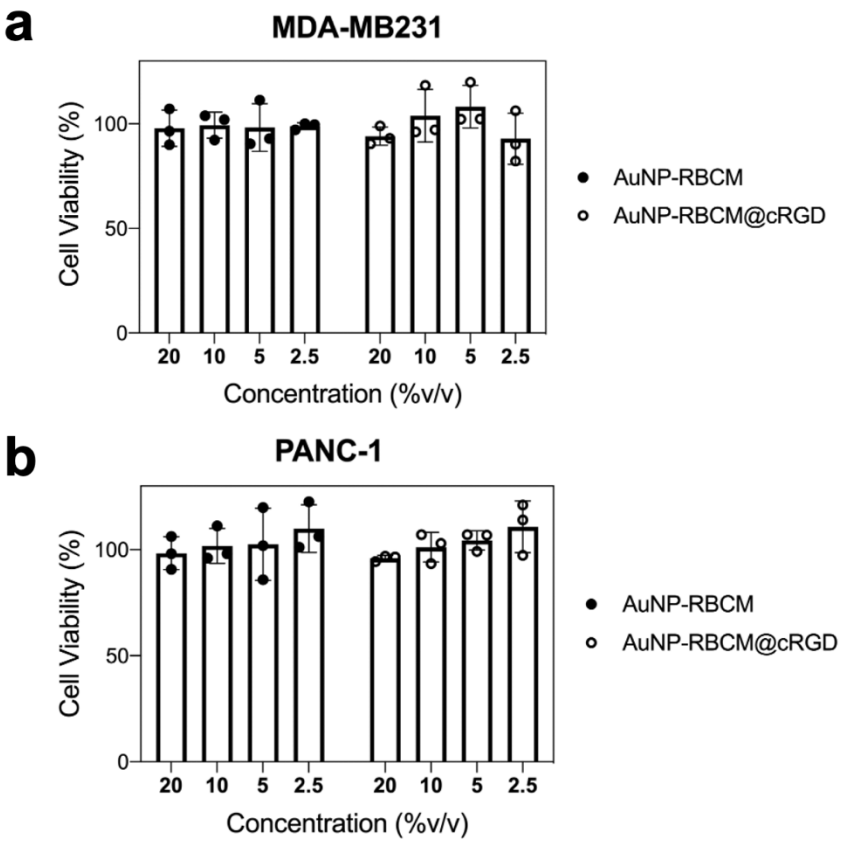

Supplementary Figure 4.10 MTT assay for evaluation of cytotoxic effects of AuNP-RBCM & AuNP-RBCM@cRGD in (A) MDA-MB231, and (B) PANC-1 cell lines.

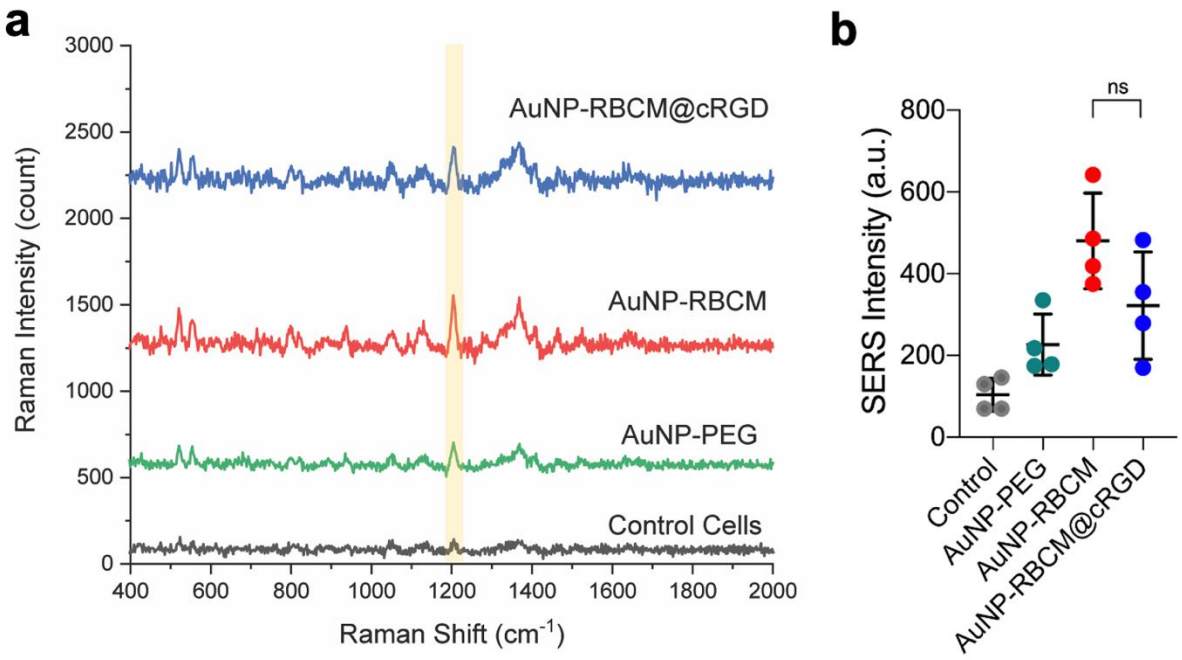

Supplementary Figure 4.11 (A) *In vitro* SERS spectra obtained from different dye-tagged samples in PANC-1 cell line which do not express αvβ3 integrin receptors. (B) Comparative SERS intensity at 1205 cm^{-1} was plotted to investigate the role of lipid-insertion on cellular internalization.

CHAPTER 5: PHOTOACOUSTIC-SERS DUAL-MODALITY IMAGING AGENTS FOR IMAGE-GUIDED DIAGNOSTIC AND SURGERY

5.1 Motivation – Photoacoustic-SERS Dual-Modality for Pre-operation Diagnostic and Intra-operative Image-Guided Tumor Resection

Surgical resection remains the only curative treatment for many malignant cancers. The complete removal of the tumor burden is of great importance in this procedure, without which there is a high possibility of tumor recurrence [166, 167]. However, malignant tumor margins are often irregular due to diffusive invading to surrounding healthy tissues, and many surgeons distinguish tumor margin only by eyes and based on experience during tumor resection [168]. Therefore, surgeons usually choose to resect large margins of healthy surrounding tissues to remove all potential lesions, which may cause increased mortality and reduced quality of life of the patients.

An imaging method with high sensitivity, deep tissue penetration depth and high spatial resolution will be ideal for both pre-operative tumor location and intra-operative tumor margin delineation. Among current imaging techniques, magnetic resonance imaging (MRI) and positron emission tomography (PET) are preoperatively adopted to determine the location of tumors for surgical planning, but both of them suffer from limited spatial resolution and poor sensitivity [169]. Computed tomography (CT) is also used to tumor staging, but it offers poor specificity and low soft tissue contrast [65]. Besides, these modalities are usually high-costed and require long imaging time, making them improper for real-time intra-operative detection of tumor margins. Ultrasound is more affordable and provide good structural information in real-time, but it cannot detect microscopic tumor burdens due to limited sensitivity and poor specificity [170].

To date, no single imaging modality is able to delineate the full extent of the tumor and provide accurate intraoperative guidance for achieving complete tumor resection. There is thus an increasing research interest in using single imaging agent to realize dual-modality image-guided surgery that provide both preoperative tumor demarcation and intraoperative image-guided surgery [76, 171, 172]. Among all imaging modalities, surface-enhanced Raman spectroscopy (SERS) has gained attention for accurate delineation of tumor margins and detection of microscopic tumors by offering extremely high sensitivity, unique Raman signatured peaks, minimum photobleaching and great multiplexing ability. In a pioneering work by Nie group, a handheld spectroscopic device called the "Raman Pen" was developed for high-sensitivity detection of tumor margins, metastatic lymph nodes, and micro-metastases during surgery [173]. Au is the main nanomaterials that provide plasmonic properties for surface enhancement. By attaching reporter molecules on Au nanoparticle surface, the synthesized SERS nanotags provide strong and distinct Raman signal that can be easily differentiated from biological tissues. In addition to the plasmonic properties that commonly used for SERS, Au nanostructures also feature excellent photoacoustic (PA) imaging capability that can realize 3-D image of tumor tissue with high spatial resolution and centimeter-scale penetration depth [174].

Because their surface resonant plasmon strongly depends on size and geometry, numerous methods have been developed to fabricate various types of AuNPs. Among various Au nanostructures, star-shaped AuNPs ('nanostars') have plasmon bands that are tunable into the NIR region, and the structure contains multiple sharp branches that act as "lightning rods" to greatly enhance the local EM-field [32]. Previous work has shown that Au nanostars (AuNS) is typically 2 to 3 orders of magnitude stronger SERS enhancement factor (EF) than Au spheres. [87] Moreover, AuNS was also reported to show as large as 35-fold PA intensity enhancement with

respect to Au nanospheres due to higher energy conversion efficiency [175]. There are some previous work that reported using AuNS as imaging agents for both SERS and PA imaging, but the silica coating used in their work provides poor in-vivo stability, as well as complex surface conjugation chemistry with targeted ligands [176, 177].

In this chapter, we present a RBCM protected AuNS agents for dual-modality of SERS and PA imaging. The LSPR peak of the AuNS were tuned to NIR window to enable better tissue penetration depth for biological image. Resonant chromophore, IR-780, was encoded to the AuNS to induce resonant Raman scattering with additional enhancement. Natural red-blood-cell membrane was applied as protective coating of AuNS to provide better biocompatibility by reducing macrophage uptake and to enable easier chemistry for target ligand conjugation by lipid-insertion strategy. An ex-vivo tissue tumor detection phantom study was then conducted to show the potential of RBCM-coated AuNSs as imaging agents for SERS-PA dual-modality. Our results show that AuNS-RBCM could be excellent candidates for preoperative and intraoperative PA-SERS dual-modality tumor imaging.

5.2 Experimental Section

Materials. Deionized water (DI water) was used throughout the work. The following chemicals were used as purchased without any further purification: IR-780 iodide (dye content ≥95%), N,N-dimethylformamide (DMF), sodium citrate tribasic dihydrate, gold(III) chloride trihydrate ($HAuCl_4$), sodium borohydride ($NaBH_4$), poly(sodium 4-styrenesulfonate) (Na-PSS) solution (average Mw ~70,000, 30 wt. %), silver nitrate ($AgNO_3$), L-ascorbic acid, sodium bromide (NaBr), hexadecyltrimethylammonium bromide (CTAB) and poly(ethylene glycol) methyl ether thiol (mPEG-thiol, Mn 2000 Da) from Sigma Aldrich, hexadecyltrimethylammonium chloride (CTAC)

from Tokyo Chemical Industry Co., LTD., poly(ethylene glycol) methyl ether thiol (mPEG-thiol, Mn 5000 Da) from Laysan Bio Inc.

AuNS-dye-RBCM preparation. Glassware and stir bars for gold nanoparticle synthesis were washed by aqua regia before use. Gold nanostars (AuNS) were synthesized using a seed-mediated method [87]. First, 15-nm small AuNPs were synthesized as the seed. A water solution of 2.2 mM sodium citrate (60 mL) was heated to boiling under vigorous stirring. Once boiling had commenced, 400 μL of $HAuCl_4$ solution (25 mM) was quickly injected. The reaction completed within 10 min where the solution turned from yellow to purple grey and then to burgundy. The resulted solution was centrifuged 3 times and stored as Au seed for the next step. For Au nanostars synthesis, to 4 mL $HAuCl_4$ solution (0.25 mM), 4 μL of 1N HCl and 280 μL of 15-nm citrate gold seeds were added followed by simultaneous addition of 40 μL $AgNO_3$ solution (3 mM) and 40 μL of ascorbic acid solution (100 mM) under stirring. The reaction was performed at room temperature, and the process was completed in less than 2 min. Raman reporter molecules IR-780 stock solutions were prepared by dissolving 1 mg of the dye molecules into 1 mL of DMF. The stock solutions were diluted by DI water to form a dye concentration of 2.62 μM for fresh use. Typically, 136 μL above dye molecule solution was dropwise added to AuNS under moderate stir. RBCs derived from BALB/C mouse blood were purchased directly from BioIVT. Subsequently, it was subjected to hemolysis where the RBCs was suspended in lysis buffer, i.e., 0.25X PBS at 4ºC for 1h. The resulting solution was centrifuged 4 times at 20000g to eliminate hemoglobin until a pink pellet (RBCM concentrate) was obtained, and the supernatant solutions was colorless. The pink pellet was resuspended in distilled water (~50mL) and vigorously mixed and sonicated for 10 minutes in ice-water mixture. The RBCM solution was eventually added to AuNS solution with the RBCM vesicle/AuNS volume ratio of 1/3 and bath sonicated for 10 minutes to form AuNS-

RBCMs. The resulting solution was centrifuged at 700g for 15 minutes to eliminate residual RBCM vesicles.

AuNS-dye-PEG preparation. After 10 min incubation with reporter molecules, 1 mL SH-PEG solution (51.8 μM) was dropwise added to the AuNS@dye solution to form PEGylated AuNS. The solution was then incubated at room temperature for 1 hour, then the SERS nanoparticles were washed twice by centrifugation at 1100g to remove excess PEG and dye molecules.

Nanoparticle characterization. Dynamic light scattering (DLS) measurements were conducted to measure the hydrodynamic size distribution (intensity average) of the nanoparticles on Malvern Zetasizer ZS90 instrument (Malvern Instruments Ltd, United Kingdom) at a fixed angle of 90°. Zeta potential (ζ) values were determined using a Malvern Zetasizer (Malvern Instruments Ltd, United Kingdom) of Nano series. Ultraviolet-visible (UV-Vis) absorbance of was recorded on GENESYSTM 10S UV-Vis Spectrophotometer (Thermo Scientific, MA, USA). Absorbance spectra were collected at an interval of 1 nm scanning from 300nm-1000 nm.

Transmission Electron Microscopy (TEM) Imaging. A drop of RBC-coated or bare (non-RBC-coated) nanoparticle solution was deposited onto a glow-discharged, carbon-coated TEM grid and incubated for 5 minutes. Excess liquid was removed, and samples dried overnight in a desiccation chamber. For negative staining, samples were stained with 1% uranyl acetate for 30 seconds immediately before imaging. All samples were imaged using a JEOL JEM-2100 transmission electron microscope at 200kV.

SERS data collection and processing. Raman spectra were obtained using a BaySpec Agility transportable 785/1064 nm dual-band benchtop Raman spectrometer (East JHX, Inc.). 785 nm laser (200 mW) was used as the excitation source. Each Raman measurement includes 3 scans, and the averaged Raman spectrum was plotted. Averaged Raman intensity of 1205 cm^{-1} peak from

the 3 scans was chosen to show Raman signal change for the SERS AuNPs, and the error bars represent the standard deviations of the scans performed for 3 separate experiments. All the Raman spectra were baseline corrected to remove fluorescence background, and the band intensities were calibrated by standard sample (benzonitrile) spectrum.

Photoacoustic imaging system. The photoacoustic imaging system is customized and is majorly composed of a Q-switched ND:Yag Opotek Phocus Mobile infrared pulse laser (OPOTEK, LLC) and Verasonics data acquisition (DAQ) system. The laser pulse width is less than 5 ns and with 10 Hz repetition rate. The wavelength used in most of the experiments except photoacoustic spectroscopy is 750nm. Light is delivered by customized bifurcated 30 linear fiber bundles (30 mm length for each output, Chunhui Science Co., Nanjing, China). The DAQ system is high-frequency, programmable ultrasound Verasonics Vantage 256^{TM} system (Verasonics Inc.). A MS250 ultrasound probe (FUJIFILM Visualsonics, Inc) with 256 elements and 21 MHz central frequency (bandwidth 13-24 MHz) is used for quantitative and qualitative PA signal detection. For tumor mimicking phantom imaging, a L12-5 50 mm ultrasound probe (Philips) with 256 elements and 7.8 MHz center frequency is used. In order to match the length of fiber bundle, only the central 128 elements are used for imaging acquisition. Ultrasound probe and optical fiber bundle are coupled together by 3D printed customized coupler and are mounted on robotic arm (Meca 500, Mecademic Robotics) for imaging scanning. To synchronize the laser and DAQ system, the flash lamp and DAQ system are triggered by a 10 Hz TTL signal function generator, and the Q-switch of the laser is triggered by Verasonics Vantage system. All procedure, including laser triggering timing control, data acquisition, and scanning motion integration were proceeded through Matlab script. After radio frequency data acquisition, delay-and-sum beamforming algorithm is applied to reconstruct the photoacoustic images.

Quantitative and qualitative AuNS properties measurement using photoacoustic detection. To demonstrate the difference between different gold nanoparticles in both qualitative and quantitative aspect, two different detection system are adopted. For visualizing the qualitative differences, agar-based tissue mimicking hole phantom is adopted. Agar powder is added into water with 5% weight concentration and is heated to 90 ^{o}C for resolving. Then, 0.2% weight concentration of glass beads are added to mimic the tissue acoustic scattering properties. The solution is placed in vacuum oven at 65 ^{o}C and vacuumed for degassing and is poured in 3D printed mold for phantom geometry consistency. The diameter of the hole is 3 mm. The holes are 15 mm below the surface of the phantom to match the optical fiber bundle bifurcated focusing and ultrasound probe focusing. The specimen solution is mixed with 10% gelatin water solution, prepared at 50 ^{o}C and cooled down to below 30^{o}C before injecting into the holes. For quantitatively determining the PA intensity, a plastic tube is fixed in plastic box and the distance between tube and ultrasound probe is kept at 15 mm for matching the focusing. The laser fluence for both quantitative and qualitative detection is 4.8 mJ/cm^2.

Linear scanning photoacoustic 3D volume imaging for tissue stacking tumor mimicking imaging. To capture the AuNS targeted tumor mimicking phantom beneath tissue, linear scanning is adopted to acquired 3D volume photoacoustic signals. The scanning step size is 0.5 mm and the number of steps is 40 to give a 20 mm imaging length. Two optical fluences, 18 mJ/cm^2 and 4.8 mJ/cm^2 are adopted to image the tumor phantom at different tissue depth. The photoacoustic intensities are normalized to the corresponding applied laser fluence. For the groups with tissue thickness less than 3 mm, 4.8 mJ/cm^2 are applied. For the groups above 3 mm, 18 mJ/cm^2 is adopted. For 3 mm group, both fluences are used to verify the fluence normalization. To assure the consistency of light delivery and acoustic focusing, the tumor mimicking phantom is always kept at same depth

related to ultrasound probe, regardless of the tissue thickness. The remaining space between tissue and probe is filled with water for acoustic wave coupling and is separated from water using plastic films. The 3D volume is projected along depth axis (z-axis) through maximum intensity projection (MIP) to demonstrate the complete structure of tumor phantom. After MIP, a square box region-of-interest (ROI) is chosen to determine the photoacoustic intensity trend for different tissue depth.

Lipid-insertion of tumor-targeting peptides. Stock solutions of DSPE-PEG-cRGD with concentrations of 100 µg/mL were made in DI water. RBCM prepared earlier were thawed, bath-sonicated in ice water. Subsequently, 1mL of RBCM was added to 1 mL of each DSPE-PEG-cRGD and vortexed vigorously for 1 min. The solutions were incubated for 30 minutes in the refrigerator followed by centrifugation at 600g for 15 minutes at 4℃. The supernatant was removed, and 2 mL of DI water was added to each tube.

In vitro SERS study. To verify the effective binding of AuNS-RBCM@cRGD to endothelial cells, a comparative targeting study was performed in vitro with 4T1 and PANC-1 cells. Both cell lines were grown in Eagle's Minimum Essential Medium (MEM), supplemented with 1.5 g/L sodium bicarbonate, non-essential amino acids, L-glutamine and sodium pyruvate and cultured until they reached ~80-90% confluency. Subsequently, they were plated in a 6-well plate and allowed to grow for 24h at 37°C at the cell density of 10^6 cells/well. Dye-tagged AuNSs (AuNS-RBCM, and AuNS-RBCM@cRGD) were added to the media and allowed to incubate overnight. Following this, AuNS-containing media was removed by aspiration, and cells were rinsed two times with PBS. The cells were then collected and measured for SERS signal intensities using a BaySpec Agility transportable 785/1064 nm dual-band benchtop Raman spectrometer (East JHX, Inc.).

MTT Assay of different AuNPs. The cytotoxic effects of various AuNPs in two different endothelial cell lines (MDA-MB231, PANC-1) was investigated using MTT assay established previously.

Tissue penetration depth study. The fresh *ex vivo* porcine tissues are purchased from grocery stores and frozen before use. Three types of tissues are used, i.e. muscle, skin and fat. Specifically, the pork tenderloin is chosen for muscle samples, and side pork for skin and fat samples. A meat slicer is applied to cut the frozen tissues into thin layers with different thicknesses. The length and width of tissues are over 3 cm to fully cover the NP gel. For the Raman penetration depth measurement, the laser probe was vertically fixed by a clamp, and the gel was placed on a fixed stage platform. Porcine tissues were put above the SERS gel and fully cover it, ensuring no air bubble in-betweens. The spectra were recorded at the best focus position.

5.3 Results and Discussion

We first compare the SERS and PA behavior of Au nanostars versus Au nanospheres. Here, AuNPs with the shape of sphere, rod and star are prepared at the same Au concentration (absorbance at 450 nm equals to 0.4), and attached with same amount of Raman reporter molecule IR-780 (final concentration of 0.05 um). The hydrodynamic sizes of the three AuNPs were all 40-50 nm in diameter. SERS performance and photoacoustic intensity of the AuNPs were measured. Figure 5.1A shows that Au nanostars exihibit 2 and 1 orders of magnitude of surface enhancement with respect to the nanospheres and nanorods, respectively. The great Raman enhancement is believed to be resulted from the localized electromagnetic enhancement at hot spots of the sharp tip geometry. In addition to SERS, we also found that the photoacoustic intensity of Au nanostars are much stronger than Au nanospheres that measured at the same condition, which is in accordance with previous findings.

We then coated the dye-attached Au nanostars with natural red-blood-cell membranes (RBCM) via similar method discussed in Chapter 4. Characterizations of the prepared AuNS-dye-

RBCM are shown in Figure 5.2, where AuNS-PEG was used as the control. Negative-staining TEM image show a complete RBCM coating on Au nanostars (Figure 5.2A). From the UV-vis spectra, a LSPR peak shift was observed after RBCM coating (Figure 5.2B). The hydrodynamic size of AuNS-dye changes from 54 ± 5 nm to 144 ± 4 nm after RBCM coating, while still maintain very narrow size distribution (PDI = 0.195), indicating uniform RBCM coating on AuNS. The Zeta potential changes from -31 mV to -21 mV upon RBCM coating, indicating partially screening of the intrinsic charge of citrate-stabilized AuNS by the cell membrane. PA and SERS performances of the RBCM coated AuNSs were also tested. Figure 5.3 shows that AuNS-RBCM exhibited good linearity of its PA intensity and its SERS intensity versus NP concentration at picomolar level, which covers the common working concentrations of the NPs in-vivo.

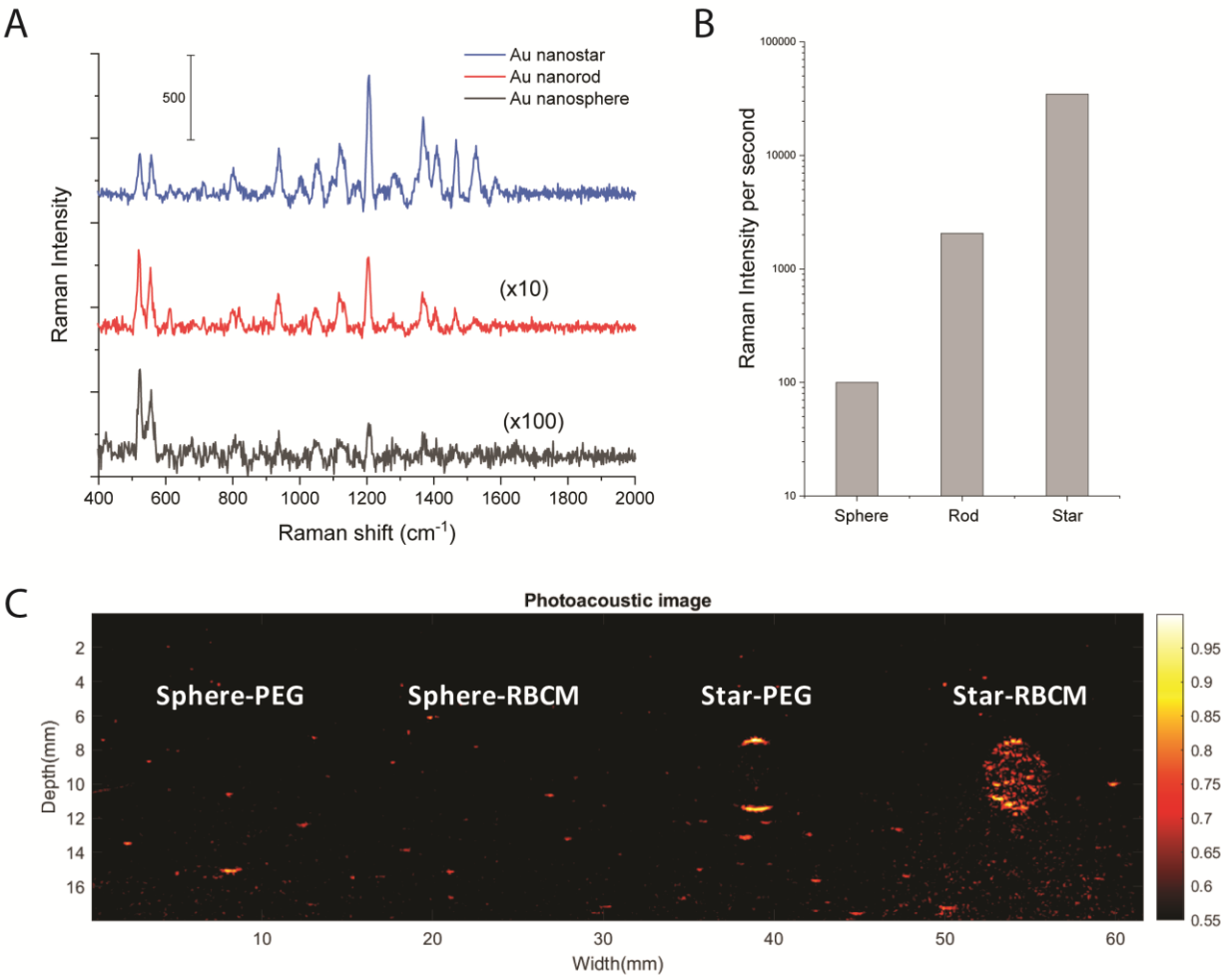

Figure 5.1 A) SERS spectra of Au stars, rods and spheres. Raman spectra were measured at the same Au concentration and the same reporter molecule concentration, using integration time of 2 seconds, 200 ms and 20 ms for sphere, rods and stars respectively. B) SERS intensity per second of 1205 cm^{-1} peak of the spectra in (A). C) Photoacoustic image of gels made from PEG and RBCM coated Au spheres and stars, respectively.

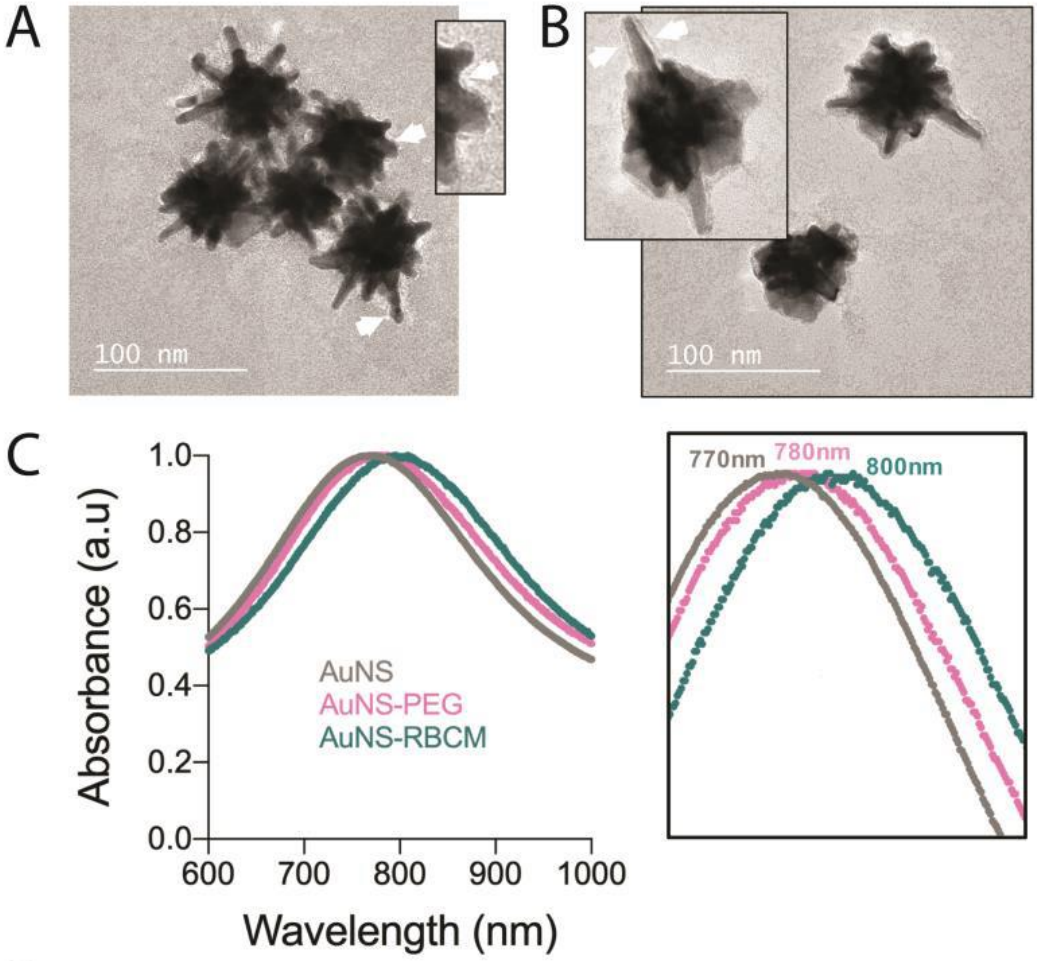

D

Sample	Hydrodynamic Diameter (nm)	Polydispersity Index (PDI)	Zeta Potential (mV)
AuNS	54 ± 5	0.304 ± 0.01	-31 ± 3
AuNS-PEG	108 ± 5	0.24 ± 0.01	-7 ± 2
AuNS-RBCM	144 ± 4	0.195 ± 0.01	-21 ± 2

Figure 5.2 Cryo TEM images of AuNS-PEG (A) and AuNS-RBCM (B), respectively. PEG and RBCM coating was pointed out by white arrows. C) Absorbance spectra of bare AuNS, AuNS-PEG and AuNS-RBCM respectively. D) Table of hydrodynamic size and zeta potential values of the samples.

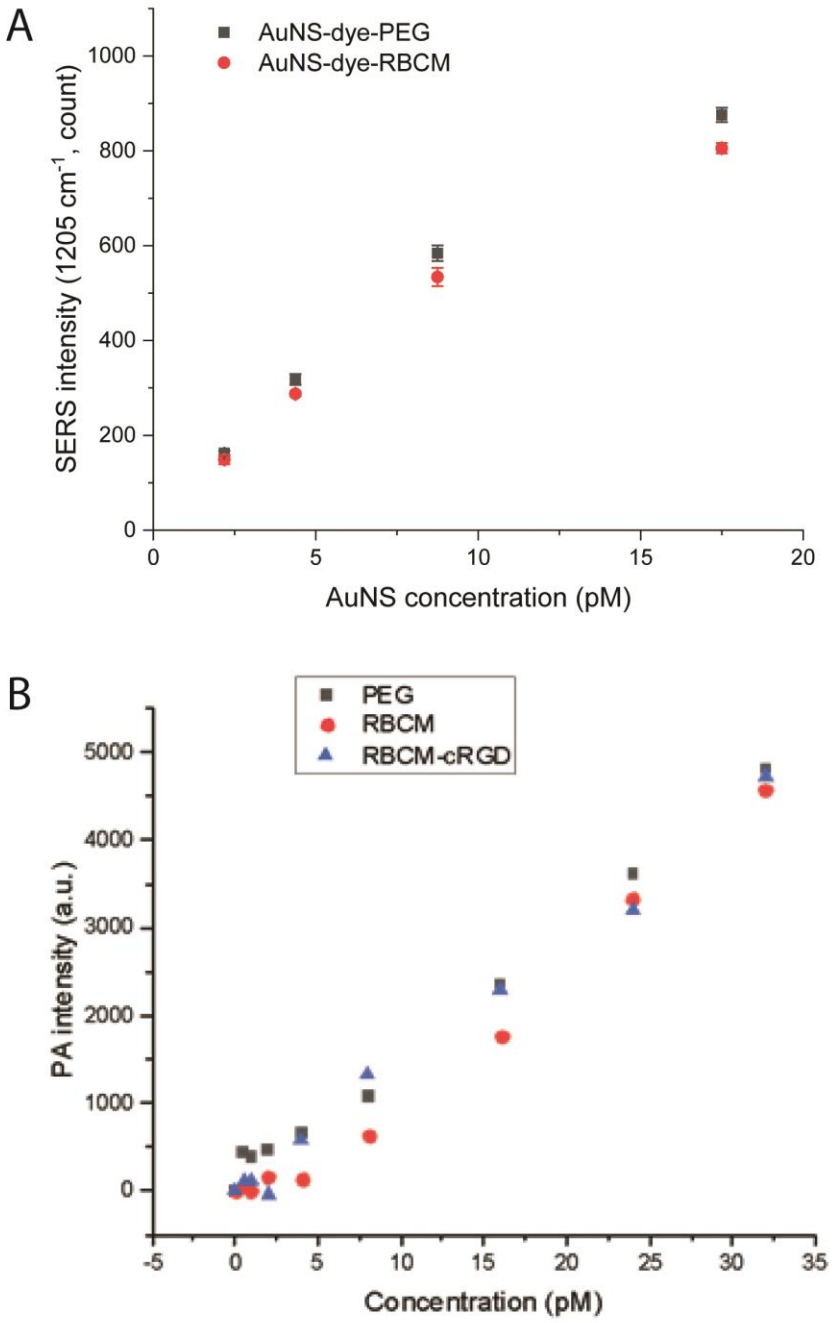

Figure 5.3 A) SERS intensity linearity versus AuNS concentration. B) PA intensity linearity versus AuNS concentration.

Then, to mimic the functionality as imaging agents for in-vivo tumor detection, a bovine tissue phantom experiment was conducted. Briefly, an artificial hole was dug on a piece of bovine tissue, then AuNS-RBCM solution mixed with gelatin were filled in the hole and formed gel phantom as temperature decreased to mimic the tumor tissue (Figure 5.4A). PA imaging was acquired from the other side of the tissue (that is, the AuNS gel was 4-5 mm beneath the tissue, as shown in Figure 5.4A). A laser fluence of 18 mJ/cm^2 was used for PA image scanning (which is below ANSI limit of laser exposure), and for each scan the samples were exposed to 1600 laser pulses. Figure 5.4Biii shows that the tumor phantoms were clearly observed in PA images. To make sure that the laser pulses do not melt the AuNPs during multiple pulses, the PA intensities of two continuous acquisitions were compared. No obvious intensity difference was observed between the two scans by comparing the PA intensity of the selected region of interest (ROI) (Figure 5.4D&E). These results indicates that the laser fluence intensity we used do not cause melting of the nanostars and can provide strong enough PA intensity for imaging. SERS measurement of the gels was also performed after PA imaging. The results showed that after multiple laser pulses, the SERS NPs still showed distinct Raman peaks at only 200-ms integration time (Figure S5.1). These results prove that the RBCM coated SERS NPs are excellent candidates for intraoperative PA-SERS dual-modality tumor imaging.

As a natural cell membrane, RBCM was reported to improve nanoparticle biocompatibility, reduce immune response and elongate blood circulation time. Here we tested the immune response of RBCM coated PA-SERS dual-modality agent by incubating Cy5 modified AuNS-RBCM with RAW 264.7 macrophage cell lines for 4 hours, then measuring macrophage uptake by flow cytometry. As shown in Figure 5.5, a much reduced macrophage uptake was shown in RBCM-coated NPs compared with PEGylated NPs.

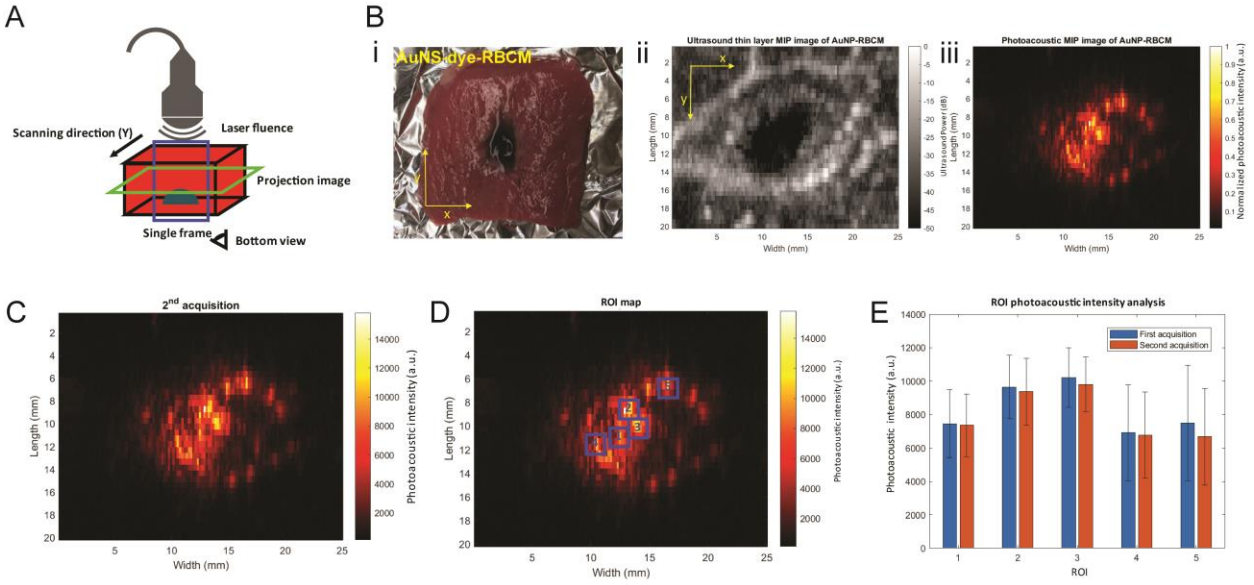

Figure 5.4 A) Schematic illustration of AuNP gel embedded bovine tissue and PA measurement setup. B) i) photos of the prepared gel embedded tissue samples; ii) Ultrasound thin layer maximum intensity projection (MIP) images; iii) photoacoustic MIP images; C) Repeated imaging scan of the AuNP-dye-RBCM gel in bovine tissue. D) Selected regions of interest (ROI) and E) photoacoustic intensity comparison at the ROI between the first and the second scan.

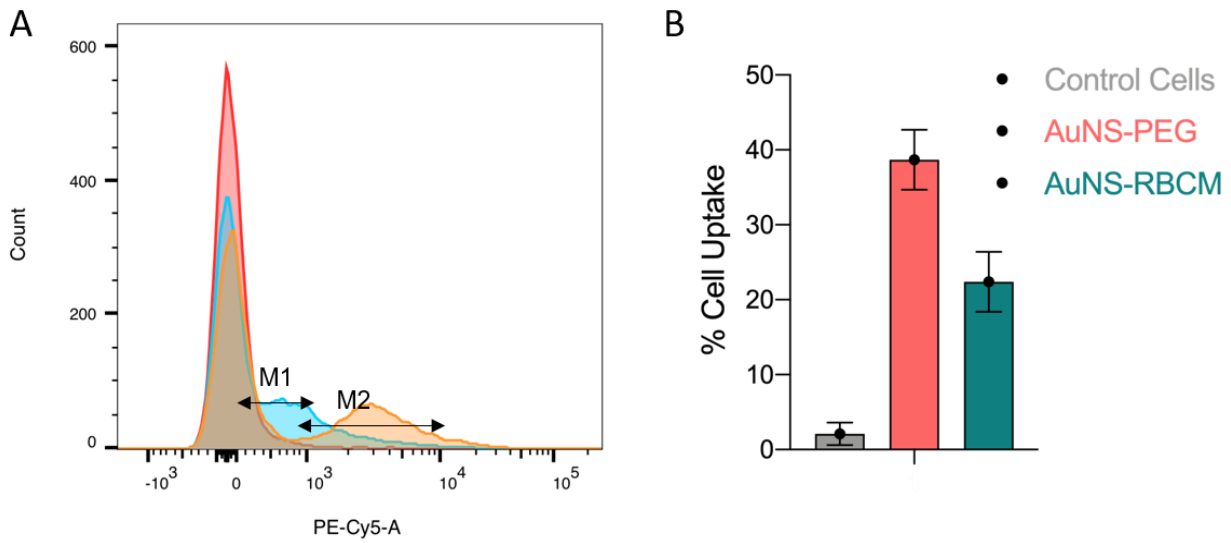

Figure 5.5 Reduced macrophage uptake by RBCM coating. A) Flow cytometry profile of control cells, AuNS-PEG and AuNS-RBCM in Cy5 channel. B) Percentage of cells that have AuNS uptake.

The RBCM-coated AuNS was then inserted with DSPE-PEG-cRGD to enable its targeting ability, using similar strategy that was discussed in Chapter 4. To test the function of the inserted cRGD, the cRGD functionalized NPs were then incubated with a high integrin expression cell line (4T1) and a low integrin expression cell line (PANC) for different time periods. The un-bounded AuNPs were then washed out, and the cell suspension was transferred to 96-well plate for SERS measurement. It shows that after 8-h incubation, the cRGD modified AuNS-RBCM showed around 2-folds higher uptake in respect with untargeted AuNS-RBCM by the tumor cells. Similar result was found from the photoacoustic measurement of the cells, where the PA intensity of the cell suspension incubated with cRGD modified AuNS-RBCM is roughly 2-folds of that incubated with AuNS-RBCM. The in-vitro results here proved the successful modification of cRGD peptide on RBCM coating via lipid insertion strategy, and the functionality of the inserted peptide.

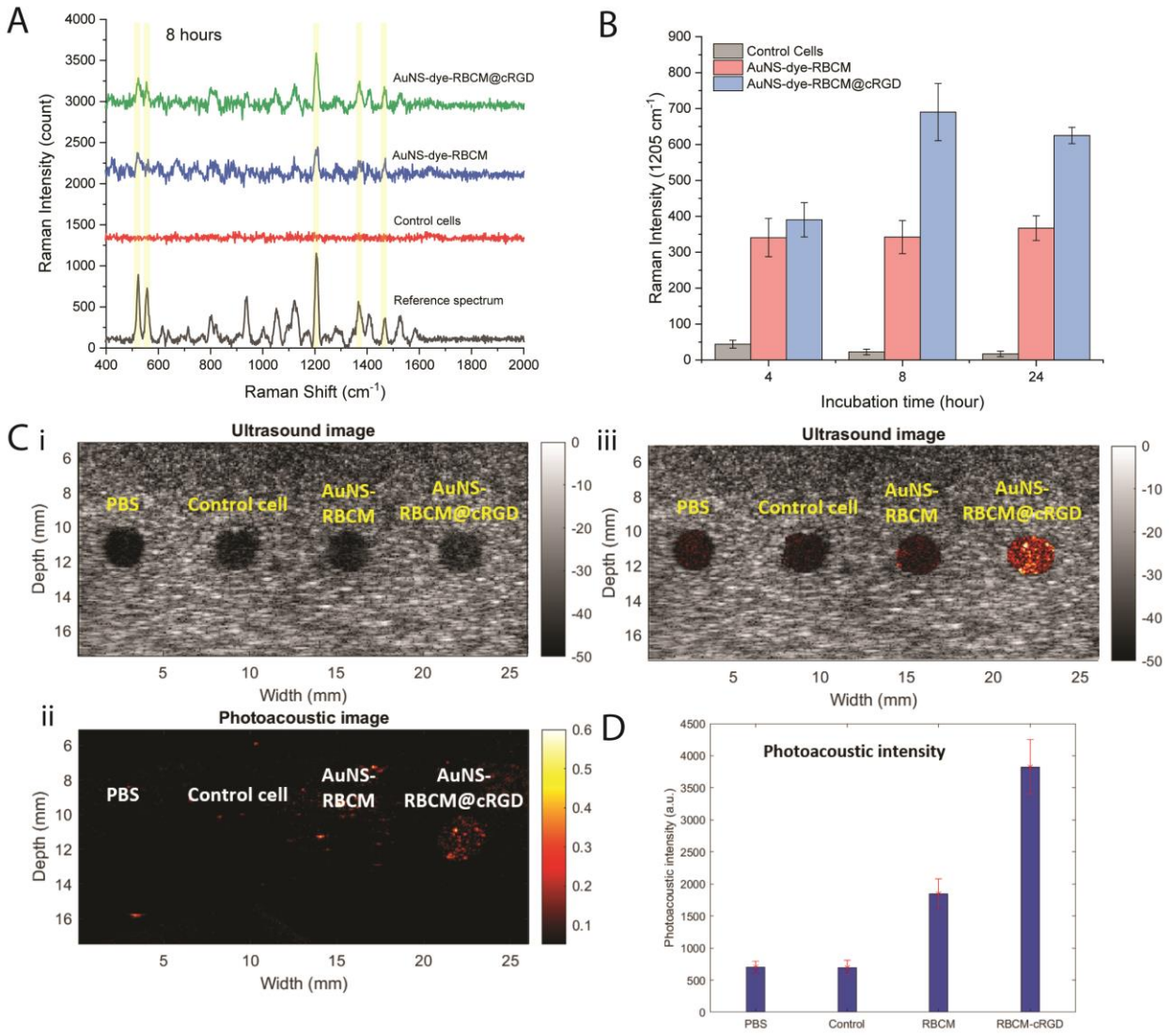

Figure 5.6 In-vitro study. A) SERS spectra of the cell suspension after washed out free AuNPs after 8-h incubation. Spectra measured at a cell concentration of 2 million/mL in 96-well plate, 5-second integration time, 200 mW. B) SERS intensity of 1205 cm^{-1} of the samples at 4, 8 and 24 hours incubation with 4T1 cells. C) PA measurement of the cell suspension incubated with AuNPs: i) ultrasound image, ii) photoacoustic image and iii) combined image of the gels. D) Photoacoustic intensity calculated from the PA image in (C).

As a dual-modality imaging agent of both photoacoustic imaging and SERS, the AuNS-RBCM need to first perform as PA image contrast for pre-operative tumor location, which requires tissue penetration depth of centimeter level, then as a SERS nanotag for intra-operative tumor margin detection and microscopic tumor detection, which requires penetration depth of 1-2 millimeters. We thus performed a systematic ex-vivo tissue penetration depth study of AuNS-RBCM using porcine tissues. The AuNS-RBCM solution was first mixed with gelatin and tumor cells to form a gelatin gel that mimics the tumor tissue targeted by the NPs (Figure 5.7Ai). The PA and SERS intensity of the pure gel were first measured at optimal measurement condition, then muscle and fat tissues of different thickness were covered on the gelatin gel to mimic deep-located tumor covered by natural biological tissues. Porcine tissues were carefully placed to avoid air bubbles between tissues or between tissue and the gel. PA and SERS intensity of the gel were then measured with different thickness of tissues (Figure 5.7A). The SERS signal of the gel drops fast with increased tissue thickness, with 1-mm of muscle the SERS signal is less than 10% of the original intensity. The tissue penetration of the gel was determined to be 2 mm for SERS, with a SNR calculated to be 6.4 (SNR $\geq$ 5) at this condition. For photoacoustic imaging, the gel covered by various thickness of tissue shows quite distinct PA intensity and spatial resolution until 4 mm of muscle. These results provide a quantitative penetration guidance of using the AuNS-RBCM as PA-SERS dual-modality imaging agents, indicating its strong potential as a preoperative and intraoperative tumor resection guidance.

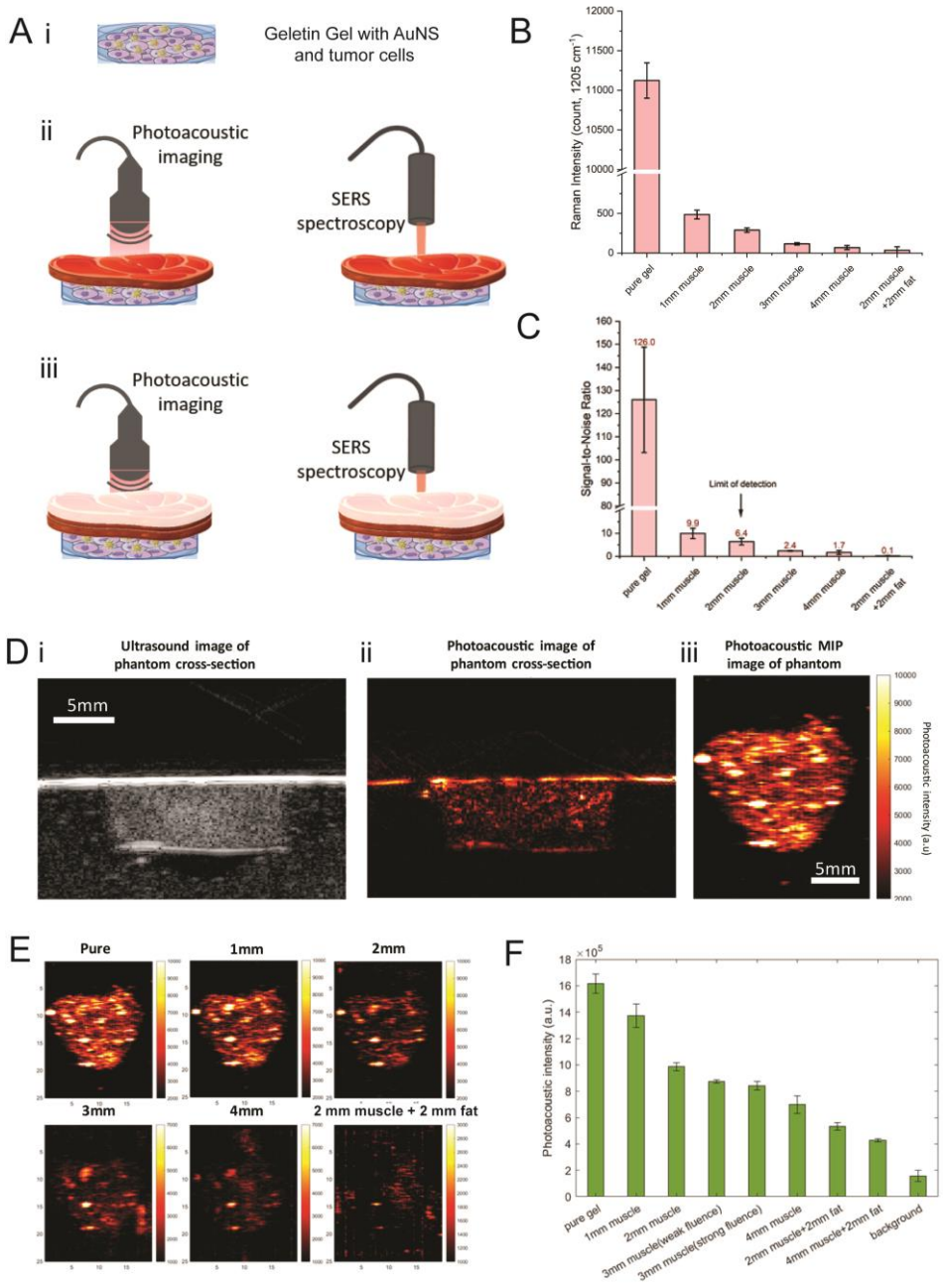

Figure 5.7 A) Schematic illustration of i) gelatin gel preparation with tumor cells and AuNS; ii) PA and SERS measurement of the gel with one type of tissue; iii) PA and SERS measurement of the gel with two types of tissue. B) Raman intensity of 1205 cm^{-1} peak of the gel with different thickness of tissues covered. C) Signal-to-noise ratio (SNR) of 1205 cm^{-1} peak of the gel with different thickness of tissues covered. D) i) ultrasound image, ii) photoacoustic image, and iii) the maximum intensity projection (MIP) image of that volume. E) The MIP image of different tissue slices stacking between tumor and transducer. F) PA intensity of (E).

5.4 Conclusion

In this chapter, we present a RBCM protected AuNS agents for dual-modality of SERS and PA imaging. The LSPR peak of the AuNS were tuned to NIR window to enable better tissue penetration depth for biological image. Resonant chromophore, IR-780, was encoded to the AuNS to induce resonant Raman scattering with additional enhancement. Natural red-blood-cell membrane was applied as protective coating of AuNS, which was shown to provide better biocompatibility by reducing macrophage uptake, and to realize target ligand conjugation by lipid-insertion strategy. An ex-vivo tissue tumor detection phantom study was then conducted to show the potential of RBCM-coated AuNSs as imaging agents for SERS-PA dual-modality. Our results show that AuNS-RBCM could be excellent candidates for intraoperative PA-SERS dual-modality tumor imaging.

5.5 Supplementary Figures

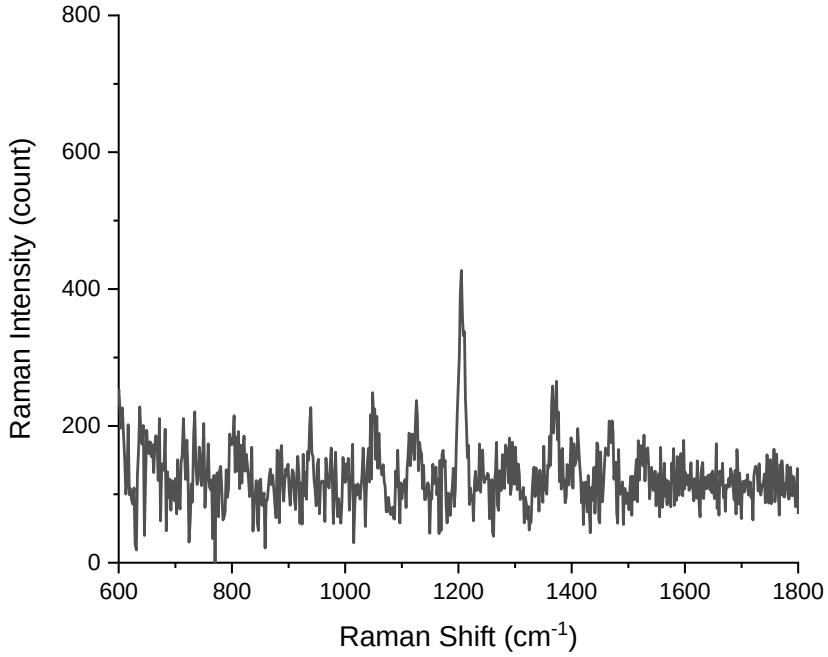

Supplementary Figure 5.1 SERS spectra of the embedded gel samples after laser pulses treatment and freeze-thawed.

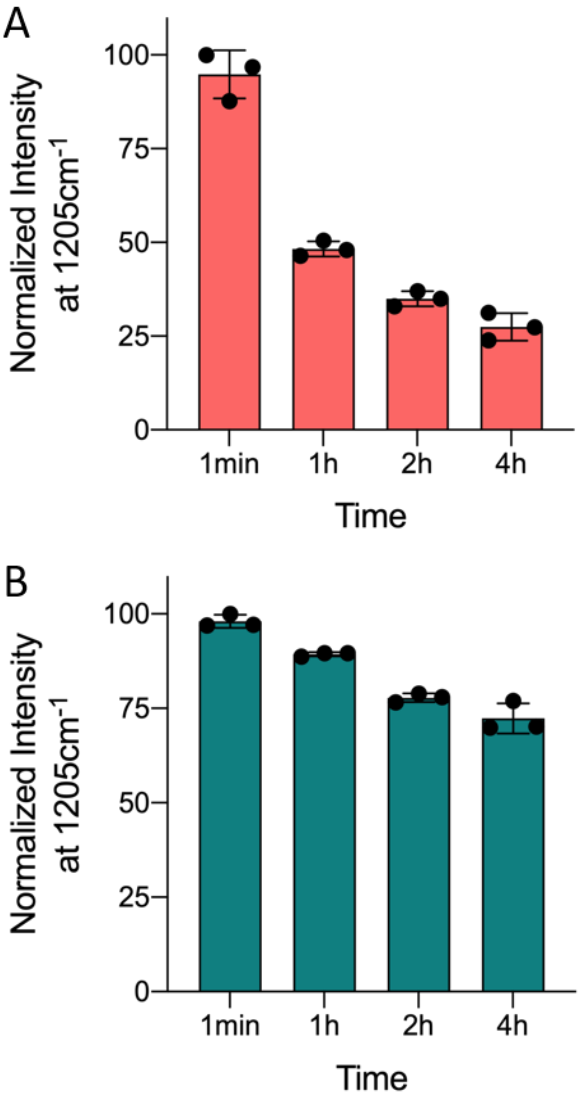

Supplementary Figure 5.2 SERS signal stability of AuNS-dye-PEG (A) and AuNS-dye-RBCM (B) in RPMI cell media.

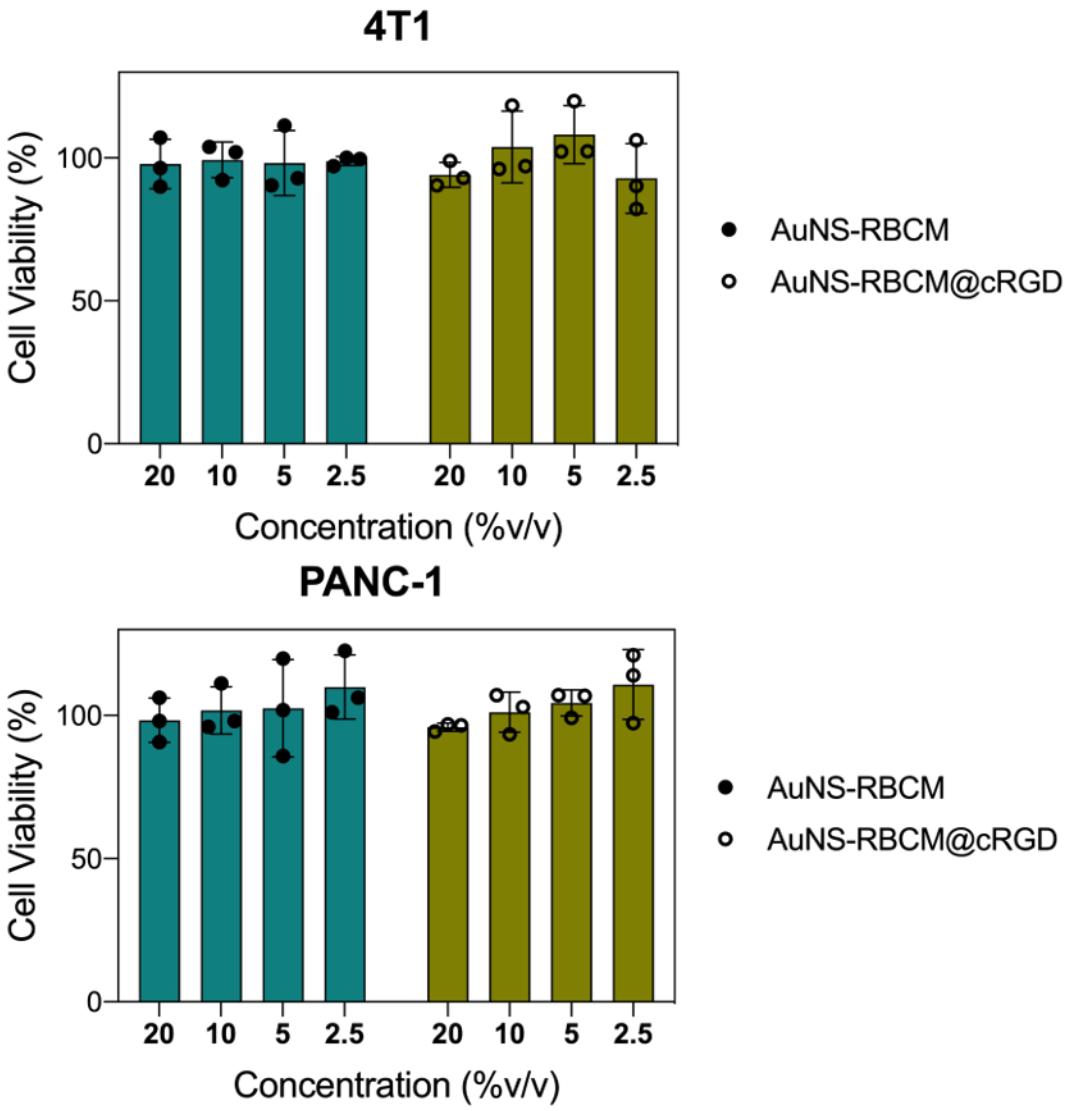

Supplementary Figure 5.3 MTT results of AuNS-RBCM and AuNS-RBCM@cRGD incubated with 4T1 and PANC-1 cell lines.

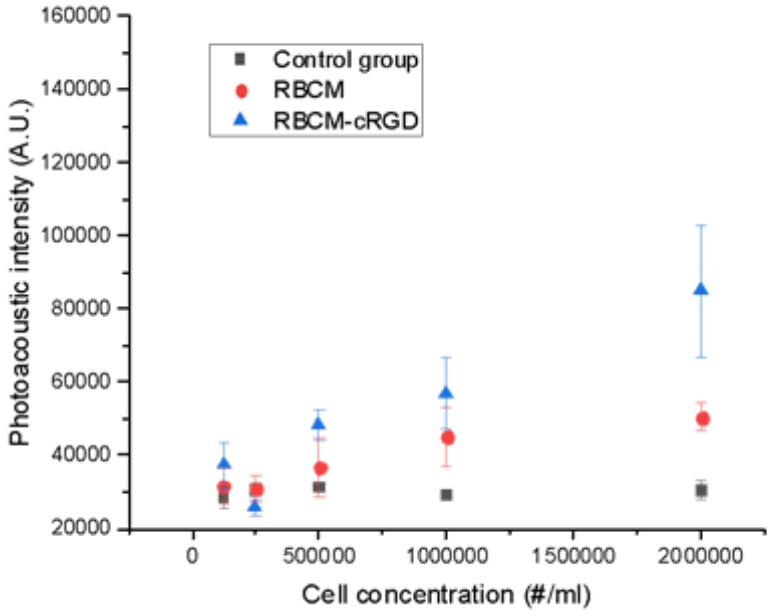

Supplementary Figure 5.4 4T1 cell with AuNS intakes cell concentration and PA sensitivity. For RBCM-cRGD coated group, the PA sensitivity at 8h: 1 million per mL.

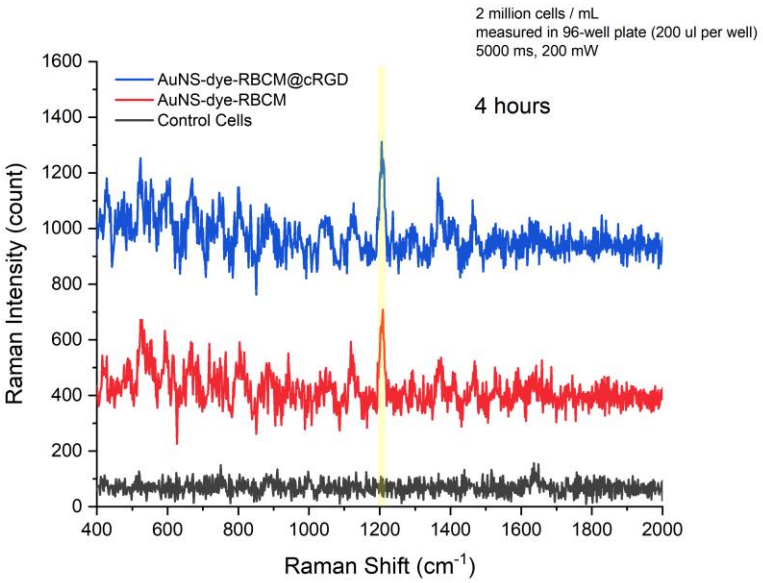

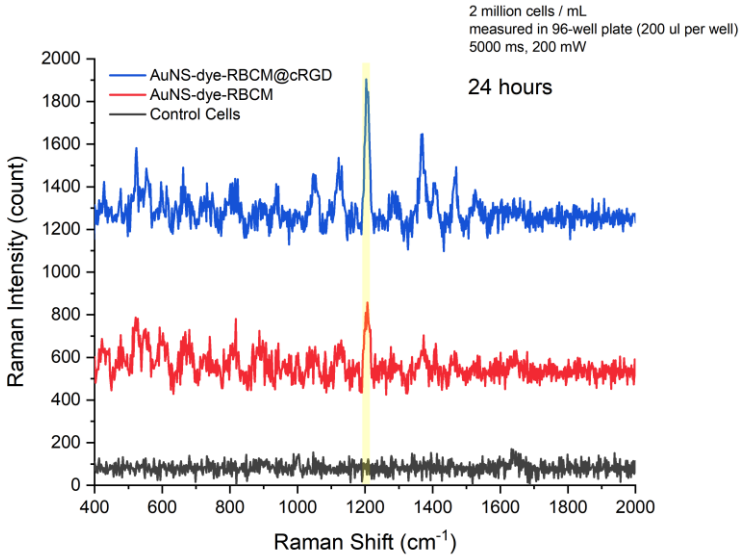

Supplementary Figure 5.5 SERS spectra of the cell suspension after washed out free AuNPs after 4h and 24h incubation. Spectra measured at a cell concentration of 2 million/mL in 96-well plate, 5-second integration time, 200 mW.

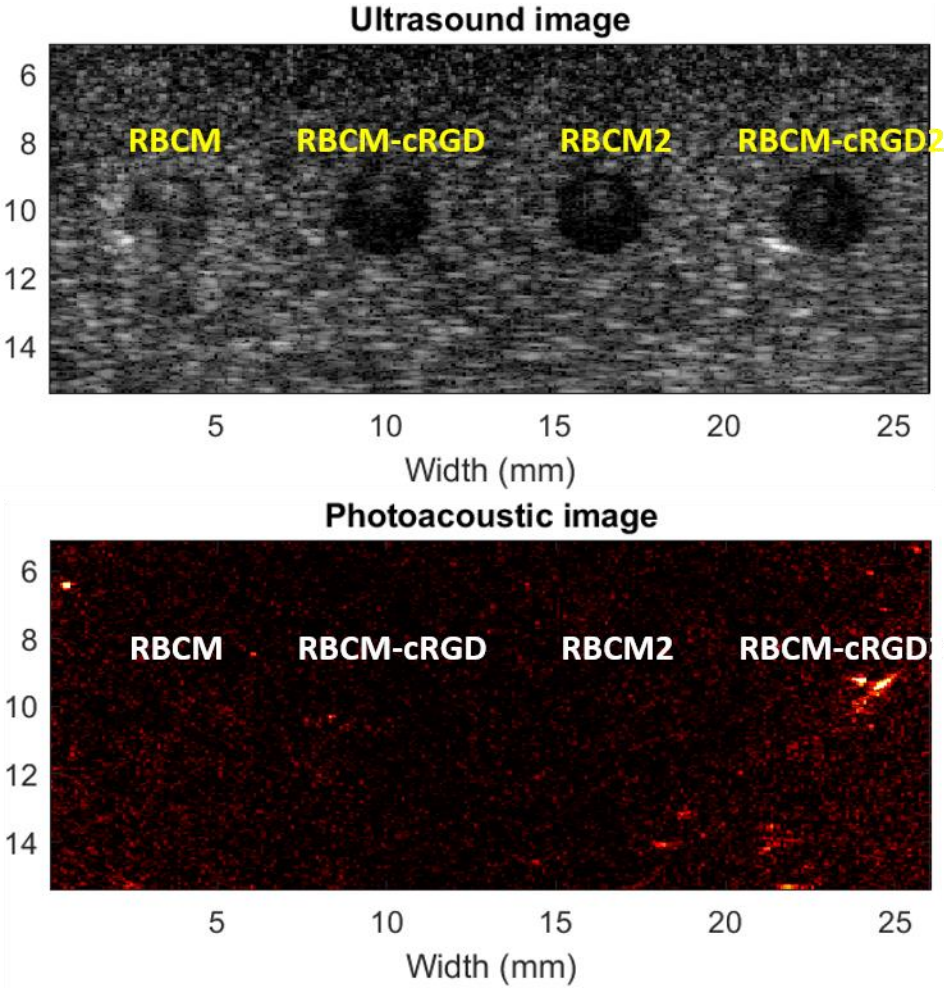

Supplementary Figure 5.6 PA measurement of the PANC-1 cell suspension incubated with AuNPs. Upper: ultrasound image; Lower: photoacoustic image.

CHAPTER 6: QUANTITATIVE SERS TISSUE PENETRATION STUDY AND NEXT-GENERATION NIR-II SERS NPS DESIGN

6.1 Introduction – Penetration Depth Limit of SERS

Remarkable advances of *in vivo* diagnostics and physiologic monitoring from biological studies to clinical applications has been witnessed at the near-infrared (NIR) window in recent decades, facilitating the field of intraoperative imaging and wearable spectroscopic devices [118, 178]. These techniques rely on the characteristic light propagation in turbid biological tissue to probe chemical information of either an endogenous biomarker or an exogenous agent [179]. With the use of imaging agents, the fluorescence and Raman spectroscopy provide favorable properties well suited for the spectroscopic bioimaging and detections. However, the *in vivo* bioimaging and detections are restricted to limited penetration depth of photons that are highly attenuated by tissue scattering and absorption [180] (Figure 6.1A). Many efforts have been made to circumvent this problem, including extending the excitation to longer wavelength [12, 59]. The widely applied traditional NIR window (NIR-I, 650-950 nm in wavelength) shows the reduced tissue scattering and absorption compared to the visible spectrum (400-700 nm in wavelength). Further reduction of photon scattering, absorption and autofluorescence is observed in the second NIR window (NIR-II, 1000-1700 nm in wavelength), which allows deeper tissue detection with improved signal-to-noise ratio (SNR), higher sensitivity and better spatial resolution [59] (Figure 6.1). The deep tissue fluorescence imaging has been excelled in the through-skull imaging on mice at the NIR-II window, and the penetration depth could be over 5 mm with good spatial resolution [181]. Similarly, the surface-enhanced Raman spectroscopy (SERS) was reported to detect objects buried in 1-4 mm thick tissues [12]. Combined with deep Raman techniques such as the spatial offset

Raman or the transmission Raman, an improved penetration of SERS have been achieved up to 2-5 centimeters [182-184]. Generally, high penetration in biological tissues is required for spectroscopic signals to achieve quality detection or imaging.

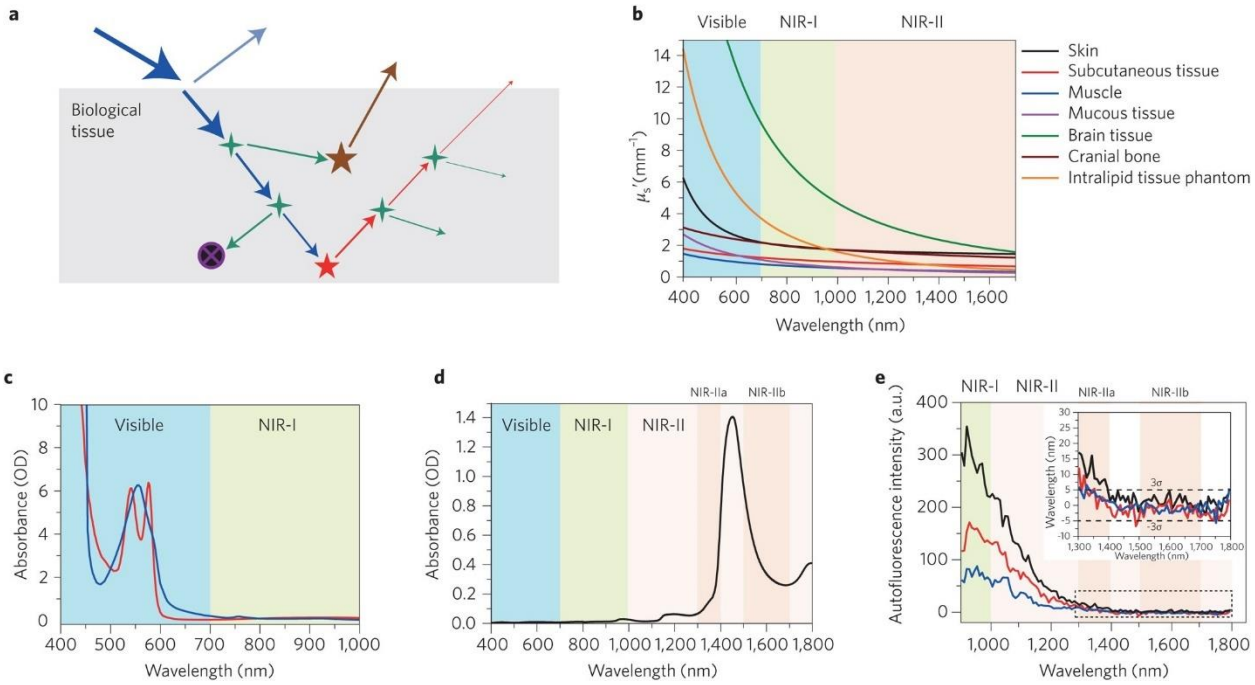

Figure 6.1 A) Light–tissue interactions resulting from impinging excitation light (blue). Interface reflection (cyan), scattering (green), absorption (black circle with purple cross) and autofluorescence (brown) all contribute to the loss of signal (fluorescence, red) and the gain of noise. B) Reduced scattering coefficients of different biological tissues and of intralipid scattering tissue phantom as a function of wavelength in the 400 – 1700 nm region, which covers the visible, NIR-I and NIR-II windows (blue, green and red shaded regions, respectively). They all show reduced scattering at longer wavelengths2. C) Absorption spectra of oxyhaemoglobin (red) and deoxyhaemoglobin (blue) through a 1-mm-long path in human blood2. D) Absorption spectrum of water through a 1-mm-long path. OD, optical density. E) Autofluorescence spectra of ex vivo mouse liver (black), spleen (red) and heart tissue (blue) under 808-nm excitation light, showing the absence of autofluorescence in the >1,500 nm NIR-II window123. Inset: Autofluorescence spectra at high wavelengths. The dashed lines denote the values at three standard deviations from the baseline. [179]

However, the idea of quantitative assessment of tissue penetration *ex vivo* is surprisingly underexplored with the lack of a standard definition and the benchmark setup of measurement. Here we present the concepts and a benchmark experimental procedure to quantitatively evaluate NIR tissue penetration *ex vivo* with the use of SERS. Raman spectroscopy is advantageous in quantitative studies with high photostability and characteristic fingerprint spectrum. SERS enhances the normal Raman intensity by 10^9-10^{14}, providing exceptional sensitivity and specificity. In this work, we put forward the concepts of quantitative tissue penetration by defining an effective signal based on the spectral SNR. A benchmark experimental procedure was presented and the agarose gels containing SERS nanoparticles (NPs) were adopted as signal sources. Before the assessment, the distance of laser probe to tissue is optimized to get better signals. Then the direct comparisons of signal penetration depths were compared with different measurement conditions and SERS gel intensities on porcine tissues. The highest penetration depths on muscle, fat, and skin were 6, 3, 3 mm, respectively. We further reveal the relationship between SNR of SERS gels and corresponding penetration depths, making it possible to predict the tissue penetration depth of other types of spectroscopic imaging agents. The wavelength-dependent tissue attenuations and background interferences were compared between NIR-I (785 nm) and NIR-II (1064 nm). The SNR attenuation through 1 mm of tissue decreased at the NIR-II window by 18% on muscle, 7% on fat, and 17% on skin. The highly reduced tissue background interference at 1064 nm further demonstrates the superiority of NIR-II deep tissue bioimaging applications. This work provides the general criteria to quantitatively evaluate tissue penetration, offering valuable foundational information for the design and implementation of spectroscopic in vivo imaging and wearable devices.

On the other hand, with the understanding of the superiority of NIR-II window, the development of NIR-II SERS NPs is attracting increasing attention. An ideal NIR-II SERS NP should have strong resonance at NIR-II window, while keeping their size below 100 nm to maintain good in-vivo performance. Colloidal gold nanostructures with a variety of sizes and shapes offer a broad degree of freedom for tuning the plasmonic bands to the NIR-II region [117]. For example, gold star structures with a LSPR band that covers both the NIR-I and NIR-II were reported, where their multiple sharp branches serve as hotspots for electromagnetic Raman enhancement [31, 32]. However, AuNS structure with such sharp tips is rarely seen in literatures as the high-curvature tip geometry is not energy-favorable, and easily turns round with time [185, 186]. Hollow gold nanocages or nanoshells are another type of plamonic nanostructures that can be tuned to NIR-II region, but the synthesis steps are often very complicated and time-consuming [40, 187]. Besides, the commonly used galvanic replacement process in the synthesis of this kind of AuNP is not friendly to physically attached chromophore Raman reporters [188, 189]. Therefore, in the second part of this chapter, we discuss the synthesis and stabilization of NIR-II resonant SERS NP for improved tissue penetration depth by MUA-PEG coating.

6.2 Experiment Section

Materials. All chemicals were used as received without any further purification. Cetyltrimethylammonium chloride (CTAC, ≥ 99.0%), sodium borohydride ($NaBH_4$, 98%), chloroauric acid tetrahydrate ($HAuCl_4 \cdot 4H_2O$), 4-nitrobenzenethiol (4-NBT), L-ascorbic acid, 11-mercaptoundecanoic acid (MUA, 95%), diethyl ether (≥ 99.7%), Dimethylformamide (DMF), sodium citrate, 5k poly(ethylene glycol) methyl ether (mPEG, Mn 5000 Da), 4-[2-[2-Chloro-3-[(2,6-diphenyl-4H-thiopyran-4-ylidene)ethylidene]-1-cyclohexen-1-yl]ethenyl]-2,6-

diphenylthiopyrylium tetrafluoroborate (IR-1061, dye content 80%), bovine serum albumin (BSA), dimethyl sulfoxide (DMSO), phosphate-buffered saline (PBS) and ascorbic acid were purchased from Sigma-Aldrich. Phosphate-buffered saline (PBS) was purchased from Corning. Silver nitrate ($AgNO_3$, 99.8%) was purchased from Aladdin (China). Poly (ethylene glycol) methyl ether thiol (mPEG thiol, Mn 5000 Da) from Laysan Bio Inc. Agarose was purchased from Fisher Scientific. De-ionized water was used in all experiments.

Preparation of SERS nanoparticles. The core-shell SERS NPs are synthesized using our reported method [36]. Basically, the Au NPs for 785 nm excitation is synthesized by preparing 20 nm Au core (1 nM) firstly using a seed-mediated method. [37] Then 500 μL of 4-NBT ethanol solution (10 mM) is mixed with 10 mL of Au core colloids under vigorous sonication. After 0.5 h, the colloids are centrifuged and washed with CTAC aqueous solution (50 mM) to remove excess NBT molecules. Then 1 mL of 4-NBT modified core are added into the mixture of 16 mL of CTAC solution (50 mM), 480 μL of ascorbic acid (40 mM), and 960 μL of $HAuCl_4$ (4.86 mM). The products are collected after the 10-min reaction.

The Au/Ag NPs for 785/1064 nm excitation is further synthesized by coating Ag layers on as-synthesized Au NPs [190]. 10 mL of Au NPs are incubated with 300 μL of 4-NBT molecules (10 mM) for 0.5 h, then washed three times and concentrated to 2 nM. For the formation of the Ag shell, 0.05 mL of $AgNO_3$ (5.832 mM), 0.1 mL as-synthesized NPs (2 nM) and 25 μL of ascorbic acid (0.6 M) are added into the 2 mL of CTAC solution (50 mM). The colloids are kept at 70 °C for 3 h, then collected by three rounds of wash and dispersed in CTAC solution (50 mM). Both products are characterized by the UV-Vis spectrometer, and the transmission electron microscopy (TEM) images are acquired with a JME-2100F transmission electron microscope (JEOL, Japan).

Preparation of SERS gels. For the preparation of SERS gels, the obtained SERS NP colloids are washed by water twice to remove excess stabilizer, then redispersed in water with a concentration of 3 nM. Agarose aqueous solution (1 wt %) is heated up until the agarose is completely dissolved and the turbid solution turns clear. Then different volumes of agarose solution are mixed with SERS NP colloids to get a final NP concentration of 1 nM, 300 pM, 100 pM, 30 pM and 10 pM, respectively. The slight shaking and swirling are applied to ensure that the NPs are well dispersed. Then 3 mL of mixtures are quickly transferred into the wells of a 12-well plate. Let sit at room temperature for 1 h, until the agarose gel has cooled down and completely solidified. The SERS gel is obtained with a thickness of around 1 cm.

Ex vivo porcine tissues. The fresh *ex vivo* porcine tissues are purchased from grocery stores and frozen before use. Three types of tissues are used, i.e. muscle, skin and fat. Specifically, the pork tenderloin is chosen for muscle samples, and side pork for skin and fat samples. The skin samples are composed of ~1 mm skin layers and subcutaneous fat layers. A meat slicer is applied to cut the frozen tissues into thin layers with different thicknesses. The length and width of tissues are over 3 cm to fully cover the SERS gel. A vernier caliper is adopted to measure the thickness of each slice. Considering the softness of tissue samples, a 5-10% deviation in thickness is acceptable.

Experimental settings and Raman penetration depth measurement. The 785/1064 dual-mode hand-held Raman spectrometer (Bayspec Inc., USA) and its matching optical XYZ-linear stage are applied. The spectral resolution is ~2 cm^{-1} for 785 nm and ~11 cm^{-1} for 1064 nm measurement. The laser spot is 150 μm in diameter. Its focal length and focal depth was measured via a reported method as follows [191]: a silicon wafer was placed on the stage platform, then sequential acquisition of Raman spectra was performed when keeping the laser probe stationary and moving the platform up and down vertically with a step of 0.2 mm. The intensity of 520 cm^{-1} mode of the

silicon wafer was used to calculate the SNR. The plotted SNR-distance profile was a curve of Gaussian distribution with a decrease in both sides of the ideally focal plane (Figure S6.2, Right). The focal length of laser beam, where the SNR reached highest, was 6.80 mm. The focal depth, defined as an effective layer of the same area as SNR-distance profile (marked by the dashed rectangle), was calculated to be 1.22 mm.

For the Raman penetration depth measurement, the laser probe was fixed on top of the stage, and the SERS gel was placed on the glass substrate at the stage platform. Porcine tissues were put above the SERS gel and fully cover it, ensuring no air bubble in-betweens. The spectra were recorded at the best focus position.

The raw spectra are processed to remove the non-Raman background using a wavelet transform algorithm [192]. The Raman intensities of SERS gel signal (1338 cm^{-1}) are calculated by averaging the data in the region of 1337-1442 cm^{-1}; while the noise is calculated as the standard deviation in the region of 1950-2050 cm^{-1}.

Hydrophobic domain PEG ligand synthesis. Synthesis of MUA-PEG ligand follows the method outlined in Schultz et al [84]. In brief, 11-mercaptoundecanoic acid (MUA) and mPEG (5k Da) was mixed in 3:1 molar ratio in a round-bottom flask and kept under vacuum at 110 ℃ for 1 hour. Then the temperature was ramped up to 160 ℃ under N_2 atmosphere with a reflux condenser and kept for 72 hours. The unreacted MUA was removed by multiple washings of cold diethyl ether.

Synthesis of NIR-II SERS NPs. Glassware and stir bars for gold nanoparticle synthesis were washed by aqua regia before use. NIR-II AuNSs were synthesized using a seed-mediated method [87]. First, 15-nm small AuNPs were synthesized as the seed. A water solution of 2.2 mM sodium citrate (60 mL) was heated to boiling under vigorous stirring. Once boiling had commenced, 400 μL of $HAuCl_4$ solution (25 mM) was quickly injected. The reaction completed within 10 min where the

solution turned from yellow to purple grey and then to burgundy. The resulted solution was centrifuged 3 times and stored as Au seed for the next step. For NIR-II AuNSs synthesis, to 30 mL $HAuCl_4$ solution (0.25 mM) in a 50-ml centrifuge tube, 30 μL of 1N HCl and 2100 μL of 15-nm citrate gold seeds were added followed by simultaneous addition of 300 μL $AgNO_3$ solution (4 mM) and 300 μL of ascorbic acid solution (100 mM) under moderate stirring (600 rpm). The reaction was performed at room temperature, and the process was completed in less than 2 min with the solution turning from light yellow to dark grey. Raman reporter molecules IR-1061 stock solutions were prepared by dissolving 1 mg of the dye molecules into 1 mL of DMF. The stock solutions were diluted by DI water to form a dye concentration of 2.62 μM for fresh use. Before adding dye to the as-synthesized NIR-II AuNS, a 1% Pluronic® F-127 solution was first added to the system to a final concentration of 0.1% to avoid aggregation during dye addition. Typically, 3 mL above dye molecule solution was dropwise added to NIR-II AuNS under moderate stir. After 10 min incubation with reporter molecules, 5 mL SH-PEG or MUA-PEG solution (51.8 μM) was dropwise added to the AuNS@dye solution. The solution was incubated at room temperature for 1 hour, then the SERS nanoparticles were washed twice by centrifugation at 1000g to remove excess PEG and dye molecules.

6.3 Results and discussion

6.3.1 Quantitative SERS tissue penetration study

6.3.1.1 Definition and experiment setup design

A through-tissue detection is made *via* two steps: (1) penetration of incident radiation by a propagation distance to excite the Raman-active nanomaterials; and (2) diffusion of scattered Raman photons through the same distance again to be collected by the probe. The optical

information is attenuated in two ways of both incident irradiations transmitting outside-in and emission inside-out (Figure 6.2A). Therefore, we define the penetration depth as the largest thickness of tissue with which an effective signal from signal source embedded in tissues can be detected. The measurement setup is shown in Figure 6.2B. The SERS gel is served as the source of Raman signal, placed on a glass substrate, and covered by a layer of biological tissue. The handheld laser probe of a Raman spectrometer is utilized to excite and collect SERS signals from the top. As depicted in Figure 6.2C, each Raman spectrum is firstly processed by a baseline correction to remove the fluorescence background while preserving characteristic Raman peaks from the SERS gel and the tissue. The signal intensity is calculated by the difference between the maximum value of the peak and the baseline, while the noise is the standard deviation of the spectrum in a region without any specific Raman peaks. An effective Raman signal is defined based on the spectral SNR. When a Raman spectrum has the SNR:

$$SNR = \frac{I_{signal}}{\sigma_{noise}} \geq 3 \qquad \text{(Equation 6.1)}$$

,it indicates with >99.7% confidence level that this spectrum is an effective signal instead of a random noise. Consequently, the penetration depth in this study is determined as the largest thickness of tissue with which on top an effective Raman signal with the SNR of ≥3 is detected from the tissue-covered SERS gel.

The SERS gels, served as tissue phantoms and Raman signal sources, are prepared using the agarose gels containing SERS NPs (Figure 6.2D). The inset photographs in Figure 6.2C shows gels with the SERS NP concentration of 10 pM to 1 nM. In this way, we are able to obtain the Raman-active material in a solid state while maintaining the uniform dispersion of SERS NPs. The guaranteed linear correlation between NP concentration and Raman intensity provides excellent signal reproducibility for our evaluations. Two types of SERS NPs are adopted in this work. One

type is the Au NPs with a core, a petal-like shell and a Raman molecule layer in between (Figure 6.2E, i) [72]. The other type is fabricated by further coating the above NP by a second Raman molecule layer and a silver (Ag) layer, forming a bimetallic NP with the smooth surface (Figure 6.2E, ii). For clarity, the two types of SERS NPs are named as Au NP and Au/Ag NP. The Au NP shows favorable Raman performance at 785 nm excitation and are used for NIR-I penetration assessments in our studies. The Ag coating enhances the SERS intensity of NPs at the off-resonance situation, improving the Raman performance at the NIR-II window [193]. Therefore, the Au/Ag NP is applied for the comparative measurements between NIR-I and NIR-II excitation. In Figure 6.2E, the UV-Vis spectrum of Au NP and Au/Ag NP were shown. The Raman molecule 4-nitrobenzenethiol (4-NBT) is used in both NPs (Figure 6.2F). The strongest peak of SERS gel at 1338 cm^{-1} is chosen as the signal peak for intensity read-out (I_{1338}), calculated as the averaged intensity in the range of 1335-1341 cm^{-1}. The noise is calculated as the standard deviations in the region of 1950-2050 cm^{-1}. The Raman spectra of muscle, skin and fat tissues are also shown in Figure 6.2F, indicating that the peak at 1338 cm^{-1} of SERS gel is distinguishable from that of the tissues. For a mixed Raman signal collected from the SERS gels and tissues, a simple subtraction of tissue contributions is conducted to extract a real value of I_{1338} from the mixed spectrum.

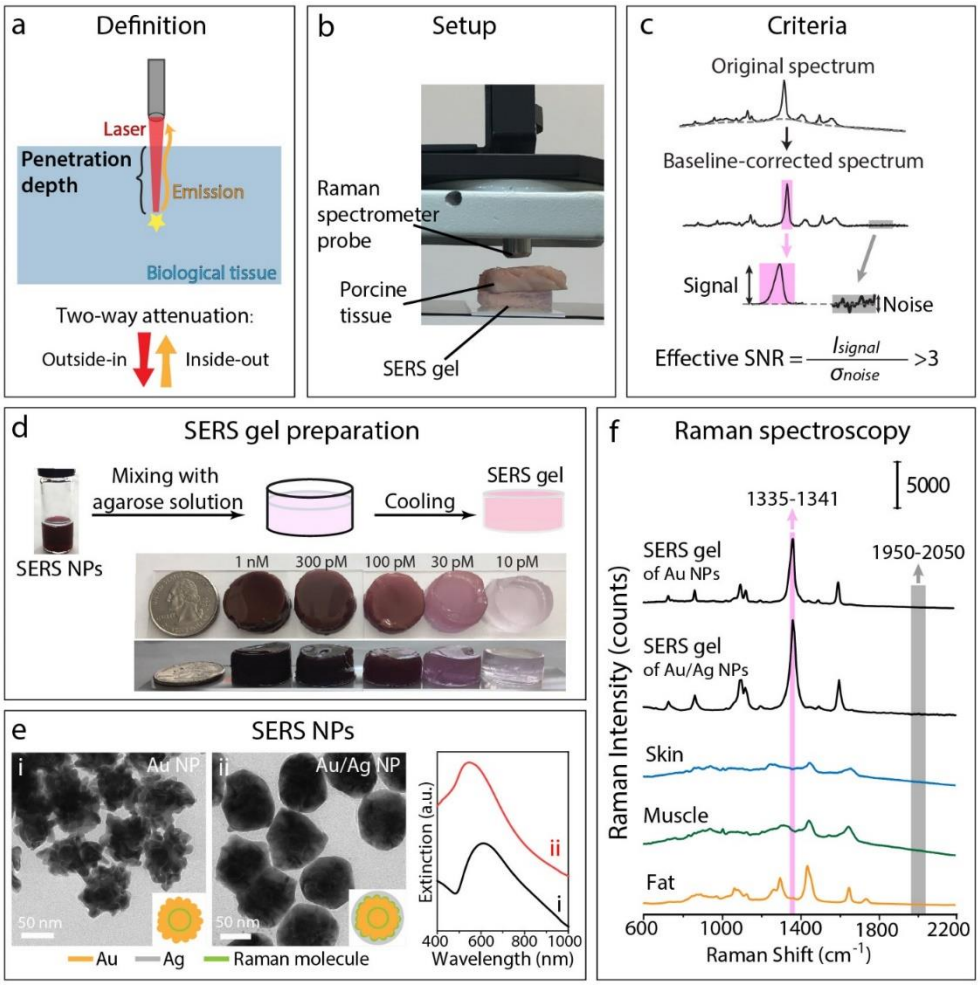

Figure 6.2 Scheme of the definition, setup, data analysis, nanomaterial preparation and Raman characterization of SERS nanomaterials for the penetration depth measurement. (A) The definition of penetration depth. (B) The experimental setup benchmarks. (C) The criteria for an effective spectral SNR. (D) SERS gel preparation process. The inset photographs show the SERS gels with Au NP concentrations of 1 nM, 300pM, 100 pM, 30 pM, and 10 pM. (E) TEM images and UV-vis spectra of SERS NPs: (i) Au NPs for measurements under 785 nm excitation, (ii) Au/Ag NPs for measurements under 785/1064 nm. The insets in TEM images show the schematic structures of NPs. (F) Raman spectra of the SERS gels and biological tissues under 785 nm excitation, measured with 100 mW and 5 s integration time.

6.3.1.2 Optimization in the focal plane for Raman measurements on tissues

Due to reflection, scattering, absorption, and auto-fluorescence during light propagation within tissues (Figure S6.1), when the laser excitation on an imaging tracer gel is blocked by tissue samples, a dramatic decrease in the collected signal is induced as well as a shift of laser beam focus spot. Therefore, prior to the penetration depth measurement, an optimization of the focal plane at 785 nm excitation is performed. The procedure consists of sequential acquisitions of Raman spectra on tissue-covered SERS gels while moving the optical stage in *z*-direction (Figure S6.1B). The SERS gel contains 1 nM Au NPs. The tissue is from 1 to 6 mm in thickness and the SERS gel is ~1 cm. When the interface between SERS gel and tissue is placed at the focal plane of the laser probe, *z* is defined as zero (Figure S6.1C); when the interface moves up or down vertically, *z* becomes negative or positive, respectively. The focal length and focal depth of the laser beam is estimated to be 6.80 and 1.22 mm by silicon wafer (Figure S6.2). If we assume that the focal length of laser beam stays the same and neglect the light distortion in tissues, the negative *z* values mean that the laser focus being in the tissues, and the positive ones mean that in the gels.

The pure SERS gel was firstly measured to determine its best focal plane. As shown in Figure S6.1D, the optimal focus position turned out to be 2 mm under the gel surface (when *z* equals to -2). This coincided with our common sense that the best focus of a laser beam is usually beneath the material surface. Next, we put muscle, fat and skin tissues with different thicknesses on top of the gel. A suitable measurement condition is considered that the integration time and power should be adequate to get a detectable signal, but not too high to induce overheating or damaging sample. Herein, 10 s integration time and 200 mW laser power were adopted. With 1 mm of muscle tissue on top, the *z* value of the maximum signal shifted to -0.18, appearing to be very close to the gel-tissue interface. When the muscle became thicker to be 1.5, 2, 3, 4, 5 and 6

mm, the optimal *z* values became -0.008, +0.452, +1.402, +2.452, +4.298 and +5.188, respectively. If the focal length of laser beam remains the same, these positive *z* values may indicate that the laser focus has moved into the muscle tissue, above the gel surface. Similar results were observed for fat and skin (Figure S6.1F and S6.1G). When 1 mm of fat tissue was placed between laser and gel, the maximum signal was obtained at the *z* value of -0.438, which means the focus spot was slightly underneath the gel surface. With 1.5, 2 and 3 mm of fat tissues, the *z* value became -0.197, +0.78 and +2.238, respectively. For 1 mm of skin tissues, the optimal *z* value was -0.408. And a shift in the *z* value was seen to +0.181, +1.198 and +2.566, when the thickness increased to 1.5, 2 and 3 mm, respectively. The data for fat and skin of more than 3 mm in thickness were not shown since their SNR decreased dramatically, making it hard to trace the best focus positions. These optimization measurements were repeatedly conducted for at least 3 times on different batches of tissues and SERS gels. Although the SNR values were not the same for each batch due to the experimental errors in slicing and measuring tissue thickness, we obtained similar SNR-*z* profiles and *z* values for each test, proving the reliability of the measurements.

Some interesting conclusions arises from these results. First, when a tissue is added on the signal source, the laser probe should consequently move up to obtain better signals. Second, although signals tend to decrease when the laser focus moved away from the ideal focal plane, the SNR measured on thinner tissues at a slightly defocusing position is still higher than that on thicker tissues at the best focal plane. This phenomenon is observed on three types of tissues, indicating that tissue diffusion plays a more decisive role in attenuating optical information than the defocusing of the laser beam. Third, the offset between the ideal focal plane and SERS gel surface can be as much as several millimeters. This provides a reference for the *in vivo* intraoperative

spectroscopic detection that when an effective signal is detected, the real locations of lesions can be millimeters away, deep in the tissues.

The quantitative penetration assessments were investigated on three types of porcine tissues (muscle, fat and skin) at the NIR-I window (785 nm). We studied three factors that affects the SNR, i.e., measurement conditions (laser power and integration time), signal source intensities and tissue properties. All the Raman spectra were measured at the best focal planes.

Measurements were firstly performed using a laser power of 5, 10, 50, 100, 200 mW with 10 s integration time on the SERS gel with 1 nM Au NPs (Figure 6.3A, top panel). The SNR attenuation in tissues fitted well with exponential decay curves. The calculated penetration depths were all shown in Table S1. The highest penetration was obtained using 200 mW, which were 6, 3, 3 mm for muscle, fat, skin. For comparison, when using a laser power of 5 mW, the penetration depth dropped to 3, 1, 1.5 mm respectively. We plotted the SNR data versus laser power (Figure S6.3) and found the curve fitting well with the growth model, confirming that the SNR increases with a higher laser power. The extension of integration time also played an important role in improving signal penetration. We measured the SNR with a shorter integration time (1 s) at different laser powers (Figure S6.4). When using 200 mW, the penetration depth was 4, 1, 1 mm for muscle, fat, and skin. As for that with 1 s and 5 mW, the penetration dropped to less than 1 mm for all types of tissues. The impacts of measurement conditions can be well explained that the increase in either the laser power or integration time helps reducing the background shot noises, leading to a better SNR.

We then conducted the comparison on the signal source intensities using SERS gels with Au NP concentrations of 1 nM, 300 pM, 100 pM, 30 pM and 10 pM, with 200 mW and 10 s integration time (Figure 6.3B, top panel). The SNR attenuation also showed an exponential decay

in tissues. Higher SNR was obtained with brighter SERS gels. The lowest penetration depth using 10 pM gel was 3, 1, 1 mm for muscle, fat and skin, respectively. In all measurements we observed the tissue-dependent penetration performance, which is due to the intrinsic optical properties of each type of tissues. Generally, skin and fat have higher absorption and scattering coefficients than muscle, since the optical properties of muscle are mainly defined by hemoglobin and water; while fat and skin are more complex with additional lipid molecules; also, skin contains melanin in its epidermis that is of high scattering [194, 195]. The higher absorption and scattering in skin and fat tissue reduce the number of photons reaching the embedded SERS gels at a deeper distance.

We further revealed the relationship between SERS gel SNR and the corresponding penetration depth (Figure 6.3C). The x-axis is the measured SNR of pure SERS gel without being covered by tissues, and the y-axis is the penetration depth measured on tissue using the same power and integration time as measuring the SERS gel. For all three types of tissues, an improved penetration was observed with brighter SERS gel. The clear correlations indicate that the penetration depths are determined by the SNR of source signals, opening the possibility to predict the penetration performance for other types of spectroscopic agents. For instance, one could estimate the concentration of SERS NPs targeting to the tumor site *in vivo*, and then simply measure the SNR of NP colloids with the same NP concentrations *in vitro*, to expect the maximum thickness of tissues around tumors through which the signals from NPs can be detected. Similarly, if one intends to get an effective signal from the tumor site buried by 1 mm fat or 2 mm muscle, then he or she could presume according to this figure that the original SNR from the imaging nanoagents designed for tumor targeting must be over 500 or 850, respectively. This result provides valuable information to benefit the design and evaluation of *in vivo* imaging studies and intraoperative spectroscopic detection on patients.

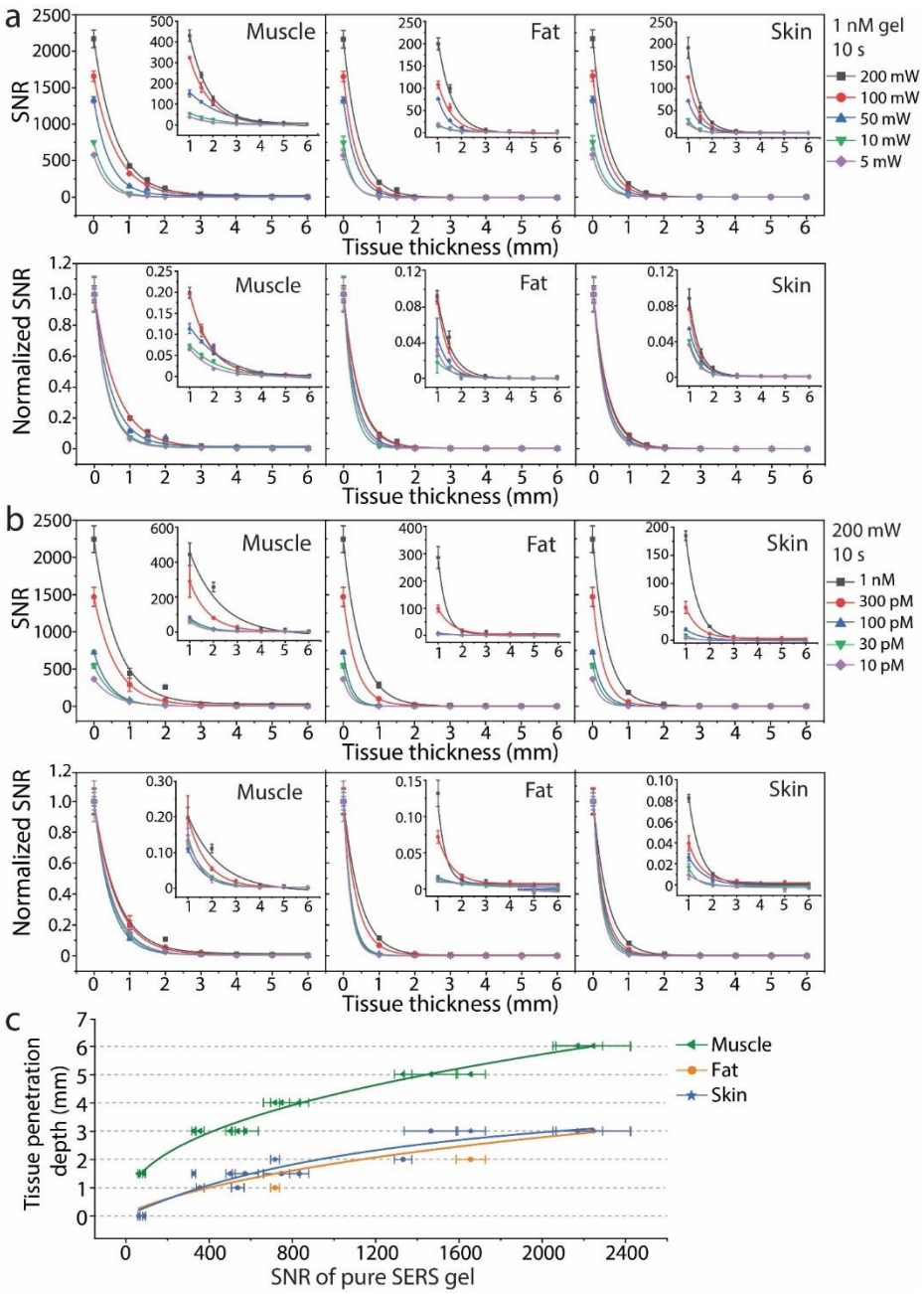

Figure 6.3 Comparison of excitation powers and SERS gel brightness for Raman penetration depth measurements under 785 nm excitation. (A) Power dependent SNR (top) and normalized SNR (bottom) measured using different powers and 10 s integration time, on the SERS gel of 1 nM NP. The powers are 5, 10, 50, 100, 200 mW. (B) Gel brightness dependent SNR (top) and normalized SNR (bottom) measured on SERS gels of different NP concentrations with 200 mW power and 10 s integration time. The NP concentrations are 1 nM, 300 pM, 100 pM, 30 pM and 10 pM. The tissue thicknesses are 1, 2, 3, 4, 5, 6 mm. (C) Quantitative tissue penetration depth in relation to the SNR of pure SERS gels.

6.3.1.3 Tissue attenuation properties and background interference: NIR-I versus NIR-II

Moving towards longer NIR wavelength is beneficial with a number of favorable optical properties, including the reduced absorbance, scattering and autofluorescence background of tissues. This provides a pratical way to alter the tissues properties and improve photon penetration since the tissue light scattering scales with $\lambda^{-\alpha}$ (α=0.2-4). [12] In the past decade, a significant amout of advances has been made on the fluorescence imaging at the emerging NIR-II window, and the investigations on NIR-II SERS are also beginning to be reported [12].

We quantitatively compared the tissue penetration properties using SERS at the NIR-I (785 nm) and NIR-II (1064 nm) windows. The measurements were performed using the same batch of tissues and SERS gel for two wavelengths. Integration time and laser power were chosen to make the pure SERS gel to have comparable intensities at two wavelengths (Figure 6.4A, black). The Raman spectra shows that the 1338 cm^{-1} peak intensity of SERS gel (marked in pink) decreases dramatically when covered by tissues and becomes unobservable with 5 mm muscle on top at 785 nm excitation. In contrast, this peak still gets exhibited with 6 mm muscle on top at 1064 nm excitation, indicating a better tissue penetration at the NIR-II window. The calculated SNR shows the tissue penetration depths at 1064 nm excitation are of 6 mm, 3 mm and 3 mm for muscle, fat and skin tissues, better than that of 4 mm, 2 mm, 2 mm at 785 nm excitation.

Figure 6.4B shows the profile of the normalized SNR versus tissue thickness. With 1 mm tissues on top, the normalized SNR drops to 16% at 785 nm and 34% at 1064 nm for muscle. The improvements are also observed on fat and skin tissues that the normalized SNR percentage is 10% at 785 nm and 17% at 1064 nm for 1 mm fat; 10% at 785 nm and 27% at 1064 nm for 1 mm skin. The improvements on fat are most limited. Although 1 mm skin appears to be easier to penetrate than fat at 1064 nm, the two tissues have similar penetration depth. This is because the porcine

skin used in measurements is composed of a thin epidermis (<1 mm) top layer and subcutaneous tissues that are mainly fat.

The *in vivo* detection on NIR-II window also benefits from the reduced auto-fluorescence background from biological tissue chromophores. We measured the Raman spectra of seven types of tissues, i.e. skin, muscle, bone, lung, kidney, liver and fat, under both 785 nm and 1064 nm excitation. The raw Raman spectra without baseline corrections are displayed to provide a direct comparison of the wavelength-dependent background interferences (Figure 6.4D). With 785 nm excitation, the auto-fluorescence background is observed for all tissues, especially for the liver, kidney, lung and bone due to the enrichment of hemoglobin and structural proteins in these tissues [196]. Some characteristic peaks of the tissues are buried in the fluorescence background interference and hard to recognize, e.g. 1446 cm^{-1} and 1653 cm^{-1} peak in complex organs like liver, kidney and lung. In contrast, all Raman peaks well emerge under 1064 nm excitation when tissue chromophores fluorescence decreases exponentially at the longer wavelength [197]. Characteristic peaks in biological tissue samples include modes at 1445 cm^{-1}, 1660 cm^{-1}, and in the range of 1200-1340 cm^{-1}, which correspond to the CH_2 deformation peak, amine I band and amine III band, respectively [168, 198]. The strong peak at 960 cm^{-1} for bones is dominated by phosphate internal mode [199]. For the SERS nanotags applied in imaging-guided tumor diagnosis and detection, it is important that their characteristic peaks should be well discriminated with tissue background peaks. Therefore, in selecting the Raman reporter molecules for NIR-II SERS tags, they are preferred to have characteristic peaks within 1100-1200 cm^{-1}, 1500-1600 cm^{-1} or 1800-2200 cm^{-1} region (marked by green) to avoid an overlap with tissue Raman peaks (marked by gray). The reduction in fluorescence background makes it possible for us to adopt longer laser exposure time on the NIR-II window. For example, the background of kidney is extremely high under 785 nm

excitation, which is over 40,000 counts with an integration time of only 4 s, and no clear Raman peaks are seen. Nevertheless, the background drops tremendously at 1064 nm excitation that the autofluorescence background is only 4,000 counts with 30 s integration time. These results demonstrate the superiority of the NIR-II detections in deep layer tissues.

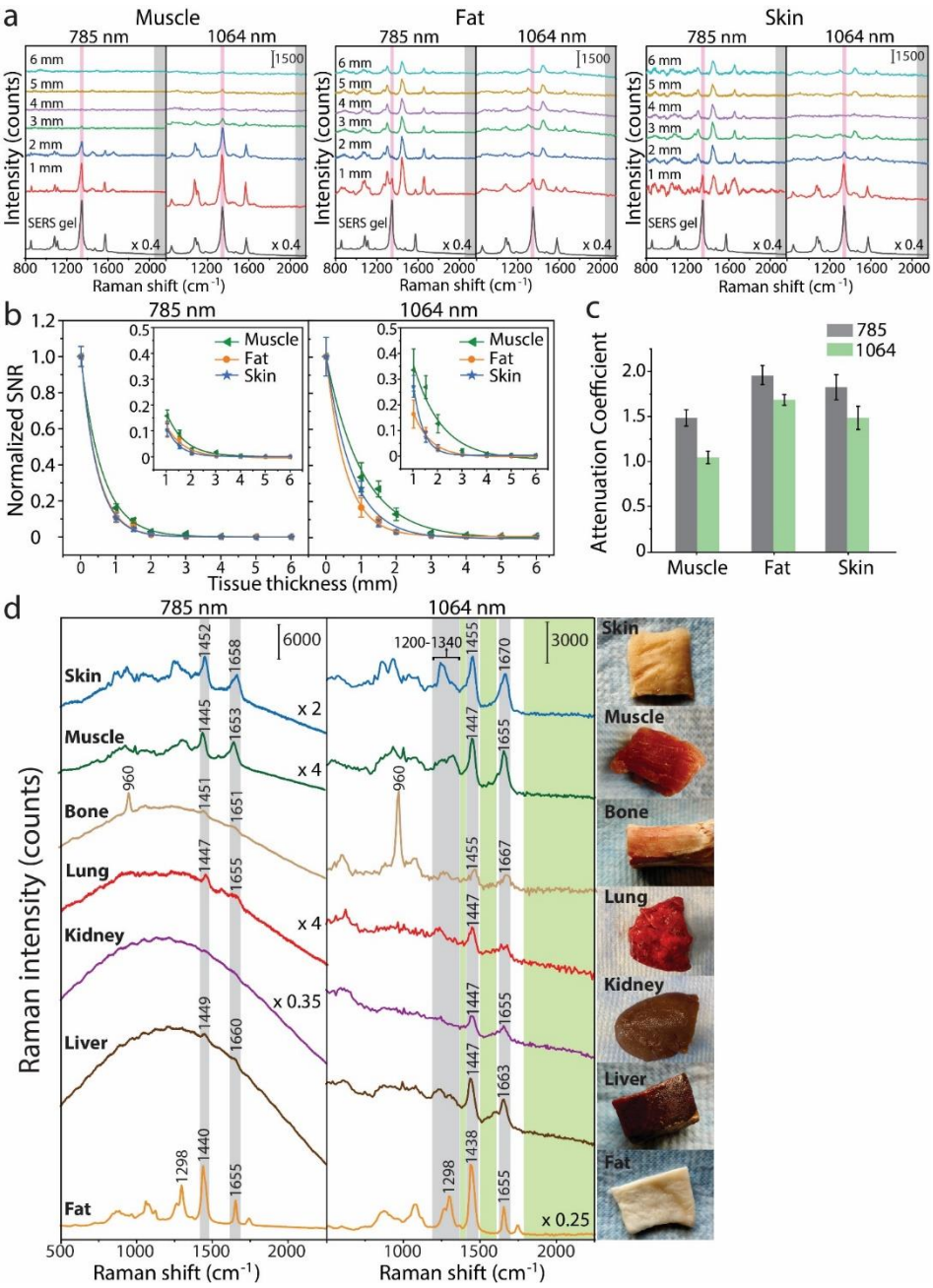

Figure 6.4 Wavelength-dependent tissue penetration and background interferences on the NIR-I/II window. (A) Representative Raman spectra of SERS gels covered with muscle, fat and skin of different thicknesses. The measurements were performed with 785 nm (200 mW, 1.5 s integration time) and 1064 nm (450 mW, 10 s integration time). The SERS gel of 300 pM Ag/Au NPs was used. (B) The profile of normalized SNR versus tissue thickness. (C) Tissue attenuation coefficients of muscle, fat and skin. (D) Tissue autofluorescence background of porcine skin, muscle, bone, lung, kidney, liver and fat. The measurements were performed with 785 nm (200 mW, 4 s integration time) and 1064 nm (450 mW, 30 s integration time).

6.3.2 NIR-II resonant SERS NP design

With the understanding of the superiority of NIR-II window, we aim at preparing SERS NPs with strong resonance at NIR-II window, while keeping their size below 100 nm to maintain good in-vivo performance. Among various plasmonic nanostructures, gold nanostars is one class of material that meets the above requirements. The LSPR peak of AuNS was reported to be proportional to the aspect ratio of the tips [32]. Therefore, if the tips are sharp and long enough, even a small AuNS particle can have its LSPR peak tuned beyond 1000 nm. I successfully synthesized AuNS with only ~ 60 nm in diameter, but with a LSPR peak around 1050 nm, very close to the commonly used NIR-II laser 1064 nm (Figure 6.5).

However, AuNS structure with such sharp tips is rarely seen in literatures as the high-curvature tip geometry is not energy-favorable, and easily turns round with time [185, 186, 200]. In this work, I adopted the new hydrophobic domain modified PEG (MUA-PEG) as the protective layer of the AuNS. It was found out that the LSPR peak of the MUA-PEG coated AuNSs barely shift after 2-week storage at room temperature, and the high absorbance of the NPs at NIR-II window was well-preserved (Figure 6.6). The LSPR peak of the traditional PEG coated AuNSs, however, shifts from 1050 nm to 900 nm within 2 weeks, resulting in decreased absorbance at NIR-II window. The better protection of the anisotropic AuNS structure by MUA-PEG was likely the contribution of the strong hydrophobic interaction between the ligands that stabilizes the surface energy and prevents the geometry from evolving.

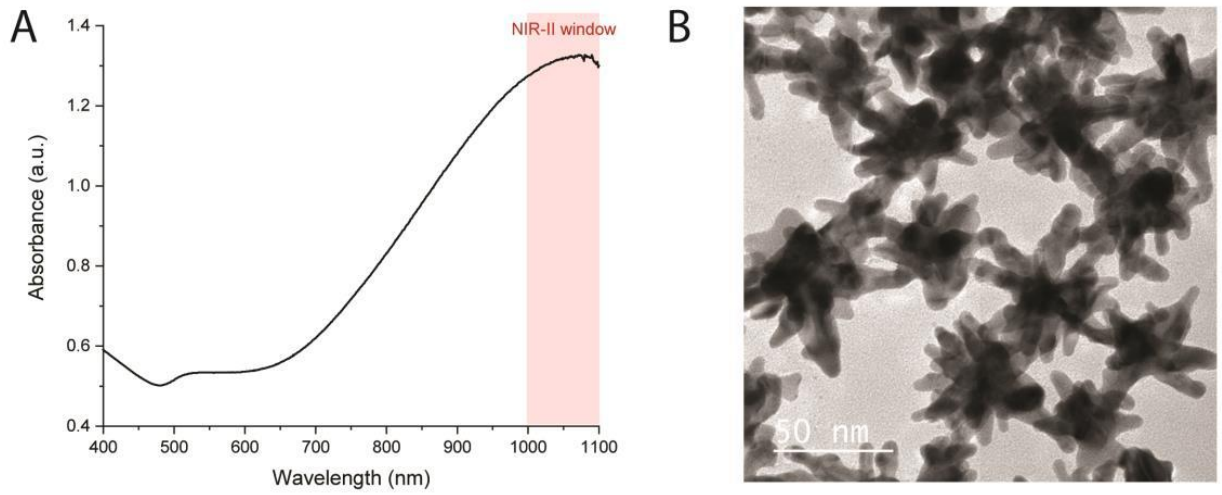

Figure 6.5 A) UV-vis spectrum of the NIR-II AuNS. High absorbance at NIR-II window was observed. B) TEM image of NIR-II AuNS coated with MUA-PEG.

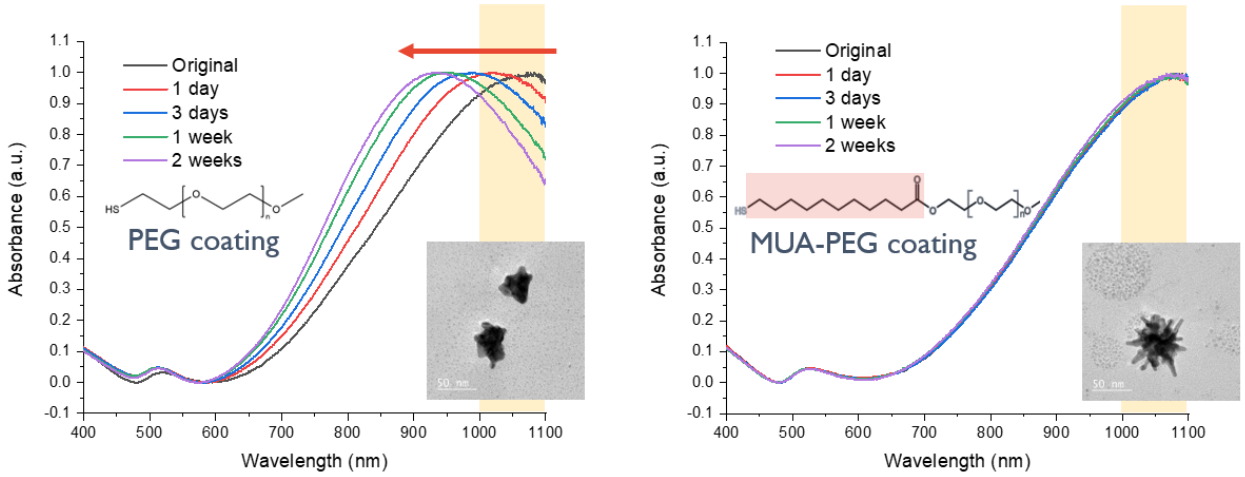

Figure 6.6 UV-vis spectrum change of the NIR-II AuNS with traditional PEG coating (left) and MUA-PEG coating (right) during 2-week storage at room temperature. TEM photos of the samples were inserted with the UV-vis spectra.

After attaching IR-1061 dye as the reporter molecule, we obtained distinct and strong Raman intensity at 1064 nm excitation (Figure 6.7A). The stability of the NIR-II SERS NP was first tested through multiple laser exposure considering that continuous laser pulses may bring the risk of tips being melt by the generated heat, and thus reduces the SERS signal. The NIR-II SERS NPs were made into agarose gels with uniform NP dispersion, and the gel was tested under 100-mW 1064-nm laser scans, with each scan of 5-second integration time (Figure 6.76B). The probe and the gel were fixed with each other during the measurement to make sure that the area exposed to laser is the same. It was found that the exposed NIR-II SERS NPs in the gels show consistent SERS signal after 20 scans, with the SERS signal remains ~90% of the original value (Figure 6.7C and Figure S6.4). The new NIR-II AuNS structures with sharp tips, protected by MUA-PEG with strong hydrophobic interaction between each other, and attached with resonant dye as reporters with stable NI-II signal, are believed to be a strong candidate for biological imaging in the NIR-II window.

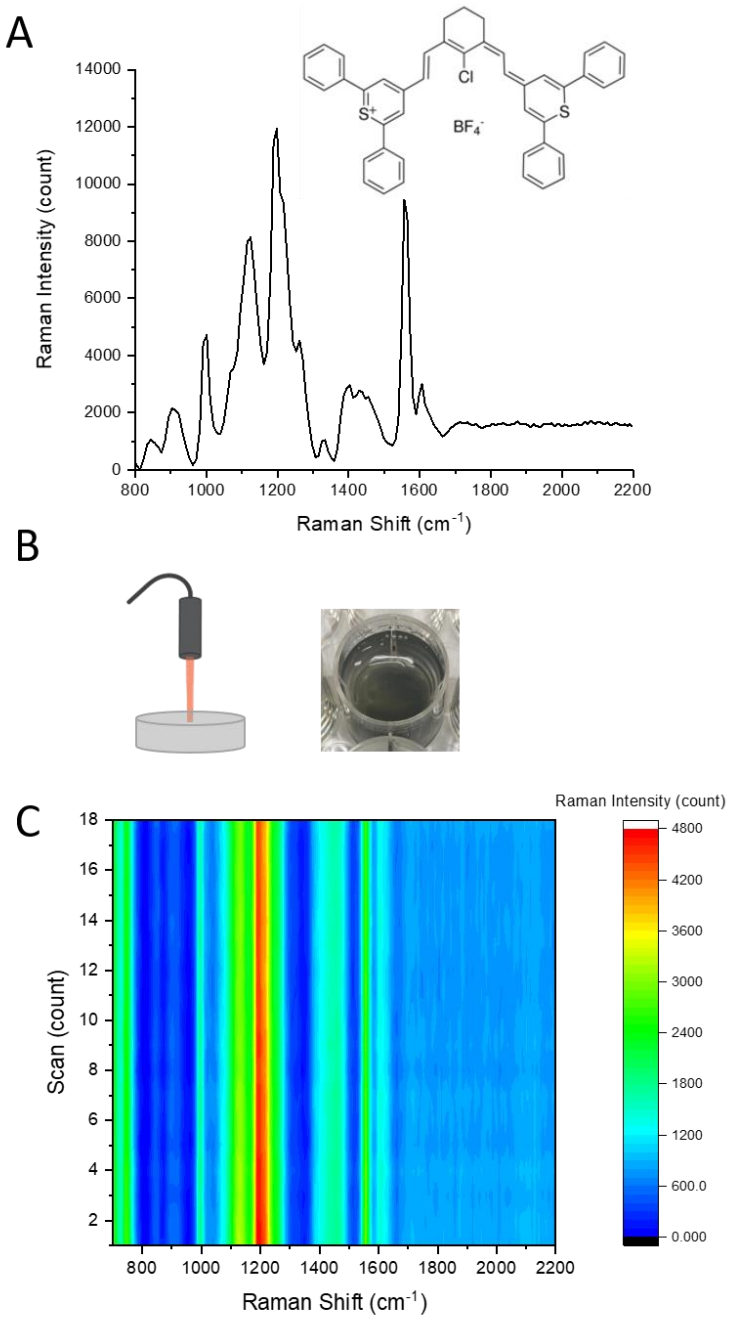

Figure 6.7 A) Raman spectrum of IR-1061 attached AuNS coated with MUA-PEG. Laser: 1064 nm, 200 mW, 2-second integration time. B) Laser exposure setup (left) and the agarose gel made from NIR-II AuNS solution (right). C) Raman signal drift of the NIR-II SERS NP gel during 18 laser scans (100 mW, 5-second integration time).

6.4 Conclusion

In this chapter we report the proof of concepts and a benchmark setup for the quantitative assessments of NIR tissue penetration *ex vivo* using SERS. The concepts, setups, and materials presented in this work provide a simple and standard assessment procedure to benefit the spectroscopic bioimaging and detection application. The penetration depth was quantitatively defined as the largest thickness of tissues with which an effective signal can be detected from tissue-covered signal source. The effective signal was determined based on the spectral SNR of $\geqslant$ 3. Through these concepts, the quantitative penetration assessments were performed using three types of porcine tissues under 785 nm excitation with the laser power of 5-200 mW and the integration time of 1-10 s. The highest penetration depths obtained are 6, 3, 3 mm on porcine muscle, fat, and skin, respectively. A clear correlation between the penetration depths and the original SNR of signal sources is revealed, which provides valuable information to predict the tissue penetration for other types of spectroscopic imaging agents.

Three factors, i.e., measurement conditions, signal source intensities and tissue properties, are shown to be closely related to the SNR as well as penetration depth. The only factor that has a wide margin of improvements is the signal source intensity. This reasonably explains why a significant number of studies has been reported on the design and invention of ultra-bright imaging agents. One promising way to circumvent the limitation of tissue attenuation is the use of longer excitation wavelength. As compared at the NIR-I (785 nm) and NIR-II (1064 nm) window, the tissue attenuation coefficients are reduced for all three types of tissues at 1064 nm. The SNR attenuation through 1 mm of tissue decreases by 18% on muscle, 7% on fat, and 17% on skin. The weakened tissue autofluorescence interference at 1064 nm also demonstrates the superiority of NIR-II deep tissue bioimaging and detections. This work provides foundational information for

the design, modification, and implementation of *in vivo* bioimaging and detections to facilitate the developments of intraoperative imaging and spectroscopic detection devices in the medical context. A comprehensive combination of innovation in imaging agent material and improvements in detector system could lead towards a new level of deep-tissue bioimaging and image-guided surgery.

Based on the understanding of more transparent bio-image window at NIR-II compared NIR-I, a novel NIR-II resonant SERS nanotag was developed and stabilized using the hydrophobic-locked PEG ligands. The new NIR-II AuNS structures with sharp tips, protected by MUA-PEG with strong hydrophobic interaction between each other, and attached with resonant dye as reporters with stable NI-II signal, are believed to be a strong candidate for biological imaging in the NIR-II window.

6.5 Supplementary Figures and Table

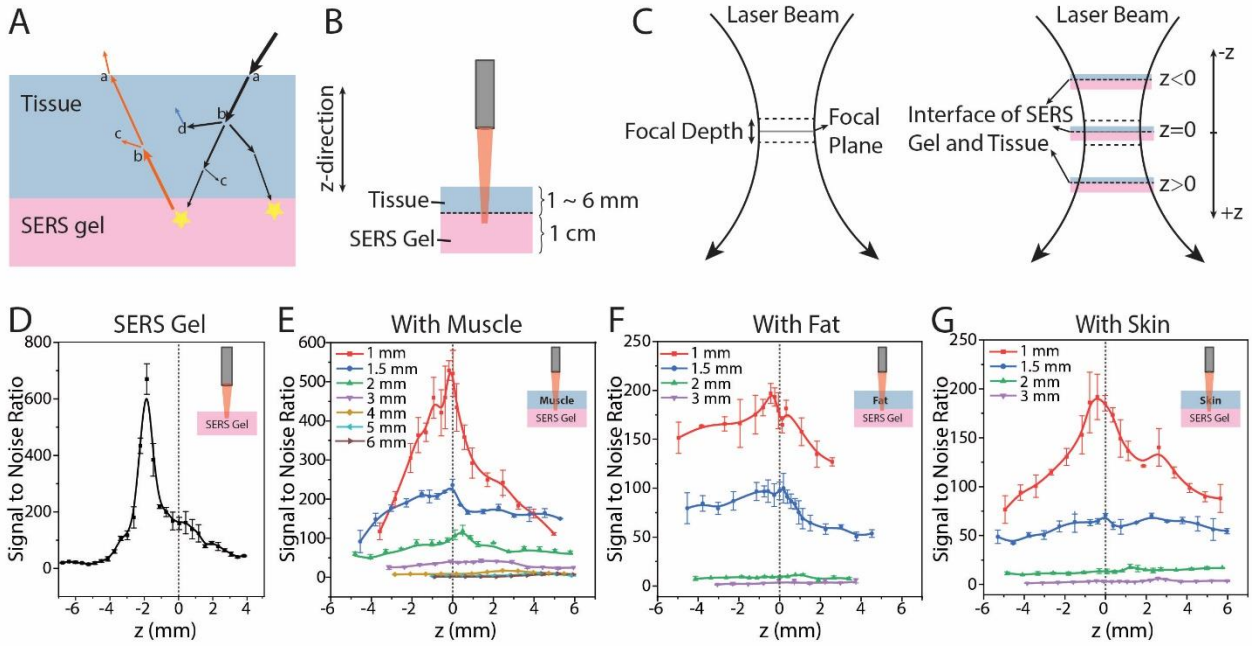

Supplementary Figure 6.1 Optimization of the laser focal plane for Raman measurements on tissues. (A) Signal attenuation during the "penetrating-in" and "transmitting-out" process: reflection at the interface (i), scattering (ii), absorption (iii), auto-fluorescence (iv). (B) Experimental set-up. (C) Schematic illustration of focal depth, focal plane, and the interface of SERS gel and tissue. (D) The SNR of the sequential Raman measurements on the SERS gel at different *z*. The measurements adopted 200 mW power and 200 ms integration time. (E-G) The SNR of Raman measurement on SERS gels with muscle (E), fat (F) and skin (G) of various thicknesses on top. The measurements adopted 200 mW power and 10 s integration time.

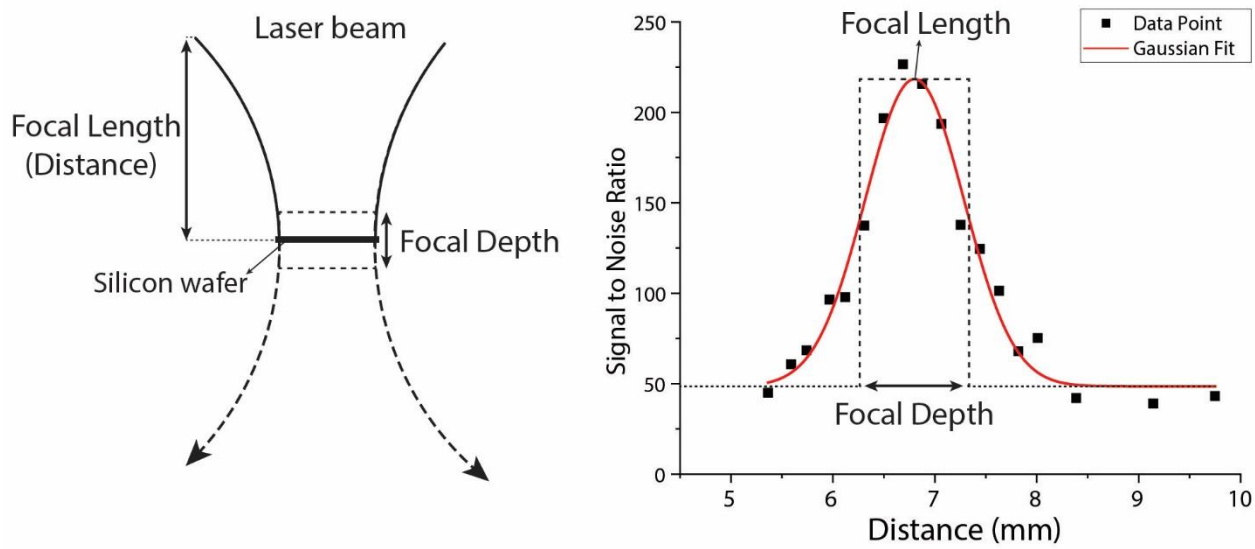

Supplementary Figure 6.2 (Left) The measurement of focus depth and focal length of the laser beam. A silicon wafer was placed on the platform, and sequential acquisition of Raman spectra was performed at different Z position by moving the platform up and down with a step of 0.2 mm, while the laser probe was kept stationary. (Right) The profile of SNR versus the distance between silicon wafer and laser probe. The intensity of 520 cm^{-1} modes of the silicon wafer was used to calculate the SNR. The focal depth is defined as an effective depth near the ideally focused plane (the dashed rectangle).

Supplementary Table 6.1 The SNR of SERS gels and corresponding tissue penetration depth of SERS signal, measured with different excitation powers, integration times and SERS NP concentrations under 785 nm excitation. The data were analyzed from the results in Figure 6.2.

Power and integration time	SERS NPs concentration	SNR of pure SERS gel	Penetration Depth		
			Muscle	Fat	Skin
5 mW, 10 s	1 nM	580±62	3 mm	1 mm	1.5 mm
10 mW, 10 s	1 nM	754±87	4 mm	1 mm	1.5 mm
50 mW, 10 s	1 nM	1336±42	5 mm	2 mm	2 mm
100 mW, 10 s	1 nM	1659±70	5 mm	2 mm	3 mm
200 mW, 10 s	1 nM	2171±119	⩾6 mm	3 mm	3 mm
5 mW, 1 s	1 nM	71±5	1 mm	<1 mm	<1 mm
10 mW, 1 s	1 nM	96±7	2 mm	<1 mm	<1 mm
50 mW, 1 s	1 nM	334±9	3 mm	1 mm	1 mm
100 mW, 1 s	1 nM	510±22	3 mm	1 mm	1 mm
200 mW, 1 s	1 nM	839±46	4 mm	1 mm	1 mm
200 mW, 10 s	10 pM	364±19	3 mm	1 mm	1 mm
200 mW, 10 s	30 pM	544±30	2 mm	1 mm	1 mm
200 mW, 10 s	100 pM	723±21	4 mm	1 mm	2 mm
200 mW, 10 s	300 pM	1369±128	5 mm	2 mm	3 mm

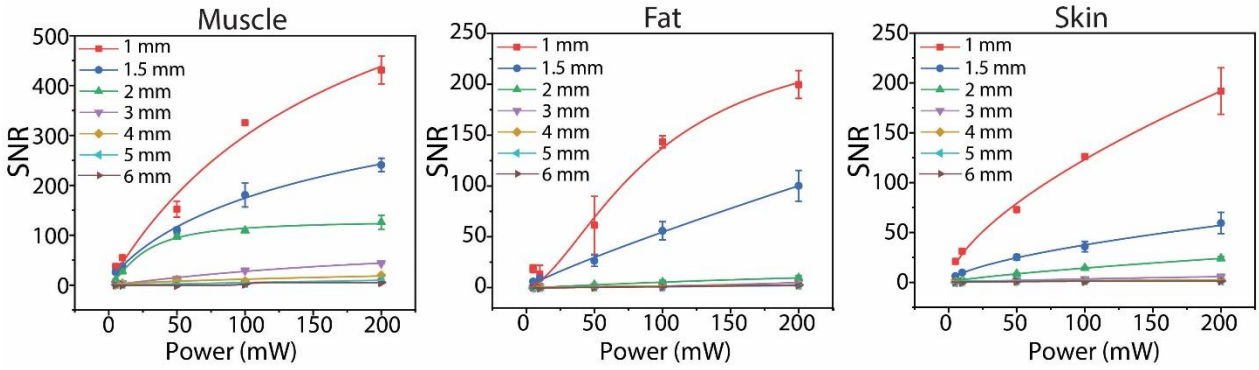

Supplementary Figure 6.3 The profile of SNR versus excitation power for Raman measurement, analyzed based on the data of Figure 3A. The power is 5, 10, 50, 100, 200 mW.

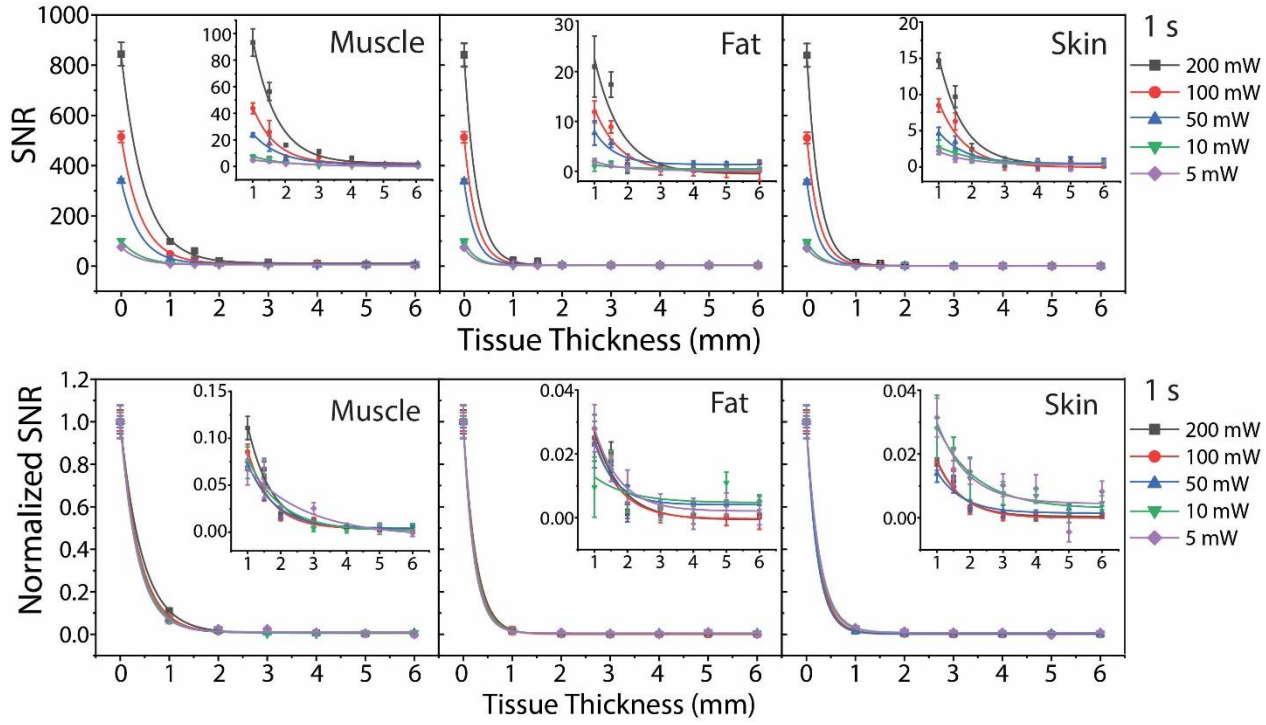

Supplementary Figure 6.4 Power dependent SNR (top) and normalized SNR (bottom) measured using different powers and 1 s integration time, on the SERS gel of 1 nM NP. The powers are 5, 10, 50, 100, 200 mW.

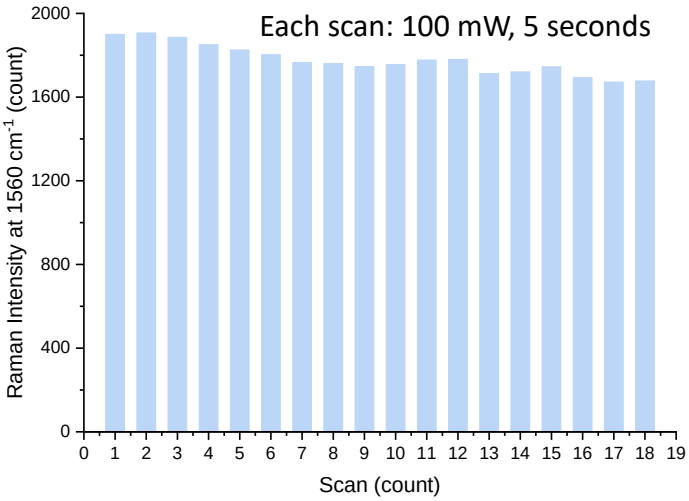

Supplementary Figure 6.5 Raman signal at 1560 cm^{-1} change during laser scans.

REFERENCES

[1] M. Fleischmann, P. J. Hendra, and A. J. McQuillan, "Raman spectra of pyridine adsorbed at a silver electrode," *Chemical Physics Letters,* vol. 26, no. 2, pp. 163-166, 1974/05/15/ 1974.

[2] J. Kneipp, H. Kneipp, and K. Kneipp, "SERS--a single-molecule and nanoscale tool for bioanalytics," *Chem Soc Rev,* vol. 37, no. 5, pp. 1052-60, May 2008.

[3] S. Nie and S. R. Emory, "Probing single molecules and single nanoparticles by surface-enhanced Raman scattering," *Science,* Article vol. 275, no. 5303, pp. 1102-1106, 1997.

[4] D. Cialla, S. Pollok, C. Steinbrücker, K. Weber, and J. Popp, "SERS-based detection of biomolecules," *Nanophotonics,* Article vol. 3, no. 6, pp. 383-411, 2014.

[5] A. Mokhtarzadeh *et al.*, "Nanomaterial-based biosensors for detection of pathogenic virus," *TrAC - Trends in Analytical Chemistry,* Review vol. 97, pp. 445-457, 2017.

[6] X. Wang *et al.*, "Fractal SERS nanoprobes for multiplexed quantitative gene profiling," *Biosens Bioelectron,* vol. 156, p. 112130, May 15 2020.

[7] B. Kang, M. M. Afifi, L. A. Austin, and M. A. El-Sayed, "Exploiting the nanoparticle plasmon effect: Observing drug delivery dynamics in single cells via Raman/fluorescence imaging spectroscopy," *ACS Nano,* Article vol. 7, no. 8, pp. 7420-7427, 2013.

[8] J. Kim, S. H. Nam, D. K. Lim, and Y. D. Suh, "SERS-based particle tracking and molecular imaging in live cells: Toward the monitoring of intracellular dynamics," *Nanoscale,* Article vol. 11, no. 45, pp. 21724-21727, 2019.

[9] L. Guerrini, N. Pazos-Perez, E. Garcia-Rico, and R. Alvarez-Puebla, "Cancer characterization and diagnosis with SERS-encoded particles," *Cancer Nanotechnology,* Review vol. 8, no. 1, 2017, Art. no. 5.

[10] M. Blanco-Formoso and R. A. Alvarez-Puebla, "Cancer diagnosis through sers and other related techniques," *International Journal of Molecular Sciences,* Review vol. 21, no. 6, 2020, Art. no. 2253.

[11] S. Nie and X. Qian, "Spectrally encoded sers nanoparticles for multiplexed optical detection and image-guided surgery," in *Nanophotonics, Nanoelectronics and Nanosensor, N3 2013*, 2013.

[12] L. A. Lane, R. Xue, and S. Nie, "Emergence of two near-infrared windows for in vivo and intraoperative SERS," *Current Opinion in Chemical Biology,* Review vol. 45, pp. 95-103, 2018.

[13] N. D. Israelsen, C. Hanson, and E. Vargis, "Nanoparticle properties and synthesis effects on surface-enhanced Raman scattering enhancement factor: An introduction," *Scientific World Journal,* Review vol. 2015, 2015, Art. no. 124582.

[14] G. C. Schatz and R. P. Van Duyne, "Electromagnetic Mechanism of Surface-Enhanced Spectroscopy," in *Handbook of Vibrational Spectroscopy*, 2001.

[15] J. Kim *et al.*, "Study of Chemical Enhancement Mechanism in Non-plasmonic Surface Enhanced Raman Spectroscopy (SERS)," (in English), Original Research vol. 7, no. 582, 2019-August-20 2019.

[16] Y. Chen and H. Ming, "Review of surface plasmon resonance and localized surface plasmon resonance sensor," *Photonic Sensors,* vol. 2, no. 1, pp. 37-49, 2012/03/01 2012.

[17] D. J. Trivedi, B. Barrow, and G. C. Schatz, "Understanding the chemical contribution to the enhancement mechanism in SERS: Connection with Hammett parameters," *The Journal of Chemical Physics,* vol. 153, no. 12, p. 124706, 2020/09/28 2020.

[18] G. McNay, D. Eustace, W. E. Smith, K. Faulds, and D. Graham, "Surface-enhanced Raman scattering (SERS) and surface-enhanced resonance Raman scattering (SERRS): a review of applications," *Appl Spectrosc,* vol. 65, no. 8, pp. 825-37, Aug 2011.

[19] W. Xu *et al.*, "Surface enhanced Raman spectroscopy on a flat graphene surface," *Proceedings of the National Academy of Sciences,* vol. 109, no. 24, p. 9281, 2012.

[20] X. Li, J. Zhu, and B. Wei, "Hybrid nanostructures of metal/two-dimensional nanomaterials for plasmon-enhanced applications," *Chem Soc Rev,* vol. 45, no. 11, pp. 3145-87, Jun 7 2016.

[21] J. F. Li *et al.*, "Shell-isolated nanoparticle-enhanced Raman spectroscopy," *Nature,* vol. 464, no. 7287, pp. 392-5, Mar 18 2010.

[22] Y. Liu, H. Zhou, Z. Hu, G. Yu, D. Yang, and J. Zhao, "Label and label-free based surface-enhanced Raman scattering for pathogen bacteria detection: A review," *Biosensors and Bioelectronics,* vol. 94, pp. 131-140, 2017/08/15/ 2017.

[23] Y. Wang, B. Yan, and L. Chen, "SERS tags: novel optical nanoprobes for bioanalysis," *Chem Rev,* vol. 113, no. 3, pp. 1391-428, Mar 13 2013.

[24] L. A. Lane, X. Qian, and S. Nie, "SERS Nanoparticles in Medicine: From Label-Free Detection to Spectroscopic Tagging," *Chem Rev,* vol. 115, no. 19, pp. 10489-529, Oct 14 2015.

[25] X. Qian *et al.*, "In vivo tumor targeting and spectroscopic detection with surface-enhanced Raman nanoparticle tags," *Nat Biotechnol,* vol. 26, no. 1, pp. 83-90, Jan 2008.

[26] X. Bi, Y. Gu, and J. Ye, "Ag-Coated Au Nanopetals: Dual-Type Single-Nanoparticle Detection of Gap-Enhanced Resonance Raman Tags," *ACS Applied Nano Materials,* vol. 3, no. 7, pp. 6987-6995, 2020/07/24 2020.

[27] T. Zhang, L. Wang, Q. Chen, and C. Chen, "Cytotoxic potential of silver nanoparticles," (in eng), *Yonsei medical journal,* vol. 55, no. 2, pp. 283-291, 2014.

[28] L. Fabris, "Gold-based SERS tags for biomedical imaging," *Journal of Optics (United Kingdom),* Review vol. 17, no. 11, 2015, Art. no. 114002.

[29] J. Reguera, J. Langer, D. Jiménez de Aberasturi, and L. M. Liz-Marzán, "Anisotropic metal nanoparticles for surface enhanced Raman scattering," *Chemical Society Reviews,* 10.1039/C7CS00158D vol. 46, no. 13, pp. 3866-3885, 2017.

[30] H. K. Lee *et al.*, "Designing surface-enhanced Raman scattering (SERS) platforms beyond hotspot engineering: Emerging opportunities in analyte manipulations and hybrid materials," *Chemical Society Reviews,* Review vol. 48, no. 3, pp. 731-756, 2019.

[31] C. Song *et al.*, "Gold nanostars for cancer cell-targeted SERS-imaging and NIR light-triggered plasmonic photothermal therapy (PPTT) in the first and second biological windows," *Journal of Materials Chemistry B,* Article vol. 7, no. 12, pp. 2001-2008, 2019.

[32] H. Yuan, C. G. Khoury, H. Hwang, C. M. Wilson, G. A. Grant, and T. Vo-Dinh, "Gold nanostars: surfactant-free synthesis, 3D modelling, and two-photon photoluminescence imaging," (in eng), *Nanotechnology,* vol. 23, no. 7, pp. 075102-075102, 2012.

[33] N. G. Khlebtsov, L. Lin, B. N. Khlebtsov, and J. Ye, "Gap-enhanced Raman tags: Fabrication, optical properties, and theranostic applications," *Theranostics,* Review vol. 10, no. 5, pp. 2067-2094, 2020.

[34] N. Gandra and S. Singamaneni, "Bilayered raman-intense gold nanostructures with hidden tags (BRIGHTs) for high-resolution bioimaging," *Advanced Materials,* Article vol. 25, no. 7, pp. 1022-1027, 2013.

[35] G. McNay, D. Eustace, W. E. Smith, K. Faulds, and D. Graham, "Surface-enhanced Raman scattering (SERS) and surface-enhanced resonance raman scattering (SERRS): A review of applications," *Applied Spectroscopy,* Review vol. 65, no. 8, pp. 825-837, 2011.

[36] L. Lin *et al.*, "Nanooptics of Plasmonic Nanomatryoshkas: Shrinking the Size of a Core–Shell Junction to Subnanometer," *Nano Letters,* vol. 15, no. 10, pp. 6419-6428, 2015/10/14 2015.

[37] L. Lin, H. Gu, and J. Ye, "Plasmonic multi-shell nanomatryoshka particles as highly tunable SERS tags with built-in reporters," *Chemical Communications,* 10.1039/C5CC06599B vol. 51, no. 100, pp. 17740-17743, 2015.

[38] M. Sánchez-Purrà, B. Roig-Solvas, C. Rodriguez-Quijada, B. M. Leonardo, and K. Hamad-Schifferli, "Reporter Selection for Nanotags in Multiplexed Surface Enhanced Raman Spectroscopy Assays," *ACS Omega,* Article vol. 3, no. 9, pp. 10733-10742, 2018.

[39] X. Qian, S. R. Emory, and S. Nie, "Anchoring molecular chromophores to colloidal gold nanocrystals: Surface-enhanced Raman evidence for strong electronic coupling and irreversible structural locking," *Journal of the American Chemical Society,* Article vol. 134, no. 4, pp. 2000-2003, 2012.

[40] H. Kearns *et al.*, "Sensitive SERS nanotags for use with a hand-held 1064 nm Raman spectrometer," *Royal Society Open Science,* vol. 4, no. 7, p. 170422.

[41] J. Wang, D. Liang, J. Feng, and X. Tang, "Multicolor Cocktail for Breast Cancer Multiplex Phenotype Targeting and Diagnosis Using Bioorthogonal Surface-Enhanced Raman Scattering Nanoprobes," *Analytical Chemistry,* Article vol. 91, no. 17, pp. 11045-11054, 2019.

[42] J. Wang, D. Liang, Q. Jin, J. Feng, and X. Tang, "Bioorthogonal SERS Nanotags as a Precision Theranostic Platform for in Vivo SERS Imaging and Cancer Photothermal Therapy," *Bioconjugate Chemistry,* vol. 31, no. 2, pp. 182-193, 2020/02/19 2020.

[43] J. Wu *et al.*, "Bioorthogonal SERS Nanoprobes for Mulitplex Spectroscopic Detection, Tumor Cell Targeting, and Tissue Imaging," *Chemistry - A European Journal,* Article vol. 21, no. 37, pp. 12914-12918, 2015.

[44] J. Manson, D. Kumar, B. J. Meenan, and D. Dixon, "Polyethylene glycol functionalized gold nanoparticles: the influence of capping density on stability in various media," *Gold Bulletin,* vol. 44, no. 2, pp. 99-105, 2011/06/01 2011.

[45] F. Barbero *et al.*, "Formation of the Protein Corona: The Interface between Nanoparticles and the Immune System," *Seminars in Immunology,* vol. 34, pp. 52-60, 2017/12/01/ 2017.

[46] L. A. Lane, X. Qian, A. M. Smith, and S. Nie, "Physical Chemistry of Nanomedicine: Understanding the Complex Behaviors of Nanoparticles in Vivo," *Annual Review of Physical Chemistry,* vol. 66, no. 1, pp. 521-547, 2015/04/01 2015.

[47] M. Debayle *et al.*, "Zwitterionic polymer ligands: an ideal surface coating to totally suppress protein-nanoparticle corona formation?," *Biomaterials,* Article vol. 219, 2019, Art. no. 119357.

[48] W. Stöber, A. Fink, and E. Bohn, "Controlled growth of monodisperse silica spheres in the micron size range," *Journal of Colloid and Interface Science,* vol. 26, no. 1, pp. 62-69, 1968/01/01/ 1968.

[49] W. E. Doering and S. Nie, "Spectroscopic Tags Using Dye-Embedded Nanoparticles and Surface-Enhanced Raman Scattering," *Analytical Chemistry,* vol. 75, no. 22, pp. 6171-6176, 2003/11/01 2003.

[50] A. Oseledchyk, C. Andreou, M. A. Wall, and M. F. Kircher, "Folate-Targeted Surface-Enhanced Resonance Raman Scattering Nanoprobe Ratiometry for Detection of Microscopic Ovarian Cancer," *ACS Nano,* vol. 11, no. 2, pp. 1488-1497, Feb 28 2017.

[51] X. S. Zheng *et al.*, "BSA-coated nanoparticles for improved SERS-based intracellular pH sensing," *Anal Chem,* vol. 86, no. 24, pp. 12250-7, Dec 16 2014.

[52] M. Arruebo, M. Valladares, and Á. González-Fernández, "Antibody-Conjugated Nanoparticles for Biomedical Applications," *Journal of Nanomaterials,* vol. 2009, p. 439389, 2009/12/03 2009.

[53] X. Wang *et al.*, "Detection of circulating tumor cells in human peripheral blood using surface-enhanced Raman scattering nanoparticles," (in eng), *Cancer research,* vol. 71, no. 5, pp. 1526-1532, 2011.

[54] S. C. H. Tsao, J. Wang, Y. Wang, A. Behren, J. Cebon, and M. Trau, "Characterising the phenotypic evolution of circulating tumour cells during treatment," *Nature Communications,* Article vol. 9, no. 1, 2018, Art. no. 1482.

[55] B. N. Khlebtsov, D. N. Bratashov, N. A. Byzova, B. B. Dzantiev, and N. G. Khlebtsov, "SERS-based lateral flow immunoassay of troponin I by using gap-enhanced Raman tags," *Nano Research,* vol. 12, no. 2, pp. 413-420, 2018.

[56] J. Perumal, Y. Wang, A. B. E. Attia, U. S. Dinish, and M. Olivo, "Towards a point-of-care SERS sensor for biomedical and agri-food analysis applications: A review of recent advancements," *Nanoscale,* Review vol. 13, no. 2, pp. 553-580, 2021.

[57] V. Tran, B. Walkenfort, M. Konig, M. Salehi, and S. Schlucker, "Rapid, Quantitative, and Ultrasensitive Point-of-Care Testing: A Portable SERS Reader for Lateral Flow Assays in Clinical Chemistry," *Angew Chem Int Ed Engl,* vol. 58, no. 2, pp. 442-446, Jan 8 2019.

[58] F. Nicolson *et al.*, "Multiplex imaging of live breast cancer tumour models through tissue using handheld surface enhanced spatially offset resonance Raman spectroscopy (SESORRS)," *Chem Commun (Camb),* vol. 54, no. 61, pp. 8530-8533, Jul 26 2018.

[59] A. M. Smith, M. C. Mancini, and S. Nie, "Bioimaging: second window for in vivo imaging," (in eng), *Nature nanotechnology,* vol. 4, no. 11, pp. 710-711, 2009.

[60] M. Kim *et al.*, "Dealloyed Intra-Nanogap Particles with Highly Robust, Quantifiable Surface-Enhanced Raman Scattering Signals for Biosensing and Bioimaging Applications," *ACS Central Science,* Article vol. 4, no. 2, pp. 277-287, 2018.

[61] J. Hwang, S. Lee, and J. Choo, "Application of a SERS-based lateral flow immunoassay strip for the rapid and sensitive detection of staphylococcal enterotoxin B," *Nanoscale,* vol. 8, no. 22, pp. 11418-25, Jun 2 2016.

[62] X. Fu, Z. Cheng, J. Yu, P. Choo, L. Chen, and J. Choo, "A SERS-based lateral flow assay biosensor for highly sensitive detection of HIV-1 DNA," (in eng), *Biosens Bioelectron,* vol. 78, pp. 530-537, Apr 15 2016.

[63] J. Li *et al.*, "Biomimetic Platelet-Camouflaged Nanorobots for Binding and Isolation of Biological Threats," *Advanced Materials,* Article vol. 30, no. 2, 2018, Art. no. 1704800.

[64] L. A. Lane, X. Qian, and S. Nie, "SERS Nanoparticles in Medicine: From Label-Free Detection to Spectroscopic Tagging," *Chemical Reviews,* vol. 115, no. 19, pp. 10489-10529, 2015/10/14 2015.

[65] D. T. Ginat and R. Gupta, "Advances in Computed Tomography Imaging Technology," *Annual Review of Biomedical Engineering,* vol. 16, no. 1, pp. 431-453, 2014/07/11 2014.

[66] J. W. Kang, P. T. So, R. R. Dasari, and D. K. Lim, "High resolution live cell Raman imaging using subcellular organelle-targeting SERS-sensitive gold nanoparticles with highly narrow intra-nanogap," *Nano Lett,* vol. 15, no. 3, pp. 1766-72, Mar 11 2015.

[67] Y. Wang, Y. Zhang, and S. Schlücker, "Chapter 17 - Immuno-SERS: from nanotag design to assays and microscopy," in *Vibrational Spectroscopy in Protein Research*, Y. Ozaki, M. Baranska, I. K. Lednev, and B. R. Wood, Eds.: Academic Press, 2020, pp. 485-528.

[68] S. Lee *et al.*, "Rapid and sensitive phenotypic marker detection on breast cancer cells using surface-enhanced Raman scattering (SERS) imaging," *Biosensors and Bioelectronics,* Article vol. 51, pp. 238-243, 2014.

[69] H. Maeda, "Macromolecular therapeutics in cancer treatment: The EPR effect and beyond," *Journal of Controlled Release,* vol. 164, no. 2, pp. 138-144, 2012/12/10/ 2012.

[70] S. Sindhwani *et al.*, "The entry of nanoparticles into solid tumours," *Nature Materials,* vol. 19, no. 5, pp. 566-575, 2020/05/01 2020.

[71] Z. Bao, Y. Zhang, Z. Tan, X. Yin, W. Di, and J. Ye, "Gap-enhanced Raman tags for high-contrast sentinel lymph node imaging," *Biomaterials,* vol. 163, pp. 105-115, May 2018.

[72] Y. Zhang, Y. Gu, J. He, B. D. Thackray, and J. Ye, "Ultrabright gap-enhanced Raman tags for high-speed bioimaging," *Nat Commun,* vol. 10, no. 1, p. 3905, Aug 29 2019.

[73] B. Kang, L. A. Austin, and M. A. El-Sayed, "Real-time molecular imaging throughout the entire cell cycle by targeted plasmonic-enhanced Rayleigh/Raman spectroscopy," *Nano Lett,* vol. 12, no. 10, pp. 5369-75, Oct 10 2012.

[74] H. Karabeber *et al.*, "Guiding Brain Tumor Resection Using Surface-Enhanced Raman Scattering Nanoparticles and a Hand-Held Raman Scanner," *ACS Nano,* vol. 8, no. 10, pp. 9755-9766, 2014/10/28 2014.

[75] Y. W. Wang *et al.*, "Comprehensive spectral endoscopy of topically applied SERS nanoparticles in the rat esophagus," *Biomed Opt Express,* vol. 5, no. 9, pp. 2883-95, Sep 1 2014.

[76] Y. Liu, Z. Chang, H. Yuan, A. M. Fales, and T. Vo-Dinh, "Quintuple-modality (SERS-MRI-CT-TPL-PTT) plasmonic nanoprobe for theranostics," *Nanoscale,* Article vol. 5, no. 24, pp. 12126-12131, 2013.

[77] M. F. Kircher *et al.*, "A brain tumor molecular imaging strategy using a new triple-modality MRI-photoacoustic-Raman nanoparticle," *Nature Medicine,* vol. 18, no. 5, pp. 829-834, 2012/05/01 2012.

[78] T. M. Shaffer *et al.*, "Silica nanoparticles as substrates for chelator-free labeling of oxophilic radioisotopes," *Nano Lett,* vol. 15, no. 2, pp. 864-8, Feb 11 2015.

[79] C. D. Walkey, J. B. Olsen, H. Guo, A. Emili, and W. C. W. Chan, "Nanoparticle Size and Surface Chemistry Determine Serum Protein Adsorption and Macrophage Uptake," *Journal of the American Chemical Society,* vol. 134, no. 4, pp. 2139-2147, 2012/02/01 2012.

[80] S. Nam, D. V. Parikh, B. D. Condon, Q. Zhao, and M. Yoshioka-Tarver, "Importance of poly(ethylene glycol) conformation for the synthesis of silver nanoparticles in aqueous solution," *Journal of Nanoparticle Research,* Article vol. 13, no. 9, pp. 3755-3764, 2011.

[81] A. R. Lokanathan *et al.*, "Mixed poly (ethylene glycol) and oligo (ethylene glycol) layers on gold as nonfouling surfaces created by backfilling," *Biointerphases,* vol. 6, no. 4, pp. 180-188, 2011/12/01 2011.

[82] M. Yang *et al.*, "Development of Polymer-Encapsulated Metal Nanoparticles as Surface-Enhanced Raman Scattering Probes," *Small,* https://doi.org/10.1002/smll.200800777 vol. 5, no. 2, pp. 198-202, 2009/01/19 2009.

[83] G. Bodelón, V. Montes-García, C. Fernández-López, I. Pastoriza-Santos, J. Pérez-Juste, and L. M. Liz-Marzán, "Au@pNIPAM SERRS Tags for Multiplex Immunophenotyping Cellular Receptors and Imaging Tumor Cells," *Small,* https://doi.org/10.1002/smll.201500269 vol. 11, no. 33, pp. 4149-4157, 2015/09/01 2015.

[84] F. Schulz, T. Vossmeyer, N. G. Bastús, and H. Weller, "Effect of the Spacer Structure on the Stability of Gold Nanoparticles Functionalized with Monodentate Thiolated Poly(ethylene glycol) Ligands," *Langmuir,* vol. 29, no. 31, pp. 9897-9908, 2013/08/06 2013.

[85] B. Nikoobakht and M. A. El-Sayed, "Preparation and Growth Mechanism of Gold Nanorods (NRs) Using Seed-Mediated Growth Method," *Chemistry of Materials,* vol. 15, no. 10, pp. 1957-1962, 2003/05/01 2003.

[86] J. G. Mehtala, D. Y. Zemlyanov, J. P. Max, N. Kadasala, S. Zhao, and A. Wei, "Citrate-Stabilized Gold Nanorods," *Langmuir,* vol. 30, no. 46, pp. 13727-13730, 2014/11/25 2014.

[87] C. G. Khoury and T. Vo-Dinh, "Gold nanostars for surface-enhanced Raman scattering: synthesis, characterization and optimization," *Journal of Physical Chemistry C,* Article vol. 112, no. 48, pp. 18849-18859, 2008.

[88] W. P. Wuelfing, S. M. Gross, D. T. Miles, and R. W. Murray, "Nanometer gold clusters protected by surface-bound monolayers of thiolated poly(ethylene glycol) polymer electrolyte," *Journal of the American Chemical Society,* Letter vol. 120, no. 48, pp. 12696-12697, 1998.

[89] F. S. Damos, R. C. S. Luz, and L. T. Kubota, "Determination of thickness, dielectric constant of thiol films, and kinetics of adsorption using surface plasmon resonance," *Langmuir,* Article vol. 21, no. 2, pp. 602-609, 2005.

[90] S. Zeng, D. Baillargeat, H. P. Ho, and K. T. Yong, "Nanomaterials enhanced surface plasmon resonance for biological and chemical sensing applications," *Chemical Society Reviews,* Review vol. 43, no. 10, pp. 3426-3452, 2014.

[91] J.-M. Nam, J.-W. Oh, H. Lee, and Y. D. Suh, "Plasmonic Nanogap-Enhanced Raman Scattering with Nanoparticles," *Accounts of Chemical Research,* vol. 49, no. 12, pp. 2746-2755, 2016/12/20 2016.

[92] E. Le Ru and P. Etchegoin, "Principles of Surface-Enhanced Raman Spectroscopy," *Principles of Surface-Enhanced Raman Spectroscopy,* vol. 29, 01/01 2009.

[93] S. Schöttler *et al.*, "Protein adsorption is required for stealth effect of poly(ethylene glycol)- and poly(phosphoester)-coated nanocarriers."

[94] T. A. Larson, P. P. Joshi, and K. Sokolov, "Preventing protein adsorption and macrophage uptake of gold nanoparticles via a hydrophobic shield," *ACS Nano,* Article vol. 6, no. 10, pp. 9182-9190, 2012.

[95] C. D. Bain, E. B. Troughton, Y. T. Tao, J. Evall, G. M. Whitesides, and R. G. Nuzzo, "Formation of Monolayer Films by the Spontaneous Assembly of Organic Thiols from Solution onto Gold," *Journal of the American Chemical Society,* Article vol. 111, no. 1, pp. 321-335, 1989.

[96] E. L. Smith, C. A. Alves, J. W. Anderegg, M. D. Porter, and L. M. Siperko, "Deposition of Metal Overlayers at End-Group-Functionalized Thiolate Monolayers Adsorbed at Au. 1. Surface and Interfacial Chemical Characterization of Deposited Cu Overlayers at Carboxylic Acid-Terminated Structures," *Langmuir,* Article vol. 8, no. 11, pp. 2707-2714, 1992.

[97] J. C. Love, L. A. Estroff, J. K. Kriebel, R. G. Nuzzo, and G. M. Whitesides, "Self-Assembled Monolayers of Thiolates on Metals as a Form of Nanotechnology," *Chemical Reviews,* vol. 105, no. 4, pp. 1103-1170, 2005/04/01 2005.

[98] P. Harder, M. Grunze, R. Dahint, G. M. Whitesides, and P. E. Laibinis, "Molecular conformation in oligo(ethylene glycol)-terminated self-assembled monolayers on gold and silver surfaces determines their ability to resist protein adsorption," *Journal of Physical Chemistry B,* Article vol. 102, no. 2, pp. 426-436, 1998.

[99] F. Schulz, W. Friedrich, K. Hoppe, T. Vossmeyer, H. Weller, and H. Lange, "Effective PEGylation of gold nanorods," *Nanoscale,* Article vol. 8, no. 13, pp. 7296-7308, 2016.

[100] F. Schulz *et al.*, "Structure and Stability of PEG- and Mixed PEG-Layer-Coated Nanoparticles at High Particle Concentrations Studied In Situ by Small-Angle X-Ray Scattering," *Particle and Particle Systems Characterization,* Article vol. 35, no. 2, 2018, Art. no. 1700319.

[101] H. D. Hill, J. E. Millstone, M. J. Banholzer, and C. A. Mirkin, "The role radius of curvature plays in thiolated oligonucleotide loading on gold nanoparticles," *ACS Nano,* Article vol. 3, no. 2, pp. 418-424, 2009.

[102] J. S. Suk, Q. Xu, N. Kim, J. Hanes, and L. M. Ensign, "PEGylation as a strategy for improving nanoparticle-based drug and gene delivery," *Advanced Drug Delivery Reviews,* Review vol. 99, pp. 28-51, 2016.

[103] P. B. Johnson and R. W. Christy, "Optical Constants of the Noble Metals," *Physical Review B,* vol. 6, no. 12, pp. 4370-4379, 12/15/ 1972.

[104] M. A. Rampi, O. J. A. Schueller, and G. M. Whitesides, "Alkanethiol self-assembled monolayers as the dielectric of capacitors with nanoscale thickness," *Applied Physics Letters,* Article vol. 72, no. 14, pp. 1781-1783, 1998.

[105] B. Kumar, J. C. Bonvallet, and S. R. Crittenden, "Dielectric constants by multifrequency non-contact atomic force microscopy," *Nanotechnology,* Article vol. 23, no. 2, 2012, Art. no. 025707.

[106] M. D. Porter, T. B. Bright, D. L. Allara, and C. E. Chidsey, "Spontaneously Organized Molecular Assemblies. 4. Structural Characterization of n-Alkyl Thiol Monolayers on Gold by Optical Ellipsometry, Infrared Spectroscopy, and Electrochemistry," *Journal of the American Chemical Society,* Article vol. 109, no. 12, pp. 3559-3568, 1987.

[107] C. Li, V. C. Torres, and K. M. Tichauer, "Noninvasive detection of cancer spread to lymph nodes: A review of molecular imaging principles and protocols," *J Surg Oncol,* vol. 118, no. 2, pp. 301-314, Aug 2018.

[108] A. Goyal, "New Technologies for Sentinel Lymph Node Detection," *Breast Care,* vol. 13, no. 5, pp. 349-353, 2018.

[109] N. K. Tafreshi *et al.*, "Noninvasive detection of breast cancer lymph node metastasis using carbonic anhydrases IX and XII targeted imaging probes," *Clinical Cancer Research,* Article vol. 18, no. 1, pp. 207-219, 2012.

[110] K. M. Tichauer *et al.*, "Microscopic lymph node tumor burden quantified by macroscopic dual-tracer molecular imaging," *Nat Med,* vol. 20, no. 11, pp. 1348-53, Nov 2014.

[111] L. Sinha *et al.*, "Quantification of the binding potential of cell-surface receptors in fresh excised specimens via dual-probe modeling of SERS nanoparticles," (in eng), *Scientific reports,* vol. 5, pp. 8582-8582, 2015.

[112] N. Hamzei *et al.*, "Comparison of Kinetic Models for Dual-Tracer Receptor Concentration Imaging in Tumors," (in eng), *Austin journal of biomedical engineering,* vol. 1, no. 1, pp. austinpublishinggroup.com/biomedical-engineering/fulltext/ajbe-v1-id1002.php, 2014.

[113] N. L. Gruenke, M. O. McAnally, G. C. Schatz, and R. P. Van Duyne, "Balancing the Effects of Extinction and Enhancement for Optimal Signal in Surface-Enhanced Femtosecond Stimulated Raman Spectroscopy," *The Journal of Physical Chemistry C,* vol. 120, no. 51, pp. 29449-29454, 2016/12/29 2016.

[114] S. T. Sivapalan *et al.*, "Off-Resonance Surface-Enhanced Raman Spectroscopy from Gold Nanorod Suspensions as a Function of Aspect Ratio: Not What We Thought," *ACS Nano,* vol. 7, no. 3, pp. 2099-2105, 2013/03/26 2013.

[115] M. Li, J. W. Kang, R. R. Dasari, and I. Barman, "Shedding Light on the Extinction-Enhancement Duality in Gold Nanostar-Enhanced Raman Spectroscopy," *Angewandte Chemie International Edition,* https://doi.org/10.1002/anie.201409314 vol. 53, no. 51, pp. 14115-14119, 2014/12/15 2014.

[116] W. Xie, P. Qiu, and C. Mao, "Bio-imaging, detection and analysis by using nanostructures as SERS substrates," *Journal of Materials Chemistry,* Article vol. 21, no. 14, pp. 5190-5202, 2011.

[117] X. Huang, P. K. Jain, I. H. El-Sayed, and M. A. El-Sayed, "Gold nanoparticles: Interesting optical properties and recent applications in cancer diagnostics and therapy," *Nanomedicine,* Review vol. 2, no. 5, pp. 681-693, 2007.

[118] C. Chi *et al.*, "Intraoperative imaging-guided cancer surgery: from current fluorescence molecular imaging methods to future multi-modality imaging technology," (in eng), *Theranostics,* vol. 4, no. 11, pp. 1072-1084, 2014.

[119] S. P. Mulvaney, M. D. Musick, C. D. Keating, and M. J. Natan, "Glass-coated, analyte-tagged nanoparticles: A new tagging system based on detection with surface-enhanced Raman scattering," *Langmuir,* Article vol. 19, no. 11, pp. 4784-4790, 2003.

[120] C. Fernández-López, C. Mateo-Mateo, R. A. Álvarez-Puebla, J. Pérez-Juste, I. Pastoriza-Santos, and L. M. Liz-Marzán, "Highly controlled silica coating of PEG-capped metal

nanoparticles and preparation of SERS-encoded particles," *Langmuir,* Article vol. 25, no. 24, pp. 13894-13899, 2009.

[121] L. Rodríguez-Lorenzo *et al.*, "Intracellular mapping with SERS-encoded gold nanostars," *Integrative Biology,* Article vol. 3, no. 9, pp. 922-926, 2011.

[122] D. Rodríguez-Fernández, J. Langer, M. Henriksen-Lacey, and L. M. Liz-Marzán, "Hybrid Au-SiO2 core-satellite colloids as switchable SERS tags," *Chemistry of Materials,* Article vol. 27, no. 7, pp. 2540-2545, 2015.

[123] B. Mir-Simon, I. Reche-Perez, L. Guerrini, N. Pazos-Perez, and R. A. Alvarez-Puebla, "Universal one-pot and scalable synthesis of SERS encoded nanoparticles," *Chemistry of Materials,* Article vol. 27, no. 3, pp. 950-958, 2015.

[124] R. J. Stokes, A. Hernandez-Santana, A. Macaskill, P. A. G. Cormack, W. E. Smith, and D. Graham, "SERRS-active nanoparticle-polymer beads for ultra-sensitive biodiagnostic applications," *Micro and Nano Letters,* vol. 1, no. 1, pp. 57-61, 2006.

[125] A. McLintock, N. Hunt, and A. W. Wark, "Controlled side-by-side assembly of gold nanorods and dye molecules into polymer-wrapped SERRS-active clusters," *Chemical Communications,* Article vol. 47, no. 13, pp. 3757-3759, 2011.

[126] G. Bodelõn, V. Montes-García, C. Fernández-Lõpez, I. Pastoriza-Santos, J. Pérez-Juste, and L. M. Liz-Marzán, "Au@pNIPAM SERRS Tags for Multiplex Immunophenotyping Cellular Receptors and Imaging Tumor Cells," *Small,* Article vol. 11, no. 33, pp. 4149-4157, 2015.

[127] M. G. Soliman, B. Pelaz, W. J. Parak, and P. Del Pino, "Phase transfer and polymer coating methods toward improving the stability of metallic nanoparticles for biological applications," *Chemistry of Materials,* Article vol. 27, no. 3, pp. 990-997, 2015.

[128] J. Song, J. Zhou, and H. Duan, "Self-assembled plasmonic vesicles of SERS-encoded amphiphilic gold nanoparticles for cancer cell targeting and traceable intracellular drug delivery," *Journal of the American Chemical Society,* Article vol. 134, no. 32, pp. 13458-13469, 2012.

[129] S. Ip, C. M. MacLaughlin, N. Gunari, and G. C. Walker, "Phospholipid membrane encapsulation of nanoparticles for surface-enhanced raman scattering," *Langmuir,* Article vol. 27, no. 11, pp. 7024-7033, 2011.

[130] N. C. M. Tam, B. M. T. Scott, D. Voicu, B. C. Wilson, and G. Zheng, "Facile synthesis of raman active phospholipid gold nanoparticles," *Bioconjugate Chemistry,* Article vol. 21, no. 12, pp. 2178-2182, 2010.

[131] N. C. M. Tam, P. Z. McVeigh, T. D. MacDonald, A. Farhadi, B. C. Wilson, and G. Zheng, "Porphyrin-lipid stabilized gold nanoparticles for surface enhanced Raman scattering based imaging," *Bioconjugate Chemistry,* Article vol. 23, no. 9, pp. 1726-1730, 2012.

[132] M. Holay *et al.*, "Organotropic Targeting of Biomimetic Nanoparticles to Treat Lung Disease," *Bioconjugate Chemistry,* 2022/03/14 2022.

[133] L. Y. Wang, S. G. Wang, and J. Z. Bei, "Synthesis and characterization of macroinitiator-amino terminated PEG and poly(γ-benzyl-L-glutamate)-PEO-poly(γ-benzyl-L-glutamate triblock copolymer," *Polymers for Advanced Technologies,* Article vol. 15, no. 10, pp. 617-621, 2004.

[134] T. Akagi, M. Higashi, T. Kaneko, T. Kida, and M. Akashi, "Hydrolytic and enzymatic degradation of nanoparticles based on amphiphilic poly(γ-glutamic acid)-graft-L-phenylalanine copolymers," *Biomacromolecules,* Article vol. 7, no. 1, pp. 297-303, 2006.

[135] S. Sekiguchi, K. Niikura, Y. Matsuo, and K. Ijiro, "Hydrophilic gold nanoparticles adaptable for hydrophobic solvents," *Langmuir,* Article vol. 28, no. 13, pp. 5503-5507, 2012.

[136] G. Zhang *et al.*, "Influence of anchoring ligands and particle size on the colloidal stability and in vivo biodistribution of polyethylene glycol-coated gold nanoparticles in tumor-xenografted mice," *Biomaterials,* Article vol. 30, no. 10, pp. 1928-1936, 2009.

[137] A. M. Alkilany *et al.*, "Colloidal stability of citrate and mercaptoacetic acid capped gold nanoparticles upon lyophilization: Effect of capping ligand attachment and type of cryoprotectants," *Langmuir,* Article vol. 30, no. 46, pp. 13799-13808, 2014.

[138] A. Gupta *et al.*, "Ultrastable and Biofunctionalizable Gold Nanoparticles," *ACS Applied Materials and Interfaces,* Article vol. 8, no. 22, pp. 14096-14101, 2016.

[139] S. Ip *et al.*, "Dual-Mode Dark Field and Surface-Enhanced Raman Scattering Liposomes for Lymphoma and Leukemia Cell Imaging," *Langmuir,* vol. 35, no. 5, pp. 1534-1543, 2019/02/05 2019.

[140] J. Hu Che-Ming, L. Zhang, S. Aryal, C. Cheung, H. Fang Ronnie, and L. Zhang, "Erythrocyte membrane-camouflaged polymeric nanoparticles as a biomimetic delivery platform," *Proceedings of the National Academy of Sciences,* vol. 108, no. 27, pp. 10980-10985, 2011/07/05 2011.

[141] Y. Liu, J. Luo, X. Chen, W. Liu, and T. Chen, "Cell Membrane Coating Technology: A Promising Strategy for Biomedical Applications," *Nano-Micro Letters,* vol. 11, no. 1, p. 100, 2019/11/16 2019.

[142] B. T. Luk and L. Zhang, "Cell membrane-camouflaged nanoparticles for drug delivery," *Journal of Controlled Release,* Article vol. 220, pp. 600-607, 2015.

[143] C. M. J. Hu, R. H. Fang, J. Copp, B. T. Luk, and L. Zhang, "A biomimetic nanosponge that absorbs pore-forming toxins," *Nature Nanotechnology,* Article vol. 8, no. 5, pp. 336-340, 2013.

[144] F. Wang *et al.*, "Hydrogel retaining toxin-absorbing nanosponges for local treatment of methicillin-resistant Staphylococcus aureus infection," *Advanced Materials,* Article vol. 27, no. 22, pp. 3437-3443, 2015.

[145] A. Zinger *et al.*, "Enhancing Inflammation Targeting Using Tunable Leukocyte-Based Biomimetic Nanoparticles," *ACS Nano,* Article vol. 15, no. 4, pp. 6326-6339, 2021.

[146] R. H. Fang *et al.*, "Lipid-insertion enables targeting functionalization of erythrocyte membrane-cloaked nanoparticles," *Nanoscale,* Article vol. 5, no. 19, pp. 8884-8888, 2013.

[147] N. G. Bastús, J. Comenge, and V. Puntes, "Kinetically controlled seeded growth synthesis of citrate-stabilized gold nanoparticles of up to 200 nm: Size focusing versus ostwald ripening," *Langmuir,* Article vol. 27, no. 17, pp. 11098-11105, 2011.

[148] J. E. Park, Y. Lee, and J. M. Nam, "Precisely Shaped, Uniformly Formed Gold Nanocubes with Ultrahigh Reproducibility in Single-Particle Scattering and Surface-Enhanced Raman Scattering," *Nano Letters,* Article vol. 18, no. 10, pp. 6475-6482, 2018.

[149] E. Ben-Akiva, R. A. Meyer, H. Yu, J. T. Smith, D. M. Pardoll, and J. J. Green, "Biomimetic anisotropic polymeric nanoparticles coated with red blood cell membranes for enhanced circulation and toxin removal," *Science Advances,* Article vol. 6, no. 16, 2020, Art. no. eaay9035.

[150] E. Boisselier and D. Astruc, "Gold nanoparticles in nanomedicine: preparations, imaging, diagnostics, therapies and toxicity," *Chemical Society Reviews,* Article vol. 38, no. 6, pp. 1759-1782, 2009.

[151] Y. Jiang *et al.*, "The Interplay of Size and Surface Functionality on the Cellular Uptake of Sub-10 nm Gold Nanoparticles," *ACS Nano,* Article vol. 9, no. 10, pp. 9986-9993, 2015.

[152] Y. Wang *et al.*, "Enhanced dispersion stability of gold nanoparticles by the physisorption of cyclic poly(ethylene glycol)," *Nature Communications,* Article vol. 11, no. 1, 2020, Art. no. 6089.

[153] S. Ji *et al.*, "RGD-conjugated albumin nanoparticles as a novel delivery vehicle in pancreatic cancer therapy," *Cancer Biology and Therapy,* Article vol. 13, no. 4, pp. 206-215, 2012.

[154] N. Stojanovic *et al.*, "Differential effects of integrin av knockdown and cilengitide on sensitization of triple-negative breast cancer and melanoma cells to microtubule poisons," *Molecular Pharmacology,* Article vol. 94, no. 6, pp. 1334-1351, 2018.

[155] Z. Chen *et al.*, "Cancer Cell Membrane-Biomimetic Nanoparticles for Homologous-Targeting Dual-Modal Imaging and Photothermal Therapy," *ACS Nano,* Article vol. 10, no. 11, pp. 10049-10057, 2016.

[156] T. Fujimoto and I. Parmryd, "Interleaflet coupling, pinning, and leaflet asymmetry-major players in plasma membrane nanodomain formation," *Frontiers in Cell and Developmental Biology,* Review vol. 4, no. JAN, 2017, Art. no. 155.

[157] M. Manaargadoo-Catin, A. Ali-Cherif, J. L. Pougnas, and C. Perrin, "Hemolysis by surfactants - A review," *Advances in Colloid and Interface Science,* Review vol. 228, pp. 1-16, 2016.

[158] B. T. Luk *et al.*, "Interfacial interactions between natural RBC membranes and synthetic polymeric nanoparticles," *Nanoscale,* Article vol. 6, no. 5, pp. 2730-2737, 2014.

[159] C. Lemarchand, R. Gref, and P. Couvreur, "Polysaccharide-decorated nanoparticles," *European Journal of Pharmaceutics and Biopharmaceutics,* Review vol. 58, no. 2, pp. 327-341, 2004.

[160] P. Raveendran, J. Fu, and S. L. Wallen, "Completely "Green" Synthesis and Stabilization of Metal Nanoparticles," *Journal of the American Chemical Society,* Article vol. 125, no. 46, pp. 13940-13941, 2003.

[161] X. Sun, Y. Wu, Z. Song, and X. Chen, "A review of natural polysaccharides for food cryoprotection: Ice crystals inhibition and cryo-stabilization," *Bioactive Carbohydrates and Dietary Fibre,* vol. 27, p. 100291, 2022/05 2022.

[162] A. Akbarzadeh *et al.*, "Liposome: Classification, preparation, and applications," *Nanoscale Research Letters,* Article vol. 8, no. 1, 2013, Art. no. 102.

[163] S. Sur, A. C. Fries, K. W. Kinzler, S. Zhou, and B. Vogelstein, "Remote loading of preencapsulated drugs into stealth liposomes," *Proceedings of the National Academy of Sciences of the United States of America,* Article vol. 111, no. 6, pp. 2283-2288, 2014.

[164] W. Gao, C. M. J. Hu, R. H. Fang, B. T. Luk, J. Su, and L. Zhang, "Surface functionalization of gold nanoparticles with red blood cell membranes," *Advanced Materials,* Article vol. 25, no. 26, pp. 3549-3553, 2013.

[165] C. M. J. Hu, L. Zhang, S. Aryal, C. Cheung, R. H. Fang, and L. Zhang, "Erythrocyte membrane-camouflaged polymeric nanoparticles as a biomimetic delivery platform," *Proceedings of the National Academy of Sciences of the United States of America,* Article vol. 108, no. 27, pp. 10980-10985, 2011.

[166] M. Goto *et al.*, "Image-guided surgery with a new tumour-targeting probe improves the identification of positive margins," *eBioMedicine,* vol. 76, p. 103850, 2022/02/01/ 2022.

[167] S. Keereweer *et al.*, "Optical image-guided surgery--where do we stand?," *Mol Imaging Biol,* vol. 13, no. 2, pp. 199-207, Apr 2011.

[168] G. Thomas *et al.*, "Evaluating feasibility of an automated 3-dimensional scanner using Raman spectroscopy for intraoperative breast margin assessment," *Scientific Reports,* vol. 7, no. 1, p. 13548, 2017/10/19 2017.

[169] K. Y. Ju, S. Lee, J. Pyo, J. Choo, and J. K. Lee, "Bio-Unspired development of a dual-Mode nanoprobe for MRI and Raman imaging," *Small,* Article vol. 11, no. 1, pp. 84-89, 2015.

[170] P. Beard, "Biomedical photoacoustic imaging," *Interface Focus,* Review vol. 1, no. 4, pp. 602-631, 2011.

[171] M. V. Yigit *et al.*, "Noninvasive MRI-SERS imaging in living mice using an innately bimodal nanomaterial," *ACS Nano,* Article vol. 5, no. 2, pp. 1056-1066, 2011.

[172] X. Gao *et al.*, "Guiding Brain-Tumor Surgery via Blood–Brain-Barrier-Permeable Gold Nanoprobes with Acid-Triggered MRI/SERRS Signals," *Advanced Materials,* Article vol. 29, no. 21, 2017, Art. no. 1603917.

[173] A. M. Mohs *et al.*, "Hand-held spectroscopic device for in vivo and intraoperative tumor detection: Contrast enhancement, detection sensitivity, and tissue penetration," *Analytical Chemistry,* Article vol. 82, no. 21, pp. 9058-9065, 2010.

[174] W. Li and X. Chen, "Gold nanoparticles for photoacoustic imaging," (in eng), *Nanomedicine (London, England),* vol. 10, no. 2, pp. 299-320, 2015.

[175] R. García-Álvarez *et al.*, "Optimizing the Geometry of Photoacoustically Active Gold Nanoparticles for Biomedical Imaging," *ACS Photonics,* vol. 7, no. 3, pp. 646-652, 2020/03/18 2020.

[176] V. Neuschmelting *et al.*, "Dual-Modality Surface-Enhanced Resonance Raman Scattering and Multispectral Optoacoustic Tomography Nanoparticle Approach for Brain Tumor Delineation," *Small,* https://doi.org/10.1002/smll.201800740 vol. 14, no. 23, p. 1800740, 2018/06/01 2018.

[177] Y. Wen, V. X. Truong, and M. Li, "Real-Time Intraoperative Surface-Enhanced Raman Spectroscopy-Guided Thermosurgical Eradication of Residual Microtumors in Orthotopic Breast Cancer," *Nano Letters,* vol. 21, no. 7, pp. 3066-3074, 2021/04/14 2021.

[178] S. Luo, E. Zhang, Y. Su, T. Cheng, and C. Shi, "A review of NIR dyes in cancer targeting and imaging," *Biomaterials,* Review vol. 32, no. 29, pp. 7127-7138, 2011.

[179] G. Hong, A. L. Antaris, and H. Dai, "Near-infrared fluorophores for biomedical imaging," *Nature Biomedical Engineering,* vol. 1, no. 1, p. 0010, 2017/01/10 2017.

[180] H. Ramakonar *et al.*, "Intraoperative detection of blood vessels with an imaging needle during neurosurgery in humans," (in eng), *Science advances,* vol. 4, no. 12, pp. eaav4992-eaav4992, 2018.

[181] G. Hong *et al.*, "Through-skull fluorescence imaging of the brain in a new near-infrared window," *Nature Photonics,* vol. 8, no. 9, pp. 723-730, 2014/09/01 2014.

[182] H.-n. Xie, R. Stevenson, N. Stone, A. Hernandez-Santana, K. Faulds, and D. Graham, "Tracking Bisphosphonates through a 20 mm Thick Porcine Tissue by Using Surface-Enhanced Spatially Offset Raman Spectroscopy," *Angewandte Chemie International Edition,* https://doi.org/10.1002/anie.201203728 vol. 51, no. 34, pp. 8509-8511, 2012/08/20 2012.

[183] F. Nicolson, B. Andreiuk, C. Andreou, H. T. Hsu, S. Rudder, and M. F. Kircher, "Non-invasive In Vivo Imaging of Cancer Using Surface-Enhanced Spatially Offset Raman Spectroscopy (SESORS)," *Theranostics,* vol. 9, no. 20, pp. 5899-5913, 2019.

[184] S. M. Asiala, N. C. Shand, K. Faulds, and D. Graham, "Surface-Enhanced, Spatially Offset Raman Spectroscopy (SESORS) in Tissue Analogues," *ACS Appl Mater Interfaces,* vol. 9, no. 30, pp. 25488-25494, Aug 2 2017.

[185] Y. Wang, A. B. Serrano, K. Sentosun, S. Bals, and L. M. Liz-Marzán, "Stabilization and Encapsulation of Gold Nanostars Mediated by Dithiols," *Small,* https://doi.org/10.1002/smll.201500703 vol. 11, no. 34, pp. 4314-4320, 2015/09/01 2015.

[186] D. Rovati *et al.*, "High Stability Thiol-Coated Gold Nanostars Monolayers with Photo-Thermal Antibacterial Activity and Wettability Control," *Nanomaterials,* vol. 9, no. 9, 2019.

[187] M. A. Bedics *et al.*, "Extreme red shifted SERS nanotags," *Chemical Science,* 10.1039/C4SC03917C vol. 6, no. 4, pp. 2302-2306, 2015.

[188] J. Li *et al.*, "Surface-Enhanced Raman Scattering Active Plasmonic Nanoparticles with Ultrasmall Interior Nanogap for Multiplex Quantitative Detection and Cancer Cell Imaging," *Anal Chem,* vol. 88, no. 15, pp. 7828-36, Aug 2 2016.

[189] Y. Zhao, F. Zheng, W. Ke, W. Zhang, L. Shi, and H. Liu, "Gap-Tethered Au@AgAu Raman Tags for the Ratiometric Detection of MC-LR," *Analytical Chemistry,* vol. 91, no. 11, pp. 7162-7172, 2019/06/04 2019.

[190] Z. Ye, L. Lin, Z. Tan, Y.-J. Zeng, S. Ruan, and J. Ye, "Sub-100 nm multi-shell bimetallic gap-enhanced Raman tags," *Applied Surface Science,* vol. 487, pp. 1058-1067, 2019/09/01/ 2019.

[191] W. B. Cai *et al.*, "Investigation of surface-enhanced Raman scattering from platinum electrodes using a confocal Raman microscope: dependence of surface roughening pretreatment," *Surface Science,* vol. 406, no. 1, pp. 9-22, 1998/05/31/ 1998.

[192] P. M. Ramos and I. Ruisánchez, "Noise and background removal in Raman spectra of ancient pigments using wavelet transform," *Journal of Raman Spectroscopy,* https://doi.org/10.1002/jrs.1370 vol. 36, no. 9, pp. 848-856, 2005/09/01 2005.

[193] X. Jin, B. N. Khlebtsov, V. A. Khanadeev, N. G. Khlebtsov, and J. Ye, "Rational Design of Ultrabright SERS Probes with Embedded Reporters for Bioimaging and Photothermal

Therapy," *ACS Applied Materials & Interfaces,* vol. 9, no. 36, pp. 30387-30397, 2017/09/13 2017.

[194] A. N. Bashkatov, E. A. Genina, and V. V. Tuchin, "OPTICAL PROPERTIES OF SKIN, SUBCUTANEOUS, AND MUSCLE TISSUES: A REVIEW," *Journal of Innovative Optical Health Sciences,* vol. 04, no. 01, pp. 9-38, 2011/01/01 2011.

[195] S. L. Jacques, "Optical properties of biological tissues: a review," *Physics in Medicine and Biology,* vol. 58, no. 11, pp. R37-R61, 2013/05/10 2013.

[196] J. B. Epstein and J. J. Sciubba, "Chapter 4 - Strategies for Oral Cancer Detection," in *Early Diagnosis and Treatment of Cancer Series: Head and Neck Cancers*, W. M. Koch, Ed. Philadelphia: Content Repository Only!, 2010, pp. 45-58.

[197] S. Diao *et al.*, "Biological imaging without autofluorescence in the second near-infrared region," *Nano Research,* vol. 8, no. 9, pp. 3027-3034, 2015/09/01 2015.

[198] S. Rivas-Arancibia, E. Rodríguez-Martínez, I. Badillo-Ramírez, U. López-González, and J. M. Saniger, "Structural Changes of Amyloid Beta in Hippocampus of Rats Exposed to Ozone: A Raman Spectroscopy Study," *Frontiers in Molecular Neuroscience,* 10.3389/fnmol.2017.00137 vol. 10, p. 137, 2017.

[199] M. Kozielski, T. Buchwald, M. Szybowicz, Z. Błaszczak, A. Piotrowski, and B. Ciesielczyk, "Determination of composition and structure of spongy bone tissue in human head of femur by Raman spectral mapping," *Journal of Materials Science: Materials in Medicine,* vol. 22, no. 7, pp. 1653-1661, 2011/07/01 2011.

[200] M. M. Vega, A. Bonifacio, V. Lughi, S. Marsi, S. Carrato, and V. Sergo, "Long-term stability of surfactant-free gold nanostars," *Journal of Nanoparticle Research,* vol. 16, no. 11, p. 2729, 2014/11/09 2014.